

Volcanology of the A154N kimberlite at Diavik:  
implications for eruption dynamics

by

Stephen William Moss

M.Sc., The University of Montana, 2001

B.Sc., Wheaton College, 1999

A THESIS SUBMITTED IN PARTIAL FULFILLMENT OF THE REQUIREMENTS  
FOR THE DEGREE OF

DOCTOR OF PHILOSOPHY

in

The Faculty of Graduate Studies

(Geological Sciences)

THE UNIVERSITY OF BRITISH COLUMBIA

(Vancouver)

September 2009

© Stephen William Moss, 2009

## Abstract

Eruptions of kimberlite volcanoes are a poorly-understood phenomena, as there have been no historical eruptions of kimberlite, and primary deposits and edifices of kimberlite volcanoes are rarely preserved. In particular, the styles of explosion, magma fragmentation, and primary deposition of kimberlite remain unclear. This thesis comprises field and laboratory study of five kimberlite deposits within the A154N kimberlite volcano at Diavik, NWT, Canada. These studies provide critical descriptive and semi-quantitative data on the geometries, component variations, and relative age-relationships of deposits. These data are collected in order to link volcanic deposits with eruption processes in the following ways:

A) Pyroclastic kimberlite hosted by the A154N pipe is shown to derive from a different kimberlite volcano. Thus, kimberlite volcanoes can act as receptacles for primary volcanic products from the eruptions of adjacent kimberlite pipes, leading to a 'cross-fertilizing' distribution of magma batches.

B) Image analysis, based on manual and computer-assisted digitization, is used to establish characteristic properties of olivine crystals in intrusive coherent kimberlite, including modal %, size range, shape variability, and population parameters. These properties serve as a baseline in understanding kimberlite eruption style and fragmentation.

C) Study of A154N deposits documents phase separation of kimberlite magmas in time and space during ascent and records an evolution in phase proportions (crystals: melt: gas) within and/or between emplacement events. Phase separation can determine the surface expression of kimberlite volcanoes, the degree of melt separation from olivine crystals during eruption and, thus, the amount of preserved crystallized kimberlite around olivine crystals in deposits.

D) Measured and estimated physical properties of kimberlite magmas are combined with 3-D models for conduit geometry to show eruption durations of minutes to hours for the A154N volcano.

E) Observations of primary pyroclastic products in kimberlite deposits show eruptions can both modify the sizes, shapes and distributions of olivine crystals and separate melt from olivine. Relative changes in the proportion of these two parameters as preserved in deposits may serve as a proxy for kimberlite eruption intensity.

Finally, these volcanic processes are shown to have direct implications for the distribution of diamonds within kimberlite pipes.

## Table of contents

<b>Abstract.....</b>	<b>ii</b>
<b>Table of contents .....</b>	<b>iii</b>
<b>List of figures.....</b>	<b>viii</b>
<b>List of tables.....</b>	<b>x</b>
<b>List of symbols.....</b>	<b>xi</b>
<b>Acknowledgements .....</b>	<b>xiv</b>
<b>Dedication .....</b>	<b>xvi</b>
<b>Co-authorship statement .....</b>	<b>xvii</b>
<b>1 Introduction.....</b>	<b>1</b>
<b>1.1 Previous kimberlite emplacement models .....</b>	<b>3</b>
1.1.1 Models derived from southern Africa .....	3
1.1.2 Canadian kimberlites and new models .....	5
1.1.3 Contemporary composite models .....	9
<b>1.2 Outstanding gaps in kimberlite volcanology .....</b>	<b>13</b>
1.2.1 Kimberlite eruption style .....	14
1.2.2 Physical properties of kimberlite magmas .....	16
1.2.3 Pyroclastic kimberlite .....	18
<b>1.3 Diavik kimberlites.....</b>	<b>20</b>
<b>1.4 Organization of thesis.....</b>	<b>25</b>
1.4.1 Manuscript chapters .....	25
1.4.2 Appendix overview .....	27
<b>1.5 References.....</b>	<b>30</b>
<b>2 Progressive infilling of a kimberlite pipe at Diavik, Northwest Territories, Canada: insights from volcanic facies architecture, textures, and granulometry ....</b>	<b>37</b>
<b>2.1 Introduction.....</b>	<b>37</b>
<b>2.2 Geology of the A154N kimberlite pipe.....</b>	<b>39</b>
2.2.1 The Diavik kimberlite cluster .....	39
2.2.2 The A154N kimberlite pipe .....	39
2.2.3 Massive volcanoclastic kimberlite (MVK).....	42
2.2.4 Stratified volcanoclastic kimberlite (SVK).....	44

2.2.5 Graded pyroclastic kimberlite (PK) .....	48
<b>2.3 Interpretation</b> .....	<b>55</b>
2.3.1 MVK – deposition from a collapsing eruption column .....	55
2.3.2 SVK – re-sedimentation from volcanic edifice .....	56
2.3.3 PK <sub>2</sub> - exotic tephra deposited into a crater lake .....	57
<b>2.4 Discussion</b> .....	<b>60</b>
2.4.1 Eruption model for the A154N pipe .....	60
2.4.2 Kimberlite eruption dynamics: insights from PK <sub>2</sub> .....	62
2.4.3 Cross-fertilization of kimberlite: economic implications .....	65
<b>2.5 References</b> .....	<b>66</b>
<b>3 Olivine crystal size distributions in intrusive coherent kimberlite</b> .....	<b>71</b>
<b>3.1 Introduction</b> .....	<b>71</b>
<b>3.2 Background</b> .....	<b>72</b>
3.2.1 Olivine crystals in kimberlite.....	72
3.2.2 Previous measurement and characterization .....	73
<b>3.3 Methods</b> .....	<b>74</b>
3.3.1 Sample selection .....	74
3.3.2 Manual tracing method .....	78
3.3.3 Crystal size distributions (CSDs).....	78
<b>3.4 Results</b> .....	<b>82</b>
3.4.1 Crystal sizes .....	82
3.4.2 Crystal abundances (frequencies and modal %) .....	82
3.4.3 Crystal shapes .....	86
3.4.4 Distribution characterization.....	86
<b>3.5 Discussion</b> .....	<b>92</b>
3.5.1 Olivine crystal properties.....	92
3.5.2 Olivine crystals and magmatic geologic processes.....	94
3.5.3 Further applications for olivine crystal data .....	98
<b>3.6 References</b> .....	<b>99</b>
<b>4 Spatial and temporal evolution of kimberlite magma at A154N, Diavik, Northwest Territories, Canada</b> .....	<b>104</b>
<b>4.1 Introduction</b> .....	<b>104</b>

<b>4.2 Field mapping</b> .....	105
4.2.1 Early dykes (CK <sub>1</sub> ) .....	107
4.2.2 Pyroclastic kimberlite (PK <sub>1</sub> ) .....	109
4.2.3 Coherent kimberlite (CK <sub>2</sub> ).....	111
4.2.4 Re-sedimented volcanoclastic kimberlite (RVK) and pyroclastic (PK <sub>2</sub> ) kimberlite .....	111
<b>4.3 Componentry</b> .....	113
4.3.1 Olivine crystal abundances .....	114
4.3.2 Juvenile pyroclasts from PK <sub>1</sub> .....	114
4.3.3 Textural evidence of volatile content.....	116
<b>4.4 Discussion and Interpretation:</b> .....	118
4.4.1 Variations in olivine content with time.....	120
4.4.2 CO <sub>2</sub> and H <sub>2</sub> O variation with time .....	123
4.4.3 Fluid phase separation in kimberlite .....	124
4.4.4 Vent geometry and mass flux (M <sub>7</sub> ).....	126
4.4.5 Eruption duration calculations .....	130
<b>4.5 Emplacement model for the A154N kimberlite</b> .....	132
<b>4.6 References</b> .....	135
<b>5 Fragmentation in kimberlite: products and intensity of explosive eruption.....</b>	<b>139</b>
<b>5.1 Introduction</b> .....	139
<b>5.2 Hypothesis 1: olivine fragmentation during explosive eruption</b> .....	144
5.2.1 Methods.....	145
5.2.2 Results.....	148
<b>5.3 Hypothesis 2: melt is stripped from olivine by eruption processes</b> .....	151
5.3.1 Methods.....	152
5.3.2 Results.....	154
<b>5.4 Discussion</b> .....	156
5.4.1 Olivine crystal breaking.....	156
5.4.2 Melt separation during eruption.....	160
<b>5.5 Interpretation</b> .....	169
<b>5.6 New eruption index</b> .....	170
<b>5.7 References</b> .....	175

<b>6</b>	<b>The volcanology of A154N: implications for kimberlites and diamonds.....</b>	<b>180</b>
6.1	Summary of descriptive data on A154N from chapters 2 – 4.....	180
6.2	Emplacement summary for A154N.....	184
6.3	Implications of this work for kimberlite volcanology.....	185
6.4	Diamond distributions in volcanic kimberlite deposits.....	187
6.4.1	Olivine and diamond in intrusive coherent kimberlite.....	188
6.4.2	Distinguishing magma ‘pulses’ or ‘batches’ using juvenile pyroclasts.....	190
6.4.3	Single pipes can contain deposits sourced from multiple pipes.....	191
6.4.4	Eruption style, intensity and diamond grade.....	194
6.5	A comparison of olivine and diamond: olivine CSDs in A154S.....	196
6.6	Limitations of the methods, results and implications within thesis.....	203
6.7	Areas for future study.....	205
6.7.1	Olivine CSDs.....	205
6.7.2	Image analysis and components in kimberlite rocks.....	205
6.7.3	Analogue experiments to determine magma properties.....	205
6.7.4	Phreatomagmatic eruptions and deposits.....	206
6.8	References.....	208
<b>7</b>	<b>Appendices.....</b>	<b>211</b>
7.1	Organization of appendices.....	211
7.2	Appendix – Chapter 2 (digital).....	213
7.3	Appendix – Chapter 3.....	213
7.3.1	Appendix – Chapter 3: Manual image analysis.....	213
7.3.2	Appendix – Chapter 3: Automatic image analysis methods for crystal size distributions of olivine in kimberlite.....	222
7.3.3	Appendix – Chapter 3 (digital).....	252
7.4	Appendix – Chapter 4 (digital).....	252
7.5	Appendix – Chapter 5 (digital).....	252
7.6	Appendix – Chapter 6 (digital).....	252
7.7	Appendix – Chapter 7 (digital).....	252
7.8	List of presentations during PhD.....	252
7.8.1	Peer-reviewed publications.....	252
7.8.2	Conference abstracts.....	252

7.8.3 Other publications .....	254
<b>7.9 Published papers (as of 06.25.06) .....</b>	<b>254</b>
7.9.1 Moss et al., 2008, JVGR (digital) .....	254
7.9.2 Moss et al., 2009, LITHOS (digital) .....	254
7.9.3 Holden et al., 2008, Computational Geosciences (digital) .....	254

## List of figures

<b>Figure 1.1:</b> Illustration of a kimberlite pipe.....	4
<b>Figure 1.2:</b> “Top-down” emplacement models.....	6
<b>Figure 1.3:</b> Explosive magmatic model (Field and Scott Smith, 1999).....	7
<b>Figure 1.4:</b> Canadian kimberlite pipe geometries.....	8
<b>Figure 1.5:</b> Composite emplacement model by Wilson and Head (2004).....	11
<b>Figure 1.6:</b> Composite emplacement model by Cas et al. (2008).....	12
<b>Figure 1.7:</b> Classic volcanological fragmentation index of Walker (1973).....	15
<b>Figure 1.8:</b> Typical intrusive coherent kimberlite.....	17
<b>Figure 1.9:</b> Location of Diavik kimberlite cluster.....	21
<b>Figure 1.10:</b> Geology of East Island, Lac de Gras (after Stubbley, 1998).....	22
<b>Figure 1.11:</b> 3-D images and summaries of kimberlite pipes at Diavik, NWT.....	23
<b>Figure 2.1:</b> Maps of Diavik kimberlite cluster.....	40
<b>Figure 2.2:</b> 3D GoCad™ model of A154N pipe.....	41
<b>Figure 2.3:</b> Features of MVK <sub>1</sub> and MVK <sub>2</sub> .....	43
<b>Figure 2.4:</b> Graphic log of MVK, SVK, and PK.....	45
<b>Figure 2.5:</b> Photographic plate of SVK features.....	47
<b>Figure 2.6:</b> Graphic log of PK <sub>2a</sub> and PK <sub>2b</sub> .....	49
<b>Figure 2.7:</b> Pyroclastic features of PK <sub>2</sub> .....	50
<b>Figure 2.8:</b> Granulometry data for PK <sub>2</sub> .....	54
<b>Figure 2.9:</b> Comparison of PK <sub>2</sub> deposit with other deposit types.....	58
<b>Figure 2.10:</b> Six-stage eruption model for A154N.....	61
<b>Figure 3.1:</b> A154N kimberlite pipe at Diavik, Northwest Territories.....	75
<b>Figure 3.2:</b> Greyscale images of manual tracings.....	77
<b>Figure 3.3:</b> Integration of digital scans of polished slab and thin section.....	79
<b>Figure 3.4:</b> 2D olivine crystal size data from t.s. and polished slabs.....	80
<b>Figure 3.5:</b> Scale-integrated (normalized) and truncated 2D olivine crystal data.....	81
<b>Figure 3.6:</b> Scale-integrated, truncated and binned olivine crystal data.....	85
<b>Figure 3.7:</b> Olivine crystal shapes.....	87
<b>Figure 3.8:</b> Normalized, truncated, and corrected CSDs.....	89
<b>Figure 3.9:</b> Geological processes and impact on olivine CSDs).....	95
<b>Figure 3.10:</b> Power-law parameters for olivine.....	97
<b>Figure 4.1:</b> Location of the Diavik kimberlite field and internal units of A154N.....	106
<b>Figure 4.2:</b> Field and hand sample photographs of pre-cursor CK <sub>1</sub> dyke at A154N.....	108
<b>Figure 4.3:</b> Distribution and properties of PK <sub>1</sub> within A154N.....	110
<b>Figure 4.4:</b> CK <sub>2</sub> within A154N.....	112
<b>Figure 4.5:</b> Olivine size distributions.....	115
<b>Figure 4.6:</b> Analysis of juvenile pyroclasts from PK <sub>1</sub> of A154N.....	117
<b>Figure 4.7:</b> Photomicrographs of select juvenile pyroclasts (Jp) from PK <sub>1</sub> .....	119
<b>Figure 4.8:</b> Vent geometries and mass fluxes for A154N.....	127
<b>Figure 4.9:</b> Model for emplacement and eruption of A154N.....	133
<b>Figure 5.1:</b> Photographs of juvenile pyroclasts of kimberlite at Diavik, NWT.....	141
<b>Figure 5.2:</b> Olivine crystal shapes in coherent and pyroclastic kimberlite.....	146
<b>Figure 5.3:</b> Location of the Diavik kimberlite field and internal units of A154N.....	147
<b>Figure 5.4:</b> Tests for olivine crystal modification.....	149
<b>Figure 5.5:</b> Variable crystal – melt relationships in pyroclastic kimberlite deposits.....	153

<b>Figure 5.6:</b> Parametric analysis of juvenile pyroclasts (JPs) .....	157
<b>Figure 5.7:</b> Properties of olivine crystals contributing to crystal breaking.....	159
<b>Figure 5.8:</b> Relative component and velocity ratios and consequences for disruption..	163
<b>Figure 5.9:</b> Fluid mechanics properties relating gas, liquid and solid surfaces .....	166
<b>Figure 5.11:</b> New fragmentation index for erupting kimberlite magmas .....	173
<b>Figure 6.1:</b> Hypothetical effects of volcanic processes on diamond size distributions .	189
<b>Figure 6.2:</b> Schematic illustration of two cross-fertilizing volcanic eruptions.....	192
<b>Figure 6.3:</b> Scenarios of true value .....	193
<b>Figure 6.4:</b> Economic implications of closely-spaced kimberlite pipes. ....	195
<b>Figure 6.5:</b> Deposit characteristics and relative value scale .....	197
<b>Figure 6.6:</b> Sample locations for A154S olivine CSD pilot study.....	199
<b>Figure 6.7:</b> Olivine crystal size distributions for A154s.....	200
<b>Figure 6.8:</b> Mean crystal size (carats) vs. number of crystals.....	201
<b>Figure A3.1:</b> Images of kimberlite from Diavik kimberlite field .....	224
<b>Figure A3.2:</b> Summary of olivine detection system .....	227
<b>Figure A3.3:</b> Texture analysis output.....	232
<b>Figure A3.4:</b> Combined likelihood images .....	232
<b>Figure A3.5:</b> Two examples of segmentation .....	233
<b>Figure A3.6:</b> Results of automatic processing .....	237
<b>Figure A3.7:</b> CSDs from manual and automatic methods .....	239
<b>Figure A3.8:</b> Regions identified by manual methods but automatic .....	240
<b>Figure A3.9:</b> Roughness test.....	242
<b>Figure A3.10:</b> Discrepancies between estimated and observed perimeters and areas...	246
<b>Figure A3.11:</b> Circularity test.....	247

## List of tables

<b>Table 3.1:</b> Summary of 2D olivine crystal size data in thin sections.....	83
<b>Table 3.2:</b> Summary of 2D olivine crystal data in slabs .....	83
<b>Table 3.3:</b> Summary of normalized 2D olivine crystal data in slabs .....	84
<b>Table 3.4:</b> Representative data from manual digitization of olivine.....	84
<b>Table 3.5:</b> Summary of best-fit parameters and RMSE .....	91
<b>Table 4.1:</b> Summary of components properties in units of A154N .....	121
<b>Table 5.1:</b> Key attributes of pyroclasts from around the world .....	140
<b>Table 5.2:</b> Summary of olivine properties in CK and PK.....	150
<b>Table 5.3:</b> Representative olivine content in CK, PK <sub>2</sub> and JPs.....	155
<b>Table 6.1:</b> Summary of component properties.....	182
<b>Table 6.2:</b> Summary of deposit attributes and eruption estimates .....	183
<b>Table A3.1:</b> Comparison of modal abundance and method.....	220
<b>Table A3.2:</b> Comparitive recognition results for automatic and manual methods .....	242

**List of symbols**  
**(In order of appearance in text)**

Chapter 1

D	dispersal, or area within > 1% of maximum deposit thickness
$T_{\max}$	maximum thickness isopach
F	'fragmentation', or % of juvenile clasts <1 mm at 0.1 $T_{\max}$
m asl	meters above sea level

Chapter 2

$N(R \geq r)$	number of fragments with a radius greater than r
$\lambda$	arbitrary constant
D	fractal dimension

Chapter 3

$\sigma_{\text{tr}}^2$	tracing variance
$\sigma_{\text{th}}^2$	threshold variance
$\sigma_{\text{N}}^2$	normalization factor variance
$n_A$	number of crystals per measured area
n	number of crystals
A	area
$R^2$	correlation coefficient
$\phi$	phi size, or the $-\log_2(\text{diameter})$
$\text{Md}\phi$	median phi size
$\sigma$	sorting efficiency
$\alpha$	kurtosis (skewness)
$n_V$	number of crystals per unit volume
N	population density, or # of crystals per unit volume per bin width
$P_{\text{eac}}$	perimeter of equivalent area circle
L	length (in mm)
D	exponent of power-law eq., or slope of straight line in log-log plot.
$\lambda$	constant of power-law eq., or y-axis value of power-law equation line when x-axis is zero
$N_V (X \geq x)$	number of fragments with a diameter greater than x
RMSE	root mean standard error
$\sigma_{\text{CK4,5}}^2$	geological variance
$\sigma_{\text{s}}^2$	sample variance
$\sigma_{\text{a}}^2$	total analytical variance

Chapter 4

JP	juvenile pyroclasts of crystalline kimberlite with enclosed olivine crystals
M	multiple-olivine juvenile pyroclast
S	selvages of melt on olivine crystals
IS	incomplete selvage of melt on olivine crystals

C	cored pyroclasts, or a juvenile pyroclast with a central crystal and > 30% crystalline kimberlite
N	number of pyroclasts
$n_t$	total number of pyroclasts
X	volume fraction
Pa s	Pascal – seconds (units for viscosity)
$M_f$	mass flux
$h$	dyke thickness
$l$	dyke length
$\rho_B$	bulk density
$\rho_m$	melt density
$\rho_f$	fluid density
$\rho_x$	crystal density
$\mu$	velocity
$v_c$	critical velocity required for turbulence
$Re_c$	critical Reynold's number required for turbulent flow
$\eta$	magma viscosity
$d_c$	characteristic conduit diameter
kPa m <sup>-1</sup>	kiloPascals per meter (units for pressure gradients)
$t$	time
$V_k$	minimum volume of erupting kimberlite
w	conduit width
z	conduit depth

### Chapter 5

FO	'free' olivine crystal
JP	juvenile pyroclast of crystalline kimberlite enclosing olivine crystals
D	exponent of power-law eq., or slope of straight line in log-log plot.
$\lambda$	constant of power-law eq., or y-axis value of power-law equation line when x-axis is zero
N	population density, or # of crystals per unit volume per bin width
$N$	number of crystals used in circularity measurement
$\sigma$	standard deviation (circularity)
$\mu$	mean (circularity)
$A$	measured area of olivine crystal
$P$	measured perimeter of olivine crystal
$T_g$	glass transition temperature
$T_{\text{magma}}$	magma temperature
$\gamma_{x-y}$	interfacial energy, surface tension between phases (dynes cm <sup>-1</sup> )
$\lambda$	wavelength
$\delta$	boundary layer thickness
$\rho$	density of liquid
$\rho_g$	gas density
$\Delta v$	velocity differential
$\lambda_{\perp}$	transverse wavelength

$We_\delta$	transverse Weber wavelength
$v_{g,l}$	velocity of gas, liquid
$We\#$	Weber number
$We\#_{crit}$	critical Weber number
$W_{adh}$	work of adhesion
$W_{crit}$	critical work
$d_o$	initial droplet size
$\theta$	contact angle between solid and adhering liquid
$\eta$	liquid viscosity
$W$	power output (watts)
VEI	volcano explosivity index
S	melt separation, as recorded in FO:JP ratio

### Chapter 6

\$	generalized value, in dollars
KIM	kimberlite indicator mineral
$\rho_d$	density of diamond
$\rho_{ol}$	density of olivine
$V_d$	volume of rock required for statistical analysis of diamond
$V_{ol}$	volume of rock required for statistical analysis of olivine
MSS	mean stone size
$\sigma$	sorting efficiency (olivine crystals)
n	number of samples
cts	carats, where 1 carat = 200 mg

### Appendix

ROI	region of interest
RGB	red green blue colour space
$m$	average colour component
$C$	covariance matrix
$k$	colour component
$D$	Mahalanobis distance
$(i,j)$	image location
$m$	mean
$\sigma$	standard deviation
$p$	likelihood image
$P$	matching likelihood image
A, B	observed maximum (A) and minimum (B) axis lengths

## Acknowledgements

It is a rare and lifelong gift to explore *anything* in great detail amid the support and encouragement of others. It is, in short, the only way any of us can come to love anything. It is in this spirit that I want to recognize the generous and nuanced ways that many have contributed to both this project and my personal development over the last 4 years.

This research was funded by an NSERC Collaborative Research and Development Grant (22R42415) held by Dr. J.K. Russell, co-sponsored by Diavik Diamond Mines, Inc. (DDMI) and entitled “Kimberlite eruption dynamics: Implications for diamond distribution in the Diavik kimberlite”. Additional funding was received from the Society of Economic Geology (SEG), the University of British Columbia’s University Graduate Fellowship, a Pacific Graduate Fellowship, and Earth and Ocean Science at UBC’s McKay scholarship. Travel grants supported attendance at the 9<sup>th</sup> International Kimberlite Conference, International Association of Volcanology and the Earth’s Interior (IAVCEI), American Geophysical Union (AGU), and the Geological Association of Canada-Mineralogical Association of Canada (GAC-MAC). I am grateful for this generous support.

There is no one I’ve ever met who carries the enthusiasm for scientific result as much as Dr. J.K. Russell. I am forever indebted to him for sharing his passion for exploring interesting things. He challenged me, encouraged me, and even dared me to think outside of the box, to communicate clearly, and to say dangerous things. He was available for discussion virtually all the time, a gift to me these last four years that cannot be overstated. But perhaps most importantly, Dr. Russell made me feel valued and interesting both as a thinker and as a human being. This kind of care is priceless. I also want to thank Greg Dipple, James Scoates, Maya Kopylova and Al Lewis, who each assisted me during my PhD as either committee members, scientific counsel, or academic encouragement. Thanks guys.

There are individuals in the kimberlite and diamond community who have been instrumental in shaping my understanding of kimberlite volcanoes: Barbara Scott Smith, for her lines of evidence, and insistence on the significance of language. I can’t tell you how many times the thought has gone through my head, “you know, Barbara is right”. Thanks also to Tom Nowicki, Kim Webb, Margaret Harder, Tom McCandless, Wayne Barnett, Liane Boyer, Murray Rayner and Ian Graham for countless science conversations and for keeping me honest. Thanks to Ray Cas, who taught me about facies analysis and the power of non-genetic description.

To the crew in the Volcanology and Petrology Lab at UBC, you are stars, all of you: Graham, you are fantastically pedantic, and I’m a better writer and scientist because of it. Geeves, thanks for teaching me about lab protocol and thoroughness, and for being a good friend. Nils, thanks for helping us troglodytes learn how to have fun. And for being Swiss. Jackie, thanks for geeking out with Curtis and I, and for food breaks☺. R.E., thanks for your all-things-rocks enthusiasm, and teaching us all about dependency. Lava you. Curtis, it can’t be said enough how great it is to have someone who shares your enthusiasm for your research, loves to talk ideas, and will put up with my frenetic pace: you’ve been a great pal. Thanks. Thanks to Jenny Lai and her able assistance in manual tracing: you might be the only know who knows my pain. Thanks to Bram

VanStraaten, Lucy Porrit, Tom Gernon and Pat Hayman. I couldn't ask for better colleagues in kimberlite volcanology: it has never been a competition, which has kept it interesting, fun and mysterious, for all of us, I think. Thanks to J.T., Chalmers, Stuart, Sasha, Daniel and Shawn Barker: who would I be today without walks to Tim Horton's? Dare we ask?

There is a top-shelf crew of people at Diavik Diamond Mines, Inc., who I am privileged to call friends as well as colleagues. Gus Fomradas, Roger Young, Doug McKay, Brian Smith, David Eichenberg, Robbie McGregor, Erica Tamboline, Erica Grolsch, Hayley McLean and Kari Thompson have been a tremendous support over the last 4 years with updates, insights, data-sharing, and interest in my research. The opportunity to map and collect kimberlite rocks in an open pit at a diamond mine will forever be the biggest vocational thrill I've ever had. The access to information and the experience of geologists at Diavik that I enjoyed during my 4 years is unparalleled in the study of kimberlite.

Thanks to Jeffrey K. Greenberg, whose passion and enthusiasm in Creation kick-started me down this road, and who will forever inspire me to see, taste and touch my way to the hidden and holy heart of things, one thin section at a time. Don Hyndman, whose patience with me as I learned to think while writing my MSc was unwavering.

I also want to thank the many friends from Out of the Cold, Crossroads, L'abri, Regent College, Rivendell, Jacob's Well, Grandview Calvary Baptist Church, and greater Vancouver who never let me misappropriate my life, and continue to teach me about a different way. How many frustrating days melted away in simple touch: a meal in a home, the encouraging word of a friend, the art of the community, prayer for one in need, the sight of green, alive people in an urban greyscape. And all that music. Indeed: wisdom not in ideas, but in *things*. Nacho, thanks for validating my "Cub-ness". Scheibe, for showing me how to hold onto The Dude while growing out of it at the same time. Sizzlethwaite, for teaching me about joy and jazz. Malyon, for friendship and a beer to smooth over the rough spots. Dr. Lee, for commiserating with me about life in the academe. JVaughan, for being a brother in Christ with which to learn about academic character. Tim Dickau, for our times together solving all the world's problems before 10am at Café Napoli. Teak, for dragging me out of my brain long enough to battle salmon. Dwayne, thanks. Peter, thanks. Brad, Julie, Megan and Libby, thanks for your friendship, and opening up your lives and home to me. And to my beautiful 'birdie' who sang me home to a place I'd never been those dark final days. Thanks, J.

And finally, to the One who transcends and pulls close; who Himself rumbles and masquerades one moment, and explodes into a fiery dance the next, and who continually shows me that the *surprise is the thing*.....may the labors of these 4 years be a small gratitude.

## Dedication

*This thesis is dedicated to the One who sees, alas, what, when, and where we do not;  
who taught me that faith is the imagination to see an alternative and substantive  
reality....*

## Co-authorship statement

This thesis comprises six complementary manuscripts prepared for publication in international scientific journals.

Chapter 2 has been published in *Journal of Volcanology and Geothermal Research* (Moss et al., 2008; Appendix 7.9.1). I am the first author, and my co-authors are Dr. J.K. Russell and Dr. Graham Andrews. I was responsible for all field mapping, graphic logs, image analysis, and wrote the majority of the manuscript. Dr. J.K. Russell, and co-authored the discussion section of the manuscript. Dr. Graham Andrews All authors contributed multiple stages of editorial comments during preparation of the manuscript.

Chapter 3 has been submitted for publication (Moss et al., 2009). I am the first author, and my co-authors are Dr. J.K. Russell, Barbara Scott Smith, and R.C. Brett. Manual tracing of olivines in images of polished slabs and thin sections was mostly accomplished by a research assistant, Jenny Lai. Dr. J.K. Russell assisted in general paper structure, co-wrote the discussions and conclusions, and generated MATLAB script for determining covariance envelopes for data plotted in Figure 8b. Barbara Scott Smith co-wrote the section on sample selection and assisted in general framing of the paper. R.C. Brett provided model original xenocryst olivine crystal populations based on 5% crystallization of new olivine (Fig. 3.7c). I wrote all other MATLAB computer code, the manuscript, and drafted all figures and tables. All authors contributed multiple stages of editorial comments during preparation of the manuscript.

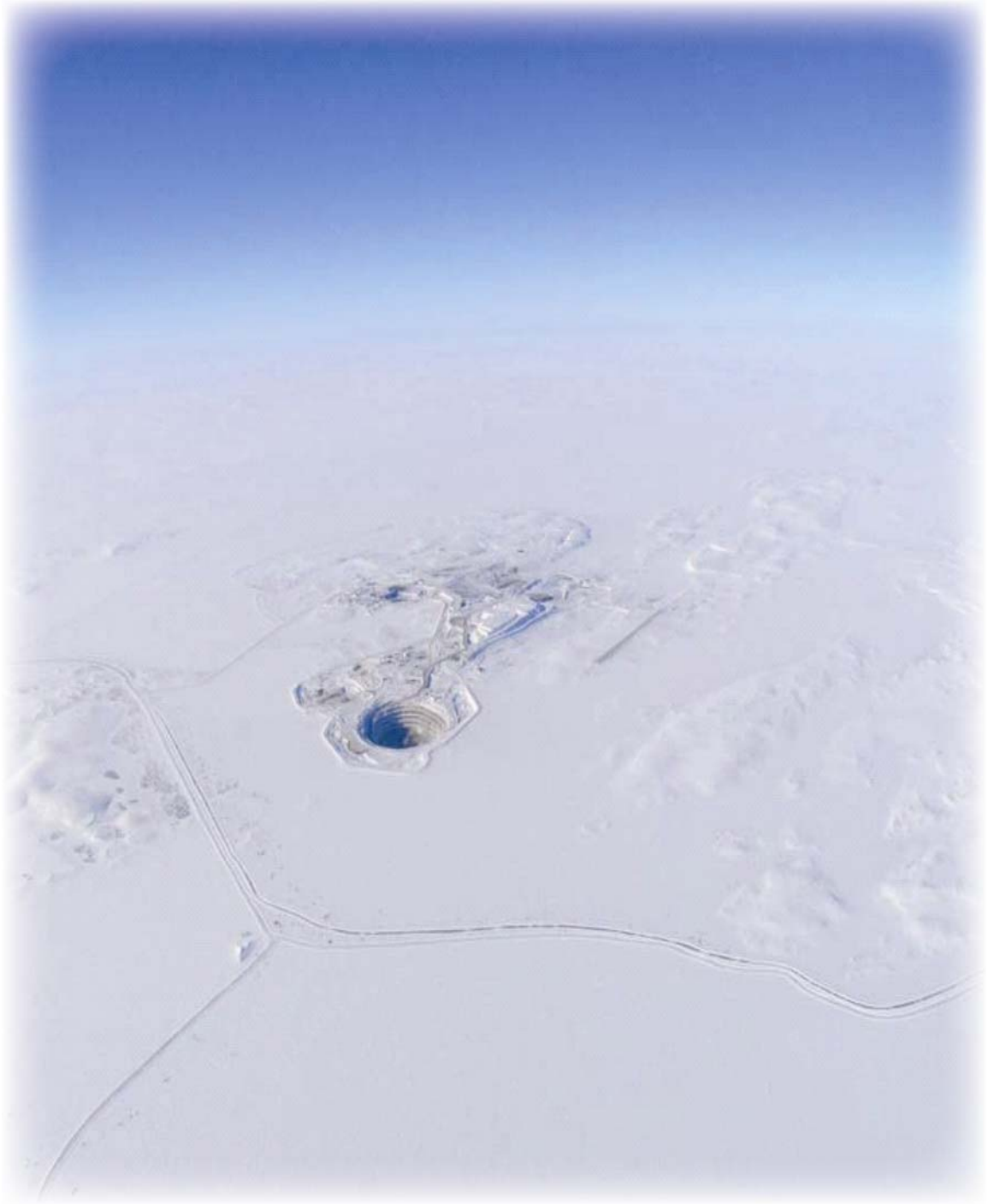
Chapter 4 has been published in a special volume of *Lithos* (9<sup>th</sup> International Kimberlite Conference, Eds. Koole; Moss et al., 2009; Appendix 7.9.2). I am the first author, and my co-authors are Dr. J.K. Russell, Dr. Graham Andrews, and R.C. Brett. I conducted all field mapping and manual tracing of olivine crystals and juvenile pyroclasts, wrote all MATLAB script for processing crystal data and creating figures, and wrote the manuscript. Dr. J.K. Russell provided assistance in structuring the paper, and was a co-progenitor of the idea of phase separation noted in the manuscript. Dr. Graham Andrews helped in designing and drafting of several figures, assisted in structuring the manuscript, and co-authored the abstract. R.C. Brett co-authored the abstract, and contributed to several of the geological observations in the paper. All authors contributed multiple stages of editorial comments during preparation of the manuscript.

Chapter 5 is intended for submission. I am the first author, and Dr. J.K. Russell is my co-author. I wrote the manuscript, drafted all figures, and performed all image analysis used to obtain crystal and juvenile pyroclast data sets. Dr. J.K. Russell assisted in the structuring of the manuscript, and was the progenitor and co-author of several of the ideas in the discussion section of the paper. All authors contributed multiple stages of editorial comments during preparation of the manuscript.

A portion of Chapter 6 is intended for submission. I am the first author, and my co-authors are Dr. J.K. Russell and Barbara Scott Smith. I wrote the summary of important developments in the volcanology of kimberlite, and co-wrote the implications of these

developments on diamond distributions. Dr. J.K. Russell helped develop and refine the ideas for significant contributions to kimberlite volcanology. Barbara Scott Smith co-authored two of the implications on diamond distributions. All authors contributed multiple stages of editorial comments during preparation of the manuscript.

Appendix 7.3.2 has been published in *Computational Geosciences* (Holden et al., 2009; Appendix 7.9.3). I am second author, and this paper is the result of collaboration between the University of British Columbia and the University of Western Australia, Perth (UWA). Dr. E.J. Holden (UWA) is the primary author, and co-authors include me, Dr. J.K. Russell, and M.C. Dentith. Dr. Holden was in charge of organizing the manuscript, and writing MATLAB script for processing raw images. My responsibility was to write the Introduction, generate data by using a manual method of image analysis for comparison, and to write the discussion and implications section of the paper. Dr. J.K. Russell also co-authored the discussion section. M.C. Dentith assisted with MATLAB script for processing raw images. The workload breakdown was approximately 60:40 between Dr. E.J. Holden and myself, respectively. Dr. Holden has kindly agreed to allow inclusion of the manuscript within my thesis, as it contributes to the general trajectory of how particle data on kimberlite rocks will be collected in the future. All authors contributed multiple stages of editorial comments during preparation of the manuscript.



# 1 Introduction

Kimberlite is an ultra-basic volcanic rock. These rocks are found exclusively in or adjacent to cratons around the world as 1 – 10 m thick dykes and sills, or in circular, downward-tapering bodies known as “pipes”, up to 1000 m in diameter at surface. These pipes are the result of volcanic eruptions and probably represent the near surface (1-3 km) conduits and craters of the kimberlite volcano. No one has ever observed a kimberlite eruption. Aside from the inferred Quaternary kimberlite volcanism at Igwisi Hills, Tanzania (Dawson, 1994), the youngest published dates for kimberlite pipes on the planet are of Eocene (~47 Ma) age (Sweet et al., 2003). Consequently, most of our understanding of kimberlite eruptions is a result of the mining of kimberlite for diamonds, and is based on inferred processes from a few scales of observation most efficient in the economic evaluation of kimberlite bodies, such as core logging and petrography of rock samples. Furthermore, because the study of kimberlite mainly occurs in conjunction with the mining industry, only a small fraction of the total information on kimberlite occurrences is introduced into the public domain.

Volcanology has advanced largely because of observations made on the volcanic edifice and/or extra-crater deposits of active systems, and field studies of well-preserved dormant systems. However, the number of studies of exhumed volcanic conduits is few (Stasiuk et al., 1996; Junqueira-Brod et al., 2005; Valentine and Krogh, 2006). Kimberlite volcanoes are highly dissected or completely removed by erosion. Commonly, all that is left is the volcanic “plumbing system”, comprising a downward-tapering conduit filled with a mixture of kimberlite products, country rock and even surface materials (e.g., wood). No volcanic edifices and only a few extra-crater deposits of kimberlite have been recorded in the literature.

Thus, establishing relationships between well-understood volcanic processes and kimberlites has been limited by the nature of the available data, and the perspectives from which observations are made. These limitations present a conundrum in attempting to understand eruption processes in kimberlite volcanoes: classic volcanology relies on field observations of active and historical systems to relate deposits with process, but is limited in conduit observations. Conversely, kimberlite studies offer a wealth of detailed petrologic information on conduit shapes and infill, but do not have active or historical eruptions to connect such observations with process. The result is that there are

significant gaps in our understanding of kimberlite eruptions, and there is little consensus as to the specific style and dynamics of their eruption, or how kimberlite is emplaced in the upper crust.

The aim of this dissertation is to begin to address the gaps in our understanding of kimberlite volcanology by providing descriptive data from kimberlite deposits. To accomplish this, kimberlite rocks are investigated from one of the first diamond mines in Canada, at Diavik Diamond Mine Inc. (DDMI), in the Lac de Gras region of the Northwest Territories. Multiple kimberlite pipes were studied at an active mine over a 4-year period, providing the unique opportunity to make in-situ, mine-scale observations of kimberlite deposits as they were exposed. The focus of this thesis is the A154N kimberlite pipe at Diavik, comprising a diversity of coherent and fragmental kimberlite rocks, previously interpreted as re-sedimented volcanoclastic kimberlite, pyroclastic kimberlite, and hypabyssal kimberlite (Graham et al., 1999).

Here, descriptive data is collected from A154N by using a combination of volcanic facies analysis<sup>1</sup>, three-dimensional modeling and image analysis software. Volcanic facies analysis is an approach which recognizes that each deposit type is a *direct result of a volcanic event or set of events*, and these deposits have unique properties in terms of geometry, componentry, internal structure, and sorting. Volcanic facies analysis techniques are based on observations of active and historical volcanic eruptions of other magma types, which have successfully linked textures and deposit types to specific eruption processes (Cas and Wright, 1987). Collecting descriptive data from A154N by employing facies analysis tools developed in other volcanic systems allows for analogous interpretation of kimberlite eruption processes.

The physical character of the kimberlite deposits of A154N was obtained from field mapping, and study of hand samples and thin sections (Chs. 2-4). After quantitatively describing the deposits, these data were used to build and refine 3-D models that explore and illustrate the facies variations and architecture of a single kimberlite pipe (Chs. 2,3,4). Simple numerical modeling was then used to evaluate the style, volume and duration of volcanic eruptions (Chs. 2,4). These results are shown to have direct implications on the interpretation of the emplacement of A154N, and are subsequently developed into a tool for interpreting possible eruption styles of other kimberlite

---

<sup>1</sup> Facies Analysis: Characterization of the geometry, lithology (chemistry, composition, textures), structures and space and time relationships of a particular geologic occurrence that serves to uniquely distinguish the occurrence from others.

volcanoes by examining pyroclastic deposits (Ch. 5). A composite fragmentation index was created that seeks to reconcile observed rock textures with an interpretation of eruption style by accounting for both external and internal influences on erupting kimberlite magma (Ch. 5). Finally, the results from this study are shown to have direct implications on diamond distributions (Ch. 6).

## **1.1 Previous kimberlite emplacement models**

Below, I review existing models seeking to explain the emplacement and eruption processes of kimberlite pipes and their contained deposits, in order to highlight gaps in our knowledge of explosive kimberlite eruptions.

### 1.1.1 Models derived from southern Africa

The most widely cited composite model for the morphology of kimberlites was described by Hawthorne (Hawthorne, 1975) and later modified by Mitchell (Mitchell, 1986) (Fig. 1.1). This model shows a shallow crater over a steep-sided pipe (~82°) and a feeder dyke at depth. The model identifies three petrologically and spatially distinct zones: root zone, diatreme facies, and crater facies. Root zones are characterized by dikes, sills and sheets of intrusive kimberlite. The diatreme facies consists of massive, poorly sorted volcanoclastic kimberlite, containing up to 25% country rock xenoliths. The crater facies is dominated by pyroclastic kimberlite, re-worked or collapsed pyroclastic kimberlite from a crater rim, and crater-lake mud deposits. Subsequent morphology models have also been proposed (Clement, 1982; Lorenz, 1985; Clement and Reid, 1989; Field and Scott Smith, 1999; Lorenz, 2003; Sparks et al., 2006), but most of these build on the Hawthorne (1975) model.

There are two classic models for kimberlite emplacement. The first invokes excavation from the top down whereby

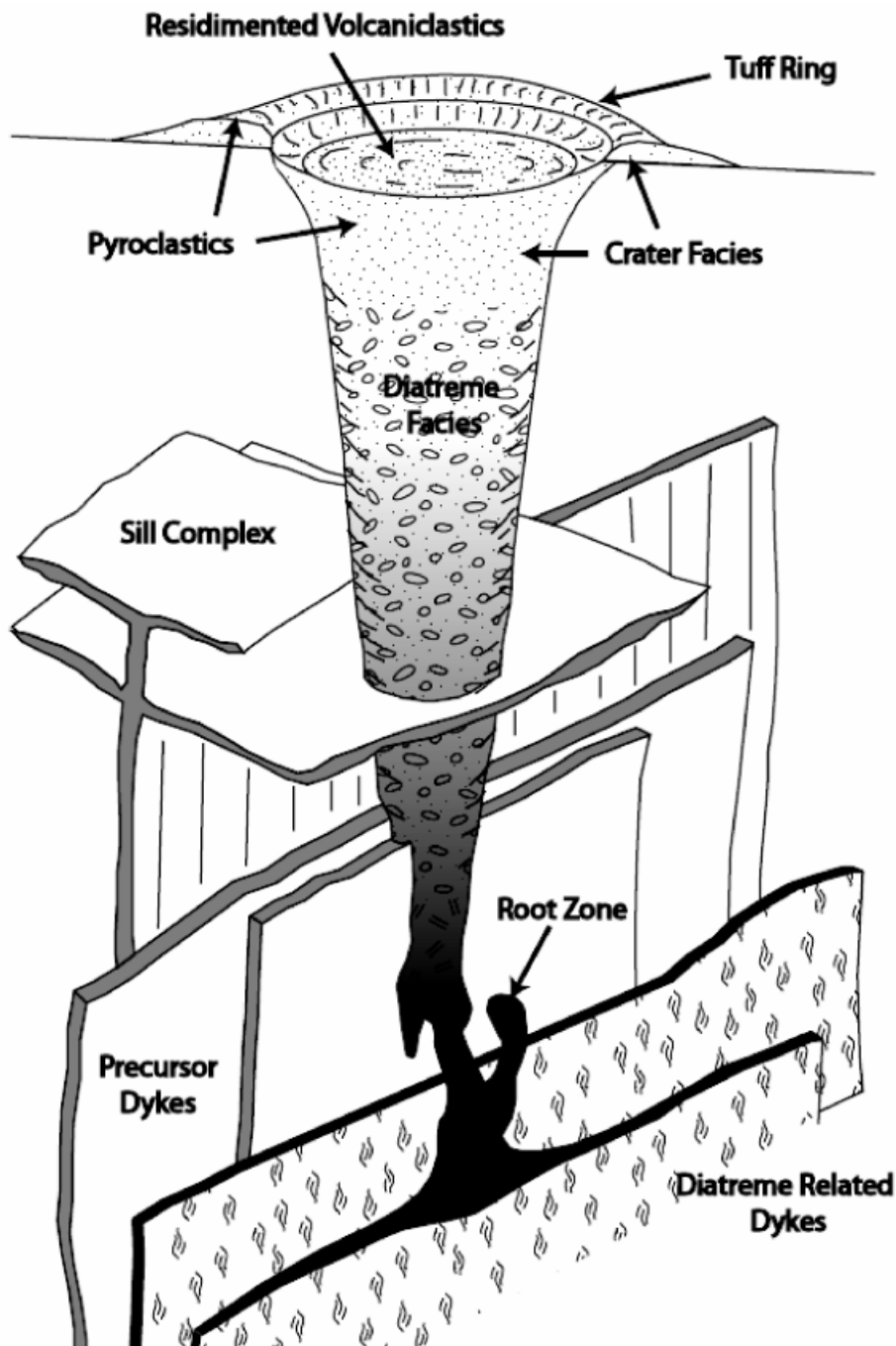


**Figure 1.1:** Illustration of a kimberlite pipe from a depth of 2-3 km to surface, showing root zone, diatreme facies, and crater facies. Modified after Hawthorne (1975), Mitchell (1986) and Porrit (2008).

country rock is removed by a downward-propagating explosion front caused by depressuring of the rising magma or by the interactions between hot kimberlite magma and meteoric water (Fig. 1.2; Sparks et al., 2006; Lorenz and Kurszlaukis, 2007). The second model features a relatively slow buildup from the bottom up where kimberlite magma fractures and fluidizes country rock at depth and culminates in an explosive excavation of the pipe when magma reaches a point in the crust where the lithostatic pressure is less than the magmatic overpressures (Clement, 1982; Skinner, 1989; Field and Scott Smith, 1999; Skinner and Marsh, 2004; Fig. 1.3). These models are largely based on kimberlites from southern Africa, and most of the southern African pipes are up to 1000 m in surface diameter, and up to 3 km in depth.

### 1.1.2 Canadian kimberlites and new models

Kimberlite bodies in Canada provide a different set of observations. The Canadian occurrences are different in size, morphology, and contents (Fig. 1.4; Field and Scott Smith, 1999; Scott Smith, 2008a). For example, kimberlites emplaced into late Mesozoic rocks in the central prairies of Canada are interpreted as broad, dish-shaped craters with little or no diatreme or root zones evident. They are believed to be largely filled with pyroclastic kimberlite. The kimberlites of the Lac de Gras region show yet another morphology comprised of small, steep-walled, relatively small radius (<200 m) and deep pipes that are reportedly filled with resedimented and primary volcanoclastic kimberlite (Pell, 1997; Field and Scott Smith, 1999; Kjarsgaard, 2001; Kolebaba, 2003; Nowicki, 2004; Scott Smith, 2008a). Observations on Canadian kimberlites have led to a number of case-specific models for the morphologies and origins of pipes (Field and Scott Smith, 1999; Hetman et al., 2004; Nowicki et al., 2004; Webb et al., 2004).

Much of the petrological work done on Canadian kimberlites, and, for that matter, the rest of the globe, has used macroscopic to microscopic textural features to: a) identify the type of kimberlite (Leahy, 1997; Boyer et al., 2004), b) classify the kimberlite by facies (hypabyssal, diatreme, or crater) (Cookenboo, 1997; Field and Scott Smith, 1999) c) distinguish lithological units (Kirkley, 1998; Scott Smith et al., 1998; Zonneveld et al., 2004), and d) correlate diamond grade with rock type for the

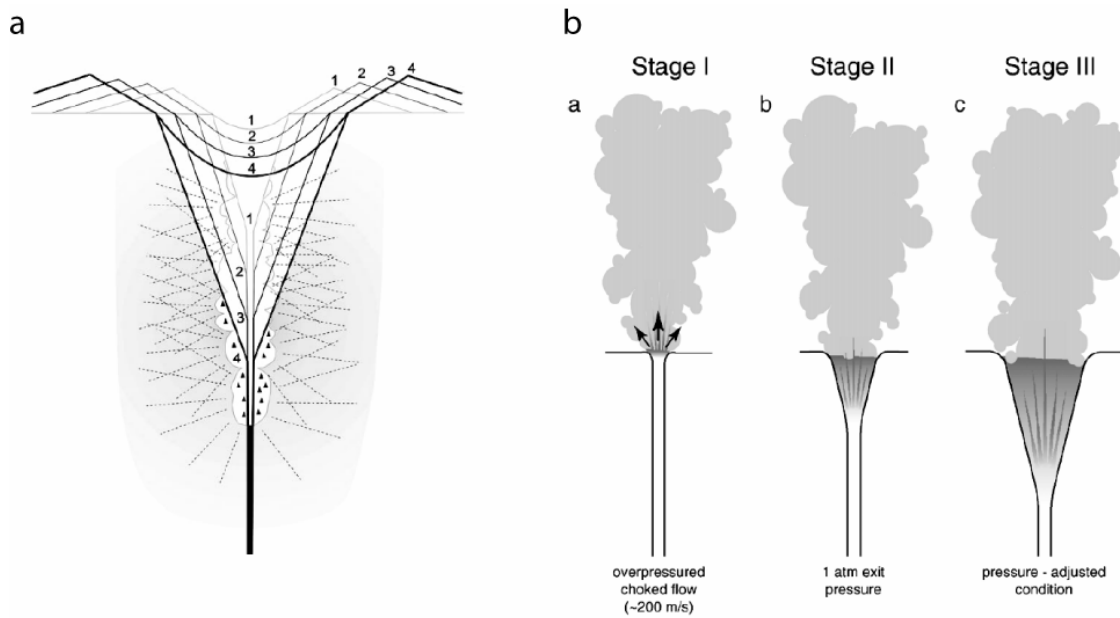


**Figure 1.2:** “Top-down” emplacement models: (a) Schematic evolution in four stages of a downward penetrating root zone with repeated collapse of the overlying diatreme and surrounding rocks, indicating also the downward cutting on the feeder dyke (modified after Lorenz et al., 2003). The numbers 1–4 indicate the four stages in the evolution of the tephra ring, the crater floor, and the lower end of the diatreme (modified after Kurszlaukis and Lorenz, 2006); (b) Schematic depiction of a three-stage model for kimberlite eruption modified after Sparks et al., 2006.

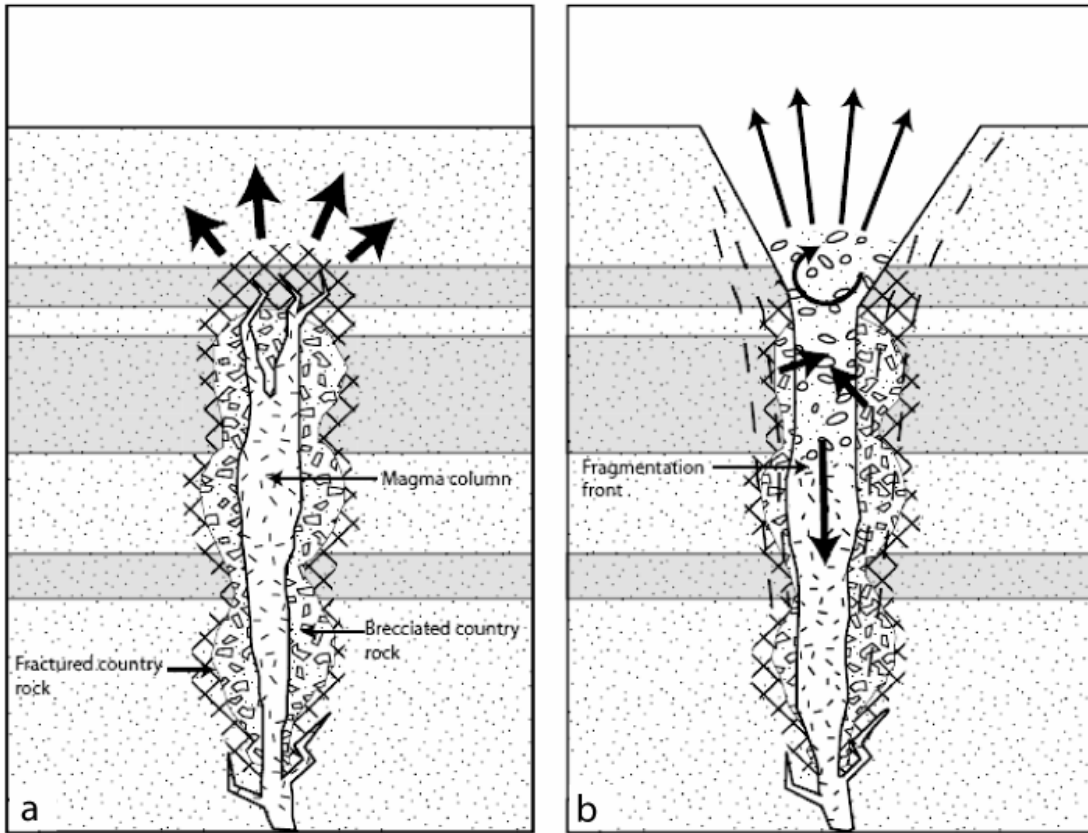


**Figure 1.3:** Schematic depiction of the explosive magmatic model for the formation of kimberlite pipes, modified from Field and Scott Smith (1999): (a) ascending magma utilizes existing fractures in the country rock, and volatiles accumulated at the head of the magma column fracture the country rock ahead of the magma. Lithological barriers in the country rocks (e.g., dolerite sills) provide barriers at which volatile pressure builds up and explosive brecciation occurs, pre-conditioning large volumes of country rock; (b) explosive breakthrough leads to the excavation of a crater, rapid exsolution causes volatile streaming and fluidization of the magma and rapid, downward migration of a fragmentation front in the magma. Sustained eruption leads to erosion of country rocks and the formation of a smooth-sided diatreme. Modified after Field and Scott Smith (1999).

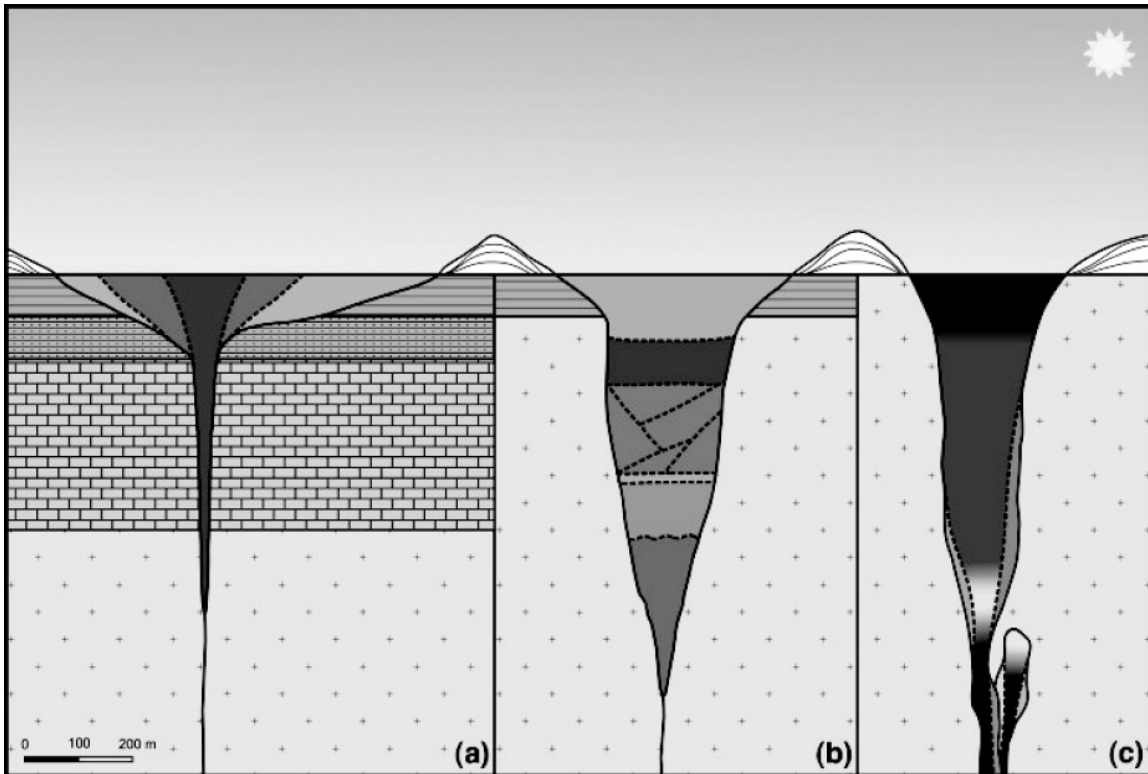


**Figure 1.4** Schematic representation of the internal geology of three types of kimberlite pipe geometries observed in Canada: (a) broad, dish-shaped pipes and generalized interpretation of observed infills from the Canadian Prairies; (b) deep, narrow pipes and generalized interpretation of observed infills from Lac de Gras, NWT, Canada, characterized by a combination of pyroclastic and re-sedimented volcaniclastic kimberlite; (c) steep-sided, deep pipes with steep, sharp internal contacts. Modified after Scott Smith (2008).

purposes of industry (Leckie, 1997; Berryman et al., 2004; Hetman et al., 2004; Scott Smith, 2009b).

The Canadian occurrences have led to an important revision of kimberlite emplacement models (Field and Scott Smith, 1999). After studying a global set of kimberlite pipe occurrences, Field and Scott Smith (1999) observe that pipe morphologies (overall size, shape, depth) vary significantly. They argue that regional near-surface geology is the most significant factor in controlling the morphology of kimberlite pipes. As kimberlites are observed across space-time throughout global cratonic bodies, Scott Smith (personal commentary; Mitchell, 1986) identifies kimberlite and its related rocks as a petrological “clan”; i.e., they are derived from the same depth, have approximately the same chemistry and volatile content, and bear essentially the same components at all localities worldwide. However, kimberlites in South Africa were emplaced into heterogeneous host rocks that are very different from the host rocks in Canada. On this basis, the authors concluded that observed differences in pipe morphology and textures are a function of the country rocks and their ability to control how gas-charged kimberlite magma makes its way to the surface, and not because of differences in the nature of the kimberlite magma.

Although reworked kimberlite deposits are volumetrically important in the Lac de Gras kimberlites of Canada (Field and Scott Smith, 1999; Kolebaba, 2003), very few models of sedimentological processes in kimberlite pipes exist. After examining drill core from Lac de Gras pipes, Kolebaba (Kolebaba, 2003) schematized the infill of an “open-hole” diatreme, characterizing the nature of deposits expected from seasonal, mass flow, and interflow settling of tephra material into an excavated diatreme. Examination of core from the Star kimberlite occurrence in Fort-a-la-Corne, Saskatchewan, led Zonneveld et al. (2004) to invoke a process of near-shore wave re-working of extra-crater deposits from multiple kimberlite eruptions.

### 1.1.3 Contemporary composite models

The lack of consensus in kimberlite emplacement and eruption processes has led to more studies of kimberlites from an explicitly volcanologic perspective in recent years. Consequently, several new models for kimberlite emplacement have emerged,

incorporating principles developed in the study of active and/or historical volcanic systems.

Sparks et al. (2006) built upon conventional kimberlite emplacement models by using well-known magmatic dike properties and near-surface eruption dynamics of volcanoes to constrain an alternative four-stage model based on the observation of a suite of De Beers pipes in South Africa. In this new model, an initial high-velocity eruption from a narrow vent gives way to a deepening and widening crater, lower exit velocities of volcanic material, and a subsequent low-velocity late fluidization/degassing stage (Walters et al., 2006a; Gernon et al., 2008b). Finally, a late-stage hydrothermal metamorphism which utilizes available meteoric water breaks down olivine to form serpentine, leading to a positive volume change, pore space-filling, and overprinting of primary textures.

Wilson & Head (2004) combine understandings of dike propagation, pressure differentials and volatile exsolution to put forward a 6-stage model for rapidly occurring kimberlite emplacement that focuses on the pressure distribution in a dike throughout its ascent (Fig. 1.5). They envision a CO<sub>2</sub> foam developing below the dike tip as it propagates, effectively maintaining cavity pressure at ~70 MPa, and leading to significant tensile failure and entrainment of wall rocks during the ascent of the kimberlite magma.

A common and distinctive rock texture found in many kimberlite volcanoes is a massive, poorly sorted, compositionally homogeneous fabric. Such massive volcanoclastic kimberlite (MVK) is often the most volumetrically dominant portion of kimberlite pipes. A current hypothesis among some volcanologists (e.g., Cas et al., 2008b; Porritt et al., 2008), however, is that MVK is formed from the collapse of the volcanic column and subsequent fluidization (gas-driven stirring) of kimberlite material within the excavated pipe during the waning stages of eruption (Fig. 1.6). The hypothesis holds that as intensity wanes towards the end of an eruption, a point comes when the potential energy of erupted kimberlite exceeds the kinetic energy of erupting kimberlite, thereby initiating the return of erupted kimberlite into the vent area. This is also directly related to the overpressure experienced by the erupting magma; as the magmatic fluid

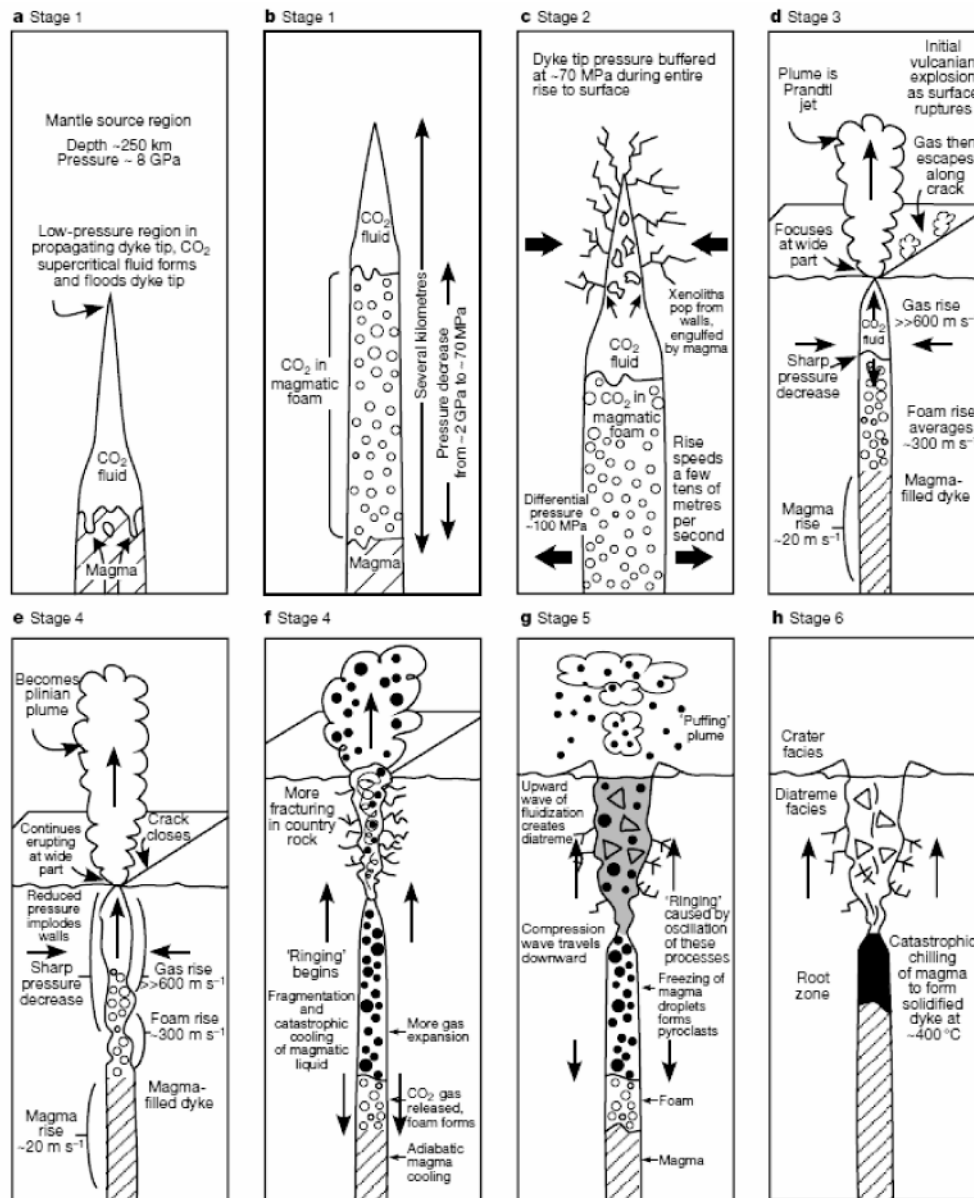


**Figure 1.5:** Schematic composite model by Wilson and Head (2004) for kimberlite emplacement, showing sequence of events in the generation, ascent and eruption of kimberlitic magmas and diatreme formation (see text for details). Modified after Wilson and Head (2004).

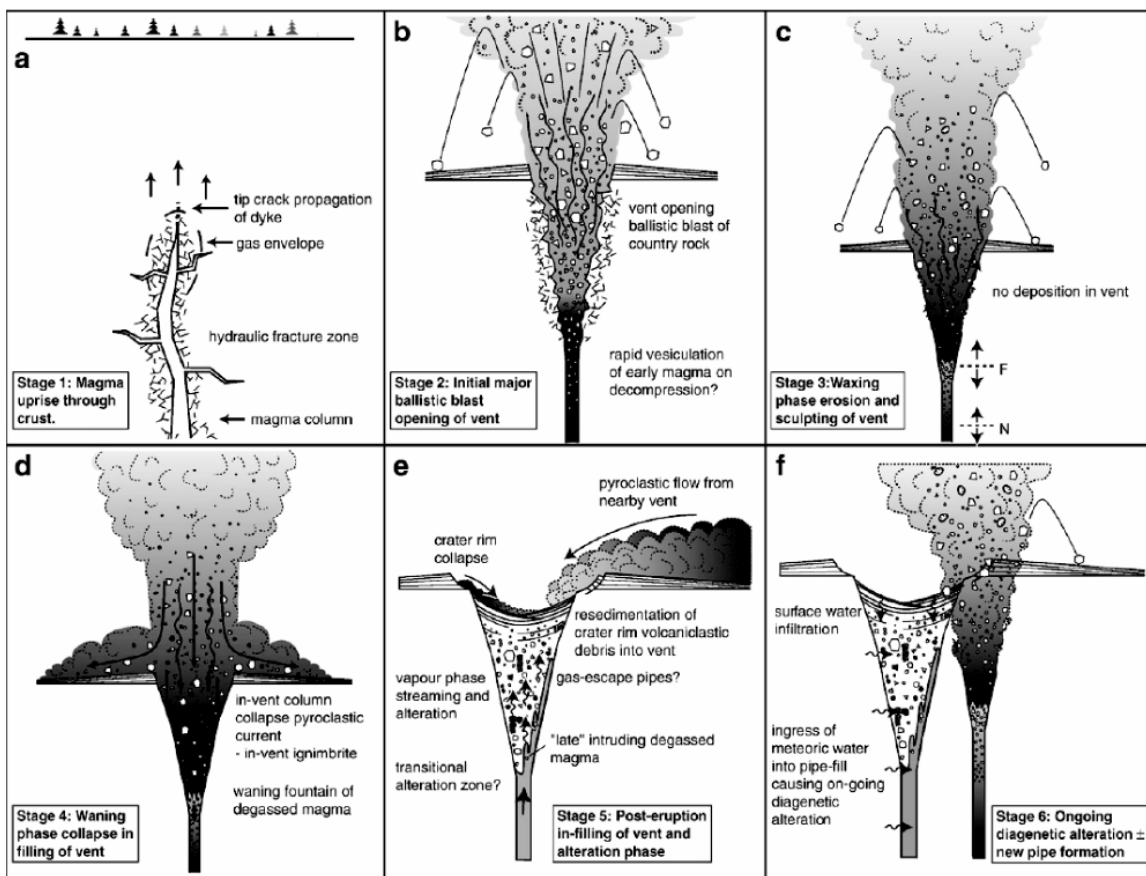


**Figure 1.6:** Schematic composite model by Cas et al. (2008b) for kimberlite emplacement, showing sequence of events in the generation, ascent and eruption of kimberlitic magmas and diatreme formation (see text for details). Modified after Cas et al. (2008b).

pressure approaches atmospheric levels, the ability of erupting magma to continue thrusting material out of the vent is limited. The depositional event would be characterized by an en-masse, vertical collapse of poorly sorted material in the volcanic column, along with simultaneous “fluidization” of the intra-vent material by the less-powerful but still emanating volcanic gases. This is similar to what is observed in the collapses of pyroclastic columns generating pyroclastic flows in andesitic volcanism (Sparks, 1986; Sparks, 1997). When material moves via laminar flow, clasts and grains have minimal freedom of movement, and therefore remain poorly-sorted when finally deposited (ex: turbidites, avalanches, debris flows). However, little is known about what this collapsing column would look like should it be falling into an open hole.

Several authors have proposed an alternative mechanism for creating such massive texture (McClintock and White, 2006; Ross et al., 2008a; Ross et al., 2008b), whereby repeated, upward-traveling mixtures of juvenile particles, country rock fragments, magmatic gases, and in some cases externally derived fluids homogenize the beds of particles within a diatreme. These mixtures are called “debris jets”. The debris jets are suggested to propagate within the existing diatreme fill and may or may not reach the surface; they are proposed to be generated by explosions in deeper portions of the pipe or in the root zone (e.g., Lorenz and Kurszlauskis, 2007). As debris jets in active systems would dominantly occur within volcanic piles (i.e. not observable), the manner by which they propagate and agitate or deposit volcanoclastic material remains poorly constrained.

## **1.2 Outstanding gaps in kimberlite volcanology**

Despite these recent advances, kimberlite eruptions are still not well understood. Existing models are incapable of completely characterizing kimberlite eruptions for several reasons. First, eruption models based on textural observations (e.g., Porritt et al., 2008) are specific to individual occurrences and may only apply to kimberlite volcanoes with similar rock textures and pipe morphologies. Second, theoretical models (e.g., Wilson and Head, 2004) are based on poorly-constrained properties of kimberlite magma and do not explain the diversity of kimberlite rock textures or pipe morphologies. Third, models based on a combination of pipe morphology and rock textures (e.g., Field and Scott Smith, 1999) assume that the physical properties (i.e., gas, crystal content, melt viscosity) of erupting kimberlite magmas are constant. Fourth, models based on

experimentation (e.g., Gernon et al., 2008) focus on only a few key observations from within kimberlite pipes and do not explain the diversity of pipe morphologies or deposits. Lastly, there are no models seeking to explain mechanisms responsible for the formation of diverse pyroclast types within deposits of kimberlite.

The existing, generalized models indicate the need for more studies which incorporate rock observations, pipe morphology, and numerical modeling of well-constrained magma properties into interpretations of volcanic process for specific kimberlite volcanoes. In addition, existing models also highlight key gaps in our understanding of kimberlites. These gaps are discussed below, and include: a) insufficient metrics for characterizing eruption style; b) a lack of understanding of the physical properties of kimberlite magma; and c) little to no quantification of pyroclastic deposits to compare with deposits from historic eruptions of other magma types.

### 1.2.1 Kimberlite eruption style

Volcanic eruption style is typically described by parameters such as magnitude (erupted mass, in kg), intensity (eruption rate, in kg/s), peak eruption height (km), energy release (thermal + kinetic + seismic, in J), power output (W), and destructive potential (Sigurdsson, 2000). These parameters are usually estimated from observations on active eruptions. Subsequent efforts have then been made to correlate a specific style of eruption events with the resulting pyroclastic deposits (Walker, 1971; Sparks et al., 1981). For example, Walker (1973) recognized the need to investigate the wealth of global pyroclastic deposits for clues into eruption behavior for active and ancient systems (Fig. 1.7). Relative comparisons of eruption dynamics of volcanoes are approximated by examining a combination of clast size distributions and area extents of pyroclastic deposits (Walker et al., 1971; Walker, 1981; Sparks, 1986; e.g., Bursik et al., 1992). Most kimberlite volcanoes, however, cannot be analyzed for either eruption characteristics or resulting pyroclastic deposits for several reasons. First, there have been

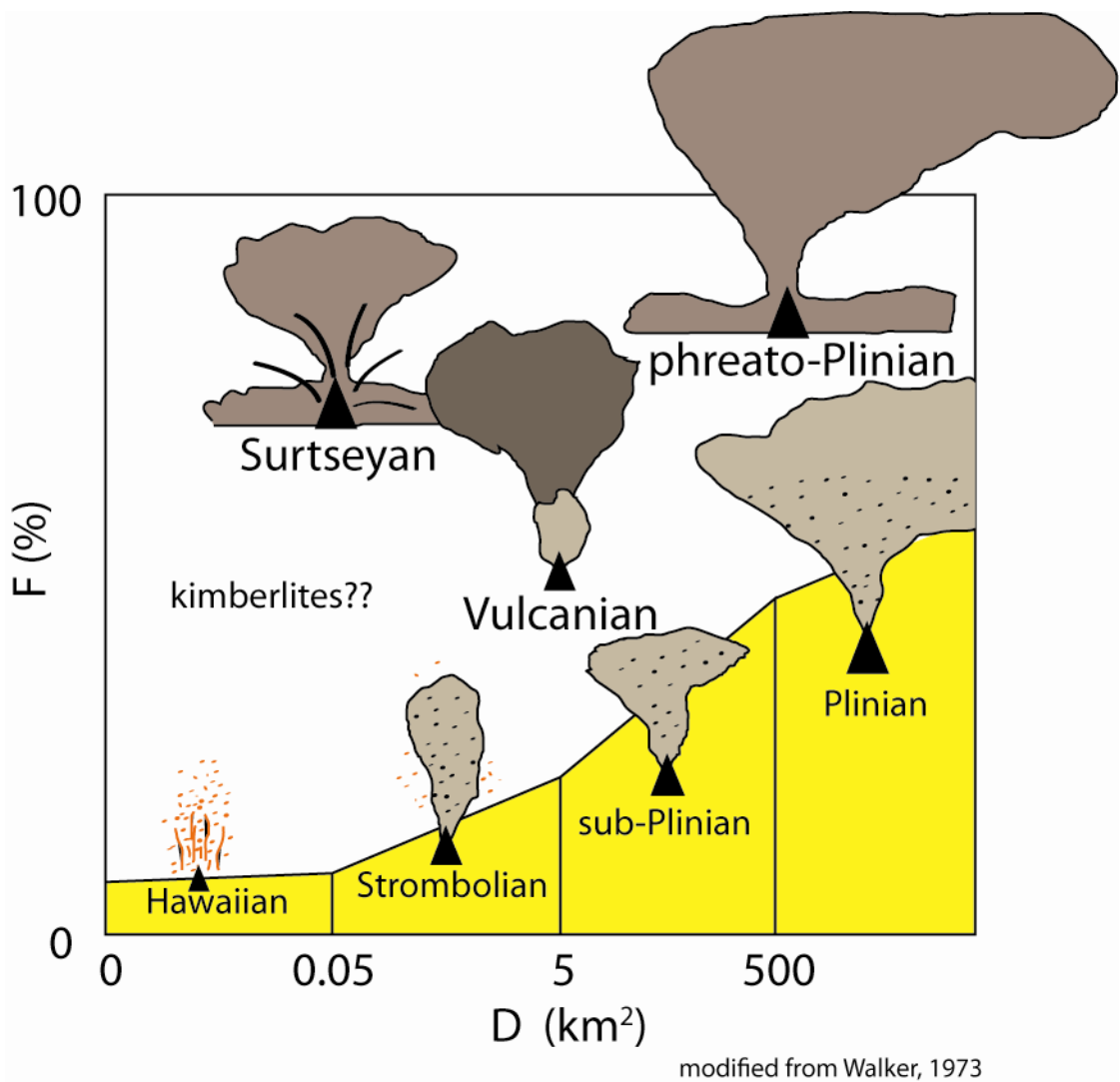


**Figure 1.7:** Classic volcanological fragmentation index of Walker (1973). Dispersal ( $D$ ) is the area within  $0.01 T_{\max}$  isopach ( $>1\%$  of maximum deposit thickness). Fragmentation ( $F$ ) is the % of juvenile clasts  $<1\text{mm}$  at the  $0.1 T_{\max}$  isopach. Enclosed boxes (shaded yellow) represent parameter space ( $D$  vs.  $F$ ) occupied by pyroclastic deposits resulting from different styles of explosive eruption (i.e., Hawaiian, Strombolian, sub-plinian, Plinian). Other explosive eruption styles involving various amounts of water and degassing magma are also shown (i.e., Surtseyan, phreato-Plinian, Vulcanian). Kimberlite deposits are precluded from this kind of analysis (see text). Modified after Walker (1973).

no historical eruptions of kimberlite. Second, extra-crater deposits of kimberlite are poorly-preserved, and there are no examples of kimberlites with completely preserved volcano architectures (e.g., root zone, volcanic vent, extra-crater tephra ring, full lateral extent of deposits). Third, post-emplacement alteration of kimberlite rocks complicates efforts to measure particle size distributions using conventional methods (i.e., sieving). *Therefore, accurate assessment of magnitude (kg) or intensity (kg/s) of kimberlite eruptions by conventional methodologies is not possible.* Because of this, kimberlite volcanologists and petrologists continue to debate the eruption intensities (e.g., Hawaiian, sub-Plinian, Surtseyan; Fig. 1.7) and depositional styles (e.g., fall, surge, flow, fluidized fountain) responsible for most pyroclastic deposits observed within kimberlite pipes (e.g., Lorenz, 1975; Sparks et al., 2006; Gernon et al., 2008b; Porritt et al., 2008).

### 1.2.2 Physical properties of kimberlite magmas

Occurrences of intrusive coherent kimberlite of all ages and around the world exhibit similar mineralogical attributes. The mineralogical attributes of kimberlite allow for a petrographic definition of kimberlite as a rock type: that is, kimberlite rocks are primarily identified by a particular mineral and textural assemblage (Mitchell, 1995; Woolley et al., 1996) rather than by rock chemistry (e.g., dacite, latite, shonkinite). Intrusive coherent or hypabyssal (*sensu* Mitchell, 2008) kimberlites are hybrid rocks comprising mantle-derived xenocrysts and primary phases (i.e., olivine, spinel, perovskite, apatite, phlogopite, serpentine, calcite/dolomite), crystallized from the kimberlite magma (Mitchell, 1986). There are abundant studies which examine the mineral chemistry and textures of different phases found within intrusive coherent kimberlite rocks (Mitchell, 2008). Kimberlite rocks are shown to be crystal-rich (Fig. 1.8), and kimberlite magma is believed to be more volatile-rich and lower in viscosity than all other magma types (Eggler, 1989; Price et al., 2000; Dingwell et al., 2004; Sparks et al., 2006; Mitchell, 2008).

To understand volcanic eruptions and emplacement of kimberlite magma, it is essential to understand the physical properties of kimberlite magmas. Yet, such physical properties have received much less attention than mineral chemistry and petrography.

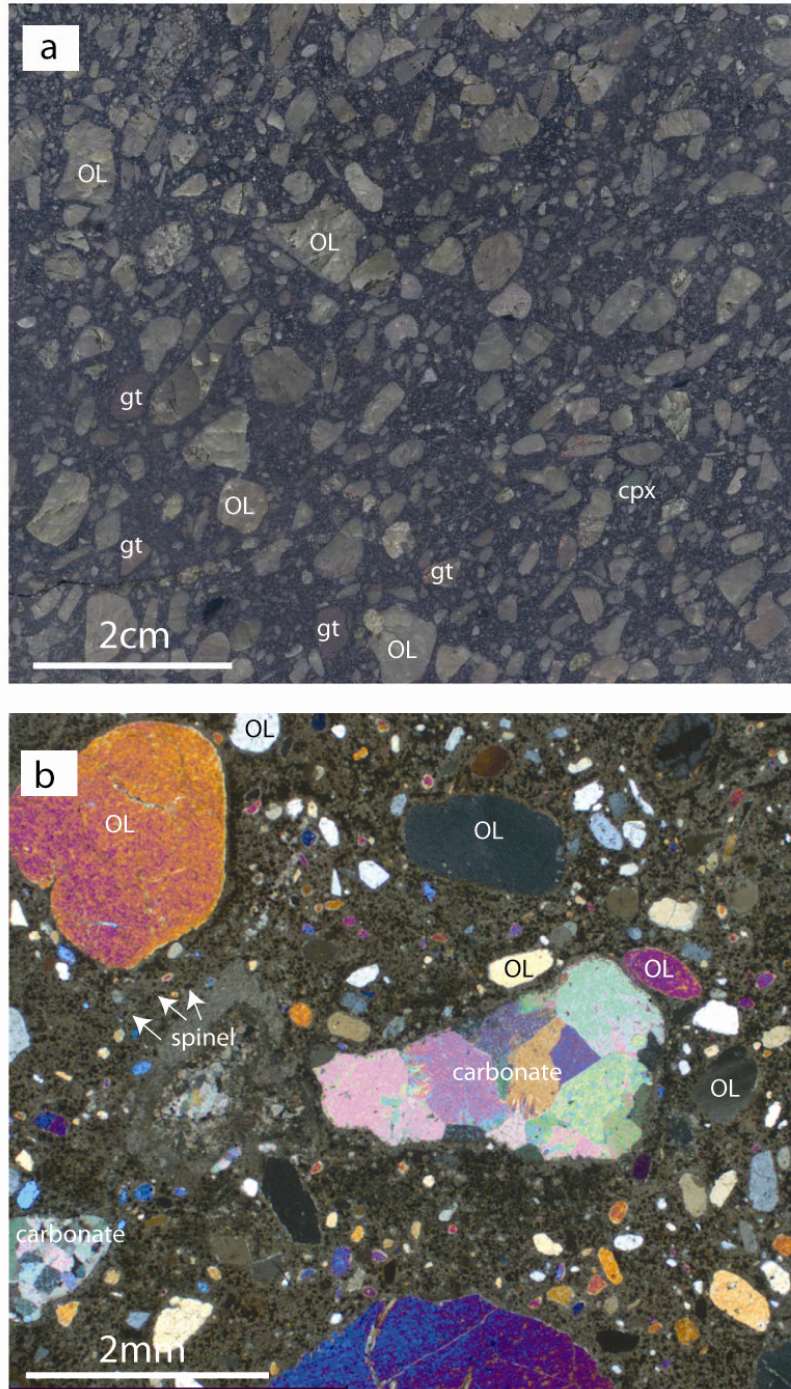


**Figure 1.8:** Typical intrusive coherent kimberlite from A154N, Diavik, NWT, Canada: (a) polished slab of intrusive coherent kimberlite, showing high olivine content (~50%), garnet and clinopyroxene xenocrysts (gt, cpx), country rock fragments in a massive fabric; (b) polished thin section of intrusive coherent kimberlite in crossed polars, showing olivine crystals set in a matrix of serpentine, carbonate and spinel.

For example, olivine crystal contents have only been measured in a statistically limited way; data was collected from a single scale of observation (e.g., thin sections; Clement, 1982), a single sample or for a single parameter (e.g., modal %; Shee, 1985). These limited data have *not* been useful in interpreting a) the paragenesis of crystals in kimberlite magma, b) the rheological behaviour of kimberlite magma during ascent, or c) the methods and styles of fragmentation of kimberlite magmas.

Volatile contents have been estimated based on measurements by whole-rock geochemical methods in crystallized, intrusive coherent rocks (e.g., Dalton and Presnall, 1998; Price et al., 2000; Sparks et al., 2006), and are suggested to be representative of kimberlite magmas that have not de-gassed (Mitchell, 2008). However, intrusive coherent kimberlite rocks are, by definition, un-eruptive. In other volcanic systems, rocks formed by crystallization of intrusive and un-erupted magma are relatively poor in volatile content in comparison to correlated extrusive rocks (e.g., Houghton and Gonnermann, 2008; Namiki and Manga, 2008). This suggests that intrusive coherent kimberlite rocks may be relatively de-gassed in comparison with kimberlite magmas responsible for pyroclastic deposits resulting from explosive eruption. Moreover, volatiles may be added to a crystallizing body of intrusive coherent kimberlite by late-stage influx from depth or by post-emplacement alteration. Thus, such measurements represent, at best, a minimum volatile content associated with a kimberlite melt, and are unlikely to characterize the true volatile content of ascending or erupting melt.

Furthermore, accurate measurement of the viscosity of kimberlite melts has not been accomplished, due to the experimental difficulties posed by working with volatile-rich melts (Kurszlaukis et al., 1998; Brooker et al., 2001a; Dingwell et al., 2004; Mitchell, 2008). Quantitative data reflecting these physical properties is essential to advance understanding of kimberlite ascent and eruption. *Thus, physical properties of kimberlite magma such as crystal content, volatile content, and viscosity, remain poorly understood.*

### 1.2.3 Pyroclastic kimberlite

Crater-facies kimberlite is generally comprised of either primary pyroclastic material or re-sedimented primary volcanic material sloughing into the volcanic crater (Mitchell, 1986; Mitchell, 1995; Field and Scott Smith, 1999; Skinner and Marsh, 2004). Primary pyroclastic deposits are recognized by the presence of juvenile pyroclasts

comprising melt, crystals and xenoliths and xenocrysts, and an absence of features suggesting reworking. Resedimented kimberlite deposits are identified by the presence of: (a) rounding of grains; (b) high matrix mud content; and (c) tractional bed forms (Clement and Skinner, 1985; Field and Scott Smith, 1999; Scott Smith, 1999a).

On this basis, there are few easily recognized bodies of crater-facies kimberlite. At present, crater-facies kimberlite has been identified and described at Orapa (Field et al., 1997; Gernon et al., 2008a) and Jwaneng (Machin, 2001; Webb et al., 2003) in Botswana, Tokapal, India (Mainkar et al., 2004), Victor, ON. (Webb, 2003; van Straaten et al., 2008), Tli Kwi Cho (Doyle et al., 1998), Buffalo Hills (Boyer et al., 2003; Boyer et al., 2004), Ekati, NWT (Porritt et al., 2008; Porritt and Cas, 2009), and Fort-a-la-Corne<sup>2</sup>, SK. (Leahy, 1997; Leckie, 1997; Berryman et al., 2004; Zonneveld et al., 2004; Pittari et al., 2008). The number of bodies at which primary pyroclastic kimberlite has been positively identified in true crater-facies is even fewer (Field et al., 1997; Berryman et al., 2004; Boyer et al., 2004; Porritt and Cas, 2009).

The relationships between pyroclast textures in deposits of pyroclastic volcanic rocks and fragmentation mechanisms (e.g., brittle fragmentation, gas foaming) is well-documented in other magma types (Papale, 1999; Cashman et al., 2000; Mastin, 2004; e.g., Bindeman, 2005). However, the relationship between such textures and eruption dynamics in kimberlite volcanoes is poorly constrained: only a few location-specific studies exist that attempt to link such textural observations within deposits of pyroclastic kimberlite with eruption processes (Walters et al., 2006a; Brown et al., 2008; Gernon et al., 2008a; Pittari et al., 2008; Porritt and Cas, 2009), but these studies are sub-quantitative and descriptive in nature. There are also no comprehensive studies that attempt to account for the diversity of pyroclast textures from global occurrences. The manner in which kimberlite magma disrupts or fragments to produce pyroclastic deposits has only recently been modeled (i.e., Cas et al., 2008a), and remains unclear. Moreover, there have been few experimental studies aimed at understanding kimberlite eruption and/or fragmentation processes (Kurszlauskis et al., 1998; Gernon et al., 2008c).

---

<sup>2</sup> The Fort-a-la-Corne (FALC) bodies are the largest in Canada, some as large as 1.5 km<sup>2</sup> in surface expression, and contain many features suggestive of pyroclastic kimberlite. It is believed that FALC could represent the only previously-known global occurrence of crater-edifice or extra-crater pyroclastic kimberlite.

As there are few examples of *bona fide* pyroclastic kimberlite, few studies that attempt to quantify relationships between pyroclastic deposits and eruption style, and no analogue experimentation attempting to understand kimberlite fragmentation, it is difficult to determine the relationship between deposits of pyroclastic kimberlite and the pyroclast textures therein with specific fragmentation processes. Thus, *the lack of studies quantifying pyroclastic kimberlite deposits hinders any direct linking between kimberlite deposits and eruption processes.* Kimberlite occurrences with pyroclastic kimberlite must be identified, and descriptively and quantitatively studied in order to link kimberlite volcanism with the more well-understood processes documented for systems such as rhyolite, andesite or basalt.

### **1.3 Diavik kimberlites**

There are upwards of 200 pipes in the Lac de Gras region, distributed along a NW-trending axis in excess of 120 km in length (Figs. 1.9,1.10; Graham et al., 1999). The cluster of economic pipes at Diavik are among the youngest pipes known in the world, and occur in an area of Lac de Gras characterized by pipes of Late Cretaceous and Eocene ages (Amelin, 1996; Heaman, 1996). The Diavik pipes included in the current mine plan are A154N, A154S, A418, and A21 (Fig. 1.11). These bodies form steep-sided to near vertical cones, between 100-150 m in plan diameter, and penetrate the basement rocks to upwards of 700 m below the present-day surface. Two pipes (A154N and A154S) are currently being mined from a large open pit on the east side of an island at the north end of Lac de Gras. These pipes are within 200 m of each other, and A418 is less than 700 m away to the south of A154S. In addition, there are 20 other kimberlite pipes within 10 km of the Diavik occurrences.

The kimberlite pipes at Diavik intrude a package of Late Archean plutonic rocks within the Slave Structural Province of the Northwest Territories, Canada (Fig. 1.10). The plutonic rocks likely represent the final stabilizing event in the formation of

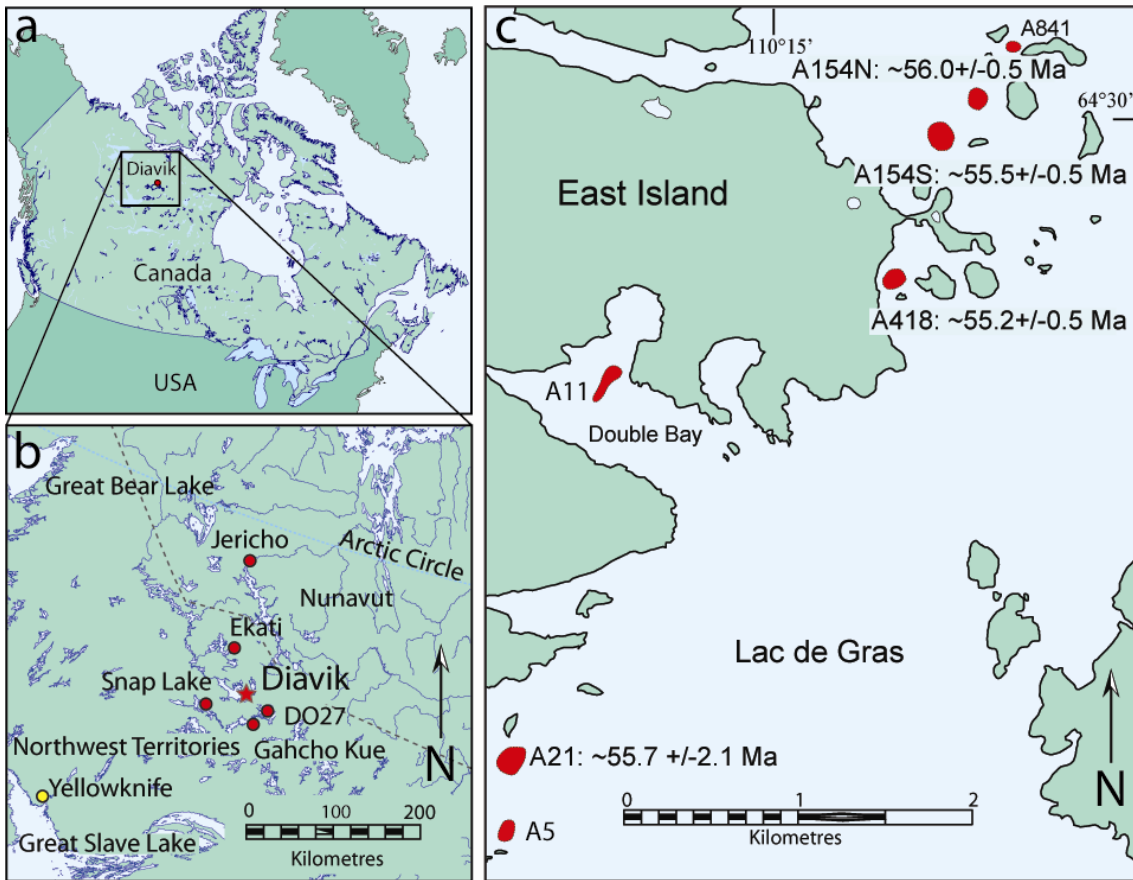


**Figure 1.9:** Location of Diavik kimberlite cluster, Northwest Territories, Canada. Diavik is in the Northwest Territories of Canada; (b) Diavik is surrounded by multiple occurrences of diamondiferous kimberlite pipes (e.g., DO-27), clusters (e.g., Ekati, Gahcho Kue), and dykes (e.g., Snap Lake); (c) The pipes are located offshore of an island in the eastern portion of Lac de Gras in the Northwest Territories, Canada (red dots). There are over 60 kimberlite occurrences on the Diavik property, and three kimberlite pipes are currently being mined.

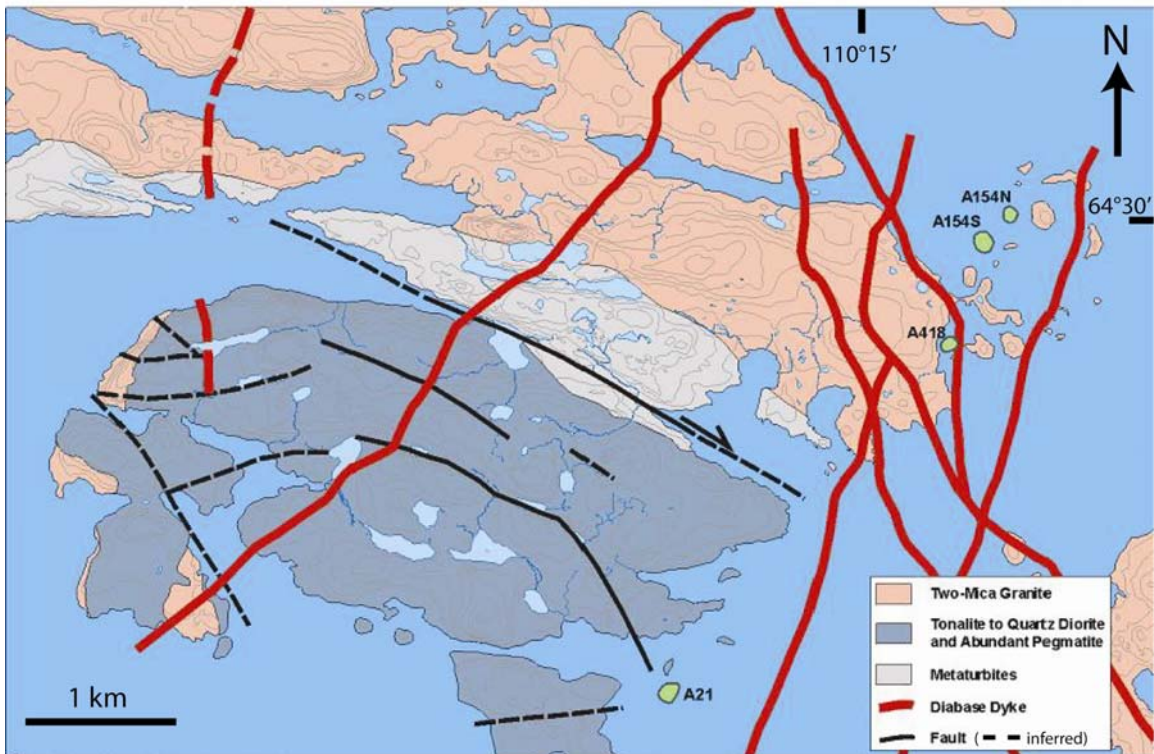


**Figure 1.10:** Local geology of East Island of Lac de Gras. Kimberlite pipes are indicated as green circles. Blue indicates water. Modified after Stublely (1998).



Pipe	<b>A418</b>	<b>A154S</b>	<b>A154N</b>	<b>A21</b>
Volume	$4.6 \times 10^6 \text{ m}^3$	$5.7 \times 10^6 \text{ m}^3$	$5.6 \times 10^6 \text{ m}^3$	$2.7 \times 10^6 \text{ m}^3$
Surface Area	11231 m <sup>2</sup>	15769 m <sup>2</sup>	10990 m <sup>2</sup>	~10540 m <sup>2</sup>
Max diameter	~145 m	~140 m	~135 m	~110 m
Lithologies	organic-rich mud bedded volcanoclastic kimb massive volcanoclastic kimb coherent (intrusive) kimb	resedimented kimberlite pyroclastic kimberlite massive volcanoclastic kimb coherent (intrusive) kimb	pyroclastic kimberlite resedimented kimberlite massive volcanoclastic kimb coherent (intrusive) kimb	volcanoclastic kimberlite resedimented kimberlite coherent (intrusive) kimb
Grade	3.1 carats/tonne	3.4 carats/tonne	2.5 carats/tonne	1.9 carats/tonne
Current activity	open pit underground bulk sampling	open pit underground bulk sampling	open pit underground bulk sampling	ongoing evaluation; underground bulk sampling

**Figure 1.11:** 3-D images and summaries of kimberlite pipes at Diavik, NWT. Elevation in meters above sea level (m asl) is shown on the left. Red lines represent current mining levels (as of 07.07.09). Pipe dimensions are approximations subject to change with new drilling information. Grade values represent mean ore grade for the entire pipe. 3-D images are generated from Diavik geology models in Vulcan<sup>TM</sup> mining software. Kimb = kimberlite.

the Slave craton (Davis, 1994). Current surface exposures in the region comprises approximately 65% late Archean granitoids (2.7-2.55 Ga) and 35% supracrustal rocks (mostly 2.72-2.66 Ga) (Kjarsgaard and Wyllie, 1994). The local country rocks at the Diavik mine site are comprised of two major granitoids, with remnant blocks of biotite schist (Fig. 1.10). Proterozoic diabase dike swarms in the area trend N-NW, and likely provided the structural weaknesses utilized by the magmas of the Lac de Gras kimberlites (Fig. 1.10). Remnants of Phanerozoic cover strata are largely missing, although xenoliths preserved within Diavik kimberlites suggest that Cretaceous marine shales (~20 – 300 m), terrigenous arenite sandstone (minor) and organic peat capped the basement rocks during Eocene time. The basement complex is currently overlain by variably thick, Quaternary, glacially deposited till cover. These tills are locally capped by a thin veneer of lacustrine sediments and/or peat.

The A154N kimberlite pipe at Diavik comprises a diversity of coherent and fragmental kimberlite rocks, previously interpreted as re-sedimented volcanoclastic kimberlite, pyroclastic kimberlite, and hypabyssal kimberlite (Graham et al., 1999). Study of this diverse suite of deposits from a single kimberlite volcano at Diavik provides an opportunity to investigate properties of kimberlite magma and characteristics of pyroclastic deposits deriving from kimberlite eruption. For example, intrusive coherent kimberlite rocks at A154N are useful for understanding the nature of kimberlite magma because they represent unerupted, crystallized kimberlite magma. Moreover, pyroclastic kimberlite deposits in A154N are useful for providing first-order data on the types, abundances, sizes, shapes of juvenile pyroclasts deriving from eruption of kimberlite.

An emphasis of this thesis is on studying the properties (e.g., size, abundance, shapes, etc.) of olivine crystals in kimberlite deposits. As olivine crystals are the dominant component in nearly all deposits of kimberlite, they serve as a ‘lens’ through which we can view kimberlite eruption: comparison of olivine properties in both coherent and pyroclastic deposits of kimberlite at A154N allows for interpretations of processes responsible for these properties. In addition, olivine and diamond have similar physical properties (e.g., size, shape, density), and, as a result, likely exhibit similar hydraulic behavior in volcanic eruptions. Thus, the accurate characterization of olivine in coherent and pyroclastic kimberlite rocks has additional economic implications.

Identifying the specific properties of diverse deposits at A154N allows for the interpretation of volcanic emplacement processes. In addition, specific observations and

interpretations at A154N rooted in facies analysis principles may have applicability to other kimberlite volcanoes at Diavik, as well as general applications to other kimberlite volcanoes. These results also have implications in the field of volcanology, by providing first-order data on the physical properties of low-viscosity kimberlite magmas and component data on conduit infill.

## **1.4 Organization of thesis**

### 1.4.1 Manuscript chapters

Above, I highlighted the following outstanding gaps in kimberlite volcanology: a) insufficient metrics to characterize the volcanic style and intensity of kimberlites; b) a lack of understanding of the physical properties of kimberlite magma; and c) minimal quantification of pyroclastic deposits. The main goal of this thesis is to make contributions that begin to address aspects of these important issues, through the study of the kimberlite deposits in the A154N kimberlite pipe at Diavik. Specifically, this is accomplished in the following ways:

1. To ascertain the physical properties of kimberlite magma, this thesis: a) quantifies and characterizes the olivine crystal content of intrusive coherent kimberlite bodies (Ch. 3), and b) characterizes the evolving physical nature of kimberlite magmas from unique emplacement events in space and time (Ch. 4).
2. To assist in characterizing the style and intensity of kimberlite eruptions, this thesis quantifies and describes the physical character of components and geometries of specific deposits of pyroclastic kimberlite, leading to an interpretation of eruption and depositional styles for multiple deposit types (Chs. 2,4).
3. In order to better describe the volcanic style and intensity of kimberlite eruptions, it is necessary to recover energy properties associated with ascending and erupting kimberlite magmas. To recover such properties, this thesis: a) uses the physical nature of magma and geometric constraints of kimberlite bodies to calculate eruption durations and magma fluxes (Ch. 4), and b) compares olivine and crystallized melt components in intrusive coherent kimberlite rocks with those

observed in pyroclastic deposits to characterize the degree of component modification due to eruption (Ch. 5).

Addressing specific gaps in the knowledge of kimberlite eruptions allows for more general interpretations of the nature and style of fragmentation during kimberlite eruptions. Based on observations at A154N, I develop a tool for interpreting the style of kimberlite eruptions based on consistently observable features in pyroclastic deposits.

This thesis represents a collection of research manuscripts at various stages of publication aimed at achieving these objectives. Many of the chapters have already been published (chapters 2, 4, and Appendix 7.2.2) in peer-reviewed international journals or submitted for publication (chapter 3), while others have undergone extensive internal review to allow for future publication in international journals (chapters 5 and 6). Efforts have been made to minimize repetition, though some redundancy is unavoidable. The order of chapters in the thesis is intended to descriptively “build” a single kimberlite volcano (A154N) from the bottom up. Before each chapter, a short paragraph is included to give context to assist the reader, and to segue between separate manuscript-based chapters. Below, a short précis is provided for each chapter:

In Chapter 2, we describe the geometries, structures, and componentry of deposits from the uppermost 130 m of the A154N kimberlite pipe. We then interpret the processes responsible for their emplacement on the basis of these characteristics. Facies analysis of a deposit filling the uppermost portions of A154N suggest a pyroclastic origin and hydraulic sorting during *en-masse* deposition of pyroclastic kimberlite into a deep water column. Granulometric analysis shows the PK<sub>2</sub> deposit was originally transported as a pyroclastic density current that was sourced from one of the many adjacent pipes in the Diavik area and inundated the A154N pipe.

Chapter 3 contains the results of the first quantitative characterization of olivine crystal size distributions (CSD) for magmatic or coherent kimberlite using 2D image analysis techniques with scaling and stereological corrections. These CSDs yield olivine crystal properties for olivine in intrusive coherent kimberlite at A154N. The olivine properties are shown to be capable of uniquely describing deposits of kimberlite. Such properties are also useful for comparison with other global occurrences of olivine crystals in intrusive coherent kimberlite, and useful in testing volcanologic hypotheses of crystal size and shape modification due to emplacement of kimberlite magma.

In Chapter 4, facies analysis of the A154N kimberlite pipe shows that deposits filling the pipe record a sequence of four discrete eruptive and intrusive events, for which relative times and modes of emplacement can be established. Observations from field mapping and image analysis of polished slabs and thin sections are used to characterize the magma that erupted to produce each deposit. The ascent of a vigorously degassing magma is shown to create separate regimes of kimberlite magma due to the physical separation of phases: (a) the gas-charged front of the magma created by decoupling the more buoyant gas phase from the silicate melt; (b) a transient, gas-rich body of magma in which later-stage exsolved fluids/gases are essentially coupled to the melt; and (c) a fluid-depleted tail of magma which remains buoyant within the lithosphere but ascends more slowly than the fluid and exsolving gas phases. These magma properties are combined with steady-state assumptions to estimate velocity, magma flux and calculate total eruption durations.

Chapter 5 represents the application of concepts developed in earlier chapters to the physical volcanology of kimberlites. Two hypotheses are tested regarding fragmentation of kimberlite magma during explosive eruption: 1) olivines break, and 2) melt separates from crystals. Results from these two tests are used to explain observations of pyroclast textures at Diavik and around the world. Furthermore, these results are used to create a theoretical fragmentation index for interpreting observations in pyroclastic deposits of kimberlite with respect to volcanic style and intensity.

Chapter 6 gives a summary of the significant findings of the thesis, discusses the significance of these findings on the assessment of diamond grade within kimberlite deposits. An experiment is conducted on olivine crystal size distributions in another kimberlite pipe at Diavik, A154S, using methods developed in Chapter 3 and testing ideas found in Chapter 5. Lastly, I identify key areas for further research based on the conclusions of this study.

#### 1.4.2 Appendix overview

Details of methods and data discussed in each chapter are part of an adjoining digital appendix found at the back of the thesis, organized by chapter into five categories: 1) General notes, datasets, and software macros; 2) Digital images; 3) Matlab script for

figures and numerical modeling, 4) Methods, and 5) Output Data. Data collected in this study include the following:

- open pit maps
- graphic logs
- drillhole logs
- digital images: open pit exposures, structures, drillholes, polished slabs, thin sections scans, and thin section micrographs
- polished slabs and thin sections (descriptions, physical samples)
- crystal and pyroclast component data from field maps, polished slabs and thin sections (modal %, sizes, relative abundances, etc.)
- sample locations and rock types
- 3D models built in Vulcan and GoCad mining software

Appendix 7.3.1 shows the details of the methodology described in Chapter 3. Appendix 7.3.2 demonstrates the utility of an automatic image analysis method by comparing CSDs for olivine within coherent kimberlite using this method versus those resulting from manual digitization of olivine grains (Chapter 3). Statistical results from the automatic detection system are shown to correlate well with manual results, while proving to be much more efficient. Discrepancies between the two methods and shortcomings of both methods are discussed in detail.

Open pit mapping of A154N was conducted during 12 trips of 1 week or more to the Diavik mine site over a 3 year period (2005 – 2008), during which the uppermost 160 m (415 m asl to 255m asl) of kimberlite were mined from A154N. In total, 8 bench-scale field maps and 11 grid maps (2 x 2 m) were made of open pit exposures. Over 1000 digital photos of rock textures, bench faces, and hand samples were taken in the open pit. In total, 28 drillholes intersecting all major lithological units and rock types in A154N were examined; 10 drillholes were logged using Diavik’s logging template (confidential), and volcanologic graphic logs constructed for 2 drillholes; digital photos and detailed logs from 15 additional drillholes through A154N from an archived database at Diavik were also examined. I re-interpreted and re-compiled three-dimensional models in Vulcan<sup>TM</sup> mining software from existing datasets and models compiled by Diavik mine geologists. Sampling was conducted in-situ in the open pit, from underground drifts, and from

drillholes into A154N. Over 500 individual rock samples were collected and catalogued, and 250 thin sections prepared for kimberlite from A154N, A154S, A418 and A21 kimberlite pipes.

## 1.5 References

- Amelin, Y., 1996. Report on Rb-Sr and U-Pb study of kimberlite samples VR44444A through VR44465A. Confidential Report for Kennecott, Canada Inc.
- Berryman, A.K., Scott Smith, B.H. and Jellicoe, B.C., 2004. Geology and diamond distribution of the 140/141 kimberlite, Fort a la Corne, central Saskatchewan, Canada. *Lithos* 76(1-4), 99-114.
- Bindeman, I.N., 2005. Fragmentation phenomena in populations of magmatic crystals. *American Mineralogist* 90, 1801-1815.
- Boyer, L., Hood, C.T., McCandless, T.E., Skelton, D. and Tosdal, R.M., 2003. Volcaniclastic kimberlites of the Buffalo Head Hills, Alberta, Canada. GAC-MAC Joint Annual Meeting 28, 498.
- Boyer, L., Hood, C.T., McCandless, T.E., Skelton, D. and Tosdal, R.M., 2004. Volcanology of the Buffalo Hills Kimberlites, Alberta, Canada: some preliminary observations. 8th International Kimberlite Conference Long Abstract.
- Brooker, R.A., Kohn, S., Holloway, J.R. and McMillan, P.F., 2001. Structural controls on the solubility of CO<sub>2</sub> in silicate melts: Part I: Bulk solubility data. *Chemical Geology* 174, 225–239.
- Brown, R.J., Gernon, T., Stiefenhofer, J. and Field, M., 2008. Geological constraints on the eruption of the Jwaneng Centre kimberlite pipe, Botswana. *Journal of Volcanology and Geothermal Research* 174(1-3), 195-208.
- Bursik, M.I., Sparks, R.S.J., Gilbert, J.S. and Carey, S.N., 1992. Sedimentation of tephra by volcanic plumes: I. Theory and its comparison with a study of the Fogo A plinian deposit, Sao Miguel (Azores). *Bulletin of Volcanology* 54(4), 329-344.
- Cas, R.A.F., Porrit, L., Hayman, P. and Pittari, A., 2008a. Pyroclast formation processes during explosive kimberlite eruptions. 9th International Kimberlite Conference extended abstract no. 9IKC-A-00030.
- Cas, R.A.F., Porritt, L., Pittari, A. and Hayman, P., 2008b. A new approach to kimberlite facies terminology using a revised general approach to the nomenclature of all volcanic rocks and deposits: Descriptive to genetic. *Journal of Volcanology and Geothermal Research* 174(1-3), 226-240.
- Cas, R.A.F. and Wright, J.V., 1987. Volcanic successions, modern and ancient. Chapman & Hall, London, 528 pp.
- Cashman, K.V., Sturtevant, B., Papale, P. and Navon, O., 2000. Magmatic fragmentation. In: H. Sigurdsson (Editor), *Encyclopedia of Volcanoes*. Academic Press, London, pp. 421-430.
- Clement, C.R., 1982. A comparative geological study of some major kimberlite pipes in the Northern Cape and Orange Free State, University of Cape Town, Cape Town, South Africa, 410 pp.
- Clement, C.R. and Reid, A.M., 1989. The origin of kimberlite pipes: an interpretation based on a synthesis of geological features displayed by southern African occurrences. In: J. Ross (Editor), *Kimberlites and Related Rocks*; Geological Society of Australia Special Publication. Geological Society of Australia, pp. 632-646.
- Clement, C.R. and Skinner, E.M.W., 1985. A textural-genetic classification of kimberlites. *Transactions of the Geological Society of South Africa* 88, 403-409.

- Cookenboo, H., 1997. Emplacement history of the Jericho kimberlite northwest of Conwoyto Lake, NWT. In: E.a.G.I. Northwest Territories Mining, NWT Geology Division, DIAND (Editor), pp. 3-10.
- Dalton, J.A. and Presnall, D.C., 1998. The continuum of primary carbonatitic-kimberlite melt compositions in equilibrium with lherzolite: data from the system CaO–MgO–Al<sub>2</sub>O<sub>3</sub>–SiO<sub>2</sub>–CO<sub>2</sub> at 6 GPa. *Journal of Petrology* 39, 1953–1964.
- Davis, W.J., Fryer, B.J., King, J.E., 1994. Geochemistry and evolution of Late Archean plutonism and its significance to the tectonic development of the Slave Craton. *Precambrian Research* 67, 207-241.
- Dawson, J.B., 1994. Quaternary kimberlite volcanism on the Tanzanian Craton. *Contributions to Mineralogy and Petrology* 116, 473-485.
- Dingwell, D.B., Courtial, P., Giordano, D. and Nichols, A.R.L., 2004. Viscosity of peridotite liquid. *Earth and Planetary Science Letters* 226, 127–138.
- Doyle, B.J., Kivi, K. and Scott Smith, B.H., 1998. The Tli Kwi Cho (DO27 and DO18) Diamondiferous Kimberlite Complex, Northwest Territories, Canada. In: J.J. Gurney, J.L. Gurney, M.D. Pascoe and S.H. Richardson (Editors), VIIth International Kimberlite Conference. Red Roof Design, University of Cape Town, South Africa, pp. 194-204.
- Eggler, D.H., 1989. Kimberlites: How do they form? In: J. Ross (Editor), *Kimberlites and Related Rocks*. Geological Society of Australia Special Publication, pp. 489-504.
- Field, M., Gibson, J.G., Wilkes, T.A., Gababotse, J. and Khutjwe, P., 1997. The Geology of the Orapa A/K1 Kimberlite Botswana: Further insights into the emplacement of kimberlite pipes. *Russian Geology and Geophysics* 38(1), 24-39.
- Field, M. and Scott Smith, B.H., 1999. Contrasting geology and near-surface emplacement of kimberlite pipes in southern Africa and Canada, VIIth International Kimberlite Conference. Red Roof Designs, Cape Town, South Africa, pp. 214-237.
- Gernon, T., Field, M. and Sparks, R.S.J., 2008a. Depositional processes in a kimberlite crater: the Upper Cretaceous Orapa South Pipe (Botswana). *Sedimentology* 56(3), 623-643.
- Gernon, T., Gilbertson, M., Sparks, R.S.J. and Field, M., 2008b. Gas-fluidisation in an experimental tapered bed: Insights into processes in diverging volcanic conduits. *Journal of Volcanology and Geothermal Research* 174(1-3), 49-56.
- Gernon, T.M., Gilbertson, M.A., Sparks, R.S.J. and Field, M., 2008c. Gas-fluidisation in an experimental tapered bed: Insights into processes in diverging volcanic conduits. *Journal of Volcanology and Geothermal Research* 174(1-3), 49-56.
- Graham, I., Burgess, J.L., Bryan, D., Ravenscroft, P.J., Thomas, E., Doyle, B.J., Hopkins, R. and Armstrong, K.A., 1999. Exploration History and Geology of the Diavik Kimberlites, Lac de Gras, Northwest Territories, Canada. In: J.J. Gurney, J.L. Gurney, M.D. Pascoe and S.H. Richardson (Editors), *Proceedings of the VIIth International Kimberlite Conference*. Red Roof Design, Cape Town, South Africa, pp. 262-279.
- Hawthorne, J.B., 1975. Model of a kimberlite pipe. *Physics and Chemistry of the Earth* 9, 1-15.
- Heaman, L.M., Kjarsgaard, B., Creaser, R.A., Cookenboo, H.O., Kretschmar, U., 1996. Multiple episodes of kimberlite magmatism in the Slave Province, North America.
- Hetman, C.H., Scott Smith, B.H., Paul, J.L. and Winter, F., 2004. Geology of the Gahcho Kue' kimberlite pipes, NWT, Canada: Root to diatreme magmatic transition zones. *LITHOS* 76, 51-74.

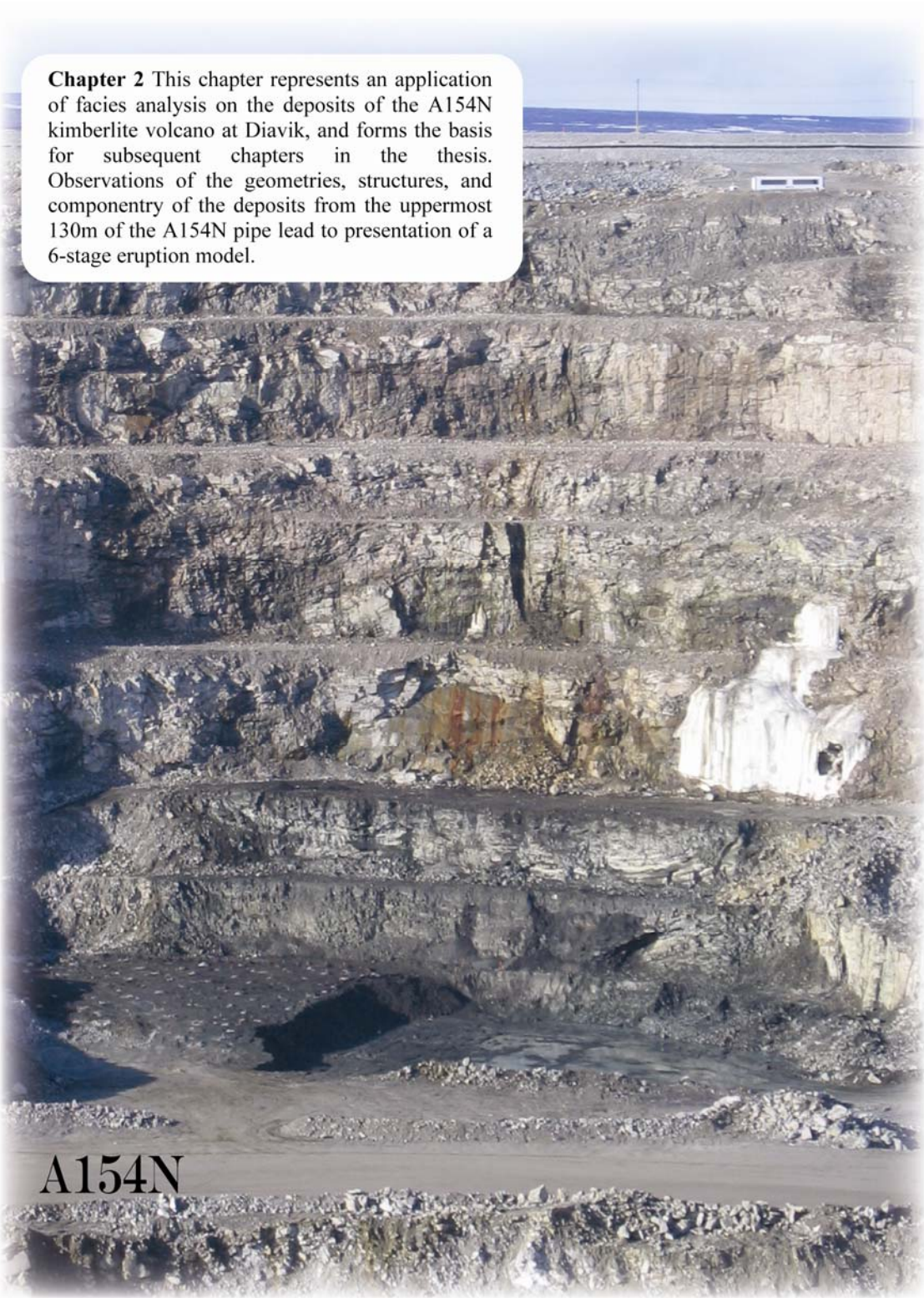
- Houghton, B.F. and Gonnermann, H.M., 2008. Basaltic explosive volcanism: Constraints from deposits and models. *Chemie der Erde - Geochemistry* 68(2), 117-140.
- Junqueira-Brod, T.C., Gaspar, J.C., Brod, J.A. and Kafino, C.V., 2005. Kamafugitic diatremes: Their textures and field relationships with examples from the Goias alkaline province, Brazil. *Journal of South American Earth Sciences* 18(3-4 SPEC. ISS.), 337-353.
- Kirkley, M.B., Kolebaba, M.R., Carlson, J.A., Gonzales, A.M., Dyck, D.R., and Diercker, C., 1998. Recent major kimberlite discoveries in Canada, VIIth International Kimberlite Conference. Long Abstracts. Red Roof Designs, Cape Town, South Africa, pp. 429-431.
- Kjarsgaard, B.A., Wilkinson, L., Armstrong, J.A., 2001. Geology of the Lac de Gras kimberlite field, central Slave Province, NWT-Nunanvut. GSC open file, scale 1:125,000. In: GSC (Editor).
- Kjarsgaard, B.A. and Wyllie, R.J.S., 1994. Geology of the Paul Lake area, Lac de Gras du Sauvage region of the central Slave Province, District of Mackenzie, Northwest Territories. *Geological Society of Canada Current Research 1994-C*, 23-32.
- Kolebaba, M., 2003. Deep infill crater model for Lac de Gras kimberlites: implications for diamond distribution., VIIIth International Kimberlite Conference Program with Abstracts.
- Kurszlaukis, S., Buttner, R., Zimanowski, B. and Lorenz, V., 1998. On the first experimental phreatomagmatic explosion of a kimberlite melt. *Journal of Volcanology and Geothermal Research* 80(3-4), 323-326.
- Leahy, K., 1997. Discrimination of reworked pyroclastics from primary tephra-fall tuffs: a case study using kimberlites of Fort a la Corne, Saskatchewan, Canada. *Bulletin of Volcanology* 59, 65-71.
- Leckie, D.A., Kjarsgaard, B.A., Bloch, J., McIntyre, D., McNeil, D., Stasiuk, L., Heaman, L., 1997. Emplacement and reworking of Cretaceous, diamond-bearing, crater-facies kimberlite of central Saskatchewan, Canada. *GSA Bulletin* 109(8), 1000-1020.
- Lorenz, V., 1975. Formation of phreatomagmatic maar–diatreme volcanoes and its relevance to kimberlite diatremes. *Physics and Chemistry of the Earth* 9, 17–29.
- Lorenz, V., 1985. Maars and diatremes of phreatomagmatic origin: a review. *Transactions of the Geological Society of South Africa* 88, 459-470.
- Lorenz, V. and Kurszlaukis, S., 2007. Root zone processes in the phreatomagmatic pipe emplacement model and consequences for the evolution of maar-diatreme volcanoes. *Journal of Volcanology and Geothermal Research* 159(1-3), 4-32.
- Lorenz, V., Kurszlaukis, S., 2003. Kimberlite Pipes: Growth models and resulting implications for diamond exploration, Program Abstracts, VIIIth International Kimberlite Conference, pp. 4.
- Machin, K.J., 2001. Processes and products in kimberlitic crater facies of the South Lobe, Jwaneng Mine, Botswana, MSc thesis, Rhodes University, Grahamstown, South Africa.
- Mainkar, D., Lehmann, B. and Haggerty, S.E., 2004. The crater-facies kimberlite system of Tokapal, Bastar District, Chhattisgarh, India. *Lithos* 76(1-4), 201-217.
- Mastin, L.G., 2004. The hydrodynamics of magma-water mixing and its effects on fragmentation and eruptive violence. , Abstract Volume of the 2nd International Maar Conference. Occasional papers of the Geological Institute of Hungary, pp. 76.

- McClintock, M. and White, J., 2006. Large phreatomagmatic vent complex at Coombs Hills, Antarctica: Wet, explosive initiation of flood basalt volcanism in the Ferrar-Karoo LIP. *Bulletin of Volcanology* 68(3), 215-239.
- Mitchell, R.H., 1986. *Kimberlites: Mineralogy, Geochemistry and Petrology*. Plenum Press, New York, 442 pp.
- Mitchell, R.H., 1995. *Kimberlites, Orangeites and related rocks*. Plenum Press, New York.
- Mitchell, R.H., 2008. Petrology of hypabyssal kimberlites: Relevance to primary magma compositions. *Journal of Volcanology and Geothermal Research* 174(1-3), 1-8.
- Namiki, A. and Manga, M., 2008. Transition between fragmentation and permeable outgassing of low viscosity magmas. *Journal of Volcanology and Geothermal Research* 169(1-2), 48-60.
- Nowicki, T., Crawford, B., Dyck, D., Carlson, J., McElroy, R., Oshust, P. and Helmstaedt, H., 2004. The geology of kimberlite pipes of the Ekati property, Northwest Territories, Canada. *Lithos* 76(1-4), 1-27.
- Nowicki, T., Crawford, B., Dyck, D., Carlson, J., McElroy, R., Oshust, P., Helmstaedt, H., 2004. The Geology of kimberlite pipes of the Ekati property, Northwest Territories, Canada. *LITHOS* 76, 1-27.
- Papale, P., 1999. Strain-induced magma fragmentation in explosive eruptions. *Nature* 397, 425-428.
- Pell, J.A., 1997. Kimberlites in the Slave Craton, Northwest Territories, Canada: A preliminary review. *Russian Geology and Geophysics* 38(1), 516.
- Pittari, A., Cas, R.A.F., Lefebvre, N., Robey, J., Kurszlauskis, S. and Webb, K., 2008. Eruption processes and facies architecture of the Orion Central kimberlite volcanic complex, Fort à la Corne, Saskatchewan; kimberlite mass flow deposits in a sedimentary basin. *Journal of Volcanology and Geothermal Research* 174(1-3), 152-170.
- Porritt, L.A. and Cas, R.A.F., 2009. Reconstruction of a kimberlite eruption, using an integrated volcanological, geochemical and numerical approach: A case study of the Fox Kimberlite, NWT, Canada. *Journal of Volcanology and Geothermal Research* 179(3-4), 241-264.
- Porritt, L.A., Cas, R.A.F. and Crawford, B.B., 2008. In-vent column collapse as an alternative model for massive volcanoclastic kimberlite emplacement: An example from the Fox kimberlite, Ekati Diamond Mine, NWT, Canada. *Journal of Volcanology and Geothermal Research* 174(1-3), 90-102.
- Price, S., Russell, J.K. and Kopylova, M., 2000. Primitive magma from the Jericho pipe, N.W.T., Canada: Constraints on primary melt chemistry. *Journal of Petrology* 41(6), 789-808.
- Ross, P.S., White, J., Zimanowski, B. and Büttner, R., 2008a. Multiphase flow above explosion sites in debris-filled volcanic vents: Insights from analogue experiments. *Journal of Volcanology and Geothermal Research* 178(1), 104-112.
- Ross, P.S., White, J.D.L., Zimanowski, B. and Buttner, R., 2008b. The role of debris jets in the evolution of diatremes: field and experimental evidence. 9th International Kimberlite Conference Extended Abstract No. 9IKC-A-00017, 3.
- Scott Smith, 1999. Near-surface emplacement of kimberlites by magmatic processes. . Invited article in IAVCEI commission on explosive volcanism newsletter Spring, 1999, p. 314.
- Scott Smith, 2008. Canadian kimberlites: Geological characteristics relevant to emplacement. *Journal of Volcanology and Geothermal Research* 174(1-3), 9-19.

- Scott Smith, B.H., 2009. The Economic Implications of kimberlite emplacement. 9th International Kimberlite Conference extended abstracts 9IKC-A-00335, 3.
- Scott Smith, B.H., Orr, R.G., Robertshaw, P. and Avery, R.W., 1998. Geology of the Fort a la Corne kimberlites, Saskatchewan. Extended abstracts of the Seventh International Kimberlite Conference, Cape Town, South Africa, 1998, p. 772-774.
- Shee, S.R., 1985. The petrogenesis of the Wesselton Mine kimberlite, Kimberley, Cape Province, R.S.A., University of Cape Town, Cape Town, South Africa.
- Sigurdsson, H. (Editor), 2000. Encyclopedia of Volcanoes. Academic Press, San Diego, 1417 pp.
- Skinner, E.M.W., 1989. Contrasting Group I and Group II kimberlite petrology: towards a genetic model for kimberlites. In: J. Ross, Jaques, A.L., Ferguson, J., Green, D.H., O'Reilly, S.Y., Danchin, R.V., Janse, A.J.A., (eds.) (Editor), Proceedings of the IVth International Kimberlite Conference. Kimberlites and related rocks: their composition, occurrence, origin, and emplacement. Geological Society of South Africa Special Publication 14, pp. 528-544.
- Skinner, E.M.W. and Marsh, J.S., 2004. Distinct kimberlite pipe classes with contrasting eruption processes. LITHOS 76, 183-200.
- Sparks, R.S.J., 1986. The dimensions and dynamics of volcanic eruption columns. Bulletin of Volcanology 48, 3-15.
- Sparks, R.S.J., Baker, L., Brown, R.J., Field, M., Schumacher, J., Stripp, G. and Walters, A., 2006. Dynamical constraints on kimberlite volcanism. Journal of Volcanology and Geothermal Research 155(1-2), 18-48.
- Sparks, R.S.J., Bursik, M.I., Carey, S.N., Gilbert, J.S., Glaze, L.S., Sigurdsson, H., Woods, W.C., 1997. Volcanic Plumes. Wiley.
- Sparks, R.S.J., Wilson, L. and Sigurdsson, H., 1981. The Pyroclastic Deposits of the 1875 Eruption of Askja, Iceland. Philosophical Transactions of the Royal Society of London. Series A, Mathematical and Physical Sciences 299(1447), 241-273.
- Stasiuk, M., Barclay, J., Carroll, M.R., Jaupart, C., Ratte, J., Sparks, R.S.J. and Tait, S., 1996. Degassing during magma ascent in the Mule Creek vent (USA). Bulletin of Volcanology 58, 117-130.
- Valentine, G.A. and Krogh, K.E.C., 2006. Emplacement of shallow dikes and sills beneath a small basaltic volcanic center - The role of pre-existing structure (Paiute Ridge, southern Nevada, USA). Earth and Planetary Science Letters 246(3-4), 217-230.
- van Straaten, B.I., Kopylova, M.G., Russell, J.K., Webb, K.J. and Scott Smith, B.H., 2008. Discrimination of diamond resource and non-resource domains in the Victor North pyroclastic kimberlite, Canada. Journal of Volcanology and Geothermal Research 174(1-3), 128-138.
- Walker, G.P.L., 1971. Grainsize characteristics of pyroclastic deposits. Journal of Geology 79, 696-714.
- Walker, G.P.L., 1981. Plinian eruptions and their products. Bulletin of Volcanology 44, 223-240.
- Walker, G.P.L., Wilson, L. and Bowell, E.L.G., 1971. Explosive Volcanic Eruptions I: Rate of fall of pyroclasts. Geophysical Journal of the Royal Astronomical Society 22, 377-383.
- Walters, Phillips, J.C., Brown, R.J., Field, M., Gernon, T., Stripp, G. and Sparks, R.S.J., 2006. The role of fluidisation in the formation of volcanoclastic kimberlite: Grain size observations and experimental investigation. Journal of Volcanology and Geothermal Research 155(1-2), 119-137.

- Webb, K.J., Scott Smith, B.H., Paul, J.L. and Hetman, C.M., 2004. Geology of the Victor Kimberlite, Attawapiskat, Northern Ontario, Canada: cross-cutting and nested craters. *Lithos* 76(1-4), 29-50.
- Webb, K.J., Stiefenhofer, J. and Field, M., 2003. Overview of the geology and emplacement of the Jwaneng DK2 kimberlite, southern Botswana. 8th International Kimberlite Conference Long Abstract.
- Wilson, L. and Head, J.W., 2004. Diatremes and kimberlites 2: an integrated model of the ascent and eruption of kimberlitic magmas and the production of crater, diatreme and hypabyssal facies. . *Lithos* 75 3.
- Woolley, A.R., Bergman, S.C., Edgar, A.D., Le Bas, M.J., Mitchell, R.H., Rock, N.M.S. and Scott Smith, B.H., 1996. Classification of lamprophyres, lamproites, kimberlites and the kalsilitic, melilitic, and leucitic rocks. *Journal of the Mineralogical Association of Canada* 34, 175-186.
- Zonneveld, J.P., Kjarsgaard, B.A., Harvey, S.E., Heaman, L.M., McNeil, D.H. and Marcia, K.Y., 2004. Sedimentologic and stratigraphic constraints on emplacement of the Star Kimberlite, east-central Saskatchewan. *Lithos* 76(1-4), 115-138.

**Chapter 2** This chapter represents an application of facies analysis on the deposits of the A154N kimberlite volcano at Diavik, and forms the basis for subsequent chapters in the thesis. Observations of the geometries, structures, and componentry of the deposits from the uppermost 130m of the A154N pipe lead to presentation of a 6-stage eruption model.



A154N

## **2 Progressive infilling of a kimberlite pipe at Diavik, Northwest Territories, Canada: insights from volcanic facies architecture, textures, and granulometry<sup>3</sup>**

### **2.1 Introduction**

Kimberlite pipes represent the near surface (1-3 km deep) conduits of kimberlite volcanoes (Mitchell, 1986). As such, they preserve evidence of the different stages of their formation: (1) the eruptive phase, explosive eruption of kimberlite from the pipe and deposition of pyroclasts onto the pipe margins and into the pipe; and (2) the post-eruptive phase, infilling of the pipe by foundering of the volcanic edifice, hydrothermal alteration, and deposition of exotic tephtras. They are of interest because of their high economic potential as hosts to diamonds, and because a kimberlite eruption has never been observed. The youngest known kimberlites date from the Eocene (~47 Ma Creaser et al., 2004; Heaman et al., 2004). Thus, our understanding of kimberlite eruptions and diamond distributions is based almost exclusively on observations from core logging and petrographic analyses of rocks found within kimberlite pipes.

Understanding the volcanic processes attending kimberlite emplacement is a challenge because of differences in data sets. Conventional volcanology advances mainly on the basis of observations made on volcanic edifices and their “*extra-crater*” deposits because the number of exhumed and well-exposed volcanic conduits is very limited (Stasiuk et al., 1996; Junqueira-Brod et al., 2005; Valentine and Krogh, 2006). However, kimberlite volcanoes are either highly-dissected or completely removed by erosion which precludes study of the volcanic edifice or its associated extra-crater deposits. Commonly, all that remains is the volcanic ‘plumbing system’, comprising a carrot-shaped conduit filled with a mixture of kimberlite products, country rock and even surface materials (e.g., wood). The few rare occurrences of kimberlitic volcanic crater-facies deposits are identified at Mwadui, Tanzania (Edwards and Howkins, 1966; Stiefenhofer and Farrow, 2004); Orapa and Jwaneng, in Botswana (Field et al., 1997; Machin, 2001); and Tokapal, India (Mainkar et al., 2004). In Canada, crater-facies kimberlite is known from: Victor,

---

<sup>3</sup> A version of this chapter has been published. Moss, S., Russell, J.K., and Andrews, G.D.M. (2008) Progressive infilling of a kimberlite pipe at Diavik, Northwest Territories, Canada: Insights from volcanic facies architecture, textures and granulometry. *Journal of Volcanology and Geothermal Research*, 174, 103-116.

(Webb et al., 2004); Tli Kwi Cho (Doyle et al., 1998); Buffalo Hills (Boyer et al., 2003; Boyer et al., 2004; Boyer, 2005); and Fort a la Corne, (Leahy, 1997; Leckie, 1997; Berryman et al., 2004; Zonneveld et al., 2004). Crater facies kimberlite is characterized by bedded to massive sequences of moderately-well sorted to poorly sorted pyroclastic and resedimented volcanoclastic materials. The origins of crater facies kimberlite has been ascribed to: primary pyroclastic fall-out (Graham et al., 1998; Berryman et al., 2004); debris and turbidity flows (Machin, 2001); massive collapse and slumping of surficial pyroclastic material (Nowicki et al., 2004; Stiefenhofer and Farrow, 2004); alluvial fan formation (Field et al., 1997; Nowicki et al., 2004); deposition of sediments into a crater lake (Mannard, 1962; Edwards and Howkins, 1966); and fluvial sedimentation (Smith, 1986). Deposition of re-sedimented volcanoclastic kimberlite is usually interpreted to occur post-eruption, however, syn-eruptive re-working and re-sedimentation of pyroclastic deposits is highly likely (Webb et al., 2003). The post-eruptive sedimentation processes can fill the kimberlite crater and conduit to a substantial depth, implying the presence deep holes left by the eruption. For example, sedimentary processes may be responsible for up to 230 m of crater infill at Mwadui (Edwards and Howkins, 1966; Stiefenhofer and Farrow, 2004).

This study examines the crater-facies deposits filling the uppermost part of the A154N pipe at Diavik, Northwest Territories, Canada, and discusses their volcanological and economic implications. We combine stratigraphic mapping of open-pit exposures with granulometry data for volcanoclastic kimberlite deposits to produce a facies model for the uppermost 130 m of the preserved A154N kimberlite pipe. First, we demonstrate that the original eruption of kimberlite at A154N filled less than 80% of the volume of the present-day pipe with pyroclastic kimberlite; this resulted in a >200 m-deep crater. Second, we show that this crater was partly infilled by re-sedimented kimberlite, accidental lithics, and sediment derived from the volcanic edifice while simultaneously filling with water. Third, we demonstrate how eruption from another kimberlite pipe adjacent to A154N led to a '*cross-fertilization*' event whereby exotic primary pyroclastic kimberlite was deposited into the remaining crater of A154N.

## 2.2 Geology of the A154N kimberlite pipe

### 2.2.1 The Diavik kimberlite cluster

The kimberlite pipes at Diavik (Fig. 2.1) intrude the Slave structural province which consists of (by surface area) approximately 35% supracrustal rocks (mostly 2.72-2.66 Ga) and 65% late Archean granitoids (2.7-2.55 Ga, Kjarsgaard and Wyllie, 1994). There are approximately 200 kimberlite pipes in the Lac de Gras region, distributed along a NW-trending axis in excess of 120 km in length (Graham et al., 1998). The cluster of economic pipes at Diavik are among the youngest known in the Slave structural province (56-55 Ma; Amelin, 1996), and occur in an area characterized by pipes of Late Cretaceous and Eocene ages (75-45 Ma) (Amelin, 1996; Creaser et al., 2004).

The country rocks at the Diavik mine site comprise two areally extensive granitoids, minor domains of biotite schist, and N- and NW-trending Proterozoic diabase dikes that may have formed the structural weaknesses exploited by the Lac de Gras kimberlite magmas (Graham et al., 1998). Phanerozoic strata are missing at Diavik, although crustal xenoliths preserved within Diavik kimberlite deposits suggest an original succession of Cretaceous marine shales, terrigenous arenite, and organic peat capping basement rocks during the Eocene, with variable estimates of thickness ranging from a thin (< 50 m) veneer to ~300 m (Pell, 1997; Stasiuk, 1999; Sweet et al., 2003). The basement complex is now overlain by variably thick (5 – 50 m), Pleistocene till, locally capped by a thin veneer of lacustrine sediments and/or peat.

### 2.2.2 The A154N kimberlite pipe

The A154N pipe at Diavik is a deep (~600 m), steep-sided, carrot-shaped body with multiple overhangs and diverse internal geology (Fig. 2.2a). The present-day pipe has an estimated volume of  $5.4 \times 10^6 \text{ m}^3$ , and is 120 m in diameter at the present-day surface (390 meters above sea level (m.a.s.l.)). Field mapping within the A154N pipe, study of drill cores, and petrographic analysis of samples have been used to identify mappable stratigraphic units or packages and establish a lithofacies for these kimberlite bodies. Three stratigraphic units are identified (Fig. 2.2a), including: massive volcanoclastic kimberlite (MVK; c.f. PK<sub>1</sub> from Ch. 4); stratified volcanoclastic kimberlite (SVK); and a graded pyroclastic kimberlite deposit (PK<sub>2a,b</sub>; Fig. 2.2b).

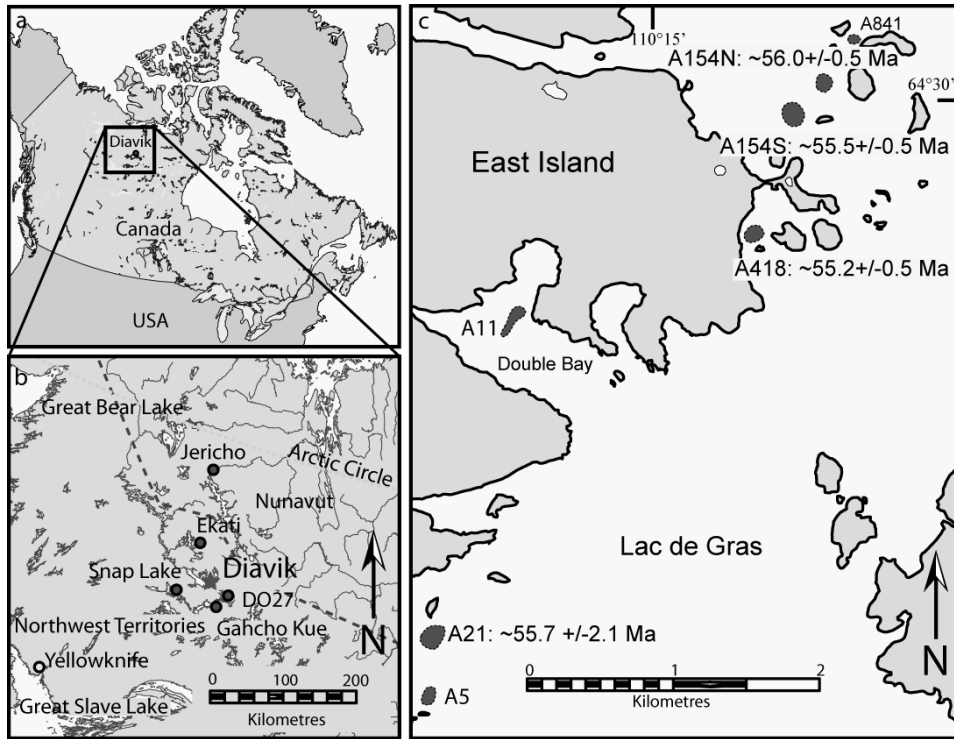


**Figure 2.1:** Maps of Diavik kimberlite cluster, including: (a) location of Diavik within Northwest Territories of northern Canada; (b) location of Diavik relative to a selection of other diamondiferous kimberlite pipes of Slave Craton; and (c) the kimberlite bodies at Diavik. Ages of Diavik pipes are based on Rb-Sr determinations on mica (Amelin, 1996).

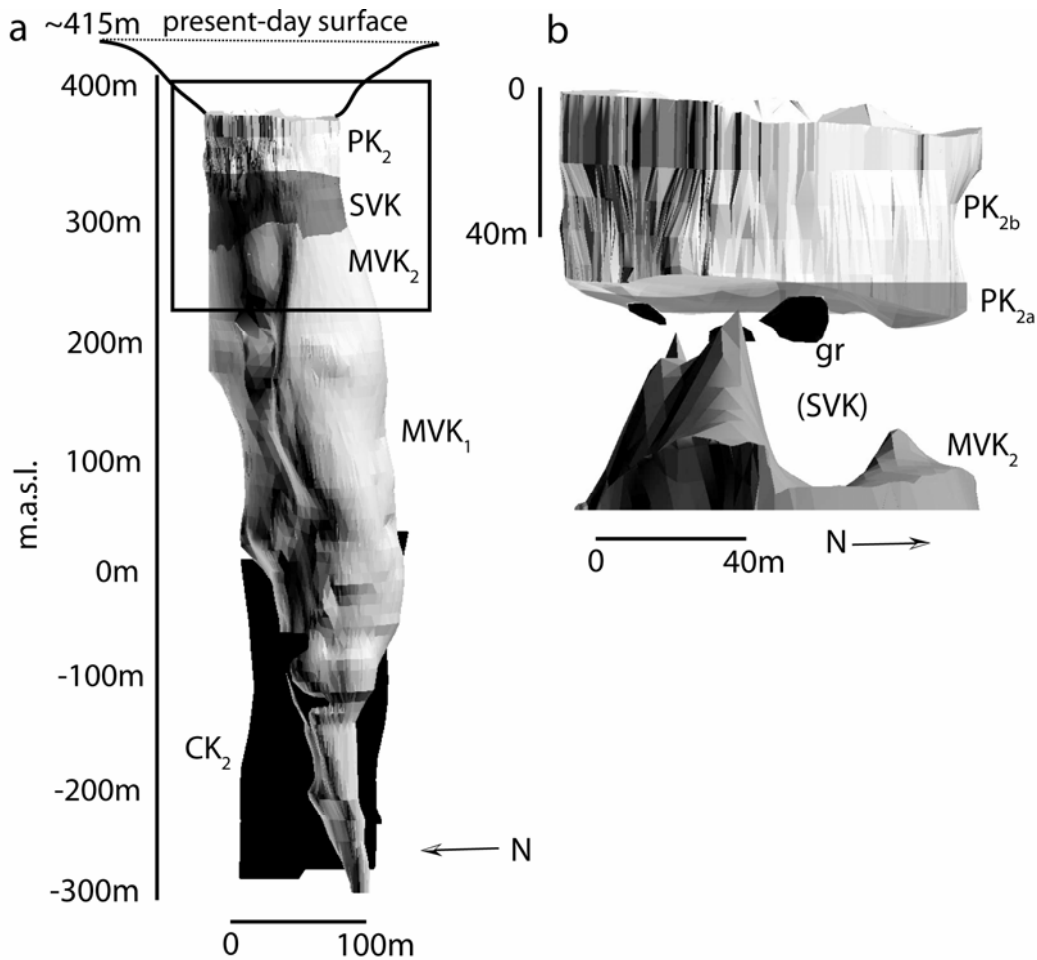


**Figure 2.2:** Three-dimensional model constructed in GoCad™ based on open pit survey and drill core intercepts showing distribution and geometry of major mappable units within the A154N kimberlite pipe: (a) model for entire pipe (view facing east) showing late, intrusive dykes of coherent kimberlite (CK<sub>2</sub>; c.f. CK in Chapter 3), massive volcanoclastic kimberlite (MVK<sub>1</sub>; MVK<sub>2</sub>; c.f. PK<sub>1</sub> in Chapter 4), stratified volcanoclastic kimberlite (SVK) and pyroclastic kimberlite (PK<sub>2</sub>); (b) Larger scale model (view facing west) with SVK removed to show the detailed geometry and facies subdivisions of the PK unit (e.g., PK<sub>2a</sub> and PK<sub>2b</sub>) and morphology of contact between MVK and SVK. Large granite blocks (gr) are shown underneath PK<sub>2a</sub>.

### 2.2.3 Massive volcanoclastic kimberlite (MVK)

The lowest exposed unit within the A154N pipe (< 260 m.a.s.l.) is a deposit of competent, green-brown, poorly-sorted massive volcanoclastic kimberlite (MVK<sub>1,2</sub>; Fig. 2.2). Observation of the MVK is essentially restricted to drill core, as there is minimal (<5 m) exposure of the unit in the open pit. Three-dimensional modeling of drill core logs shows that the MVK unit exceeds 350 m in thickness, and increases in magnetic susceptibility towards the center of the pipe. From bottom to top, the deposit records a subtle gradational change in structure and texture that is used to subdivide the MVK into a massive and weakly stratified facies (MVK<sub>1</sub>, MVK<sub>2</sub>).

#### *Massive volcanoclastic kimberlite (MVK<sub>1</sub>)*

The MVK<sub>1</sub> is massive, fragmental, and consists of poorly-sorted clasts supported by a matrix of serpentine, carbonate, and variable proportions of ash-sized grains (Fig. 2.3a); carbonate and serpentine veins (2 - 20 mm thick) are also ubiquitous. The distribution of clasts is homogeneous, exhibiting no appreciable vertical differences in texture, component size distributions, or diamond grade at the mining scale (pers. comm. Thompson, 2007). The packing density of clasts varies and the deposit is locally clast-supported near the pipe wall contact with country rocks. Clasts within the MVK<sub>1</sub> deposit consist of 0.5 - 10 mm olivine macrocrysts (crystals representing xenocrysts of disaggregated mantle peridotite; sensu Clement, 1982), 0.1 - 0.5 mm olivine phenocrysts, other mantle-derived xenocrysts (e.g., garnets, clinopyroxene, ilmenite), and juvenile pyroclasts of quenched kimberlite (5 - 30 mm). Olivine crystals commonly have thin rims (1 - 5 mm) or 'selvages' (sensu Scott Smith, 1996) of crystallized kimberlite magma and are broadly similar in morphology to the 'pelletal lapilli' described from the diatreme facies of other kimberlite pipes (Clement, 1982; Mitchell, 1986). Accidental or accessory lithics of country rock (granite, biotite schist, grey shale, black shale) up to 30 cm in diameter, and accessory clasts (2 - 30 cm) of previously deposited fragmental kimberlite occur throughout the MVK<sub>1</sub>. Cretaceous mudstone xenoliths are rare to absent (Graham et al., 1998).

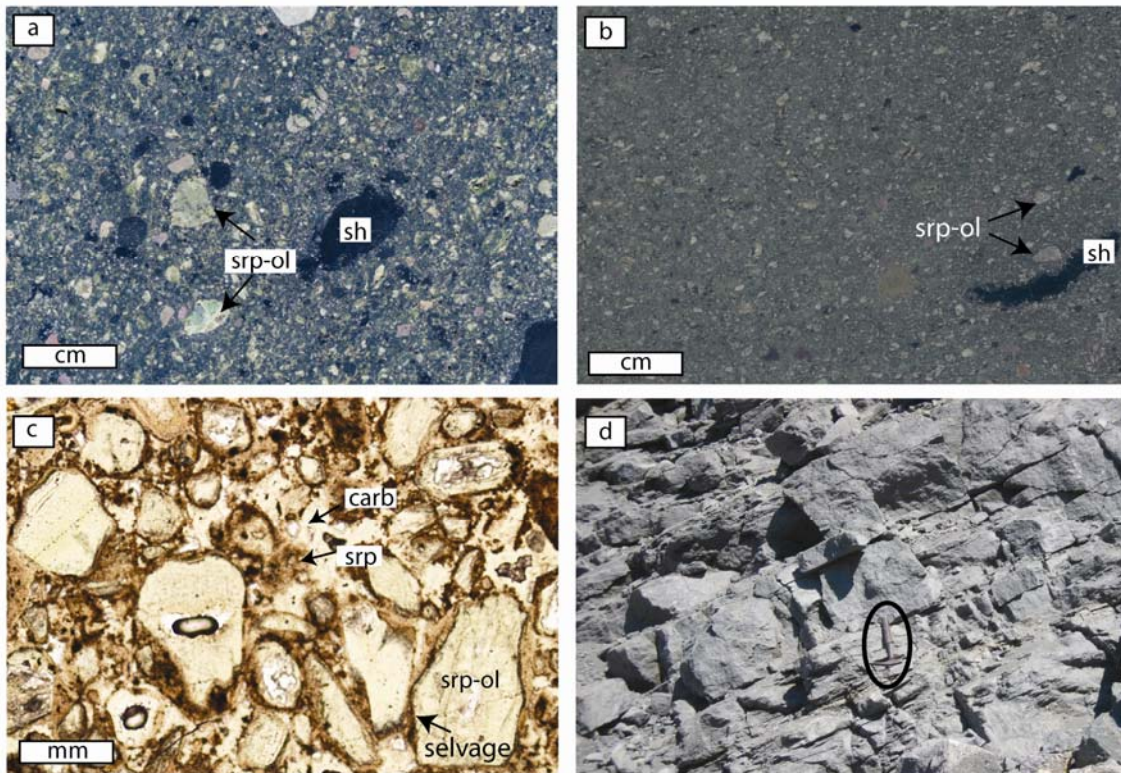


**Figure 2.3:** Photographic plate summarizing features of MVK<sub>1</sub> and MVK<sub>2</sub> deposits in the A154N pipe: (a) polished slab of massive, poorly-sorted, serpentized volcaniclastic kimberlite (MVK<sub>1</sub>) from 280 m.a.s.l. of A154N showing serpentized olivine (srp-ol) and shale fragment (sh); (b) polished slab of weakly-stratified, moderately to well-sorted, serpentized pyroclastic kimberlite (MVK<sub>2</sub>) from 285 m.a.s.l. of A154N showing serpentized olivine (srp-ol) and shale fragment (sh); (c) photomicrograph of clast-supported, moderately well-sorted MVK<sub>2</sub> showing serpentized olivine grains (srp-ol) with thin magmatic selvages, and matrix carbonate (carb) and serpentine (srp); (d) cm-scale jointing in massive, well-sorted, fine-grained kimberlite of MVK<sub>2</sub> (hammer for scale).

### *Weakly stratified volcanoclastic kimberlite (MVK<sub>2</sub>)*

The upper portion of the MVK deposit comprises 5 – 10 m of massive, fragmental, competent, green, and volcanoclastic kimberlite that is distinct because of a subtle stratification defined by elongate shale fragments. Relative to MVK<sub>1</sub>, this volcanoclastic kimberlite (MVK<sub>2</sub>) is finer-grained (1-5 mm crystals and clasts) and better-sorted (lithics < 1 cm); locally the deposit exhibits a porous clast-supported texture (Fig. 2.3b). The dominant components in the MVK<sub>2</sub> are: serpentinized olivine crystals (>50 vol. %; Fig. 2.3c); large (3 - 100 mm) shale fragments (5 - 7 vol. %); small (5 - 30 mm) juvenile pyroclasts of quenched magma (~3 - 5 vol. %); and 3 - 10 mm clasts of granite. Locally, the long axes of the shale fragments define a weak horizontal fabric that is sub-parallel and locally oblique to distinctive cm-scale horizontal jointing (Fig. 2.3d). The MVK<sub>2</sub> is well-indurated, but noticeably less dense than the underlying MVK<sub>1</sub>.

Observations in the open pit of the A154N pipe and drillcore show a gradational contact between the MVK<sub>1</sub> and MVK<sub>2</sub> deposits. In lieu of a clear, well-defined boundary between these units there is a gradual decrease in clast size, a change in proportions of xenolith types, and an increase in sorting (poorly-sorted to moderately-sorted). Therefore, although we have described the MVK<sub>1</sub> and MVK<sub>2</sub> deposits separately, they may represent different facies of the same stratigraphic unit.

### 2.2.4 Stratified volcanoclastic kimberlite (SVK)

The MVK<sub>2</sub> deposit is unconformably overlain by an approximately 55 m-thick sequence of heterogenous, massive to well-stratified kimberlite deposits (Fig. 2.2 and 2.4; SVK) containing variable proportions of consolidated mud in the matrix. The SVK deposit includes: i) thin beds (2-20 cm), comprised of shale, mantle xenocrysts and xenoliths, alternating with beds of olivine-rich kimberlite; ii) massive, coarse-grained, poorly-sorted granite and shale-rich conglomerates supported in a matrix of brown mud; iii) cross-bedded, thin (2-10 mm) beds of sand-sized olivine and shale; and iv) laminated, well-sorted mudstone (Fig. 2.4). In general, layering within these deposits is horizontal to sub-horizontal, and commonly stratiform throughout the pipe except at the margins of the conduit where bedding attitudes steepen.

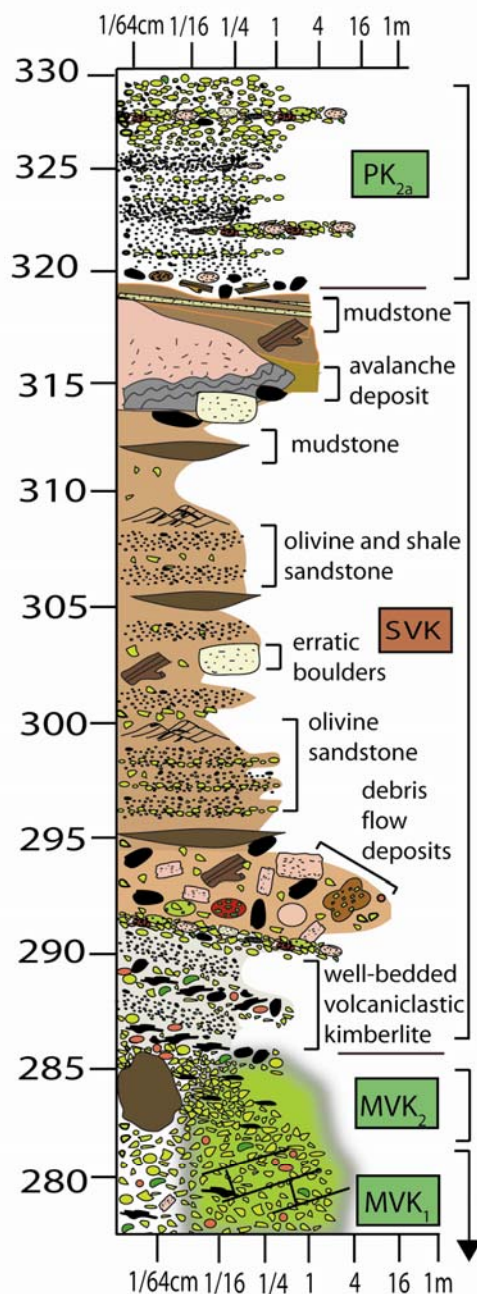
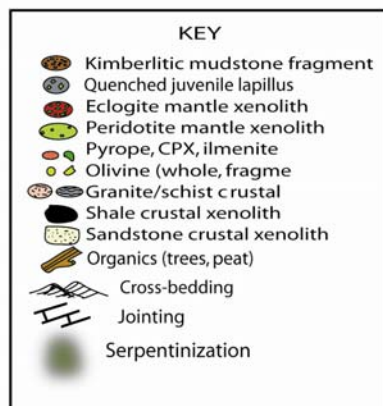


**Figure 2.4:** Graphic log summarizing stratigraphy of MVK<sub>1</sub>, MVK<sub>2</sub>, SVK, and PK<sub>1</sub> from A154N (330 m.a.s.l. to 280 m.a.s.l.), showing contacts and stratigraphic and grain size variations that correspond to changing components, processes, and environments of deposition. Marker sub-units of SVK are bracketed to illustrate relative positions of different deposit types; rock type or inferred depositional style are listed to the right. Map symbols are not to scale. Horizontal dashed lines indicate unit contacts.



The lower portion of the SVK deposit comprises coarse (5-12 mm), 2-20 cm thick, clast-supported beds of volcanoclastic kimberlite enriched in olivine, and mantle xenoliths and containing imbricated clasts of angular shale (Figs. 2.4; 2.5a; 2.5b). Near the pipe margins, the SVK features thin (5-10 cm) graded deposits (1 mm to 1 cm) of clast-supported, mantle xenocryst-rich kimberlite with a brown, mud-size matrix. The basal beds are highly variable in orientation (e.g., SE corner, 045/32°SE; NW corner, 011/24°SE; pipe center, 058/18°NW), and appear to drape an irregular paleo-topography defined by the underlying massive, moderately-sorted, and relatively fine-grained MVK<sub>2</sub> (Fig. 2.2b). In the SE corner of the pipe, the beds terminate disconformably against a thin veneer (1.3 m) of unaltered, well-sorted, clast-supported, massive, friable MVK<sub>2</sub> at the pipe wall contact (Fig. 2.5a).

Stratigraphically above the basal beds are wedge-shaped, very coarse-grained (clasts 2-20 cm), matrix-supported, mud-rich kimberlite beds (Fig. 2.5c). These wedges of sediment are internally massive and poorly sorted. Clasts consist of (in order of decreasing abundance) shale, granite, free olivine crystals, olivine-bearing mudstone, mantle xenoliths (eclogite and peridotite) and xenocrysts (garnet, clinopyroxene). The interclast matrix is composed of consolidated mud or possibly altered kimberlite ash.

The deposits within the middle of the SVK package are pipe-wide, stratiform interbedded kimberlitic mudstone and cross-bedded olivine sandstone (Figs. 2.4; 2.5d) mainly comprising olivine crystals, smaller, rounded fragments of shale, and minor amounts of mantle xenocrysts. Centimetre-scale cross-bedding is commonly observed near pipe margins. Large lithics (0.5-1 m) of granite and sandstone are commonly found near the pipe margin, and locally within the interior of the pipe. Bedding is steepest (~15-17°) near the pipe margins, and horizontal/sub-horizontal in the pipe center.

The uppermost portion of the SVK is dominated by laminated mudstone (Figs. 2.4; 2.5e) and subsidiary lenses of olivine sandstone with fragments of shale. A lense of laminated mudstone (1-2 m) containing sparse small olivine fragments (1-3 mm) is evident in the northern half of the pipe, where it is laterally continuous to the pipe walls (Fig. 2.5e). Deposits of massive, coarse, poorly-sorted debris containing shale, organic fragments, and large granite and sandstone blocks (2-10 m) are also observed in between 2-4 m-thick horizons of mudstone in the southern half of the pipe.

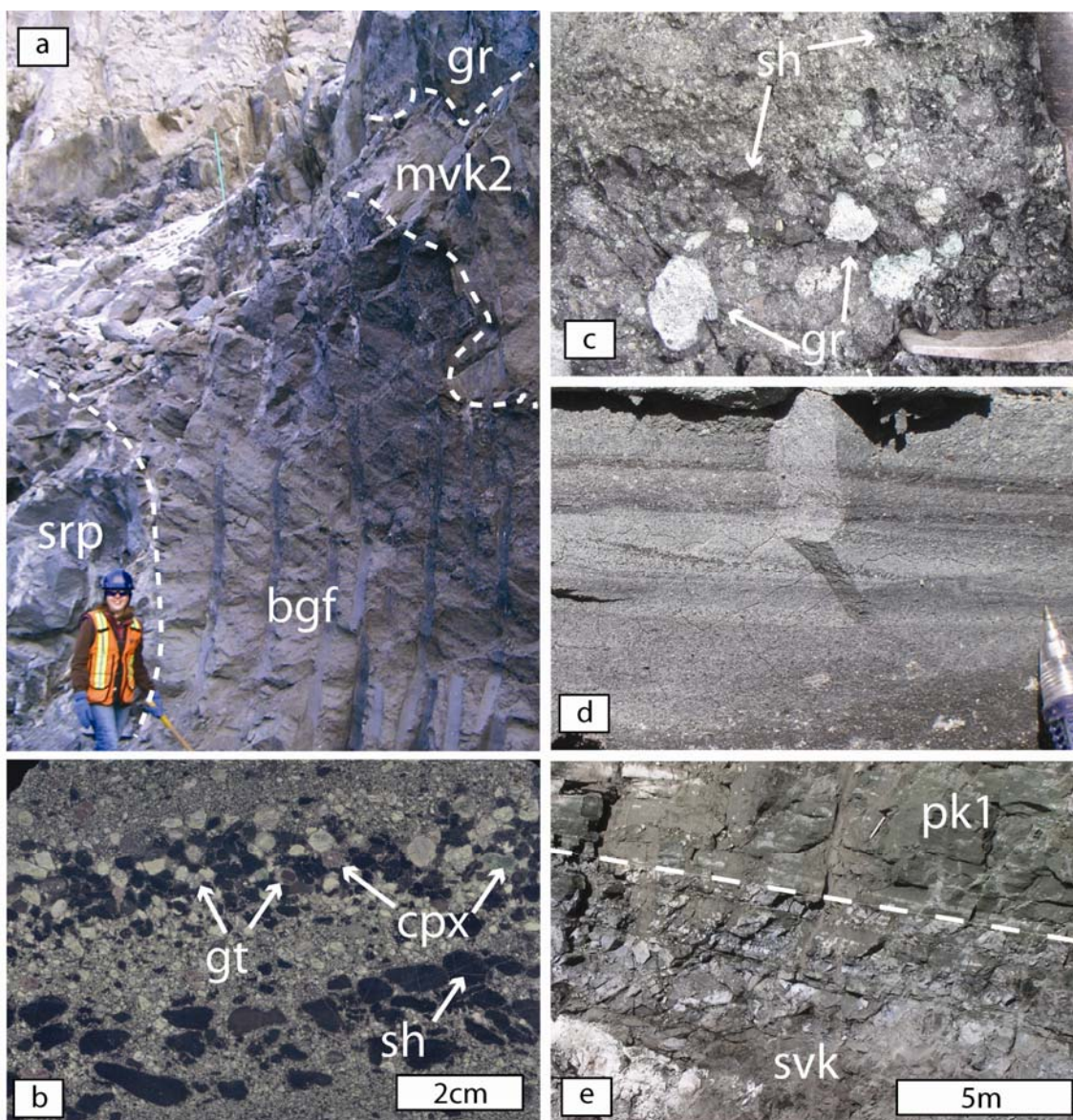


**Figure 2.5.** Photographic plate illustrating main features and properties of the stratified volcanoclastic kimberlite (SVK) facies: (a) serpentinitization front (srp left of person in foreground) superimposed over bedded grain flow deposits (bgf), terminating disconformably against (dashed line) a rind of kimberlite (MVK<sub>2</sub>) beneath overhanging granite (gr) wall-rock contact (dashed line); (b) close-up of well-sorted and imbricated shale (sh) and mantle xenocryst (gt, cpx) grain flow deposits; (c) close-up of poorly-sorted, matrix supported debris flow deposit with abundant granite (gr) and shale (sh) xenoliths; (d) cross-bedding in fine-grained olivine sandstone interbedded with siltstone bearing olivine fragments; (e) 10 m bench face (330-320 m.a.s.l.) showing sharp contact (dashed line) between SVK and PK<sub>1</sub>.

At the base of the SVK unit bedding structures are overprinted by a variable but pervasive alteration front with an irregular, undulating upper surface that extends to within 5 m of the pipe margins. The alteration front extends vertically from the MVK<sub>2</sub> into the clast-supported, coarse, xenocryst-rich beds at the bottom of the SVK (Figs. 2.4; 2.5a), where it is discordant to bedding. Within the alteration zone, olivine has been replaced by serpentine and the kimberlite is competent. The altered kimberlite occurs as either a jointed, porous, competent, green rock in which olivine has been partially serpentinized, or a very hard, dense, black rock in which olivine grains are black and appear to have been completely serpentinized. In contrast, outside of the alteration zone, olivine is relatively fresh and the rock is poorly-consolidated.

#### 2.2.5 Graded pyroclastic kimberlite (PK)

A distinctive 45-55 m thick deposit of kimberlite (Fig. 2.2a; PK) is observed at the top of the A154N pipe, unconformably capping the SVK (Fig. 2.2b). The PK unit is comprised of two sub-divisions: (1) a lower, laterally restricted and crudely bedded layer characterized by diffuse, two-directional (reverse and normal) graded bedding with fluctuations in average clast size, here named PK<sub>1</sub>; and (2) a volumetrically-dominant and laterally continuous, ~45 m-thick layer characterized by a single upward-grading sequence defined by decreasing clast size and changes in clast type, here named PK<sub>2</sub>. Details of the deposits are shown in Figure 2.6.

Five distinct populations of juvenile pyroclasts are observed throughout the PK deposit: (1) very fine-grained kimberlite ash (~5-10 m) comprising angular olivine crystals (0.1-0.4 mm), and rounded juvenile pyroclasts of olivine-free, spinel-bearing kimberlite (0.1-0.4 mm; Fig. 2.7a); (2) vesiculated (5-7% area), carbonate-rich juvenile pyroclasts (10-20 mm) with olivine macrocrysts (~15% area; Fig. 2.7b); (3) fresh, 'free' grains of macrocrystic (0.5 mm - 10 mm) and phenocrystic olivine (<0.5mm), commonly surrounded by thin (<2 mm) or incomplete selvages of crystallized kimberlite magma (Fig. 2.7c); (4) juvenile pyroclasts of phenocryst-poor kimberlite; and (5) juvenile pyroclasts of phenocryst-rich kimberlite.

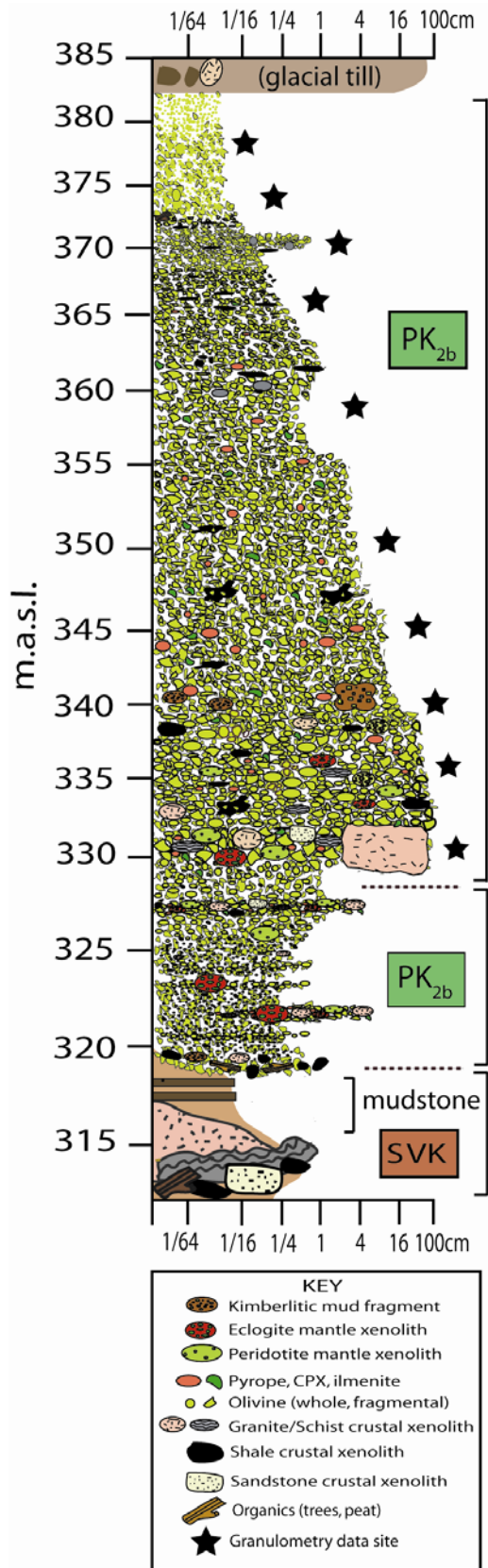


**Figure 2.6:** Graphic log summarizing stratigraphy and illustrating features of sub-units PK<sub>2a</sub> and PK<sub>2b</sub> from primary pyroclastic kimberlite deposit (PK<sub>2</sub>) from 385 m.a.s.l. to 315 m.a.s.l. in A154N pipe. Stars indicate sample locations for granulometry study. Map symbols are not to scale. Horizontal dashed lines indicate unit/sub-unit contacts.

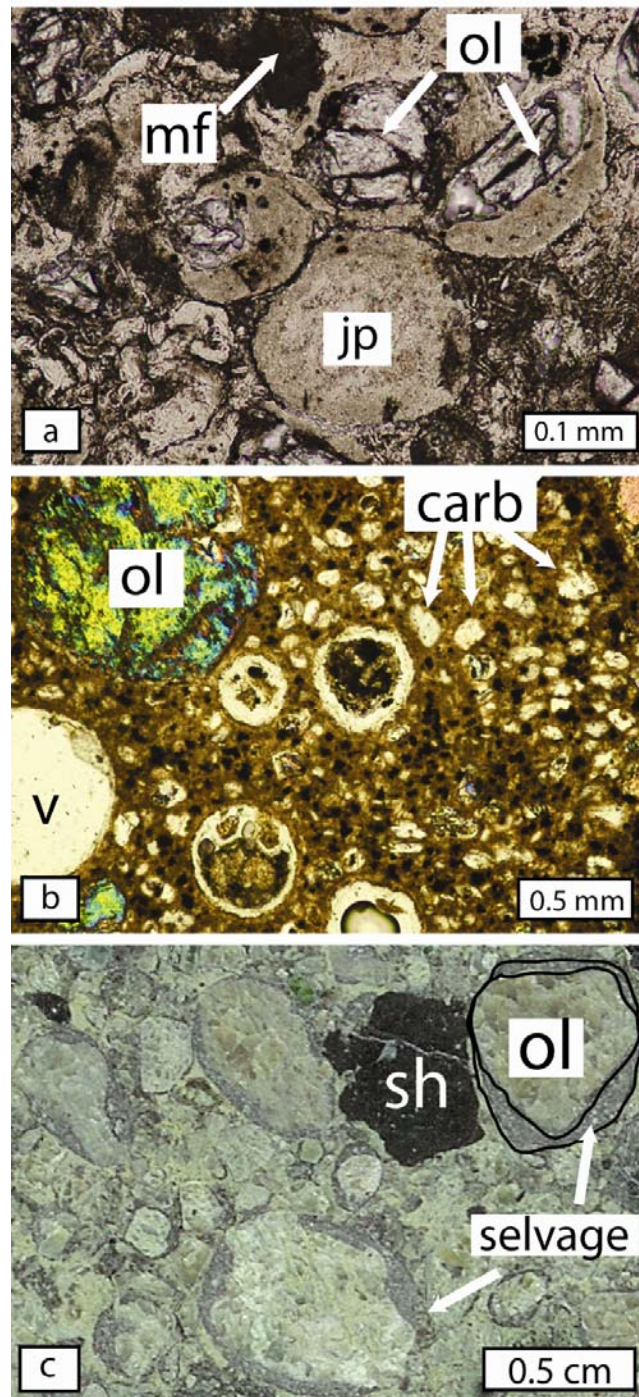


**Figure 2.7:** Pyroclastic features of PK<sub>2</sub>: a) photomicrograph showing ‘molded’ ash-sized juvenile pyroclasts (jp), olivine grains (ol), and mudstone fragments (mf) from 375 m.a.s.l. of PK<sub>2</sub>; b) vesiculated (v) juvenile pyroclast with olivine macrocryst (ol) and abundant carbonate (carb) microphenocrysts; c) selvages of crystallized kimberlite around olivine macrocrysts in a close-packed, clast-supported, ash-depleted fabric from 335 m.a.s.l. of PK<sub>2</sub>.

### Crudely-bedded pyroclastic kimberlite (PK<sub>2a</sub>)

The PK<sub>2a</sub> deposit (5 – 8 m thick) is restricted to the northern half of the pipe. It directly overlies a finely-laminated mudstone containing small proportions of olivine fragments (Figs. 2.5e; 2.6) that fills a topographic low (Fig. 2.2b). PK<sub>2a</sub> is clast-supported, features horizontal beds (5-30 cm thick) showing diffuse normal and reverse grading, and lacks any tractional bedforms (e.g., clast imbrication, cross-bedding). The diffusely-graded bedding is sharpest at the bottom and becomes less distinct up section. Clasts consist of free olivine crystals (1-10 mm), olivine grains with selvages of crystallized kimberlite magma, mantle xenocrysts and xenoliths (5-200 mm), rounded granite and biotite schist cobbles (up to 30 cm), and angular shale fragments (1-6 cm). The transition from PK<sub>2a</sub> upwards to PK<sub>2b</sub> is relatively abrupt (<0.5 m), and is defined by an upward grading from fine-grained (1-10 mm) diffusely-bedded, well-sorted kimberlite to coarse (4-200 mm), massive, poorly-sorted, kimberlite (Fig. 2.6).

### Mega-graded pyroclastic kimberlite (PK<sub>2b</sub>)

The PK<sub>2b</sub> unit is poorly- to well-sorted, and is dominantly clast-supported. The base of the deposit contains abundant mantle xenoliths and xenocrysts (5-200 mm), juvenile pyroclasts of quenched kimberlite magma (5-30 mm), and rounded to angular granite blocks (≤3 m) within a matrix of loosely-packed, fresh olivine macrocrysts (0.5-15 mm) and phenocrysts (0.1-0.5 mm), mantle xenocrysts, and shale fragments. The average grain size of the deposit decreases steadily upwards, as does the proportion of mantle xenoliths and fragments of granitic country rock (Fig. 2.6). The top of the unit (375 to 365 m.a.s.l.) consists of very-fine-grained olivine crystals and crystal fragments (≤0.5 mm) with minor amounts of elongate, aligned shale fragments. The distribution of clast sizes and clast types is discussed below.

### PK granulometry: methods

In order to better understand the volcanic origins of the PK<sub>2</sub> deposit and to constrain the dynamics of kimberlitic eruptions in general, we performed a quantitative analysis of the clast populations within the PK<sub>2</sub> deposit. Quantitative facies analysis of the PK<sub>2</sub> deposit involved generating granulometry data by processing field maps, hand

sample slabs, and thin sections using image analysis software (SCION Image™). These data are used below to interpret an emplacement mechanism for the PK<sub>2</sub> deposit, and to compare clast populations from kimberlite eruptions with populations from other volcanic (non-kimberlitic) deposits.

Observations were made at three scales to ensure that we captured the full range of size distributions for all components. Ten cross-sectional field maps (1 m<sup>2</sup> grid) of the lower (coarsest) section of the PK<sub>2b</sub> unit (340-325 m.a.s.l.) were constructed at the mine site. Subsequently, twenty oriented samples, collected from 5 m vertical intervals within PK<sub>2b</sub>, were prepared as polished slabs (~10 cm<sup>2</sup>) and as thin sections (25 x 45 mm). These prepared samples were analyzed for grain size, component type, and modal abundance. Integration of the three different scales of observation was accomplished by normalizing data from smaller scales of observation to the area of the largest scale (e.g., field map). For example, clast-size data generated for polished slabs (clasts 1-20 mm) was normalized to the area in the field map not occupied by clasts measured at the field map scale (clasts 20-300 mm); data generated from thin-sections were then normalized to the residual area in the field map not occupied by either clasts measured at the field map or slab scale.

Individual grains, crystals, and clasts in the images were digitized manually and grouped into one of six particle types: (1) olivine grains (including crystals with < 30% selvage by area); (2) juvenile pyroclasts having > 30% selvages; (3) fragments of volcanoclastic kimberlite with mud-size matrix; (4) mantle xenoliths (e.g., eclogite and peridotite) and xenocrysts (e.g., garnet and clinopyroxene); (5) country rock xenoliths (e.g., granite or metasedimentary rocks); and (6) clasts of shale. In order to estimate the error associated with manual tracing of particles, the same scanned image from the finest scale of observation (thin section) was processed five times to generate raw grain size data. The cumulative size distribution curves for 5 samples define similar slopes (+/- 8 %) over the median size ranges (middle 60% of size distribution); this variation is of similar magnitude to the standard deviations obtained for conventional sieving of pyroclastic deposits in the field (e.g. Walker, 1971). Digital images of the manual tracings were then analyzed for grain size (area in mm<sup>2</sup>), shape, orientation, and clast-type abundances (as % of the area).

Data generated from a two dimensional surface do not necessarily reflect the true sizes of the clasts in three dimensions; rather, they underestimate grainsize because a

surface that randomly cuts spherical particles is more likely to intersect a section that does not include the true (e.g., maximum) diameter (Cashman and Mangan, 1994; Sahagian and Proussevitch, 1998). Furthermore, the surfaces of olivine crystals and other clasts are rarely perfectly smooth which complicates the task of objectively measuring the maximum diameters of each clast. To account for these complications, exact areas of the individual grains calculated by SCION Image<sup>TM</sup> were converted to an equivalent circular area. The diameter of that circle is used as the model median clast diameter. The model median particle (crystal or clast) diameters were then used to compute cumulative frequency curves, size distributions, and relative volumes of each clast type.

### PK granulometry: results

Granulometry data collected from image analysis of the PK<sub>2</sub> unit are presented in Figure 2.8. Apparent size distributions of all clast types from four sample levels in PK<sub>2</sub> are shown as poly-component histograms of area percentages against model clast diameters expressed as phi ( $-\log_2(d)$ ) (Fig. 2.8a). These data demonstrate the progressive vertical changes in the relative abundance and types of components within the PK<sub>2</sub> unit; the base of the deposit is dominated by coarse olivine, mantle xenoliths (~5-9%), and country-rock xenoliths, whereas the top (upper 20 m) of the deposit consists of very fine grained free olivine, juvenile pyroclasts, and shale (1-3%). The same data are used to calculate a cumulative size distribution for the entire PK<sub>2</sub> deposit which shows an approximately log-normal distribution of pyroclasts when plotted as a histogram of area percentage against equivalent sphere diameters (Fig. 2.8b).

The size distributions of olivine crystals for each sample interval are shown as cumulative area percentage against model median clast diameter (Fig. 2.8c). The median olivine size at the slab and thin section scale shows incremental changes in size between 5 m intervals in the PK<sub>2b</sub>, gradually decreasing in size with elevation from ~4.2 mm at the base to ~0.4 mm at the top. The olivine grain size distribution curves also record an increase in sorting efficiency from the bottom to the top of the deposit. Lastly, an integrated size distribution curve for olivine from the entire deposit (dashed line, Fig. 2.8c) shows the more poorly-sorted character of the total deposit relative to the individual intervals.

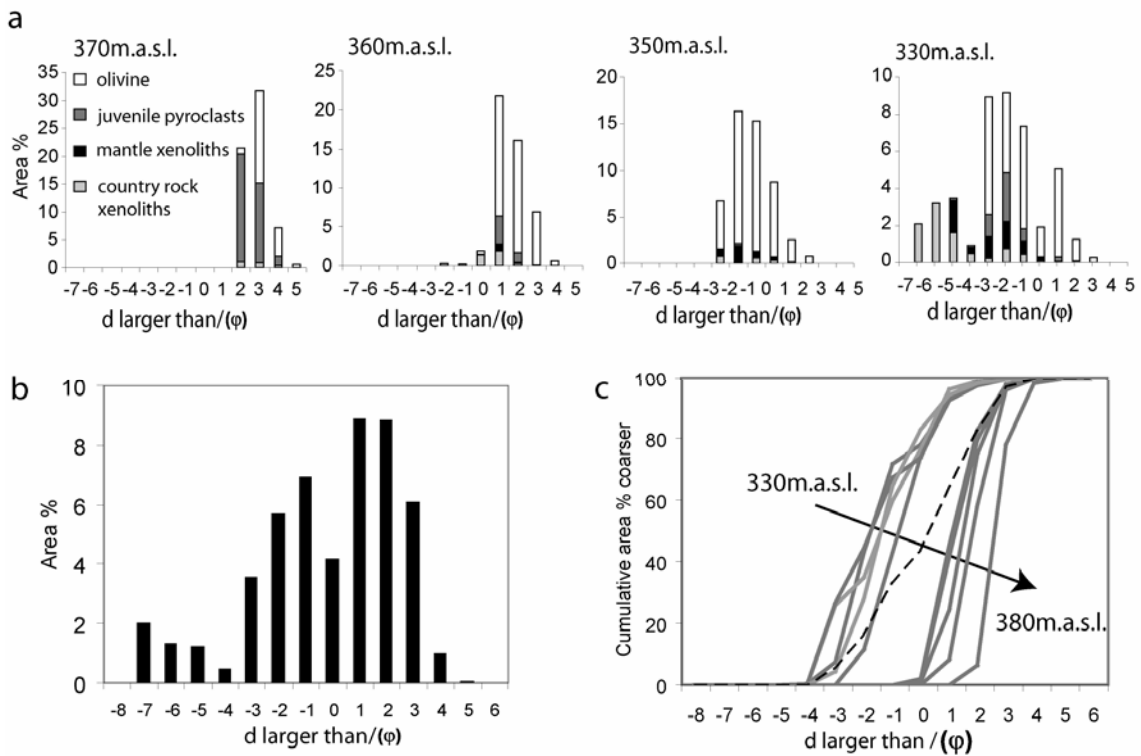


**Figure 2.8:** Granulometry data based on image analysis of samples for intervals across the PK<sub>2</sub> stratigraphic unit: (a) poly-component histograms from four levels within PK<sub>2</sub> showing relative proportions (by area) of olivine, juvenile pyroclasts, mantle xenoliths, and country rock xenoliths. Grain size expressed as  $\phi = -\log_2(d)$ , where  $d$  is clast diameter; (b) cumulative component histogram for the entire PK<sub>2</sub> deposit. Data are shown as the number of clasts in each size class ( $\phi = -\log_2(d)$ ); (c) olivine grain size distributions (steeper curve = better sorted) from bottom (330 m.a.s.l.) to top of PK<sub>2</sub> (380 m.a.s.l.). Dashed line represents cumulative olivine size distribution for entire deposit.

## 2.3 Interpretation

On the basis of the observations and data presented above, we have interpreted the origin and formation of each deposit within the A154N pipe.

### 2.3.1 MVK – deposition from a collapsing eruption column

Interpretation of the MVK deposit is made difficult by the limited exposure within the open pit workings and our reliance on analysis of drill cores. The overall similarity between MVK<sub>1</sub> and MVK<sub>2</sub>, together with the presence of a gradational contact suggests that they represent subtly different facies of the same deposit. The large volume (80% of present-day pipe) of the deposit, its massive, poorly-sorted character, the presence of juvenile pyroclasts, and the absence of a mud-sized matrix between clasts suggest that the MVK is a primary pyroclastic deposit. The absence of bedding other than in the upper parts of MVK<sub>2</sub> suggests rapid (*en masse*) deposition without efficient grain-size sorting by either tractional or aerodynamic processes. Furthermore, the absence of tractional bedforms (e.g., cross-bedding) indicates that particle transport was dominantly vertical. Therefore, due to its massive, matrix-supported, and poorly-sorted nature, we infer, tentatively, that the MVK deposit may have been deposited from a waning, fully-fluidized and collapsing pyroclastic column (e.g. Sparks et al., 2006) that was erupted from the A154N pipe. In such a scenario, only the finest grain-size fraction undergoes any aerodynamic sorting (i.e. MVK<sub>2</sub>), having been elutriated into the highest part of the eruption column before collapse; in contrast the coarsest grain-size fraction is least well-sorted reflecting its rapid emplacement from a lower altitude within the column (i.e., MVK<sub>1</sub>). Though fluidization may have been involved during the waning stages of eruption (as the pipe walls are smooth), there is no evidence to suggest the elutriation of fines during deposition (e.g. gas elutriation pipes). Furthermore, we see no evidence which might suggest phreatomagmatic fragmentation as a significant part of the emplacement of the MVK (e.g. high proportion of olivine fragments, ash/mud, or accretionary lapilli).

### 2.3.2 SVK – re-sedimentation from volcanic edifice

The heterogeneous and complex sequence of SVK deposits comprises several depositional packages. We interpret the thinly-bedded deposits at the base of the succession to signify a change in depositional style from the underlying MVK; the contact represents an interface between the end of en masse deposition of pyroclastic MVK and the onset of episodic sedimentation represented by the SVK deposit. The basal deposits indicate multiple, small-volume cascades of clasts from the collapse of an unstable volcanic edifice. Thus, they represent re-deposited pyroclastic material from the inner flanks of the kimberlite volcano (i.e., resedimented volcanoclastic kimberlite; RVK). The thinly-bedded SVK deposits contain similar components types to those found in the PK<sub>1</sub> and have minimal mud-size particles in the matrix. These traits suggest that there was a relatively short hiatus between the cessation of eruption and the onset of sedimentation. The presence of steep and overhanging pipe walls adjacent to and above the basal SVK deposits imply vertical trajectories of transport; transport dynamics were not controlled by a substrate until the kimberlite reached the base of the crater. The highly variable bedding orientations in the basal deposits suggest that they were responding to an existing topography on the crater floor, flowing into and leveling-out topographic lows left on the final eruption surface defined by massive, moderately-sorted, and relatively fine-grained MVK<sub>2</sub>. The thickness of the SVK (~55 m) deposited directly on the MVK deposits that partly filled the crater and conduit suggests the presence of a deep hole resulting from the eruption of the A154N kimberlite (Fig. 2.2b). Assuming a minimal thickness of Cretaceous cover strata at the time of eruption (~50 m), the excavated conduit to A154N would have been in excess of 200 m below the paleo-surface, leaving a hole two times deeper than the vent was wide (~100 m).

The structure, componentry and geometry of subsequent deposits in the SVK are indicative of a long-lived, deep (>100 m) body of standing water. The thinly bedded, well sorted character of the upper SVK deposits and the pipe-wide, continuous nature of the bedding is consistent with small-volume, passive, sedimentation of mud and grain flows into an increasingly deep water column. The superposition of a serpentinizing alteration front over the facies change from primary volcanic deposition to re-deposition of crater-rim tephra suggest that hot, aqueous fluids continued to impact the volcanic pile after the primary eruption had ceased.

### 2.3.3 PK<sub>2</sub> - exotic tephra deposited into a crater lake

The PK<sub>2</sub> deposit represents a clear change in the depositional style and components from the underlying re-sedimented kimberlite, which shows pipe-wide laminar bedding, imbrication of clasts, and a matrix dominated by mud-size grains. Field mapping and slab and thin section analysis of componentry of the PK<sub>2</sub> deposit provide three lines of evidence supporting a pyroclastic origin, including: (1) vesiculated juvenile pyroclasts of quenched kimberlite magma (Fig. 2.8b); (2) thin selvages of crystallized kimberlite coating fresh olivine crystals, mantle xenocrysts, and granite fragments (Fig. 2.8c); and (3) the presence of broken olivine crystals and round ash-sized clots of quenched magma at the top of the deposit (Fig. 2.8a).

The absence of internal structure (bedding, clast imbrication) and the absence of consolidated mud in the matrix of PK<sub>2</sub> preclude a debris flow origin for the deposit. Additionally, the relative paucity of shale xenoliths, the absence of tractional bedforms (e.g., cross-bedding), the lack of matrix mud or xenocrystic quartz, the relative ‘freshness’ of unaltered olivine, and the absence of re-worked grain shapes argue against the possibility of a re-sedimented origin for the PK<sub>2</sub> deposit. Furthermore, epiclastic or sedimentary processes are unlikely to have formed the PK<sub>2</sub> deposit due to the presence of abundant, well-preserved, juvenile pyroclasts, the absence of mud-size material in the matrix, and the relative paucity of country rock xenoliths (accidental lithics) and xenocrysts (e.g., quartz).

Several factors suggest the PK<sub>2</sub> deposit is unlikely to be massive volcanoclastic kimberlite (MVK, *sensu* Sparks et al., 2006) or ‘tuffisitic’ kimberlite (TK) typical of diatreme facies kimberlite in many South African pipes: (1) evidence of deposition into a crater lake (e.g., underlying laminated mudstone); (2) the presence of well-sorted, medium to fine-sized ash; (3) the absence of microlitic clinopyroxene; (4) a lack of ‘pelletal’ lapilli (*sensu stricto* Clement, 1985); and (5) systematic vertical variations of clast size and type.

Granulometry data from the graded kimberlite deposit clearly demonstrates the extent of vertical grading of both clast-size and clast-type within the PK<sub>2</sub> facies. Calculation of Inman parameters ( $Md\phi$  vs.  $\sigma$ ) from 5 m intervals in the PK<sub>2</sub> shows a range of sorting efficiency relative to median clast size (Fig. 2.9a). These data show a linear trend grading from moderately-sorted ( $\sigma \sim 2-3$ ), coarse material at the base of the deposit to

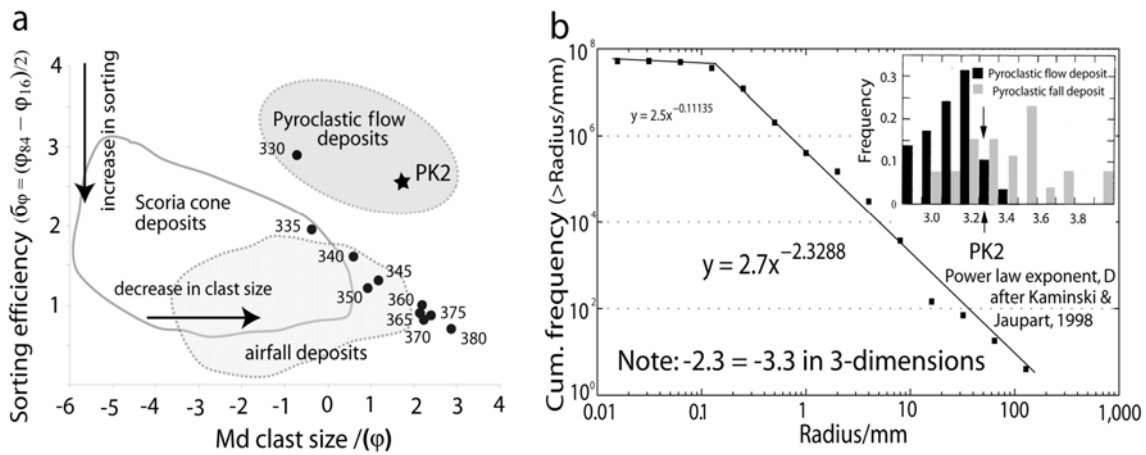


**Figure 2.9:** Comparison of granulometry from the PK<sub>2</sub> deposit with other pyroclastic deposit types: (a) Inman parameter plot (Inman, 1952) plotting sorting efficiency ( $\sigma$ ) vs. median grain size ( $Md\phi$ ) of clasts from 5 m intervals within the PK<sub>2</sub> deposit. Data points signify discrete horizons within the PK<sub>2</sub> deposit. Star (★) indicates value derived by integrating all data from the PK<sub>2</sub> deposit. Generalized fields enclose scoria cone deposits, 96% of measured pyroclastic density current deposits, and 96% of measured pyroclastic airfall deposits; modified from Cas and Wright, 1987; (b) log-log plot showing the clast size versus the cumulative frequency of clasts. Straight lines on log-log plots obey power laws with exponent  $D$ . Converting data generated from a 2 dimensional surface to 3 dimensions adds 1 to the value of  $D$ , such that  $-2.3$  in two dimensions =  $-3.3$  in three dimensions (after Walters et al., 2006). Inset shows summaries of  $D$ -values of pyroclastic density currents and pyroclastic airfall deposits from Kaminski & Jaupart, 1998.

very-fine-grained, well-sorted ( $\sigma < 1$ ) material at the top. Size distributions of olivines and relative proportions of mantle xenoliths suggest size and density as controlling factors in the deposition of the PK<sub>2</sub> unit (Figs. 2.8a; c). Sorting of this nature over a 40-45 m section of the PK<sub>2</sub> requires explanation. The high degree of sorting could result from either: (1) sub-aerial sedimentation from a steady to waning (e.g., decaying intensity) volcanic eruption column; or (2) en-masse deposition of a pyroclastic flow into a sub-aqueous setting.

Normal grading of a pyroclastic airfall deposit can result from the deposition of single eruption pulse (Cas and Wright, 1987). However, the onset and decay in eruption intensity observed in most other volcanic eruptions (Klein, 1982; Scandone and Malone, 1985; Ozerov et al., 2003; Houghton et al., 2004) is rarely linear. Therefore, the absence of distinct beds or variations in grain size on a 1-2 m scale in the entire deposit precludes sub-aerial sorting of an episodic, waning eruption. In addition, pyroclasts involved in a kimberlite eruption have an extremely high density relative to other magma types. Even for the same fluxes, volatile contents and eruption temperatures as observed in a sub-Plinian eruptions, the level of neutral buoyancy for a kimberlite eruption would be significantly lower. A lower height of neutral buoyancy would act to limit residence times in the column and, therefore, inhibit the ability of clasts in a pyroclastic column to sort sub-aerially. Pyroclastic materials falling through water, however, will sort more efficiently than if falling through air (Cashman and Fiske, 1991). Increased water depth could then promote more well-sorted deposits and thinner individual beds and bed sets. We interpret the spread in sorting efficiencies documented in Fig. 2.9a as the effect of the ambient medium (water) on clast sorting; integrating these properties allows for the recovery of properties of the deposit before sorting. The Inman parameters of the entire PK<sub>2</sub> deposit plots within the limits of > 96% of measured pyroclastic flow deposits (after Walker et al., 1980) (Fig. 2.9a, star), but outside of the boundary capturing > 96% of airfall deposits (after Walker, 1971).

We interpret the grading over a 40-50 m scale observed in the PK<sub>2b</sub> to result from sub-aqueous sorting of an en-masse deposit of a pyroclastic density current into a deep water column. The bedding observed in PK<sub>2a</sub> and the large-scale grading observed in PK<sub>2b</sub> likely result from efficient hydraulic sorting of pyroclastic material introduced as relatively small initial volumes (PK<sub>2a</sub>) followed by a single large volume (PK<sub>2b</sub>). We hypothesize that bed thickness and the relative degree of sorting in both bedding units

and individual beds can result from the interplay between the flux of pyroclastic material and the depth of the water column.

Therefore we interpret the graded pyroclastic kimberlite deposit as an exotically-sourced pyroclastic density current (pyroclastic flow) that was captured by the crater/conduit system of A154N. The sorted character of the PK<sub>2b</sub> deposit requires that the open crater/conduit hosted a standing body of water; the presence of this crater lake is strongly indicated by the nature (e.g., water-lain) of the underlying SVK deposits.

## 2.4 Discussion

### 2.4.1 Eruption model for the A154N pipe

The present-day measured volume of the A154N pipe is  $\sim 6.1 \times 10^6 \text{ m}^3$ . Assuming that the MVK deposits comprise  $\sim 5\text{-}10\%$  by volume of country rocks, the initial eruption of the A154N kimberlite excavated and dispersed a minimum volume of  $\sim 5.5 \times 10^6 \text{ m}^3$  of granite ( $\sim 90\%$  of total). Most overlying shale and sandstone country rocks was also ejected from the vicinity of the volcanic vent (Fig. 2.10a), as these xenolith types are rarely preserved in the MVK deposits (1-2%).

Infilling of the A154N immediately ensued, filling  $\sim 80\%$  ( $5.0 \times 10^6 \text{ m}^3$ ) of the present-day pipe volume with MVK (Fig. 2.10b). During the waning stages of eruption, depositional style progressed from en-masse, vertical collapse of the eruption column as a conduit filling density current (MVK<sub>1</sub>) to fall-out and crude sorting of the finer size fractions that may have been suspended in the upper (convecting?) portion of the column (MVK<sub>2</sub>). This initial eruption left a large crater  $>200 \text{ m}$  deep. Textures and bedding orientations at the boundary between MVK and SVK deposits suggest that during the waning stages of eruption, or immediately post-eruption, loose volcanic debris began to re-deposit into the open crater from all sides (Fig. 2.10c). The earliest SVK deposits are high-volume, and represent en-masse movement of coarse, country-rock and mantle xenolith and xenocryst-rich debris. Groundwater ultimately fills the crater with water at the same time that denudation of the crater walls and sedimentation into the conduit are taking place. Hot aqueous fluids serpentinize the interior of the volcanic pile and basal SVK deposits (Fig. 2.10d). Systematically smaller-volume, finer, mantle-depleted, and shale-enriched kimberlite continues to deposit into a deepening crater lake (Fig. 2.10e).

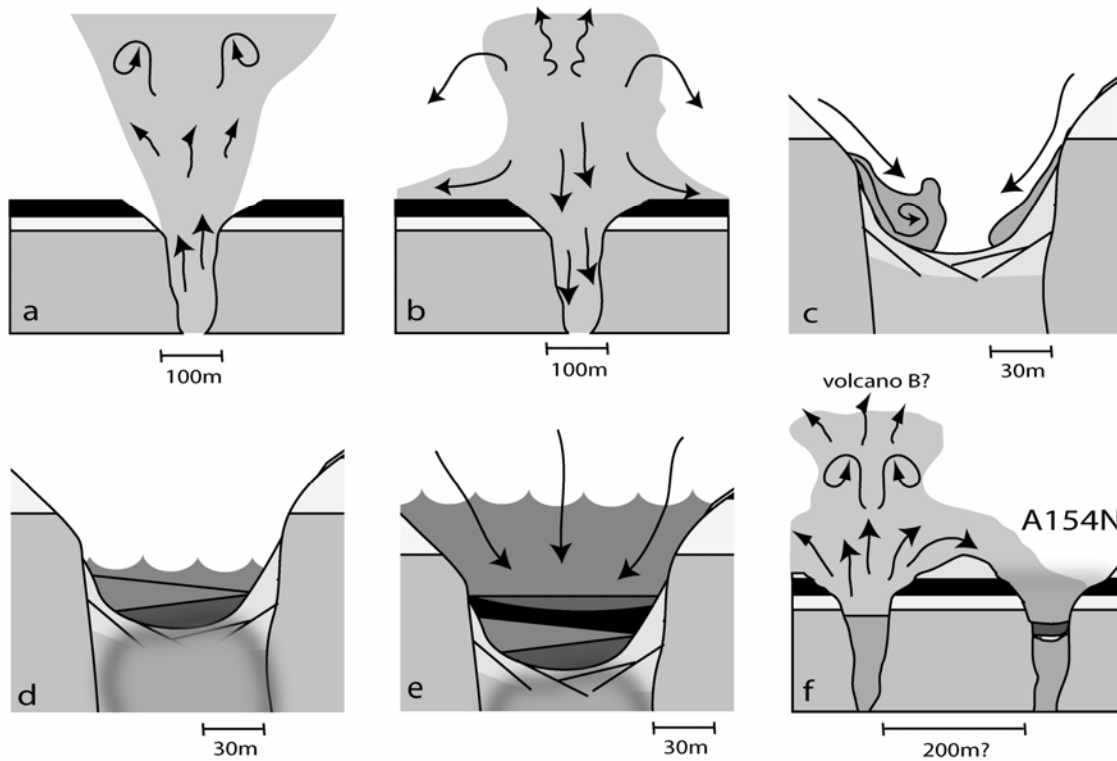


**Figure 2.10:** Six-stage eruption model for A154N: (a) pipe excavation; (b) collapse of pyroclastic column, generating poorly-sorted, massive volcanoclastic kimberlite infilling the pipe and depositing pyroclastic density currents and proximal fallout on the surrounding landscape; (c) re-deposition of tephra from crater rim introducing large-volume, kimberlite-rich avalanche deposits into crater; (d) alteration front superimposed over contact between primary volcanic pile and re-deposited tephra; sedimentation continues as olivine and shale-rich sands; (e) sedimentation of mud-rich, fine-grained kimberlite into deepening crater-lake; (f) eruption from adjacent kimberlite pipe fills crater lake with initially small volumes and finally a large volume of pyroclastic kimberlite.

Enough time transpired after the eruption of A154N for water to fill the open crater, a phenomenon observed to develop relatively quickly (weeks to months) in contemporary maar volcanoes (Kienle et al., 1980; Self et al., 1980). Pit engineers at Diavik estimate ~20,000 L/hr. of water is pumped from the A154N pit in order to maintain a consistent water level in the bottom of the pit (pers. comm. Cadrin, 2006). Assuming the same hydraulic conductivity from the wall rocks observed today, it would take over 10 years to fill up the crater with water to the water table after the eruption which made A154N. The climate during the Eocene for the Diavik area was probably temperate and wet (McIver, 1997; Graham et al., 1998) and, therefore, the time to fill the crater was probably  $\ll 10$  years. The SVK deposits record a gradational change from coarse to fine sub-aqueous sedimentation suggesting the crater lake was long-lived. Fine sedimentation is a physical manifestation of the volcanic edifice being stabilized; large-scale mass-wasting events no longer occur.

At some time after deposition of the last SVK deposits, pyroclastic kimberlite produced by eruption of a nearby kimberlite volcano was deposited into the A154N crater lake (Fig. 2.10f). There are, for example, over 20 kimberlite bodies within 20 km of A154N and many are of similar age (Heaman et al., 2004). At this time, the crater lake must have been well over 50 m deep in order to cause sorting of the entire PK<sub>2b</sub> deposit. The initial deposits were relatively small-volume, evidenced by diffuse, two-directional grading in PK<sub>2a</sub>. This was immediately followed by an en-masse influx of a pyroclastic density current.

#### 2.4.2 Kimberlite eruption dynamics: insights from PK<sub>2</sub>

Insights into volcanic eruption dynamics can be derived from clast size distributions of pyroclastic deposits (Walker et al., 1971; Walker, 1981; Sparks, 1986; Woods, 1988; Bursik et al., 1992). However, as there are few examples of well-preserved pyroclastic kimberlite and no studies which quantify the clast populations of pyroclastic kimberlite, it is difficult to draw analogies between kimberlites deposits and the eruption dynamics used to explain the nature of modern-day pyroclastic deposits.

The integrated granulometry data calculated for the complete (e.g., unsorted) PK<sub>2</sub> deposit permit comparison against data sets from known volcanic deposits in basaltic and andesitic systems. Grain size distributions for the entire deposit show an approximately

log-normal distribution (Fig. 2.8b). These data represent realistic constraints on clast sizes in a pyroclastic deposit from a kimberlite eruption; fragmented kimberlite magma in PK<sub>2</sub> rarely exceeds 2 cm in diameter, mantle xenoliths rarely exceed 15cm in diameter. The largest clasts are blocks of country rock which could represent accessory lithics ejected during eruption or accidental lithics picked up locally by a pyroclastic density current (Cas and Wright, 1987). As shown previously, Inman parameters of the entire PK<sub>2</sub> deposit plot in the middle of >96% of measured pyroclastic flow deposits (Fig. 2.9b)

Several previous studies of kimberlite have quantified lithic populations in massive volcanoclastic kimberlite (Barnett, 2004; Walters et al., 2006b) using a power law:

$$N(R \geq r) = \lambda r^{-D} \quad (2.1)$$

where  $N(R \geq r)$  is the number of fragments with a radius greater than  $r$ ,  $\lambda$  is an arbitrary constant and  $D$  is the fractal dimension. If the cumulative particle size frequency of a population of pyroclasts is plotted against particle radius on a log-log plot, a fractal distribution would appear as a straight line with a slope of  $D$ . Large changes in the size range of particles are required to change the value of  $D$  (Kaminski and Jaupart, 1998; Walters et al., 2006b). Thus,  $D$ -values can describe and distinguish pyroclast populations from different deposit types (Kaminski and Jaupart, 1998); the value of  $D$  fitted to the kimberlite pyroclastic deposit (PK<sub>2</sub>) allows for comparison against other deposits types.

The central zone on a log-log plot of the granulometry data of the PK<sub>2b</sub> (Fig. 2.9b) representing intermediate size particles shows a particle size distribution with a fractal dimension ( $D$ ) of 2.3 (equivalent to 3.3 in three dimensions); comparison with data sets from other deposit types (after Kaminski and Jaupart, 1998) show the PK<sub>2b</sub> to be higher than most pyroclastic flows, and yet lower than most pyroclastic airfall deposits (Fig. 2.9b, inset). These data are consistent with the interpretation that the PK<sub>2b</sub> is the result of a pyroclastic density current.

The analysis presented above must be taken with some caution because pyroclasts derived from kimberlite eruptions can have substantially different properties from pyroclasts produced in conventional volcanic systems. On the basis of this study, we identify the following distinctive characteristics of kimberlite pyroclasts, including:

1. Most (>80 %) pyroclasts comprise low (<10 %) melt fractions; free olivine crystals are the most abundant type of pyroclast in kimberlite eruptions. In contrast, pyroclast populations found in rhyolitic or basaltic systems are mainly quenched fragments of vesiculated melt having subordinate proportions of crystals.
2. Size range of pyroclasts: the size range of kimberlite pyroclasts are severely truncated relative to deposits from other volcanic styles. For example, the finest size fraction of clasts observed in the PK<sub>2</sub> (0.1 mm) is substantially coarser than the finest fraction of a typical Plinian eruption (64% finer than 63 μm, Brazier et al., 1983); the coarsest fraction of a Plinian eruption is much coarser (m-scale) than that observed in the PK<sub>2</sub> (cm-scale) (e.g. Carey and Sigurdsson, 1982). Furthermore, the median size of PK<sub>2</sub> pyroclasts is significantly smaller than those of typical scoria fall deposits (e.g. Parfitt, 1998). The size range of PK<sub>2</sub> is likely controlled by the initial size distribution of the olivines in the kimberlite magma. Comparison of fragmentation processes in crystal and volatile-rich, low-viscosity kimberlite magmas with those observed in other volcanic systems is needed to measure the impact of crystal content upon fragmentation processes.
3. Lack of vesiculation: pyroclasts from the PK<sub>2</sub> and from other kimberlitic eruptions contain few (<10%) or no vesicles (Lorenz, 1975). By contrast, most pumices from intermediate to felsic volcanic eruptions (e.g., dacite, rhyolite) have 40 to 70% porosity; mafic explosive volcanism can produce scoria and reticulite which have porosities of 25-60% and in excess of 75%, respectively. The consequence of low vesicularity is that kimberlite pyroclasts will not show the same behaviour in an eruption column as shown by highly vesicular pyroclasts found in conventional hawaiian, vulcanian, surtseyan, or plinian eruptions. For example, vertical sorting among grain sizes would be enhanced, and the lateral extent of distributions and rate of heat exchange from pyroclast to atmosphere in kimberlite volcanism would greatly differ than that observed in basaltic systems.
4. High density of pyroclasts: At eruption conditions, kimberlite melts likely have a density greater than basalt (2700 kg m<sup>-3</sup>). In addition, kimberlite magmas are a mechanical mixture of olivine macrocrysts (>20% by vol.), xenoliths of peridotite (3300 kg m<sup>-3</sup>) and eclogite (3440 kg m<sup>-3</sup>), and xenocrysts derived from those xenoliths. Consequently, the density of the unvesiculated kimberlite magma must have a density well in excess of 3000 kg m<sup>-3</sup>. Under minimum conditions of fragmentation (porosity > 50-60%), disrupted kimberlite magma would have an average density of ~1500 kg m<sup>-3</sup>.

However, we observe little to no vesiculation in quenched juvenile pyroclasts of kimberlite suggesting that most kimberlite pyroclasts have densities in excess of 2700 kg m<sup>-3</sup>. As a result, there are limits to the potential height to which kimberlite pyroclasts can be entrained in the eruption column (e.g. Sparks, 1986); most pyroclasts will never rise above the momentum thrust portion of the column and this height is, itself, limited by the aggregate density of the erupting kimberlite magma.

Our study reveals several features of kimberlite volcanism. First, the presence of fine ash at the top of the PK<sub>2</sub> shows that kimberlite volcanoes are capable of fine fragmentation. Secondly, the pyroclast populations in the PK<sub>2</sub> suggest kimberlite eruptions produce restricted pyroclast size distributions compared to Plinian eruptions and finer distributions relative to strombolian eruptions. Thirdly, facies analysis and granulometry of the PK<sub>2</sub> show that kimberlite eruptions can produce pyroclastic flows.

#### 2.4.3 Cross-fertilization of kimberlite: economic implications

There is no obvious internal source for the pyroclastic kimberlite (PK<sub>2a</sub> and PK<sub>2b</sub>); nowhere is there evidence of a late volcanic conduit or vent cutting through the underlying SVK deposits. The presence of sharp, well-defined contacts between the PK<sub>2a</sub> and SVK, as well as stratiform, pipe-wide, and well-bedded underlying mudstone deposits within the SVK suggests the source of material to be outside of A154N. The PK<sub>2</sub>, therefore, represents a preserved extra-crater deposit from an, as of yet, unidentified kimberlite volcano. The A154N pipe simply served as a receptacle for the explosive pyroclastic materials. The deposits in A154N suggest that infill of kimberlite pipes can be the result of multiple eruptions from multiple eruption locations. Any efforts to quantify economic grade of a given pipe must take this possibility into account.

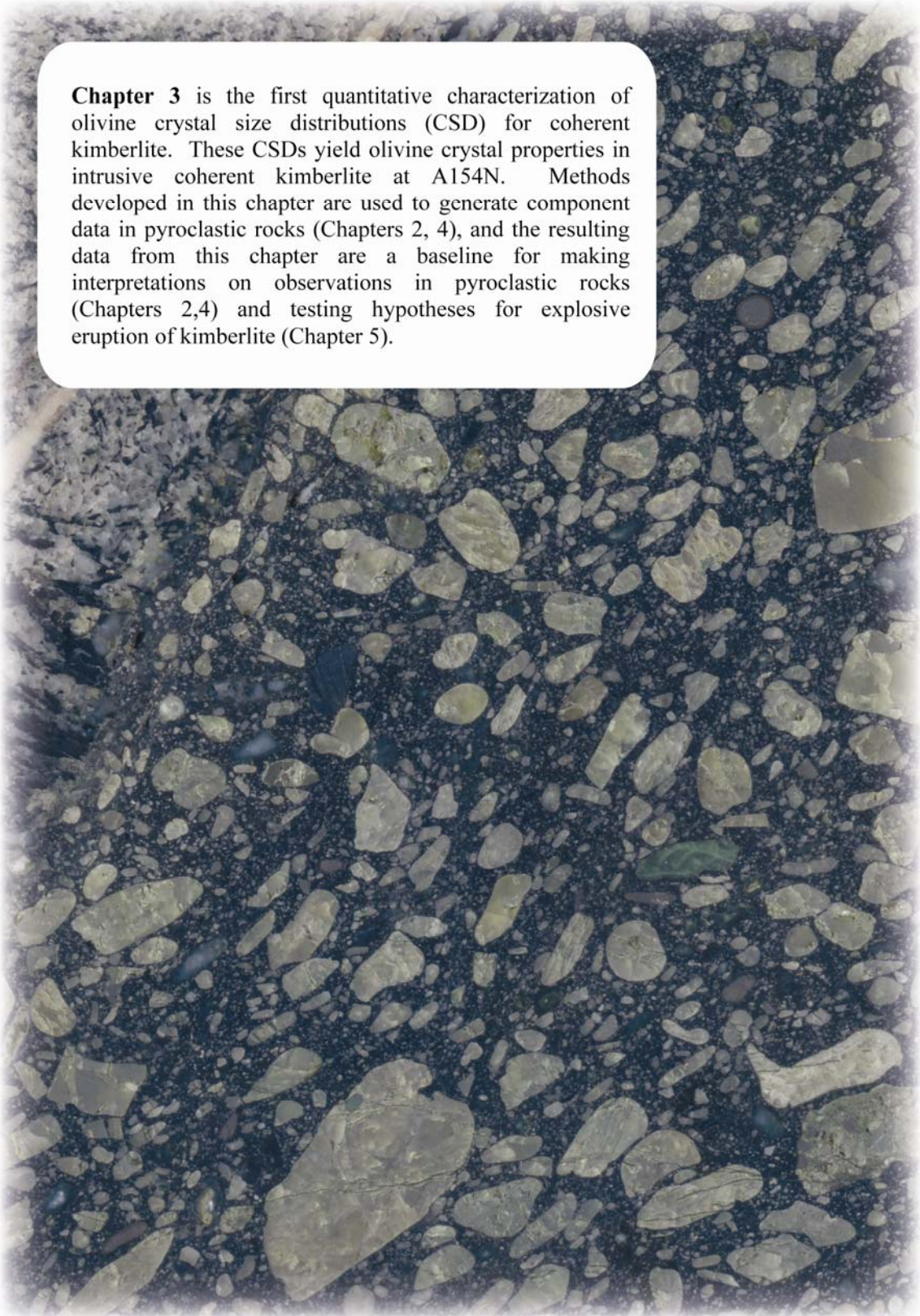
## 2.5 References

- Amelin, Y., 1996. Report on Rb-Sr and U-Pb study of kimberlite samples VR44444A through VR44465A. Confidential Report for Kennecott, Canada Inc.
- Barnett, W., 2004. Subsidence breccias in kimberlite pipes--an application of fractal analysis. *Lithos* 76(1-4), 299-316.
- Berryman, A.K., Scott Smith, B.H. and Jellicoe, B.C., 2004. Geology and diamond distribution of the 140/141 kimberlite, Fort a la Corne, central Saskatchewan, Canada. *Lithos* 76(1-4), 99-114.
- Boyer, L., 2005. Kimberlite volcanic facies and eruption in the Buffalo Head Hills, Alberta (Canada), MSc thesis, University of British Columbia, Vancouver, Canada.
- Boyer, L., Hood, C.T., McCandless, T.E., Skelton, D. and Tosdal, R.M., 2003. Volcaniclastic kimberlites of the Buffalo Head Hills, Alberta, Canada. GAC-MAC Joint Annual Meeting 28, 498.
- Boyer, L., Hood, C.T., McCandless, T.E., Skelton, D. and Tosdal, R.M., 2004. Volcanology of the Buffalo Hills Kimberlites, Alberta, Canada: some preliminary observations. 8th International Kimberlite Conference Long Abstract.
- Brazier, S., Sparks, R.S.J., Carey, S.N., Sigurdsson, H. and Westgate, J.A., 1983. Bimodal grain size distribution and secondary thickening in air-fall ash layers. *Nature* 301(5896), 115-119.
- Bursik, M.I., Sparks, R.S.J., Gilbert, J.S. and Carey, S.N., 1992. Sedimentation of tephra by volcanic plumes: I. Theory and its comparison with a study of the Fogo A plinian deposit, Sao Miguel (Azores). *Bulletin of Volcanology* 54(4), 329-344.
- Cadrin, M., 2006. Pit Engineer, DDMI personal communication.
- Carey, S. and Sigurdsson, H., 1982. Influence of particle aggregation on deposition of distal tephra from the May 18, 1980, eruption of Mount St. Helens volcano. *Journal of Geophysical Research* 87(B8), 7061-7072.
- Cas, R.A.F. and Wright, J.V., 1987. Volcanic successions, modern and ancient. Chapman & Hall, London, 528 pp.
- Cashman, K.V. and Fiske, R.S., 1991. Fallout of Pyroclastic debris from sub-marine volcanic eruptions. *Science* 253, 275-279.
- Cashman, K.V. and Manga, M.T., 1994. Physical aspects of magma degassing II, Constraints on vesiculation processes from textural studies of eruptive products In: M.R. Carroll and J.R. Holloway (Editors), *Reviews in Mineralogy. Volatiles in Magmas*. Mineralogical Society of America, Washington D.C., pp. 446-478.
- Clement, C.R., 1982. A comparative geological study of some major kimberlite pipes in the Northern Cape and Orange Free State, PhD thesis, University of Cape Town, Cape Town, South Africa.
- Creaser, R.A., Grutter, H., Carlson, J. and Crawford, B., 2004. Macrocystal phlogopite Rb-Sr dates for the Ekati property kimberlites, Slave Province, Canada: evidence for multiple intrusive episodes in the Paleocene and Eocene. *Lithos* 76(1-4), 399-414.
- Doyle, B.J., Kivi, K. and Scott Smith, B.H., 1998. The Tli Kwi Cho (DO27 and DO18) Diamondiferous Kimberlite Complex, Northwest Territories, Canada. In: J.J. Gurney, J.L. Gurney, M.D. Pascoe and S.H. Richardson (Editors), VIIth International Kimberlite Conference. Red Roof Design, University of Cape Town, South Africa, pp. 194-204.

- Edwards, C.B. and Howkins, J.B., 1966. Kimberlites in Tanganyika with special reference to the Mwadui occurrence. *Economic Geology* 61, 537-554.
- Field, M., Gibson, J.G., Wilkes, T.A., Gababotse, J. and Khutjwe, P., 1997. The Geology of the Orapa A/K1 Kimberlite Botswana: Further insights into the emplacement of kimberlite pipes. *Russian Geology and Geophysics* 38(1), 24-39.
- Graham, I., Burgess, J.L., Bryan, D., Ravenscroft, P.J., Thomas, E., Doyle, B.J., Hopkins, R. and Armstrong, K.A., 1998. Exploration History and Geology of the Diavik Kimberlites, Lac de Gras, Northwest Territories, Canada. In: J.J. Gurney, J.L. Gurney, M.D. Pascoe and S.H. Richardson (Editors), *Proceedings of the VIIth International Kimberlite Conference*. Red Roof Design, Cape Town, South Africa, pp. 262-279.
- Heaman, L.M., Kjarsgaard, B.A. and Creaser, R.A., 2004. The temporal evolution of North American kimberlites. *Lithos* 76(1-4), 377-397.
- Houghton, B.F., Wilson, C.J.N., Del Carlo, P., Coltelli, M., Sable, J.E. and Carey, R., 2004. The influence of conduit processes on changes in style of basaltic Plinian eruptions: Tarawera 1886 and Etna 122 BC. *Journal of Volcanology and Geothermal Research* 137(1-3), 1-14.
- Junqueira-Brod, T.C., Gaspar, J.C., Brod, J.A. and Kafino, C.V., 2005. Kamafugitic diatremes: Their textures and field relationships with examples from the Goias alkaline province, Brazil. *Journal of South American Earth Sciences* 18(3-4 SPEC. ISS.), 337-353.
- Kaminski, E. and Jaupart, C., 1998. The size distribution of pyroclasts and the fragmentation sequence in explosive volcanic eruptions. *Journal of Geophysical Research* 103(B12), 29759-29779.
- Kienle, J., Kyle, P.R., Self, S., Motyka, R.J. and Lorenz, V., 1980. Ukinrek Maars, Alaska, I. April 1977 eruption sequence, petrology and tectonic setting. *Journal of Volcanology and Geothermal Research* 7(1-2), 11-37.
- Kjarsgaard, B.A. and Wyllie, R.J.S., 1994. Geology of the Paul Lake area, Lac de Gras du Sauvage region of the central Slave Province, District of Mackenzie, Northwest Territories. *Geological Society of Canada Current Research* 1994-C, 23-32.
- Klein, F.W., 1982. Patterns of historical eruptions at Hawaiian volcanoes. *Journal of Volcanology and Geothermal Research* 12(1-2), 1-35.
- Leahy, K., 1997. Discrimination of reworked pyroclastics from primary tephra-fall tuffs: a case study using kimberlites of Fort a la Corne, Saskatchewan, Canada. *Bulletin of Volcanology* 59, 65-71.
- Leckie, D.A., Kjarsgaard, B.A., Bloch, J., McIntyre, D., McNeil, D., Stasiuk, L., Heaman, L., 1997. Emplacement and reworking of Cretaceous, diamond-bearing, crater-facies kimberlite of central Saskatchewan, Canada. *GSA Bulletin* 109(8), 1000-1020.
- Lorenz, V., 1975. Formation of phreatomagmatic maar-diatreme volcanoes and its relevance to kimberlite diatremes. *Physics and Chemistry of the Earth* 9, 17-29.
- Machin, K.J., 2001. Processes and products in kimberlitic crater facies of the South Lobe, Jwaneng Mine, Botswana, MSc thesis, Rhodes University, Grahamstown, South Africa.
- Mainkar, D., Lehmann, B. and Haggerty, S.E., 2004. The crater-facies kimberlite system of Tokapal, Bastar District, Chhattisgarh, India. *Lithos* 76(1-4), 201-217.
- Mannard, G., 1962. The Geology of the Singida kimberlite pipes, Tanganyika, PhD thesis, McGill University, Montreal, Canada.

- McIver, E., 1997. Report on plant remains. Confidential report for Diavik.
- Mitchell, R.H., 1986. *Kimberlites: Mineralogy, Geochemistry and Petrology*. Plenum Press, New York, 442 pp.
- Nowicki, T., Crawford, B., Dyck, D., Carlson, J., McElroy, R., Oshust, P. and Helmstaedt, H., 2004. The geology of kimberlite pipes of the Ekati property, Northwest Territories, Canada. *Lithos* 76(1-4), 1-27.
- Ozerov, A., Ispolatov, I. and Lees, J., 2003. Modeling Strombolian eruptions of Karymsky volcano, Kamchatka, Russia. *Journal of Volcanology and Geothermal Research* 122(3-4), 265-280.
- Parfitt, E.A., 1998. A study of clast size distribution, ash deposition and fragmentation in a Hawaiian-style volcanic eruption. *Journal of Volcanology and Geothermal Research* 84, 197-208.
- Pell, J.A., 1997. Kimberlites in the Slave Craton, Northwest Territories, Canada: A preliminary review. *Russian Geology and Geophysics* 38(1), 516.
- Sahagian, D.L. and Proussevitch, A., 1998. 3D particle size distributions from 2D observations: stereology for natural applications. *Journal of Volcanology and Geothermal Research* 84, 173-196.
- Scandone, R. and Malone, S.D., 1985. Magma supply, magma discharge and readjustment of the feeding system of mount St. Helens during 1980. *Journal of Volcanology and Geothermal Research* 23(3-4), 239-262.
- Self, S., Kienle, J. and Huot, J.-P., 1980. Ukinrek Maars, Alaska, II. Deposits and formation of the 1977 craters. *Journal of Volcanology and Geothermal Research* 7(1-2), 39-65.
- Smith, R.M.H., 1986. Sedimentation and paleoenvironments of Late Cretaceous crater-lake deposits in Bushmanland, South Africa. *Sedimentology* 33, 369-386.
- Sparks, R.S.J., 1986. The dimensions and dynamics of volcanic eruption columns. *Bulletin of Volcanology* 48, 3-15.
- Stasiuk, L.D., Lockhart, G.D., Nassichuk, W.W., 1999. Thermal maturity evaluation of dispersed organic matter inclusions from kimberlite pipes, Lac de Gras, Northwest Territories, Canada. *International Journal of Coal Geology* 40, 1-25.
- Stasiuk, M., Barclay, J., Carroll, M.R., Jaupart, C., Ratte, J., Sparks, R.S.J. and Tait, S., 1996. Degassing during magma ascent in the Mule Creek vent (USA). *Bulletin of Volcanology* 58, 117-130.
- Stiefenhofer, J. and Farrow, D.J., 2004. Geology of the Mwadui kimberlite, Shinyanga district, Tanzania. *Lithos* 76(1-4), 139-160.
- Sweet, A.R., Stasiuk, M., Nassichuk, W.W., McIntyre, D.J. and Catunneau, O., 2003. Stratigraphy, paleoenvironments and thickness of inferred sedimentary cover and kimberlite crater fill processes, Lac de Gras, Northwest Territories, Canada. . Proceedings of the Eighth International Kimberlite Conference, Victoria, British Columbia, Canada.
- Thompson, K., 2007. Resource Geologist, Diavik Diamond Mines Incorporated (DDMI), personal commentary.
- Valentine, G.A. and Krogh, K.E.C., 2006. Emplacement of shallow dikes and sills beneath a small basaltic volcanic center - The role of pre-existing structure (Paiute Ridge, southern Nevada, USA). *Earth and Planetary Science Letters* 246(3-4), 217-230.
- Walker, G.P.L., 1971. Grainsize characteristics of pyroclastic deposits. *Journal of Geology* 79, 696-714.

- Walker, G.P.L., 1981. Plinian eruptions and their products. *Bulletin of Volcanology* 44, 223-240.
- Walker, G.P.L., Wilson, C.J.N. and Froggatt, P.C., 1980. Fines-depleted ignimbrite in New Zealand - the product of a turbulent pyroclastic flow. *Geology* 8, 245-249.
- Walker, G.P.L., Wilson, L. and Howell, E.L.G., 1971. Explosive Volcanic Eruptions I: Rate of fall of pyroclasts. *Geophysical Journal of the Royal Astronomical Society* 22, 377-383.
- Walters, A., Phillips, J., Brown, R., Field, M. and R.S.J., S., 2006. The role of fluidisation processes in the formation of volcanoclastic kimberlite: grain size observations and experimental investigation. *Journal of Volcanology and Geothermal Research* 155(1-2), 119-137.
- Webb, K.J., Scott Smith, B.H., Paul, J.L. and Hetman, C.M., 2004. Geology of the Victor Kimberlite, Attawapiskat, Northern Ontario, Canada: cross-cutting and nested craters. *Lithos* 76(1-4), 29-50.
- Webb, K.J., Stiefenhofer, J. and Field, M., 2003. Overview of the geology and emplacement of the Jwaneng DK2 kimberlite, southern Botswana. 8th International Kimberlite Conference Long Abstract.
- Woods, A.W., 1988. The fluid dynamics and thermodynamics of eruption columns. *Bulletin of Volcanology* 50(3), 169-193.
- Zonneveld, J.P., Kjarsgaard, B.A., Harvey, S.E., Heaman, L.M., McNeil, D.H. and Marcia, K.Y., 2004. Sedimentologic and stratigraphic constraints on emplacement of the Star Kimberlite, east-central Saskatchewan. *Lithos* 76(1-4), 115-138.

A microscopic image showing a dense field of olivine crystals. The crystals are light-colored, ranging from pale yellow to light brown, and are set against a dark, almost black, matrix. The crystals vary in size and shape, with many showing characteristic octahedral or subhedral forms. Some crystals are larger and more prominent, while others are smaller and more numerous. The overall texture is granular and somewhat chaotic, typical of a crystalline rock.

**Chapter 3** is the first quantitative characterization of olivine crystal size distributions (CSD) for coherent kimberlite. These CSDs yield olivine crystal properties in intrusive coherent kimberlite at A154N. Methods developed in this chapter are used to generate component data in pyroclastic rocks (Chapters 2, 4), and the resulting data from this chapter are a baseline for making interpretations on observations in pyroclastic rocks (Chapters 2,4) and testing hypotheses for explosive eruption of kimberlite (Chapter 5).

## **3 Olivine crystal size distributions in intrusive coherent kimberlite<sup>4</sup>**

### **3.1 Introduction**

Olivine crystals are the most abundant mineral phase in coherent and fragmental kimberlite rocks. Olivine crystals can comprise between 5 and 90 volume % of kimberlite rocks, and typically vary in size from ~0.03 mm to ~10 mm in diameter (Mitchell, 1986; Scott Smith, 1996). Properties of olivine crystals in intrusive, coherent kimberlite rocks are locally heterogeneous; modal %, size range, shape, relative abundance and relationships between sizes appear to vary within and between single occurrences. However, overall these properties appear broadly similar among global occurrences of intrusive coherent kimberlite (Mitchell, 1986). These properties likely reflect end-products resulting from a number of processes, including initial equilibrium crystallization in the pre-existing mantle, disaggregation, transport, chemical corrosion and new crystallization of olivine from the kimberlite melt. Accurate estimation of these properties at all scales is critical to the interpretation of kimberlite paragenesis and emplacement processes.

In this paper, we present the first complete olivine crystal size distributions (CSDs) in intrusive coherent kimberlite. We characterize the population of olivine crystals in 5 samples of intrusive coherent kimberlite from dykes at the Diavik diamond mine, NWT, Canada using a method consisting of manual tracing of olivine crystals and image analysis of the traced crystals. The data was collected at two overlapping scales of observation: thin sections (12.5 x 28 mm) and slabs (47 x 77 mm). The two datasets were combined to create a single crystal size distribution (CSD) of olivine crystals from the full size range, 0.025 to 12 mm in diameter. This study describes the properties of size, abundance, relative size ratios and shape of the olivine crystals in samples of intrusive coherent kimberlite, and reports variances obtained using a manual tracing method. These properties are used to compare olivine populations in intrusive coherent

---

<sup>4</sup> A version of this chapter has been submitted for publication. Moss, S., Russell, J.K., Scott Smith, B.H., Brett, R.C. Olivine crystal size distributions in intrusive coherent kimberlite.

kimberlite at Diavik to previous understandings of olivines from study of occurrences in South Africa. Furthermore, we show that the entire CSD can be described by a best-fit power-law model equation over several orders of magnitude of crystal sizes. On the basis of the power-law models, we show that: a) best-fit equation parameters define a ‘type’ CSD for olivines in intrusive coherent kimberlite that can be used to uniquely characterize deposits; and b) olivine populations may be used to test hypotheses for the complex paragenetic origins of olivine crystals.

First, we summarize current understandings of olivine crystals in intrusive coherent kimberlite as well as previous approaches to characterizing the crystal populations. Second, we describe the methods used to obtain the first complete CSD for olivine in coherent kimberlite. Third, we explain this result and discuss uses and implications of olivine CSDs.

## **3.2 Background**

### 3.2.1 Olivine crystals in kimberlite

Olivine crystals in intrusive coherent kimberlite are generally considered to comprise two generations which are attributed to two distinct processes: the disaggregation of lherzolites and harzburgites from the mantle (yielding xenocrysts), and nucleation and growth of olivine due to melt saturation yielding cognate phenocrysts (e.g., Woolley et al., 1996; e.g., Fedortchouk and Canil, 2004) and/or overgrowths on xenocrysts (Kamenetsky et al., 2007b). These processes are thought to yield two populations of olivine equally represented by mode: larger, anhedral, commonly round to sub-round olivine xenocrysts termed ‘macrocrysts’ (Boyd and Clement, 1977; Clement, 1982; Clement et al., 1984; Mitchell, 1986), and smaller, sub-hedral to euhedral crystals of olivine (Clement, 1982; Shee, 1985) interpreted as ‘phenocrysts’. These populations are considered to be generally distinct in size (‘macrocrysts’  $\geq 0.5$  mm  $\geq$  ‘phenocrysts’), shape (anhedral vs. euhedral), degree of strain (i.e. undulose extinction), and mantle mineral inclusions, though there is little published data to support these distinctions (e.g., Wagner, 1914; e.g., Dawson, 1962; Mitchell, 1970).

Olivine contents are shown to be highly variable among and within dykes (Daly, 1925; Komar, 1972; Dawson and Hawthorne, 1973; Donaldson and Reid, 1982; Shee, 1985; Price et al., 2000; Arndt et al., 2006) but most occurrences of intrusive, coherent kimberlite usually contain up to ~50% of olivine crystals (Clement et al., 1984; Mitchell, 1986; Heiken et al., 1988; Woolley et al., 1996). However, existing studies tend to limit observation to thin sections (e.g., Arndt et al., 2006), and have focused on chemical characterization of olivine.

### 3.2.2 Previous measurement and characterization

Modal analyses of olivine crystals and other components in kimberlite rocks were previously accomplished by a variety of methods. Point-counting of thin sections (Clement, 1982; Shee, 1985; Webb et al., 2004) has provided estimates of modal % of olivine crystals, but little information on size distributions. Based on the petrographic criteria mentioned above, most previous workers have made genetic interpretations while point counting thin sections in order to distinguish two populations of olivine in intrusive coherent kimberlite (i.e., ‘macrocrysts’ vs. ‘phenocrysts’), and semi-quantitatively estimate modal abundances (Clement, 1982; Shee, 1985). Measured sizes of individual crystals of these point counts by both Shee (1985) and Clement (1982) suggest that at the type areas for kimberlite petrology (i.e., the Wesselton, DeBeers and Dutoitspan kimberlite pipes in Kimberley, South Africa), the two petrographic sub-types have different sizes, generally greater or less than 1 mm. Recent advances in image analysis technology have enabled olivine crystal size data to be obtained for some kimberlite magmas (Appendix 7.3.2; Field et al., 2008; Scott Smith, 2009b). The latter data, however, are exclusively collected at the hand sample scale. Manual outlining or tracing of fragments and crystals to determine clast size distributions has been conducted in massive volcanoclastic kimberlite (Walters et al., 2006a) and pyroclastic kimberlite (Chapter 2; Scott Smith, 2009b). None of the previous approaches has quantified the size distributions of olivines found in coherent kimberlite rocks over the entire range of crystal sizes.

### 3.3 Methods

To characterize olivine crystal populations in intrusive coherent kimberlite, it is necessary to: a) obtain/collect representative samples; b) accurately identify true boundaries of olivine crystals in order to measure crystal sizes and shapes; c) capture the full size range of olivine crystals observed; and d) quantify the population using measured sizes in a statistically meaningful way. In this section, we describe the methods used to select samples, recognize olivine crystals, and to statistically evaluate olivine crystal populations.

#### 3.3.1 Sample selection

Samples for this study were obtained from intrusive dykes of coherent kimberlite in pipe A154N, one of the four kimberlite pipes currently mined at Diavik Diamond Mine Inc. (DDMI), in NWT, Canada. The four pipes have different pipe shapes and infill but all contain coherent kimberlite dykes at original emplacement depths in excess of 650 m to within 10's of m of the present day surface (-200 to +350 meters above sea level or m asl; Fig. 3.1). The intersections show significant diversity in thickness (0.01 – 10's of m), olivine crystal content (5 – 65 modal %), carbonate content (0 – 40 modal %), mantle minerals (e.g., ilmenite, chrome diopside, garnet), and groundmass mineralogy. However, first-order examination of dyke interiors (centre 1/3) reveals broadly similar olivine crystal content.

Samples used for this study are intersections of intrusive coherent kimberlite which cross-cut fragmental kimberlite in drillcores through pipe A154N between +20 m asl to -200 m asl (Fig. 3.1). Though the 3-D orientation of the planar dyke walls are indiscernible for individual drillholes, intervals of intrusive coherent kimberlite identified in 25 drillholes at A154N allow for simple 3-D modeling by Diavik mine geologists of multiple, vertical and parallel dykes striking at ~35-40° (Fig. 3.1). The emplacement

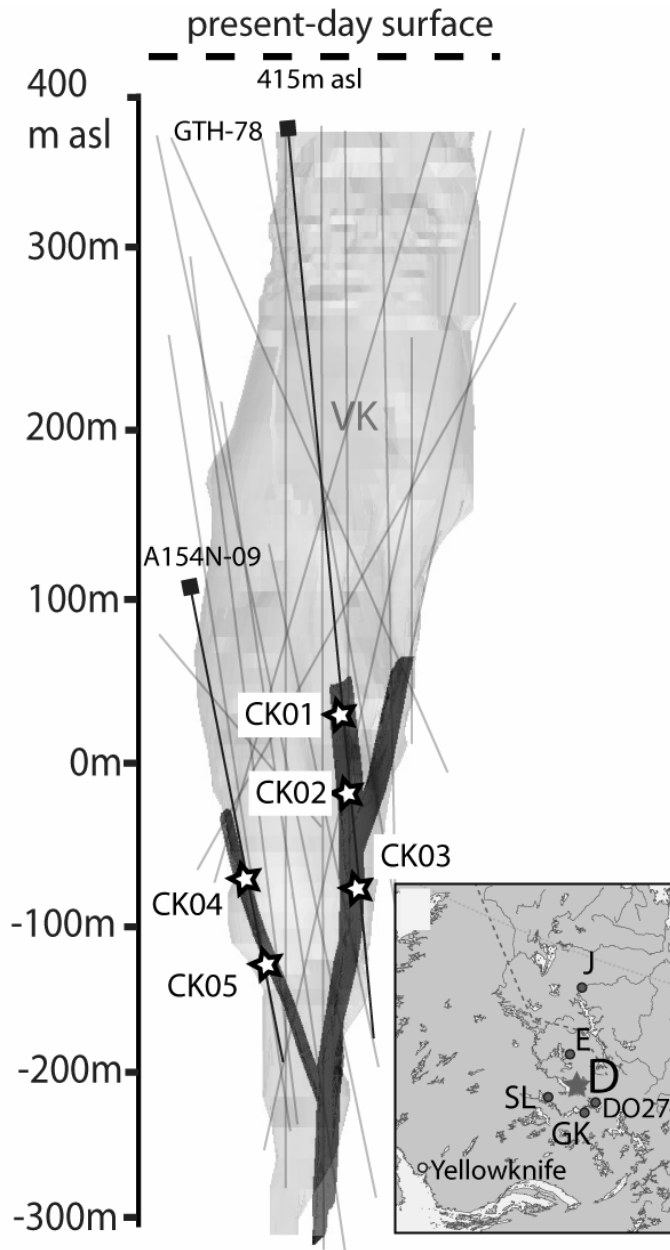


**Figure 3.1:** A154N kimberlite pipe at Diavik, Northwest Territories: oblique view looking NE of 3D geological model developed by Diavik Diamond Mines Incorporated (DDMI). Inset shows location of Diavik (D) within Northwest Territories, Canada, and location of other kimberlites including Ekati (E), Snap Lake (SL), Gahcho Kue (GK), Jericho (J) and DO-27. Pipe infill of volcaniclastic kimberlite (VK) is translucent to show location of modeled dykes of coherent kimberlite. Drillholes used to model dyke geometries are indicated with lines. Samples for this study obtained from drillholes GTH-78 and A154N-09; stars indicate sample locations.

depths of the kimberlite dykes are unknown, but the dykes are mapped in drillcore up to present-day depths of +50 m asl. Dyke rocks are found intruding through volcanoclastic kimberlite from the A154N pipe and the same dyke is observed elsewhere forming a contact between volcanoclastic kimberlite and adjacent granite and metasedimentary country rocks. In most cases, contacts with both volcanoclastic kimberlite and granite are sharp. Dyke margins are composed of relatively small (<1 mm) olivine crystals set in a groundmass of spinel, carbonate and serpentine. Finer-grained margin areas are typically only seen up to 2-3 cm away from the contact. Dyke interiors contain abundant, variably-sized olivine crystals, show no apparent preferred orientation, and appear uniform and consistent both laterally and vertically throughout the observed intersections.

The five carefully selected samples (Fig. 3.2) include three samples (CK01, CK02, CK03) from a 0.5 to 2.3 m-wide dyke that intrudes fragmental (volcanoclastic) kimberlite from the interior of the A154N pipe (drillhole GTH-78; Fig. 3.1) and two samples (CK04, CK05) are from a 1 to 2.5 m-wide dyke found 60m away on the opposite side of the pipe (drillhole A154N-09; Fig. 3.1). Though spatially-separate, the two separate intersections may represent either a single, bi-furcating sheet (as modeled; Fig. 3.1), or two or more separate intrusions into the A154N kimberlite pipe. The samples were collected from the central-third by width of each dyke intersection to minimize the impact of flow, rapid crystallization, and contact-related alteration. The samples were also selected on the basis of the lack of alteration of olivine crystals (i.e., no serpentinization) and the paucity of country rock xenoliths. Each sample is a massive, competent, black rock containing abundant randomly-oriented olivine crystals in a fine-grained groundmass. Olivine crystal sizes and shapes range from coarse (1-10 mm), anhedral to sub-rounded “macrocrysts” (sensu Clement et al., 1977), to small (0.03 – 1 mm), subhedral to euhedral crystals. Groundmass minerals comprise euhedral spinel (0.02 - 0.06 mm), monticellite micro-phenocrysts (10 – 25  $\mu\text{m}$ ), carbonate, serpentine, apatite and minor perovskite. Visual estimates of the olivine crystal content (~50 modal %; 0.03 – 10.0 mm), groundmass mineralogy, apparent dyke thickness, and crystal-rich dyke interior of coherent kimberlite at A154N suggest it is broadly similar to that observed in kimberlite sheets and dykes throughout the world (Dawson and Hawthorne, 1970; Scott Smith, 1999b; Basson and Viola, 2004; Caro et al., 2004).

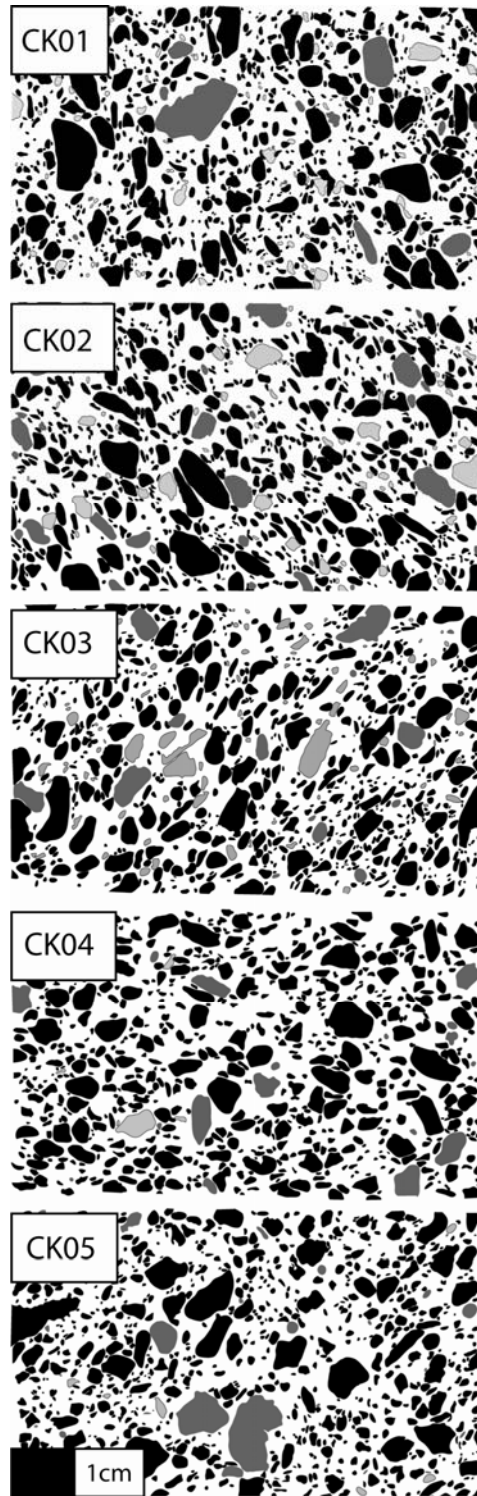


**Figure 3.2:** Greyscale images of manual tracings of 5 polished slab samples of coherent kimberlite at A154N (see Fig. 3.1). Olivine crystals = black; mantle xenocrysts/xenoliths = dark grey; crustal xenocrysts/xenoliths = light grey.

### 3.3.2 Manual tracing method

To characterize olivine crystals in coherent kimberlite, we employed a manual tracing method which involves tracing observed and interpreted boundaries of olivine crystals as seen with the human eye on two scales: in polished slabs (47 mm x 77 mm) and thin sections (12.5 mm x 25 mm). Using this method, we increase accuracy in the identification of crystal boundaries around olivine crystals, between touching crystals and within altered crystals. The measured crystals from two scales of observation were then combined to generate two-dimensional (2D) olivine crystal size data. The process necessary to obtain crystal property data for olivine crystals is described in detail in Appendix 8.2. The manual method comprises four steps: 1) tracing, image creation and analysis (Figs. 3.2, 3.3); 2) integration of data from thin sections and slabs (Fig. 3.4); 3) error estimation of scale-integrated data (Fig. 3.5); and 4) area (2D) to volume (3D) corrections. Data is shown for each step in this process (Figs. 3.3, 3.4, 3.5) to reveal different properties of olivine crystal populations in intrusive coherent kimberlite rocks.

### 3.3.3 Crystal size distributions (CSDs)

Crystals change in size, shape, and abundance due to melting, transport, crystallization, and eruption. Therefore, these crystal properties can portray petrologic information indicative of geologic processes. One way to characterize these properties is with a crystal size distribution (CSD). The CSD of a rock is the number of crystals of a mineral per unit volume within a series of defined size intervals (after Higgins, 2006). Crystal size distributions have been used to understand nucleation and growth rates of crystals (Cashman and Marsh, 1988; Cashman, 1990; Peterson, 1990), residence time in magma chambers (Mangan, 1990; Armienti et al., 1994), and the effects of physical processes such as crystal-settling (Bindeman, 2003) and fragmentation (Allen and McPhie, 2003; Bindeman, 2005). There are many ways to characterize crystal size distributions (e.g., semi-logarithmic, log-log plots), each with emphasis placed on different aspects of the crystal population (Higgins, 2000). In this study, we use crystal

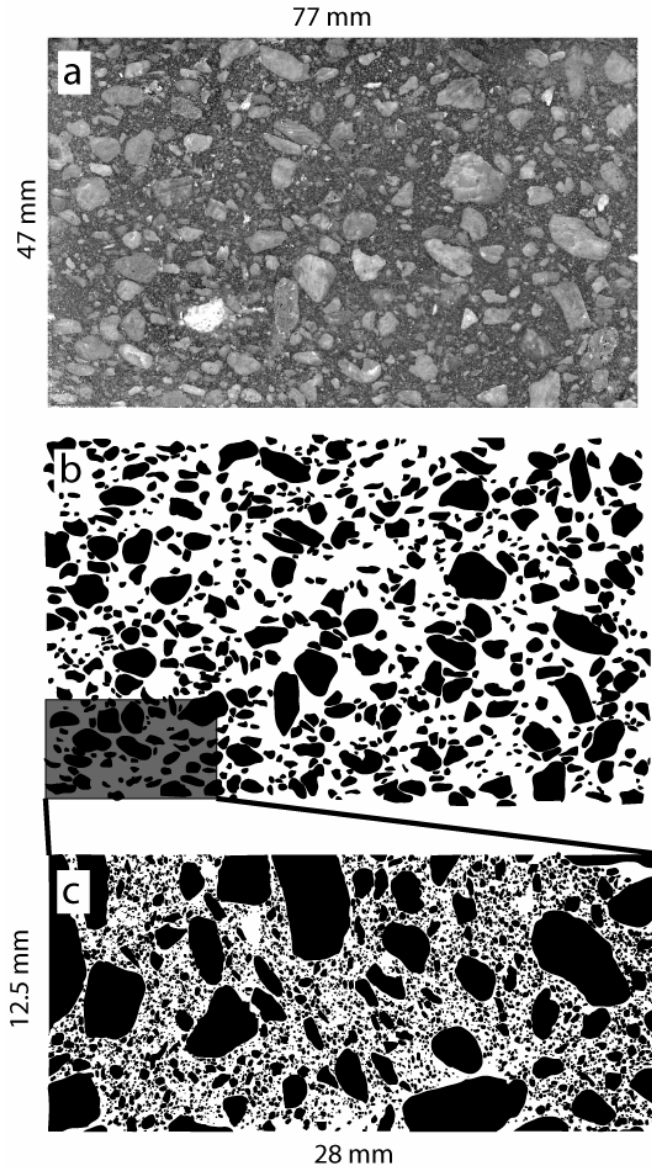


**Figure 3.3:** Digital scan of polished slab (a) and manual tracings of all particles (black) in polished slab (b) and of thin section (c) for sample CK04 from Figure 3.2. Data collected from traced images of thin sections (c; Table 1) and polished slabs (b; see Table 3.2) are integrated by normalizing observations made at the thin section scale (12.5mm x 28 mm) to those made at the slab scale (47mm x 77 mm; Table 3.3).

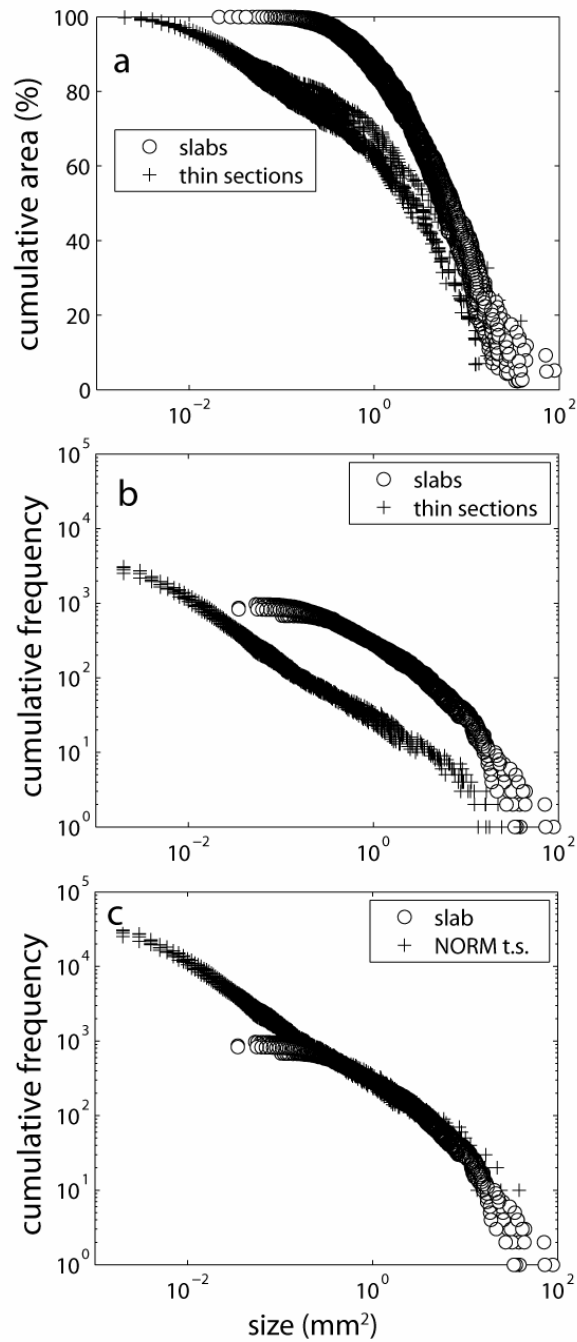


**Figure 3.4:** Plots of two-dimensional olivine crystal size data from thin sections (+; Table 3.1) and polished slabs (○; Table 3.2) of kimberlite: (a) cumulative area % vs. size (mm<sup>2</sup>); (b) cumulative frequency vs. size (mm<sup>2</sup>); (c) cumulative frequency vs. size (mm<sup>2</sup>) for combined dataset produced by normalization of thin sections to the slab scale (see Appendix 8.2).

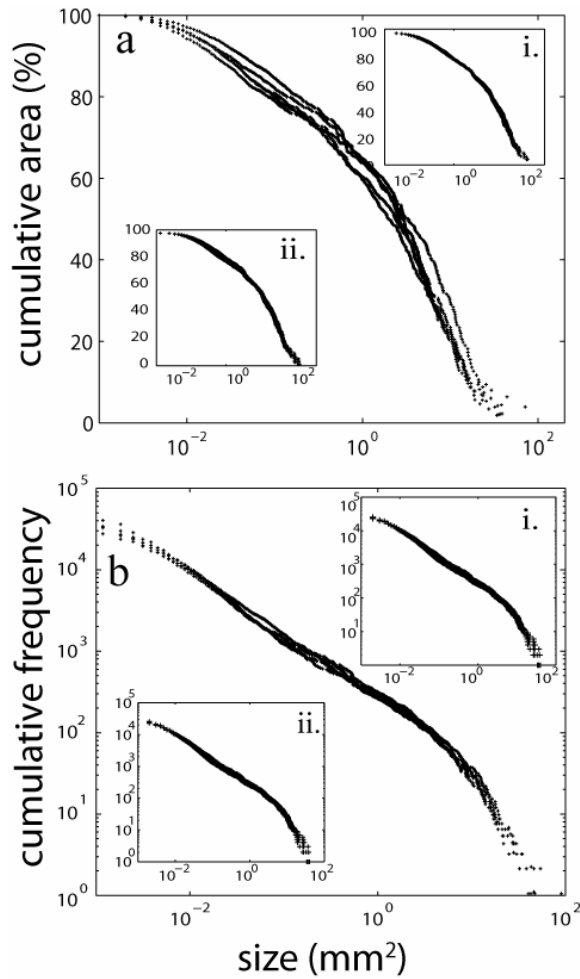


**Figure 3.5:** Scale-integrated and truncated 2D olivine crystal data plots (+; Table 3): (a) cumulative area % vs. size ( $\text{mm}^2$ ); (b) cumulative frequency vs. size ( $\text{mm}^2$ ). Insets to each figure show: (i) variations based on multiple tracings of 1 sample, and (ii) variations caused by different threshold values and normalization factors in image analysis (see Appendix 8.2).

size distributions (CSDs) to: a) statistically describe the overall populations of olivine crystals in intrusive coherent kimberlite; b) identify possible model equations which can accurately describe the crystal populations; and c) to model the effects of possible kimberlite processes on crystal populations.

### 3.4 Results

The results of this study of olivine crystals in intrusive coherent kimberlite are presented in the following order: a) crystal sizes; b) crystal abundances (frequencies, modal %, and relative abundance ratios); c) crystal shapes; and d) overall distribution characteristics. Representative 2D crystal size data for thin sections and slabs are summarized in Tables 3.1 and 3.2, respectively. Normalized and scale-integrated olivine crystal populations for each sample are shown in Table 3.3, and a representative example of stereologically-corrected data is shown in Table 3.4.

#### 3.4.1 Crystal sizes

All five samples studied have broadly similar crystal size ranges (~0.03 to ~10.0 mm in diameter), and contain olivine crystals in all logarithmic size bins therein (Fig. 3.6). The observed lower size limits were verified by high-resolution SEM analysis of polished thin sections; the smallest detected olivine crystal is ~0.025 mm in diameter. The upper size limits of crystals in different samples range from 8 to 12 mm in maximum diameter (Table 3.3). Maximum diameters and measured areas of olivine crystals each cover approximately 2.5 orders of magnitude (Fig. 3.6).

#### 3.4.2 Crystal abundances (frequencies and modal %)

The total number of crystals observed in thin section (12.5 x 25 mm) vary from 2502-5645 (Table 3.1); the number of normalized and scale-integrated total crystals calculated at the slab scale (47x77 mm) ranged from 24,509 to 39,113 (Table 3.3). These crystal frequencies represent numbers of crystals per measured area ( $n_A$ ; Table 3.4). The ratio of the number of crystals <1 mm to crystals  $\geq$ 1 mm in maximum diameter ranges from 70:1 to 135:1 (Table 3.3). The integrated and normalized data

**Table 3.1:** Summary of 2D olivine\* crystal data in thin sections (12.5x25mm) of coherent kimberlite

sample	freq (n)	ol (n) OL (n)	A <sup>  </sup> (%)	OL (%) ol (%)	maximum diameter range(mm)	best 3D shape			Inman parameter <sup>#</sup>			
						long	inter	short	R <sup>2</sup>	MdΦ	σ	α
CK01 <sup>†</sup>	3723	194.9	48.0	1.9	0.03 - 5.9	2	1.5	1	0.72	3.8	3.6	0.2
CK02 <sup>†</sup>	5359	95.3	54.1	2.3	0.03 - 6.2	1.5	1.5	1	0.73	3.6	3.3	0.3
CK03 <sup>†</sup>	3895	117.1	44.0	1.4	0.03 - 6.5	2	1.4	1	0.48	3.5	3.3	0.7
CK04	2799	129.4	41.8	1.2	0.03 - 9.9	1.5	1	1	0.65	3.5	3.2	0.7
CK05a <sup>‡</sup>	2710	83.7	47.3	1.4	0.02 - 7.8	1.15	1.15	1	0.68	3.4	3.0	0.4
CK05b <sup>‡§</sup>	3080	101.7	44.3	1.4	0.02 - 7.8	1.15	1.15	1	0.72	3.5	3.2	0.4
CK05b2 <sup>§</sup>	3464	114.5	42.9	1.4	0.03 - 7.9	1.5	1	1	0.70	3.6	3.2	0.7
CK05b3 <sup>§</sup>	3361	111.0	43.3	1.4	0.03 - 7.9	1.5	1	1	0.77	3.6	3.3	0.7
CK05b4 <sup>§</sup>	3080	101.7	44.3	1.4	0.03 - 7.8	2	1.4	1	0.56	3.5	3.2	0.7
CK05b5 <sup>§</sup>	2878	94.9	44.8	1.4	0.03 - 7.8	1.5	1	1	0.85	3.4	3.2	0.6

Note: 3D aspect ratios and correlation coefficients obtained using CSDSlice (Jerram and Morgan, 2006)

\* ol = olivine < 1 mm; OL = olivine ≥ 1 mm

† Replicate samples from a single dyke

‡ Duplicate tracings of a single sample

§ Duplicate processing of single, digitized tracing

|| Olivine content as area (%) of slab

# MdΦ = Median phi size (-log<sub>2</sub>(d)); σ = sorting efficiency =  $\frac{(\phi_{84}) - (\phi_{16})}{2}$ ; α = skewness =  $\frac{(\phi_{84}) + (\phi_{16}) - Md\phi}{\sigma}$

**Table 3.2:** Summary of 2D olivine\* crystal data in slabs (47x77mm) of coherent kimberlite

sample	freq (n)	ol (n) OL (n)	A <sup>  </sup> (%)	OL (%) ol (%)	maximum diameter range(mm)	best 3D shape			Inman parameter <sup>#</sup>			
						long	int	short	R <sup>2</sup>	MdΦ	σ	α
CK01 <sup>†</sup>	857	1.7	39.5	6.2	0.24 - 12.4	1.1	1.1	1.0	0.74	0.31	1.7	-2.5
CK02 <sup>†</sup>	768	1.3	35.1	7.1	0.23 - 9.6	1.0	1.0	1.0	0.80	0.26	1.4	-2.7
CK03 <sup>†</sup>	763	1.3	36.3	7.1	0.25 - 11.6	1.2	1.0	1.0	0.67	0.25	1.3	-2.9
CK04	793	1.1	33.8	8.1	0.17 - 8.3	1.0	1.0	1.0	0.69	0.28	1.7	-2.7
CK05a <sup>‡</sup>	659	0.6	36.9	12.5	0.33 - 8.1	1.2	1.2	1.0	0.71	-0.04	1.2	-3.4
CK05b <sup>‡§</sup>	721	1.0	36.8	11.3	0.17 - 9.7	1.2	1.2	1.0	0.72	0.15	1.2	-3.3
CK05b2 <sup>§</sup>	770	1.2	34.9	9.8	0.17 - 9.8	1.3	1.3	1.0	0.58	0.27	1.3	-3.2
CK05b3 <sup>§</sup>	751	1.1	35.7	10.7	0.17 - 9.7	1.2	1.2	1.0	0.64	0.23	1.3	-3.3
CK05b4 <sup>§</sup>	704	1.0	36.2	11.1	0.17 - 9.7	1.2	1.2	1.0	0.72	0.15	1.3	-3.4
CK05b5 <sup>§</sup>	680	0.9	37.9	12.7	0.17 - 9.6	1.2	1.2	1.0	0.67	0.10	1.3	-3.5

Note: 3D aspect ratios and correlation coefficients obtained using CSDSlice (Jerram and Morgan, 2006)

\* ol = olivine < 1 mm; OL = olivine ≥ 1 mm

† Replicate samples from a single dyke

‡ Duplicate tracings of a single sample

§ Duplicate processing of single, digitized tracing

|| Olivine content as area (%) of slab

# MdΦ = Median phi size (-log<sub>2</sub>(d)); σ = sorting efficiency =  $\frac{(\phi_{84}) - (\phi_{16})}{2}$ ; α = skewness =  $\frac{(\phi_{84}) + (\phi_{16}) - Md\phi}{\sigma}$

**Table 3.3:** Summary of normalized 2D olivine\* crystal data in slabs (47x77mm) of coherent kimberlite

sample	freq (n)	$\frac{ol(n)}{OL(n)}$	A <sup>  </sup> (%)	$\frac{OL(\%)}{ol(\%)}$	maximum diameter range(mm)	best 3D shape				Inman parameter <sup>#</sup>		
						long	int	short	R <sup>2</sup>	MdΦ	σ	α
CK01 <sup>†</sup>	37358	134.8	50.0	2.0	0.02 - 12.4	1.00	1.00	1.00	0.79	3.8	3.3	0.3
CK02 <sup>†</sup>	39113	138.2	48.2	1.6	0.02 - 9.6	1.00	1.00	1.00	0.76	3.6	3.5	0.5
CK03 <sup>†</sup>	31947	108.8	48.1	1.9	0.03 - 11.6	1.00	1.00	1.00	0.86	3.5	3.3	0.5
CK04	30659	101.2	46.7	1.6	0.03 - 8.3	1.00	1.00	1.00	0.84	3.5	3.1	0.3
CK05a <sup>†**</sup>	24509	72.6	51.2	1.8	0.02 - 8.1	1.00	1.00	1.00	0.79	3.3	2.9	0.3
CK05b <sup>†§</sup>	27814	92.3	49.9	1.9	0.03 - 9.7	1.00	1.00	1.00	0.74	3.5	3.1	0.3
CK05b2 <sup>§</sup>	31259	107.9	47.0	1.9	0.03 - 9.8	1.20	1.00	1.00	0.75	3.6	3.2	0.4
CK05b3 <sup>§</sup>	30342	101.5	48.3	1.9	0.03 - 9.7	1.20	1.00	1.00	0.74	3.6	3.1	0.4
CK05b4 <sup>§</sup>	27802	94.9	49.2	1.9	0.03 - 9.7	1.00	1.00	1.00	0.76	3.5	3.1	0.3
CK05b5 <sup>§</sup>	25590	87.4	51.4	1.9	0.03 - 9.6	1.15	1.15	1.00	0.75	3.4	3.1	0.2
CK05c <sup>**</sup>	27187	80.6	53.1	1.6	0.02 - 8.1	1.00	1.00	1.00	0.77	3.3	2.8	0.2

Note: 3D aspect ratios and correlation coefficients obtained using CSDSlice (Jerram and Morgan, 2006)

\* ol = olivine < 1 mm; OL = olivine ≥ 1 mm

† Replicate samples from a single dyke

‡ Duplicate tracings of a single sample

§ Duplicate processing of single, digitized tracing

|| Area (%) of slab comprised of olivine

# MdΦ = Median phi size (-log<sub>2</sub>(d)); σ = sorting efficiency =  $\frac{(\Phi_{84}) - (\Phi_{16})}{2}$ ; α = skewness =  $\frac{(\Phi_{84}) + (\Phi_{16}) - Md\Phi}{\sigma}$

\*\* Duplicate normalization factors of a single sample

**Table 3.4:** Representative data from manual digitization of olivine grains and corresponding stereologically corrected data from polished slab (47x77mm) of coherent kimberlite

(Φ)	d* (mm)	A (mm <sup>2</sup> )	A <sup>†</sup> (%)	n <sub>A</sub> <sup>‡</sup>	n <sub>V</sub> <sup>§</sup>	ln N <sup>  </sup>
-4	≥ 16	0.0	0.0	0	0	--
-3	≥ 8	44.2	1.2	1	6.47E-05	-11.45
-2	≥ 4	378.1	10.4	22	0.00281	-6.98
-1	≥ 2	497.0	13.7	87	0.021	-4.28
0	≥ 1	355.7	9.8	288	0.137	-1.71
1	≥ 0.5	164.1	4.5	630	0.575	0.42
2	≥ 0.25	146.2	4.0	2130	4.07	3.07
3	≥ 0.125	116.1	3.2	5240	19.4	5.32
4	≥ 0.0625	82.4	2.3	12260	90.3	7.55
5	≥ 0.0312	19.2	0.5	9550	105	8.39
6	≥ 0.0156	5.9	0.2	7150	166	9.55
total		1808.8	50.0	37358		

Note: Values of n<sub>V</sub> and ln N calculated with CSDCorrections<sup>TM</sup> 1.3 (Higgins, 2000)

\* denotes major axis length (d) of enclosing ellipse

† area % of slab

‡ n<sub>A</sub> denotes frequency of crystals normalized to slab scale.

§ n<sub>V</sub> denotes crystals per unit volume after stereological corrections

|| N denotes crystals per unit volume per bin width, or population density

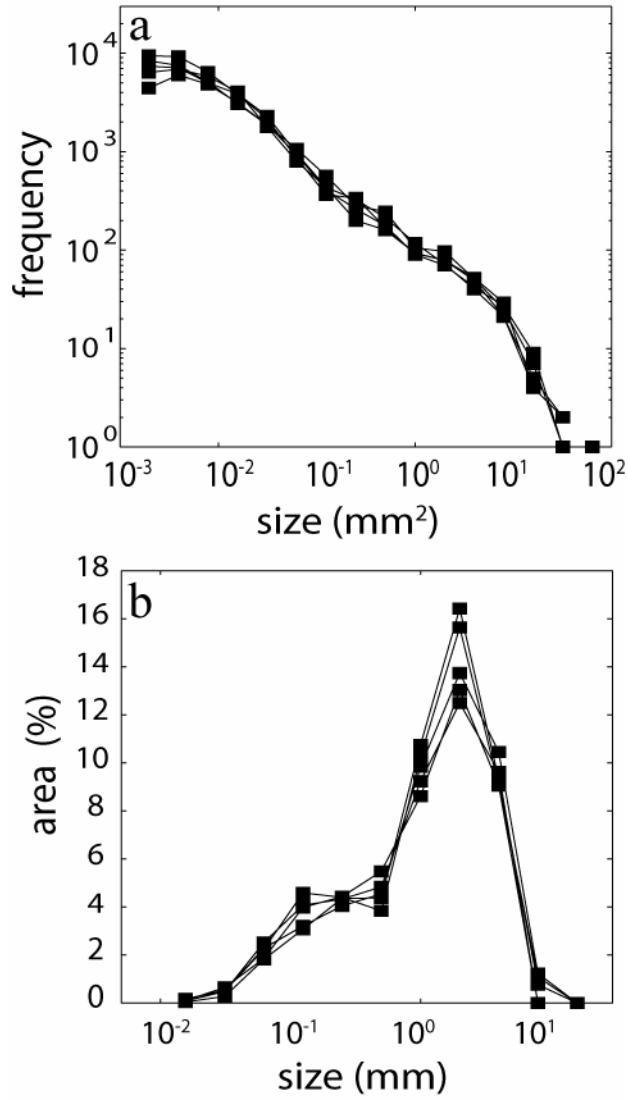


**Figure 3.6:** Scale-integrated, truncated and binned ( $\log_2$ ) two-dimensional olivine crystal data plots (Table 3.4): (a) frequency vs. size (area; mm<sup>2</sup>); (b) area (%) vs. size (diameter; mm).

show olivine crystals to comprise 46.7-51.2 % by area of the rock samples (Table 3.3). The ratio of the modal area % of olivine crystals  $>1$ :  $\leq 1$  mm in maximum diameter ranges from 1.6:1 to 2:1 (Table 3.3).

### 3.4.3 Crystal shapes

More than 95% of crystal shape intersections in 2D are convex ellipses with aspect ratios between 1:1 and 2:1 (Fig. 3.7a). Crystal shapes cannot be simply characterized as ‘circular’ or ‘angular’ by size (Fig. 3.7b,c). However, ~80% of the crystals with less ‘circular’ shapes (circularity  $<0.5$ ; Fig. 3.7b) are smaller than  $0.5 \text{ mm}^2$ , and ~85% of the crystals with irregular or more angular boundaries ( $P/P_{\text{eac}} >1.4$ ; Fig. 3.7c) are smaller than  $0.5 \text{ mm}^2$ . Best-estimate ellipsoid (3D) geometries range from 1.5:1:1 to 1:1:1 for restricted size ranges (Fig. 3.7d), but as an entire population olivine crystals are best-approximated with an equant axial ratio (1:1:1; Table 3.3).

### 3.4.4 Distribution characterization

In addition to physical properties of individual olivine crystals (i.e. sizes, shapes), crystal populations can also be described by attributes of their whole crystal size distribution. In this section, we a) calculate distribution parameters for the whole olivine population, and b) describe crystal populations using model equations fit to CSD’s.

#### Distribution parameters

Common metrics for characterizing the entire size distributions of particles include a central value (e.g., median), the spread or dispersion of data (e.g., standard deviation), and distribution symmetry (e.g., skewed vs. symmetrical). Variations of these metrics commonly used in sedimentology and volcanology are Inman parameters (Inman, 1952) of median size ( $Md\phi$ ), sorting efficiency ( $\sigma$ ), and skewness ( $\alpha$ ) of the particle population:

$$Md\phi = -\log_2[\text{median}(d)] \quad (3.1)$$

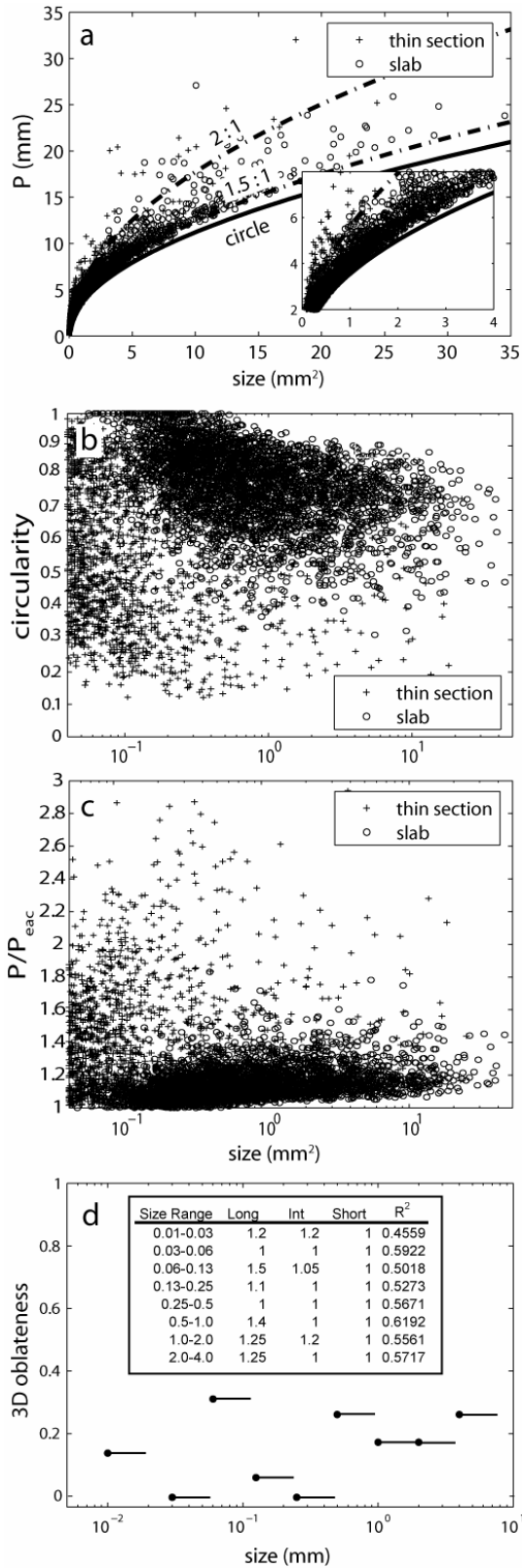


**Figure 3.7:** Olivine crystal shapes as: (a) perimeter (mm;  $P$ ) vs. area ( $\text{mm}^2$ ;  $A$ ) for olivine crystals measured in slabs ( $\circ$ ) and thin sections ( $+$ ) from five samples. Reference curves for perfect circles (solid line), and ellipses with 1.5:1 and 2:1 aspect ratios (dashed lines) are shown. Inset shows expanded view of small sizes; (b) circularity vs. size ( $\text{mm}^2$ ) as a measure of particle ‘round-ness’; (c) Perimeter ( $P$ ) / [Perimeter of equivalent area circle ( $P_{\text{eac}}$ )] vs. size ( $\text{mm}^2$ ) as a proxy for particle ‘roughness’. Olivine populations (b,c) have been truncated to remove the effect of pixilation on shape assessment of the smallest crystals observed at each scale of observation; (d) “3D” oblateness vs. size (mm) for sample CK01, where oblateness =  $1 - (\text{long axis}/\text{short axis})$ , using short : intermediate : long axial approximations found using CSDSlice™ (Morgan and Jerram, 2006). Inset shows best-fit axial ratios and corresponding low-correlation  $R^2$  values for each size interval.

$$\sigma = \frac{(\phi_{84}) - (\phi_{16})}{2} \quad (3.2)$$

$$\alpha = \frac{(\phi_{84}) + (\phi_{16}) - Md\phi}{\sigma} \quad (3.3)$$

where  $\phi_{84}$  and  $\phi_{16}$  are the crystal sizes for which 84% and 16%, respectively, of the total area of the particle population are “coarser-than” in a cumulative area % vs. size plot (e.g., Fig. 3.5a). These parameters can be meaningfully applied to olivine crystal populations because they a) evaluate the entire measured particle population, b) minimize the impact of outlier particle sizes, and c) provide a way to characterize aspects of a entire population (i.e., mid-point, spread, symmetry) of particles with a single number. These numbers may be used to compare olivine crystal populations with subsequent data collected from other occurrences of intrusive or extrusive coherent kimberlite or from olivines in pyroclastic and resedimented kimberlite to assess volcanic and related processes. Inman parameters as measured from normalized, scale-integrated 2D olivine data show limited ranges as follows:  $Md\phi = 3.3-3.8$ ;  $\sigma = 2.8-3.5$ ;  $\alpha = 0.3-0.5$  (Table 3.3).

#### *Model equations fit to CSDs*

Particle populations may also be described using model equations fit to CSD's (e.g., Cashman and Marsh, 1988; Higgins, 2002). This provides a means by which size distributions of crystals can be quantitatively compared and investigated (e.g., Cashman, 1990; Mock, 2003).

Olivine CSD's are shown as semi-log and log-log plots of population density vs. size for each of the 5 samples are shown in Figure 3.8a and Figure 3.8b, respectively. Olivine crystal populations in this study reveal a linear trend in a log-log plot CSD (Fig. 3.8b) across two orders of magnitude of crystal sizes (0.06 – 4 mm). It is implicit from this data that olivine crystals appear to follow a power law such as the following:

$$N_v(X \geq x) = \lambda x^{-D} \quad (3.4)$$

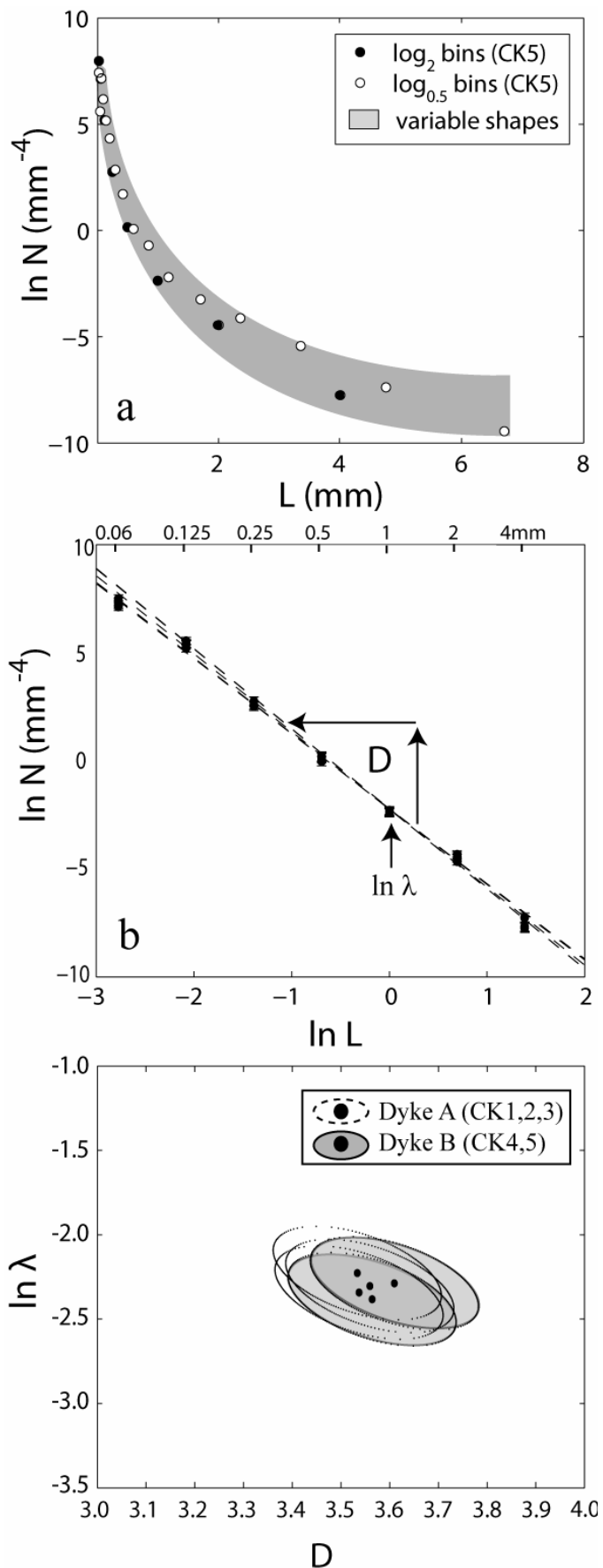


**Figure 3.8:** Crystal size distributions (CSDs) of normalized, truncated, binned and stereologically-corrected olivine crystal data: (a) classic CSD of  $\ln$  population density ( $N$ ; number/mm<sup>-4</sup>) vs. diameter ( $L$ ; mm) with varying bin sizes ( $\bullet, \circ$ ) and shape assumptions (shaded region).  $\ln N$  is calculated using CSDCorrections; approximate shape assumptions calculated from thin section intersection data in CSDSlice<sup>TM</sup> (Morgan and Jerram, 2006; see Appendix 8.2); (b) fractal diagram:  $\ln N$  vs.  $\ln L$  with best-fit power-law lines. Error bars are smaller than the figure symbols; (c) model parameters  $\ln \lambda$  (y-value at  $\ln L = 0$ ) vs.  $D$  (slope) for best-fit power-law lines in (b) from spatially-separate dykes (A,B) at A154N (see Fig. 3.1). Co-variance envelopes are shown to enclose the sample variance within and between individual dykes, and collectively define a ‘type’ description of olivine in coherent kimberlite.

where  $N_v (X \geq x)$  is the number of fragments with a diameter greater than  $x$ ,  $\lambda$  is an arbitrary constant and  $D$  is the power-law exponent. Power-law equations have been increasingly employed to describe particle populations (Carey et al., 2000; e.g., Barnett, 2004; Walters et al., 2006a). If the cumulative particle size frequency of a population of crystals is plotted against particle diameter on a log-log plot, an apparent power-law distribution would appear as a straight line with a slope of  $D$ .

However, it is difficult to confirm that a set of observations truly obeys a power-law distribution. Few sets of observations from nature can truly claim scale-invariance (Mandelbrot, 1982); we are either limited to a few scales of observation by technology or because natural phenomena only occur over a few scales of observation. Rigorous tests can be used to assess whether the data are permissive of a power-law distribution (e.g., Goldstein et al., 2004; e.g., Clauset et al., 2007), but require sufficient orders of magnitude. However, the size range of olivine crystals in kimberlite noted above is inherently inadequate for rigorous tests of power-law affinity; there are many two-parameter model equations (e.g., gamma, power, log-normal) which appear similar over small ranges of observation (Bonnet et al., 2001; Clauset et al., 2007).

Here, we use power-law equations to approximate, rather than describe, olivine crystal populations. Best-fit power-law equations are found (see Appendix 8.2) for each sample array and plotted in Figure 3.8b. The tails of cumulative frequency vs. size plots are usually flattened at the finest sizes due to the inability to visualize or capture all of the smallest size fraction of crystals, and approach the vertical at the coarsest sizes, due to the relatively fewer numbers of large crystals. However, data are linear for at least 2 orders of magnitude, and thereby adhere to equation (1). Calculated exponents ( $D$ ; slope of best-fit line) of the best-fit model equations range from 3.53 to 3.61; intercepts of the best-fit model equations ( $\log \lambda$ ; where x-axis = 0) range from -2.23 to -2.88. Error estimates for power-law fits to the CSDs are shown in Figure 3.8b, Figure 3.8c, and Table 3.5, and discussed in Appendix 7.3.1. Figure 3.8c shows 95% confidence envelopes

**Table 3.5:** Summary of best-fit parameters and root mean standard error in fitting power laws to olivine crystal distributions\*

Sample	D <sup>#</sup>	ln $\lambda$ <sup>**</sup>	RMSE <sup>††</sup>
CK01 <sup>†</sup>	3.53	-2.23	0.16
CK02 <sup>†</sup>	3.61	-2.88	0.27
CK03 <sup>†</sup>	3.56	-2.30	0.31
CK04	3.54	-2.34	0.28
CK05a <sup>‡  </sup>	3.56	-2.38	0.26
CK05b <sup>‡§</sup>	3.52	-2.17	0.27
CK05b2 <sup>§</sup>	3.56	-2.26	0.28
CK05b3 <sup>§</sup>	3.55	-2.23	0.29
CK05b4 <sup>§</sup>	3.52	-2.18	0.26
CK05b5 <sup>§</sup>	3.50	-2.15	0.24
CK05c <sup>  </sup>	3.54	-2.11	0.35

\* Crystal population density (N): the # of crystals per unit volume per bin width

† Replicate samples from a single dyke

‡ Duplicate tracings of a single sample

§ Duplicate processing of single, digitized tracing

|| Duplicate normalization factors (eq. A8.2.1) of a single sample

# Slope (D) of best-fit power-law equation (eq. 8.2.4) to olivine data

\*\* Population density-intercept ( $\lambda$ ) of best-fit power-law equation (eq. 8.2.4)

†† Root-mean standard error (see Appendix 8.2)

on the model parameters ( $D, \lambda$ ), defining all possible parameter relationships for observed crystals.

All samples show statistical equivalence: samples within and between dykes of coherent kimberlite are statistically equivalent (Fig. 3.8c). The total area enclosed by covariance envelopes from the two dykes represents a parameter range for olivine in coherent kimberlite at A154N at Diavik (Fig. 3.8c). The variance on the model parameters for samples within a single dyke (e.g.,  $\sigma_{CK4,5}^2$ ) are smaller than variance between dykes ( $\sigma_{CK1,2,3}^2 : \sigma_{CK4,5}^2$ ). The variance in parameters for all samples ( $\sigma_s^2$ ) is greater than the variance attributed to analytical methods ( $\sigma_a^2$ ) (e.g., Table 3.5).

### 3.5 Discussion

In this section, I summarize results, discuss implications of the results on previous understandings, and identify new attributes of olivine CSDs in kimberlite revealed by this study. I then discuss possible uses for olivine CSDs.

#### 3.5.1 Olivine crystal properties

Olivine crystals in this study show the following properties: a) limited size range covering no more than 3 orders of magnitude (0.03 – 10 mm in diameter); b) total modal crystal content ranging from 46.7-51.2%; c) modal % dominance by crystals >1 mm; d) frequency dominance by crystals <1 mm; e) equant-axial geometries with no distinct external morphology with respect to size; and f) apparent characteristic ranges of CSD statistical parameters (i.e. power-law exponents and Inman parameters). The data presented here correspond well to previous assessment of size ranges, the total crystal content (area %), and general shapes of olivine crystals in kimberlite based on thin section study (Clement, 1982; Apter et al., 1984; Shee, 1985), and are in general accordance with conventional understanding of intrusive coherent kimberlite, synonymous with ‘hypabyssal kimberlite’ (Mitchell, 1986).

Olivine crystals in the present study also reveal aspects of olivine crystal populations which differ from previous assessments. Histograms of olivine crystal

populations show a positively-skewed, normal distribution with a much higher ratio of small olivines (ol <1 mm) to large olivines (ol >1 mm) (~100:1) than measured in thin sections from kimberlite dykes in South Africa (13:1 to 19:3; Clement, 1982; Shee, 1985). In addition, the relative ratios between olivine crystals of different sizes reveal an area % dominance by crystals >1 mm (1.6:1 to 2:1), different from the approximate 1:1 modal distribution of olivine sub-types that correspond to specific size ranges ('macrocrysts'  $\geq 1$  mm  $\geq$  'phenocrysts') inferred by Shee (1985). Moreover, our data indicate that olivine shapes are too diverse and complex within any given size range to be easily described by 'anhedral', 'round', 'angular' or 'euhedral'. Olivine crystal shapes are best-described as convex and approximately axial-equant (short : int : long = 1:1:1) ellipsoids in both 2D and 3D geometries, across all sizes (0.03 – 12 mm).

Furthermore, this study reveals several new characteristics of olivine crystal populations in intrusive coherent kimberlite. Firstly, olivine crystal populations are consistent with a power-law distribution over at least 2 orders of magnitude. Large changes in the distributions of particles are required to change the value of power-law exponents, or *D*-values (Kaminski and Jaupart, 1998). In this sense, power-law exponents from best-fit equations for binned data from relevant size ranges can be utilized for comparative purposes. Thus, best-fit power-law exponents can approximate crystal populations in coherent rocks (e.g., Armienti and Tarquini, 2002) which could be compared to power-law exponents from cogenetic fragmental or pyroclastic rocks (e.g., Chapter 2; Kaminski and Jaupart, 1998; Walters et al., 2006). Secondly, though modal abundances (e.g., 46.7 – 51.4%) and crystal frequencies (e.g., 24,000 – 39,000) measured in 2D intersections vary, power-law exponents [i.e., slopes (*D*)] calculated for olivine crystal populations are statistically equivalent (Fig. 3.8c; Table 3.5), suggesting CSD slopes are independent of olivine crystal abundance. This allows us to define a characteristic slope for the population of olivines in coherent kimberlite dykes at A154N ( $D = 3.55 \pm 0.21$ ), despite crystal addition and removal processes such as crystal concentration or hydraulic sorting. Thirdly, the statistical equivalence (i.e., best-fit model parameters, Inman parameters) of olivine crystal populations from samples within dykes and statistical similarity between dykes at A154N suggest that spatially-separate dykes can contain similar populations of olivine crystals, and that a limited range of power-law

parameters may be descriptive of all olivine crystal populations in coherent kimberlite. Fourthly, our data show that olivine CSDs are described by a single power-law slope; there are no clear breaks in slope for the distribution in either semi-logarithmic or log-log CSD plots. Study of CSDs from other magma types has shown that the mixing of crystal populations due to new nucleation, magma batch mixing, or assimilation of xenocrysts are indicated by breaks in slope in either semilog or log-log CSD plots (Marsh, 1988; Salisbury et al., 2008). The lack of slope breaks in the CSD for olivine in intrusive coherent kimberlite suggests the observed population represents a single population of olivine crystals with a shared paragenesis, and is not the end-product of a combination of two populations of olivine.

### 3.5.2 Olivine crystals and magmatic geologic processes

Observed CSDs for olivine crystals in intrusive coherent kimberlite could reflect a variety of processes: crystal growth or re-crystallization within the mantle, mechanical disaggregation, and/or chemical corrosion by the kimberlite melt, collision and abrasion during transport, or crystallization of olivine from the melt during transport and eruption. In addition, hydraulic sorting and phase-separation processes during emplacement can affect the size distribution of olivine crystals within one phase of kimberlite. These processes would affect the slope and/or intercepts of CSD curves in semi-logarithmic or bi-logarithmic plots.

To assess the potential impact of some processes upon olivine CSDs in intrusive coherent kimberlite, one of the measured CSDs from this study (CK04) was used to represent a starting population and the hypothetical effects of example processes were calculated as model populations. The results are shown in Fig. 3.9a, b, and c.

Filter-pressing of a crystal-rich kimberlite magma, in which the liquid fraction of the ascending magma is efficiently strained out of the crystal fraction, might be reflected in a vertical movement of the CSD in which slope and maximum size remains constant, but the intercept shifts up and down to reflect relative degrees of ‘concentration’ (Fig.

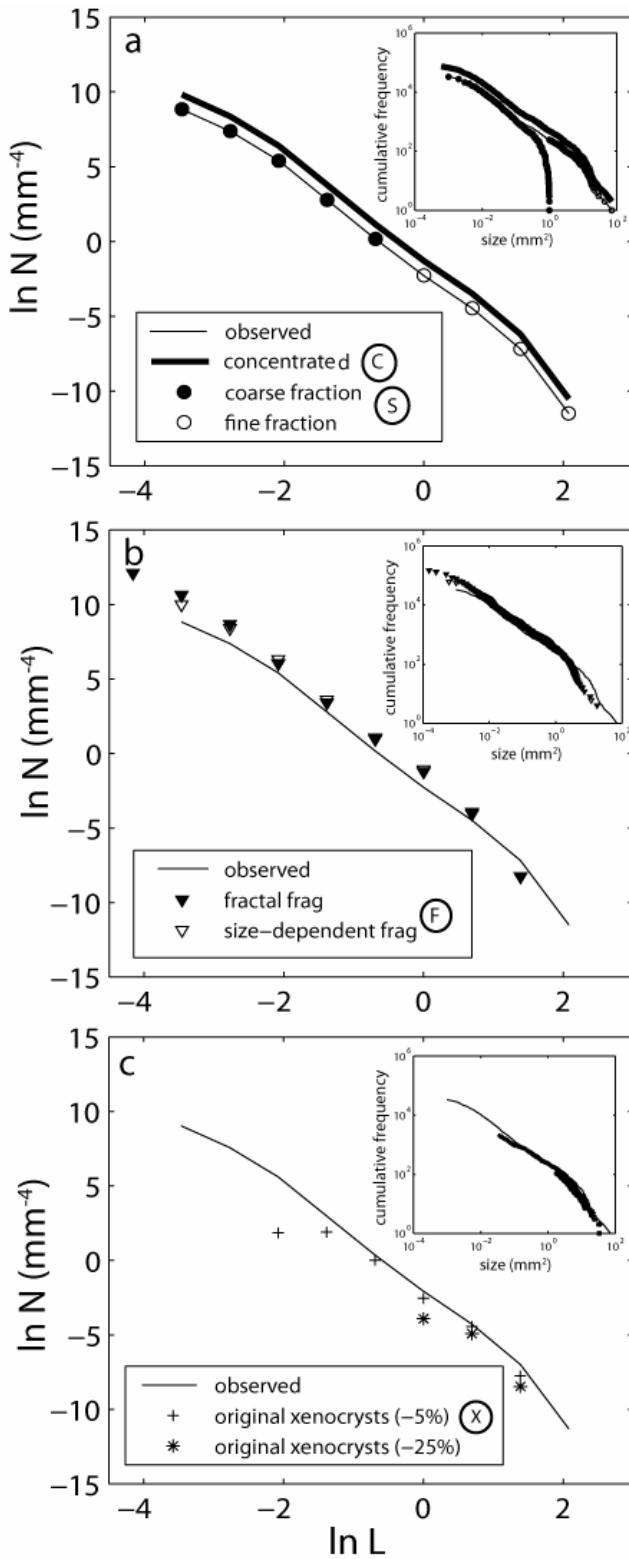


**Figure 3.9:** Theoretical geological processes and their impact upon olivine crystal size distributions (CSDs) from intrusive coherent kimberlite. Results of the following processes are plotted as  $\ln N$  vs.  $\ln L$  and cumulative frequency vs. size ( $\text{mm}^2$ ; insets): (a) perfect hydraulic sorting of crystals  $<$  or  $> 1 \text{ mm}^2$  (S), and crystal concentration due to filter-pressing or sieving of liquid fraction (C); (b) closed-system fragmentation using two different fragmentation models (F): scale-invariant fragmentation and scale-dependent fragmentation; (c) removal of 5% (X) and 25% of volume of olivine crystals from starting population to recover possible original xenocryst size distribution.

3.9a). Perfectly-efficient hydraulic sorting or flow-differentiation of intruding kimberlite magma could lead to local vertical and/or lateral variations in CSDs within dykes or sheets (cf. Field et al., 2008), resulting in either truncations of coarse or fine size fractions in the CSD (Fig. 3.9a).

Closed-system fragmentation of olivine crystals (within the magma) could occur during turbulent, fully-fluidized transport (Wilson and Head, 2003; Sparks et al., 2006) of kimberlite magma. In Figure 3.9b, the effects of two different styles fragmentation are illustrated: a) a scale-invariant or ‘fractal’ fragmentation model which assumes that olivine crystals break into the same number of equal-size fragments ( $n = 4$ ), independent of the starting crystal size (Turcotte, 1986); and b) a scale-variant model assumes that larger crystals are inherently more fragile (i.e., more cracks, mineral/fluid inclusions, etc.) than smaller crystals. Each fragmentation model reduces the largest size of olivine crystal expected, but has different net effects on the total number of small olivine crystal fragments produced, and therefore different slopes and intercepts in classic CSD plots (Fig. 3.9b).

New olivine crystallization from a saturated melt could also occur on olivine crystals in kimberlite magma; based on observations of olivine crystals in intrusive coherent kimberlite at Diavik, Brett et al. (2009) show that both coarse ( $>1$  mm), round olivine crystals, and small ( $<1$  mm), euhedral olivine crystals are comprised of a newly-crystallized olivine rim surrounding a core. If surface area-controlled crystallization is assumed, observed rim thicknesses suggest that the total volume of olivine crystallized during transport is substantially lower ( $\leq 5\%$ ) than commonly assumed (e.g.,  $\sim 25\%$ ), and that crystallization is dominantly heterogeneous (Brett et al., 2009). Starting with an observed population of olivine crystals, we remove 5% (expected) and 25% (hypothetical) of the population volume to recover two possible starting populations of xenocrysts (Fig. 3.9c).

These processes are likely to change the shape of the olivine CSD. In the case of concentration, sorting and fragmentation, CSDs retain approximately linear trends in log-log space; theoretical effects of each process on power-law parameters are shown in Figure 3.10.

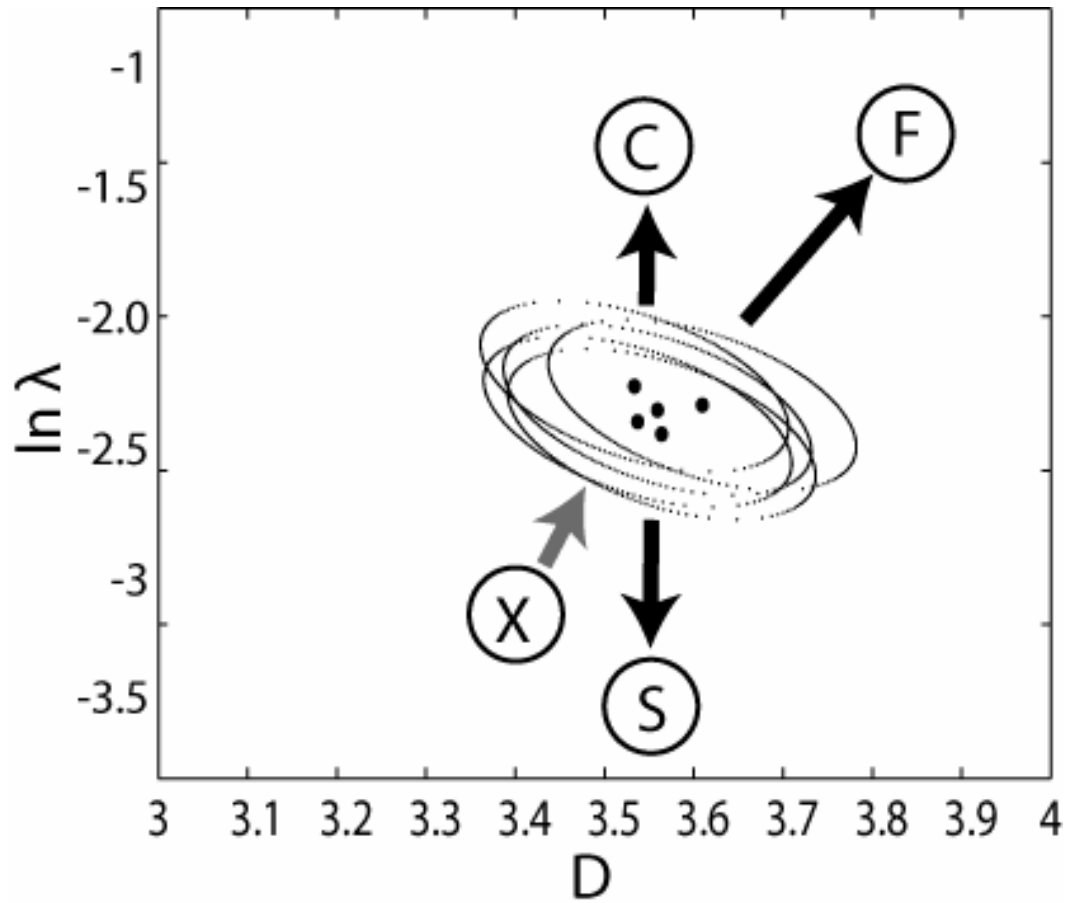


**Figure 3.10:** Power-law parameters [slope (D); y-intercept at  $x = 0$  ( $\ln \lambda$ )], for olivine from A154N, Diavik, with enclosing co-variance envelope. Arrows indicate general expected changes in power-law fit parameters due to different geologic processes described in Figure 3.9 (i.e. S, C, F, X).

### 3.5.3 Further applications for olivine crystal data

Fragmentation of olivine crystals can also occur during eruption of kimberlite melts. If we assume that the narrow range of slopes obtained from the present study correspond to other populations of olivine crystals in coherent kimberlite, then the crystal size distribution of olivine crystals in intrusive kimberlite magma (un-erupted) can be compared to best-fit power-law equations for crystal size distributions of pyroclastic (erupted) kimberlite (e.g., Chapter 2) to determine how much the solid particles in the magma break up during volcanic eruption. In addition, typical kimberlites such as those investigated in this study also have the potential to carry significant quantities of diamond. Diamond has similar physical properties to olivine, and has been proposed to be an important proxy for diamond (Field et al., 2008; Scott Smith, 2009b). The data and methodology presented here can be used to assist in understanding diamond distributions within and between different phases of intrusive coherent kimberlite and in extrusive volcanic processes.

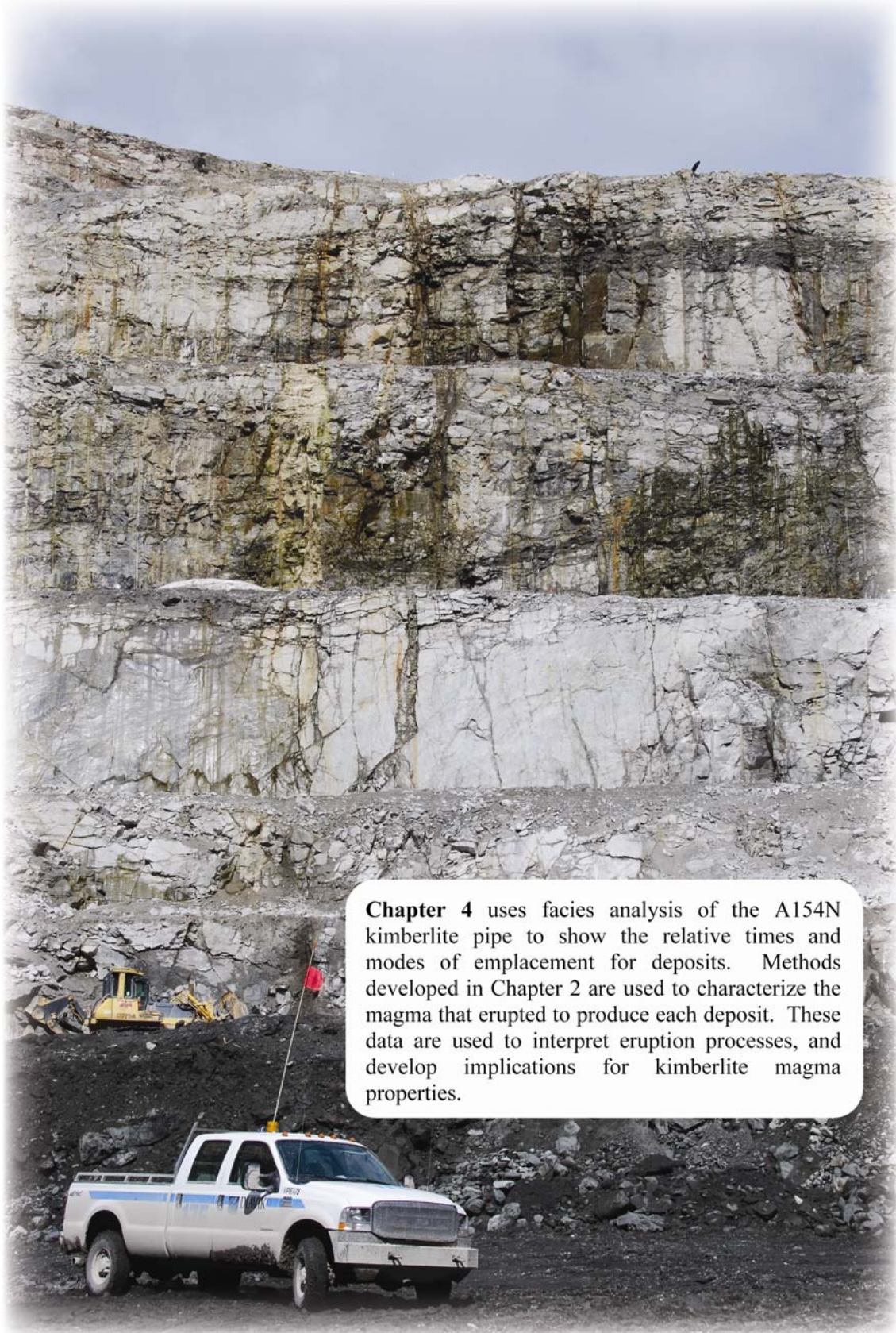
### 3.6 References

- Allen, S.R., and McPhie, J. (2003) Phenocryst fragments in rhyolitic lavas and lava domes. *Journal of Volcanology and Geothermal Research*, 126, 263-283.
- Apter, D.B., Harper, F.J., Wyatt, B.A., and Smith, B.H.S. (1984) The geology of the Mayeng kimberlite sill complex, South Africa. In J. Kornprobst, Ed. *Kimberlites and related rocks*. Third International Kimberlite Conference, no. 11A, p. 43-58. Elsevier's Development in Petrology series.
- Armienti, P., Pareschi, M.T., Innocenti, F., and Pompilio, M. (1994) Effects of magma storage and ascent on the kinetics of crystal growth. *Contributions to Mineralogy and Petrology*, 115, 402-414.
- Armienti, P., and Tarquini, S. (2002) Power law olivine crystal size distributions in lithospheric mantle xenoliths. *Lithos*, 65(3-4), 273-285.
- Arndt, N.T., Boullier, A.M., Clement, J.P., Dubois, M., and Schissel, D. (2006) What olivine, the neglected mineral, tells us about kimberlite petrogenesis. *eEarth*, 1, 15-21.
- Barnett, W. (2004) Subsidence breccias in kimberlite pipes--an application of fractal analysis. *Lithos*, 76(1-4), 299-316.
- Basson, I.J., and Viola, G. (2004) Passive kimberlite intrusion into actively dilating dyke-fracture arrays: evidence from fibrous calcite veins and extensional fracture cleavage. *Lithos*, 76(1-4), 283-297.
- Bindeman, I.N. (2003) Crystal sizes in evolving silicic magma chambers. *Geology*, 31, 367-370.
- . (2005) Fragmentation phenomena in populations of magmatic crystals. *American Mineralogist*, 90, 1801-1815.
- Bonnet, E., Bour, O., Odling, N.E., Davy, P., Main, I., Cowie, P., and Berkowitz, B. (2001) Scaling of fracture systems in geological media. *Reviews of Geophysics*, 39(3), 347-383.
- Boyd, F.R., and Clement, C.R. (1977) Compositional zoning of olivines in kimberlite from the De Beers Mine, Kimberley, South Africa. *Carnegie Institute Washington Yearbook*, 76, 485-493.
- Brett, R.C., Russell, J.K., and Moss, S. (2009) Origin of olivine in kimberlite: phenocryst or imposter? 9th International Kimberlite Conference Extended Abstract, 9IKC-A-00298, 3.
- Carey, S., Maria, A., and Sigurdsson, H. (2000) Use of fractal analysis for discrimination of particles from primary and reworked jokulhlaup deposits in SE Iceland. *Journal of Volcanology and Geothermal Research*, 104(1-4), 65-80.
- Caro, G., Kopylova, M.G., and Creaser, R.A. (2004) The hypabyssal 5034 kimberlite of the Gahcho Kue cluster, southeastern Slave craton, Northwest Territories, Canada: a granite-contaminated Group-I kimberlite. *Canadian Mineralogist*, 42, 182-207.
- Cashman, K.V. (1990) Textural constraints on the kinetics of crystallization of igneous rocks. In P.E. Ribbe, Ed. *Mineralogical Society of America Reviews in Mineralogy*, 24, p. 259-314. Geological Society of America, Washington D.C.
- Cashman, K.V., and Marsh, B.D. (1988) Crystal size distribution (CSD) in rocks and the kinetics and dynamics of crystallization II, Makaopuhi lava lake. *Contributions to Mineralogy and Petrology*, 99, 401-405.

- Clauset, A., Shalizi, C.R., and Newman, M.E.J. (2007) Power-law distributions in empirical data. arXiv, 0706\_1062v1, 1-26.
- Clement, C.R. (1982) A comparative geological study of some major kimberlite pipes in the Northern Cape and Orange Free State. Geology PhD thesis. University of Cape Town, Cape Town, South Africa.
- Clement, C.R., Skinner, E.M.W., and Scott Smith, B.H. (1984) Kimberlite redefined. *Journal of Geology*, 92, 223-228.
- Daly, R.A. (1925) Carbonate dikes of the Premier Diamond Mine, Transvaal. *Journal of Geology*, 33(7), 659-684.
- Dawson, J.B. (1962) Basutoland kimberlites. *Geological Society of America Bulletin*, 73, 545-560.
- Dawson, J.B., and Hawthorne, J.B. (1970) Intrusion Features of Some Hypabyssal South African Kimberlites. *Bulletin of Volcanology*, 34, 740-757.
- . (1973) Magmatic sedimentation and carbonatitic differentiation in kimberlite sills at Benfontein, South Africa. *Journal of the Geological Society of London*, 129(1), 61-85.
- Donaldson, C.H., and Reid, A.M. (1982) Multiple intrusion of a kimberlite dyke. *Transactions of the geological society of South Africa*, 85, 1-12.
- Fedortchouk, Y., and Canil, D. (2004) Intensive variables in kimberlite magmas, Lac de Gras, Canada and Implications for Diamond Survival. *Journal of Petrology*, 45(9), 1725-1745.
- Field, M. (2008) Variations of olivine abundance and grain size in the Snap Lake kimberlite intrusion, Northwest Territories, Canada: A possible proxy for diamonds. 9th International Kimberlite Conference Extended Abstract, No. 9IKC-A-00287, 3.
- Goldstein, M.L., Morris, S.A., and Yen, G.G. (2004) Problems with fitting to the power-law distribution. *European physical journal B*, 41, 255-258.
- Heiken, G., Wohletz, K., and Eichelberger, J. (1988) Fracture Fillings and Intrusive Pyroclasts, Inyo Domes, California. *Journal of Geophysical Research*, 93, 4335-4350.
- Higgins, M.D. (2002) Closure in crystal size distributions (CSD), verification of CSD calculations, and the significance of CSD fans. *American Mineralogist*, 87(1), 171-175.
- . (2006) *Quantitative textural measurements in igneous and metamorphic petrology*. 265 p. Cambridge University Press, Cambridge.
- Inman, D.L. (1952) Measures for describing the size distribution of sediments. *Journal of Sedimentary Petrology*, 22, 125-145.
- Kamenetsky, V.S., Kamenetsky, M.B., Sobolev, A.V., Golovin, A.V., Demouchy, S., Faure, K., Sharygin, V.V., and Kuzmin, D.V. (2007) Olivine in the Udachnaya-East Kimberlite (Yakutia, Russia): Types, Compositions and Origins. *J. Petrology*, egm033.
- Kaminski, E., and Jaupart, C. (1998) The size distribution of pyroclasts and the fragmentation sequence in explosive volcanic eruptions. *Journal of Geophysical Research* 103, 29759-29779.

- Komar, P.D. (1972) Flow Differentiation in Igneous Dikes and Sills: Profiles of velocity and phenocryst concentration. *Geological Society of America Bulletin*, 83, 3443-3448.
- Mandelbrot, B.B. (1982) *The Fractal Geometry of Nature*. W.H. Freeman, San Francisco.
- Mangan, M.T. (1990) Crystal size distribution systematics and the determination of magma storage times: The 1959 eruption of Kilauea volcano, Hawaii. *Journal of Volcanology and Geothermal Research*, 44(3-4), 295-302.
- Marsh, B.D. (1988) Crystal size distribution (CSD) in rocks and the kinetics and dynamics of crystallization. *Contributions to Mineralogy and Petrology*, 99, 277-291.
- Mitchell, R.H. (1970) Kimberlite and related rocks--A critical re-appraisal. *Journal of Geology*, 78, 686-704.
- . (1986) *Kimberlites: Mineralogy, Geochemistry and Petrology*. 442 p. Plenum Press, New York.
- Mock, A., Jerram, D.A., Breitkreuz. (2003) Using Quantitative Textural Analysis to Understand the Emplacement of Shallow-Level Rhyolitic Laccoliths--a Case Study from the Halle Volcanic Complex, Germany. *Journal of Petrology*, 44(5), 833-849.
- Peterson, T.D. (1990) Petrology and genesis of natrocarbonatite. *Contributions to Mineralogy and Petrology*, 105, 143-155.
- Price, S., Russell, J.K., and Kopylova, M. (2000) Primitive magma from the Jericho pipe, N.W.T., Canada: Constraints on primary melt chemistry. *Journal of Petrology*, 41, 789-808.
- Salisbury, M.J., Bohron, W.A., Clyne, M.A., Ramos, F.C., and Hoskin, P. (2008) Multiple Plagioclase Crystal Populations Identified by Crystal Size Distribution and in situ Chemical Data: Implications for Timescales of Magma Chamber Processes Associated with the 1915 Eruption of Lassen Peak, CA. *J. Petrology*, egn045.
- Scott Smith, B.H. (1996) Ch: 10 Kimberlites In R.H. Mitchell, Ed. *Undersaturated Alkaline Rocks: Mineralogy, Petrogenesis, and Economic Potential Short Course Volume 24*, p. 259-270. Mineralogical Association of Canada Short Course
- . (1999) Near-surface emplacement of kimberlites by magmatic processes. Invited article in IAVCEI commission on explosive volcanism newsletter, Spring 1999, p. 314.
- . (2009) The Economic Implications of kimberlite emplacement. 9th International Kimberlite Conference extended abstracts, 9IKC-A-00335, 3.
- Shee, S.R. (1985) The petrogenesis of the Wesselton Mine kimberlite, Kimberley, Cape Province, R.S.A. *Geology*, PhD. University of Cape Town, Cape Town, South Africa.
- Sparks, R.S.J., Baker, L., Brown, R.J., Field, M., Schumacher, J., Stripp, G., and Walters, A. (2006) Dynamical constraints on kimberlite volcanism. *Journal of Volcanology and Geothermal Research*, 155(1-2), 18-48.
- Turcotte, D.L. (1986) Fractals and Fragmentation. *Journal of Geophysical Research*, 91, 1921-1926.
- Wagner, P.A. (1914) *The diamond fields of southern Africa*. 347 p. Transvaal Leader, Johannesburg.

- Walters, Phillips, J.C., Brown, R.J., Field, M., Gernon, T., Stripp, G., and Sparks, R.S.J. (2006) The role of fluidisation in the formation of volcanoclastic kimberlite: Grain size observations and experimental investigation. *Journal of Volcanology and Geothermal Research*, 155(1-2), 119-137.
- Webb, K.J., Scott Smith, B.H., Paul, J.L., and Hetman, C.M. (2004) Geology of the Victor Kimberlite, Attawapiskat, Northern Ontario, Canada: cross-cutting and nested craters. *Lithos*, 76(1-4), 29-50.
- Wilson, L., and Head, J.W. (2003) Diatremes and kimberlites 2: An integrated model of the ascent and eruption of kimberlitic magmas and the production of crater, diatreme, and hypabyssal facies. *Program Abstracts of the VIIIth International Kimberlite Conference*, p. 4.



**Chapter 4** uses facies analysis of the A154N kimberlite pipe to show the relative times and modes of emplacement for deposits. Methods developed in Chapter 2 are used to characterize the magma that erupted to produce each deposit. These data are used to interpret eruption processes, and develop implications for kimberlite magma properties.

## **4 Spatial and temporal evolution of kimberlite magma at A154N, Diavik, Northwest Territories, Canada<sup>5</sup>**

### **4.1 Introduction**

Studies of modern volcanic systems have shown that variations in eruption style typically relate to the composition and physical properties of the magma, the degree of magma overpressure, the total volume of magma, and vent geometry. For example, solid, liquid and gas ratios in erupting magmas have been shown to modulate the style (i.e. effusive vs. explosive) and intensity (e.g. fountain height) of basaltic eruptions (e.g. Houghton and Gonnermann, 2008; Parfitt et al., 1995). Moreover, low viscosity magmas can outgas efficiently and allow for a concomitant reduction of magma overpressure and eruption intensity (e.g. Namiki and Manga, 2008; Stasiuk et al., 1996). Vent geometry can also be a significant factor in determining eruption style and intensity (e.g. Bower and Woods, 1998; Scandone and Malone, 1985; Wilson et al., 1980).

Similar linkages between magma properties, vent geometry, and eruption style have not been made for kimberlite eruptions for several reasons: (1) kimberlite eruptions have not been observed, and surface features and extra-crater deposits of even the youngest kimberlite volcanoes are usually highly eroded or completely removed; (2) pristine samples of kimberlite melt are rarely preserved because kimberlitic volcanic deposits are highly susceptible to post-emplacement alteration and textural modification; and (3) kimberlite magmas are volatile-rich and likely to have highly transient physical properties during transport and eruption. For example, due to the high volatile contents estimated and measured for kimberlite magmas (e.g. Eggler, 1978; Price et al., 2000; Sparks et al., 2006) the volumetric proportions of melt:solid:gas must evolve from melt-dominated systems at mantle conditions to gas-dominated systems at the point

---

<sup>5</sup> A version of this chapter has been accepted for publication. S. Moss, J.K. Russell, R.C. Brett, and G.D.M. Andrews. Spatial and temporal evolution of kimberlite magma at A154N, Diavik, Northwest Territories, Canada. *Lithos*.

of eruption. Such variations will have profound impacts on the physical properties of kimberlite magmas and, hence, the mechanisms and styles of eruption.

Though conduit geometries of active volcanoes are difficult to measure, it is accepted that conduit morphologies are dynamic and subject to change (Scandone, 1996). In conventional volcanological studies, the data used to constrain unknown conduit geometries are measured heights of eruption columns from active systems or particle size distributions in fallout deposits for unobserved systems. In contrast, mining of diamondiferous kimberlite permits characterization of conduit and vent geometries of an erupted volcano. For example, drill-core intercepts, downhole geophysical measurements, and open-pit surveys provide direct observations of subsurface contacts and, thus, constrain the 3-D geometry of kimberlite conduits.

The A154N kimberlite pipe in the Eocene Diavik kimberlite cluster (Graham et al., 1999) in the Northwest Territories, Canada, (Fig. 4.1a) comprises a sequence of extrusive and intrusive events for which the relative timing, vent geometry and mode of emplacement are clearly established. As such, it provides a unique opportunity to explore the connections between magma properties, vent geometry and eruption style.

Our analysis of this sequence of deposits suggests that transient magma properties arising from separated three-phase flow involving kimberlite melt, crystals, and an exsolved CO<sub>2</sub>-H<sub>2</sub>O fluid provide a fundamental control on the style of kimberlite eruption and emplacement. Specifically, we expect and observe the volumetric proportions of the fluid phase to: (1) increase with ascent; but (2) to decrease with time during the eruption due to decoupling of the gas and the silicate melt within the flow. We also expect the fraction of solids (i.e. crystals and xenoliths) to concentrate at the base of the ascending plug of kimberlite magma during ascent. These processes can account for the diversity of textures and compositions in pyroclasts and within dykes of coherent kimberlite.

## **4.2 Field mapping**

Field mapping in the open pit at Diavik and logging of drill-core has identified a minimum of 4 discrete volcanic (e.g. 3 eruptive and 1 intrusive) events in the A154N

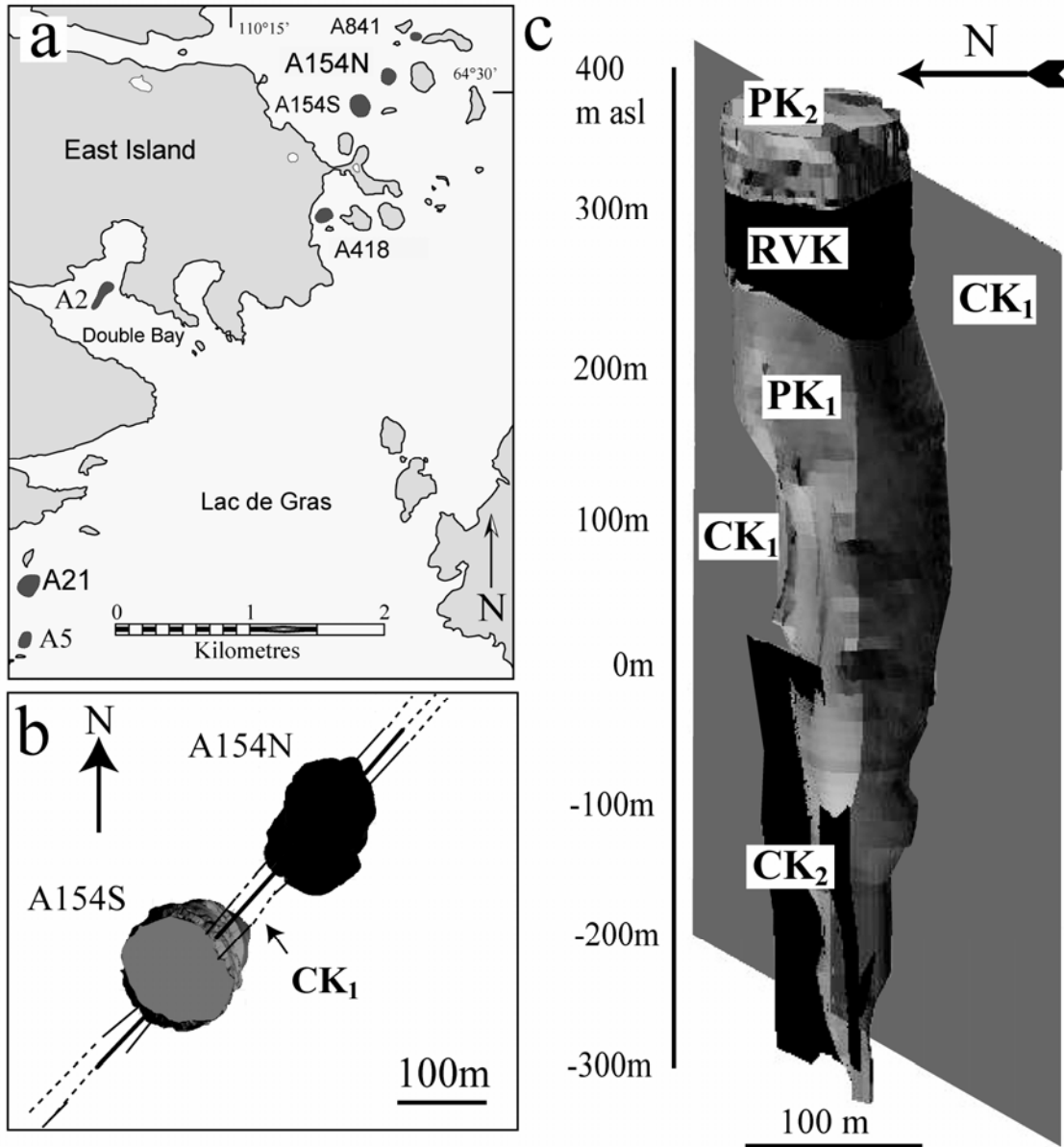


**Figure 4.1:** Location of the Diavik kimberlite field and internal units of A154N: (a) Kimberlite pipes at Diavik, East Island of Lac de Gras, NWT, Canada; (b) Plan view of the A154N and A154S pipes and mapped (solid lines) and inferred (dashed) dykes of CK<sub>1</sub>; (c) Inclined 3-D model of A154N looking E, showing five separate units of kimberlite, including: pre-cursor kimberlite dykes (CK<sub>1</sub>) (translucent); pyroclastic kimberlite (PK<sub>1</sub>); coherent kimberlite dykes (CK<sub>2</sub>; CK from Chapter 3); re-sedimented volcanoclastic kimberlite (RVK); upper pyroclastic kimberlite (PK<sub>2</sub>).

pipe (Figs. 4.1b and 4.1c), including: (1) an array of dykes (CK<sub>1</sub>) intruded into country rock exposed at the present-day surface (415 meters above sea level) during mining; (2) massive pyroclastic deposits within the pipe (PK<sub>1</sub>); (3) sub-surface intrusions of coherent kimberlite (CK<sub>2</sub>; c.f. Chapter 3) intruded into PK<sub>1</sub>. The sequence is capped disconformably by an externally-sourced pyroclastic kimberlite deposit (PK<sub>2</sub>) captured by and preserved within the vent to the A154N volcano (Chapter 2). Here, we describe the macroscopic and geometric properties of the individual deposits, the textures and components therein, and their spatial context and relative timing within the A154N kimberlite volcano.

#### 4.2.1 Early dykes (CK<sub>1</sub>)

An array of 5-150 cm-wide vertical dykes (CK<sub>1</sub>) of yellow-brown, carbonate-altered kimberlite is observed in the A154N open pit, striking ~038° for over 800 m through the adjacent country rock (Figs. 4.1b and 4.2a). The A154N and A154S kimberlite pipes cross-cut and truncate the center of the known strike length of the dyke array; there is no evidence of CK<sub>1</sub> cross-cutting the fragmental kimberlite within either pipe. The contact relationship between CK<sub>1</sub> and the A154N pipe is evidence of a clear genetic linkage to the subsequent pipe formation and pipe-filling processes within A154N: CK<sub>1</sub> precedes the formation of A154N; formation of A154N follows the CK<sub>1</sub> dyke; pipe-filling is synchronous with and immediately follows pipe formation. This implies that CK<sub>1</sub> dykes are the earliest emplacement event at the volcano. CK<sub>1</sub> is within a downward-tapering zone of vertical fractures in the country rock, which narrows to 6 m wide at a depth of 245 m (170 m asl). The dyke is variably thick (5-150 cm), vertically and horizontally discontinuous, and commonly splits into multiple, thin (5-10 cm wide) dykes (Fig. 4.2); many of the vertical fractures do not contain kimberlite.

The dyke is variably competent; most of the uppermost exposures (i.e. > 300 m asl) consist of yellow-brown mud with abundant, resistant indicator minerals (e.g. ilmenite, garnet). In contrast, deeper intersections of the dyke comprise a brown, dense rock with fine, internal fractures filled by serpentine. Portions of the dyke are rich in miarolitic cavities and carbonate-filled amygdalae (25% by volume), and flow-banding is

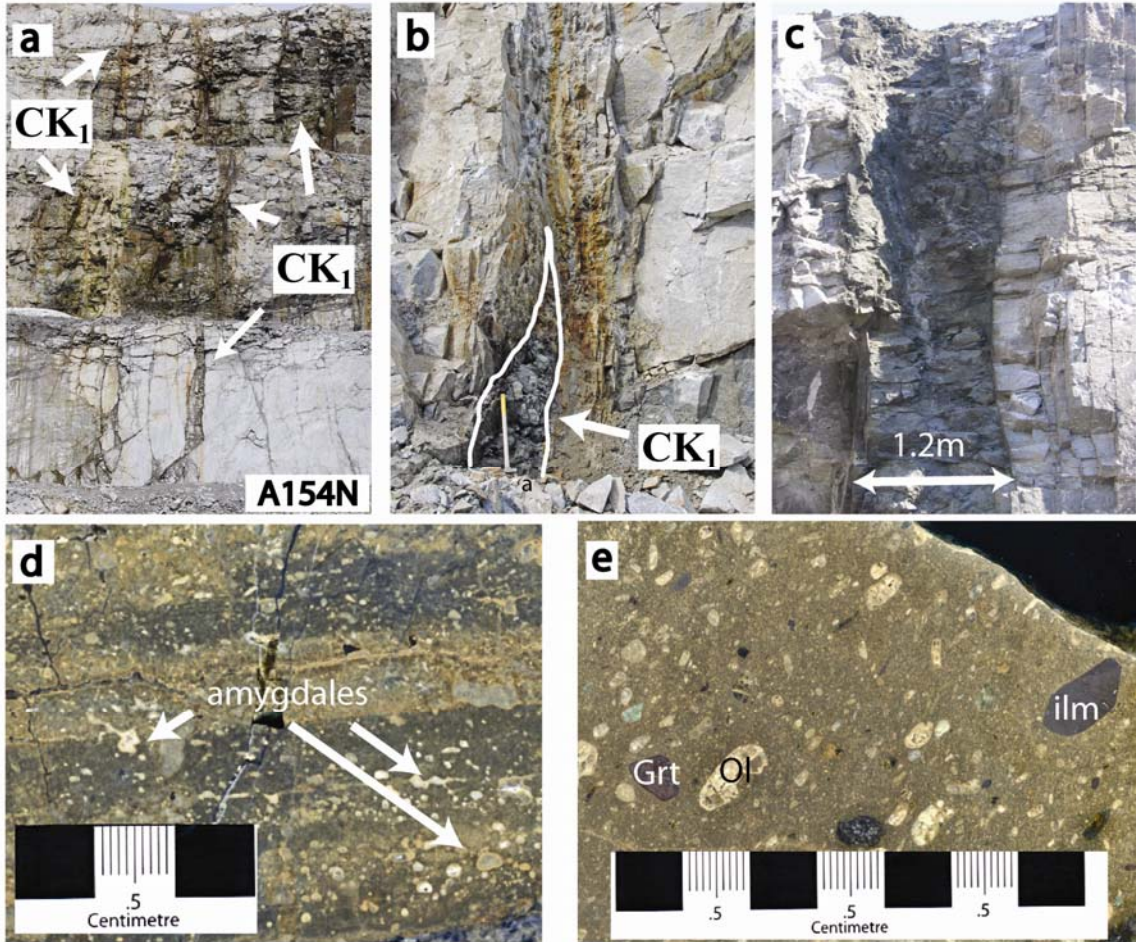


**Figure 4.2:** Field and hand sample photographs of pre-cursor CK<sub>1</sub> dyke at A154N: (a) thin dykes of CK<sub>1</sub> exposed on 10m bench-faces in open pit from 230 – 180 m asl; (b) exposed section through CK<sub>1</sub> dyke, partially-filled with coherent kimberlite (adjacent to hammer), adjacent to altered fracture zone (projecting into wall) void of kimberlite; (c) widest intersection of CK<sub>1</sub> featuring prominent tension cracks adjacent to dyke margin; (d) polished sample of CK<sub>1</sub> collected from contact in (c), showing well-developed flow-banding, and abundant carbonate filled amygdules; (e) polished sample from interior of CK<sub>1</sub> showing coarse (>1cm) ilmenite, garnet and relatively low olivine content (10-12%).

locally evident adjacent to contacts with surrounding country rock (Fig. 4.2d). Competent sections of the dyke generally comprise minor amounts (~5-15 %) of olivine (1-10 mm) set in a groundmass of spinel, serpentine and carbonate. Garnet and clinopyroxene macrocrysts (1-10 mm) and ilmenite megacrysts (3-20 mm) are also abundant. The smaller size fractions of olivine and the groundmass of the dyke are pervasively altered, and are commonly completely replaced by carbonate, serpentine, and Fe-oxides. Country rock xenoliths of granite and biotite schist are ubiquitous, but represent a small volume of the dyke (< 5%), and are typically concentrated at or near dyke margins.

#### 4.2.2 Pyroclastic kimberlite (PK<sub>1</sub>)

The A154N pipe is largely infilled by a > 500 m thick sequence ( $5.0 \times 10^6 \text{ m}^3$ ) of massive, poorly-sorted, fragmental kimberlite (Fig. 4.3a; PK<sub>1</sub>) which is interpreted as primary pyroclastic kimberlite (c.f. MVK<sub>1,2</sub> in Chapter 2; Graham et al., 1999). The contact with overlying bedded, re-sedimented volcanoclastic kimberlite (RVK) is sharp, reflecting a change in componentry (mud-rich matrix) and a change in depositional style to small-volume, high-energy sub-aerial and sub-aqueous debris flows (Chapter 2). The eruption from which PK<sub>1</sub> was deposited left a conduit that was only partially filled and, thus, an open hole at least 200 m deep (Chapter 2). The open hole was floored by a hummocky topography upon which subsequent sedimentation of crater walls (SVK; c.f. Chapter 2) and other tephra (PK<sub>2</sub>) occurred (Fig. 4.3d).

The PK<sub>1</sub> comprises mainly liberated olivine crystals and juvenile pyroclasts of quenched kimberlite (1-30 mm in diameter) supported by a heterogeneous matrix of serpentine, carbonate, and variable proportions of ash-sized grains of olivine, quenched kimberlite, and dis-aggregated shale and unconsolidated mud (Fig. 4.3b). Olivine crystals are commonly surrounded by thin rims or selvages of crystallized kimberlite magma. Accidental or accessory lithic fragments of country rock (granite, biotite schist, grey shale, black shale) up to 30 cm in diameter, and accessory clasts (2 – 30 cm) of mud-rich, fragmental kimberlite of unknown origin occur throughout PK<sub>1</sub> (Fig. 4.3c). Mantle xenoliths (0.5 – 6 cm) of garnet lherzolite, wehrlite and eclogite are common, as are

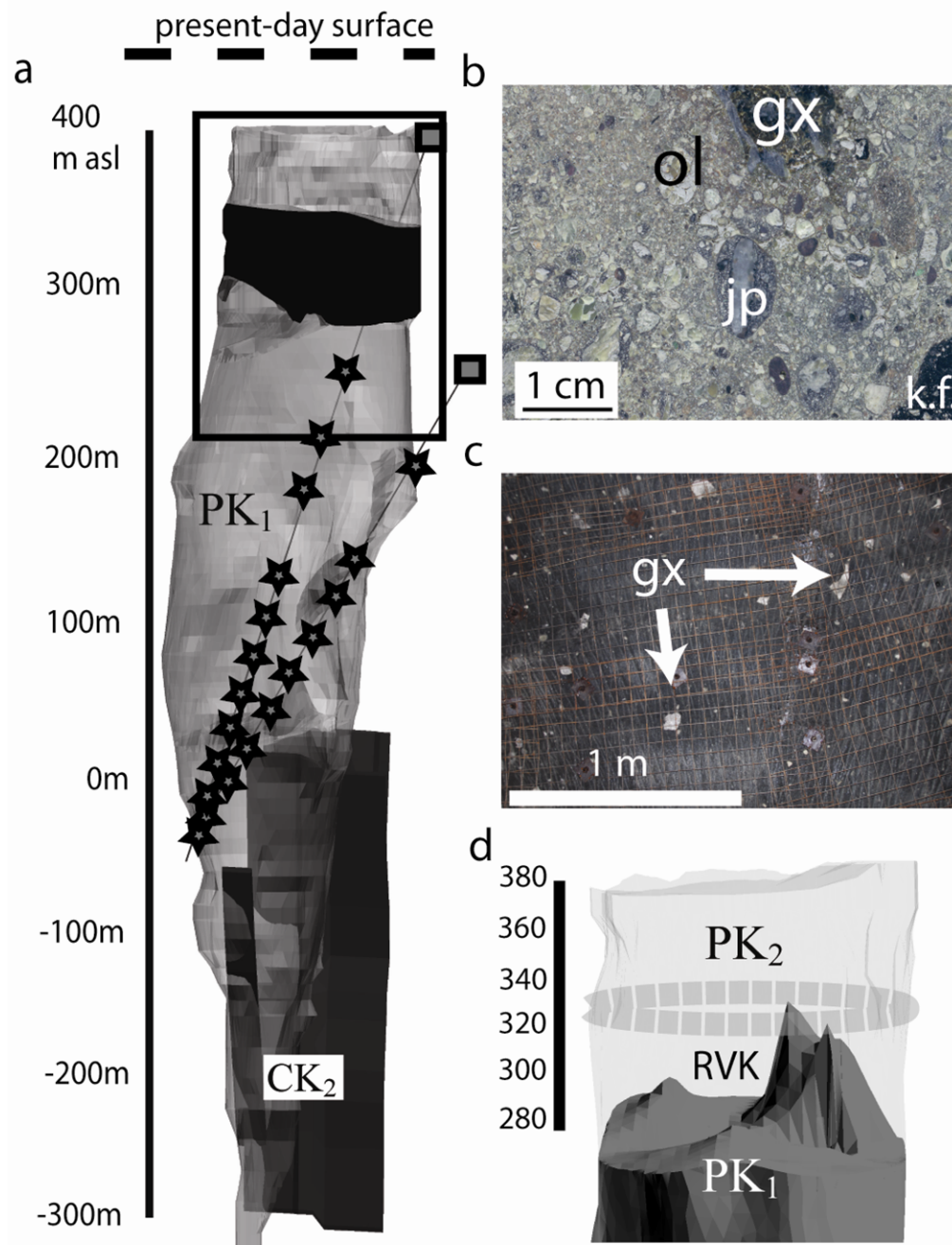


**Figure 4.3:** Distribution and properties of PK<sub>1</sub> within A154N: (a) 3-D model of A154N showing sampling locations (stars) along drillhole traces within PK<sub>1</sub>; (b) polished slab of PK<sub>1</sub> showing granite xenolith (gx), mud-rich kimberlite fragment (k.f.), juvenile kimberlite pyroclast (jp), and abundant olivine crystals (ol); (c) underground bench-face with bolt-and-screen covering showing homogeneous distribution of granite xenoliths (gx) in massive, poorly-sorted pyroclastic kimberlite; (d) close-up of inset in (a) showing upper-contact between PK<sub>1</sub> and overlying RVK and PK<sub>2</sub> (translucent). Dashed outline indicates approximate contact between RVK and overlying PK<sub>2</sub>.

derivative xenocrysts from disaggregation of mantle peridotites (e.g. garnet, clinopyroxene, strained and recrystallized olivine). The PK<sub>1</sub> shows variable amounts of clast and matrix alteration; alteration minerals include serpentine, carbonate and magnetite.

#### 4.2.3 Coherent kimberlite (CK<sub>2</sub>)

Multiple vertical dykes of olivine-rich (> 40%), dense, coherent kimberlite (CK<sub>2</sub>) are observed in the country rock and PK<sub>1</sub> up to 15 m asl (Fig. 4.4b), but not the uppermost portion of PK<sub>1</sub> or overlying RVK (Fig. 4.4d); we infer this to imply that the late intrusions did not erupt at surface. In several cases, vertical CK<sub>2</sub> dykes have intruded along the margin between the pipe wall and the PK<sub>1</sub> deposit. Within the PK<sub>1</sub> deposit, CK<sub>2</sub> form both, sharp edged sheets having minor alteration halos (< 1 cm) and thin (< 1 cm), aphyric ‘fingers’ of crystalline kimberlite.

CK<sub>2</sub> consists of abundant, fresh, sub-rounded to euhedral olivine crystals (0.03-10 mm) enclosed by a groundmass of spinel, serpentine, apatite, and minor carbonate and perovskite (c.f. Chapter 3). Garnet and clinopyroxene xenocrysts are minor, and ilmenite and phlogopite macrocrysts are rare. Granite xenoliths, and xenocrysts of quartz and altered feldspar are locally abundant (> 10%), and clasts of lithified PK<sub>1</sub> are uncommon but also present as inclusions within CK<sub>2</sub>.

#### 4.2.4 Re-sedimented volcanoclastic kimberlite (RVK) and pyroclastic (PK<sub>2</sub>) kimberlite

PK<sub>1</sub> is overlain by ~100 m of stratified volcanoclastic kimberlite interpreted as re-sedimented volcanoclastic kimberlite (Fig. 4.1c, 4.3d; RVK; c.f. SVK, Chapter 2). This unit is a critical marker, as it defines a hiatus of unknown length in the eruption sequence at A154N followed by deposition of pyroclastic kimberlite (PK<sub>2</sub>) from an exotic source (Chapter 2). The relative timing of CK<sub>2</sub> and the emplacement of RVK and PK<sub>2</sub> is unknown, and, thus, RVK and PK<sub>2</sub> will not be considered further in this present study.

The field relationships described above rigorously constrain the sequence of volcanic and subvolcanic events at the A154N pipe (Fig. 4.1c) and allow for an

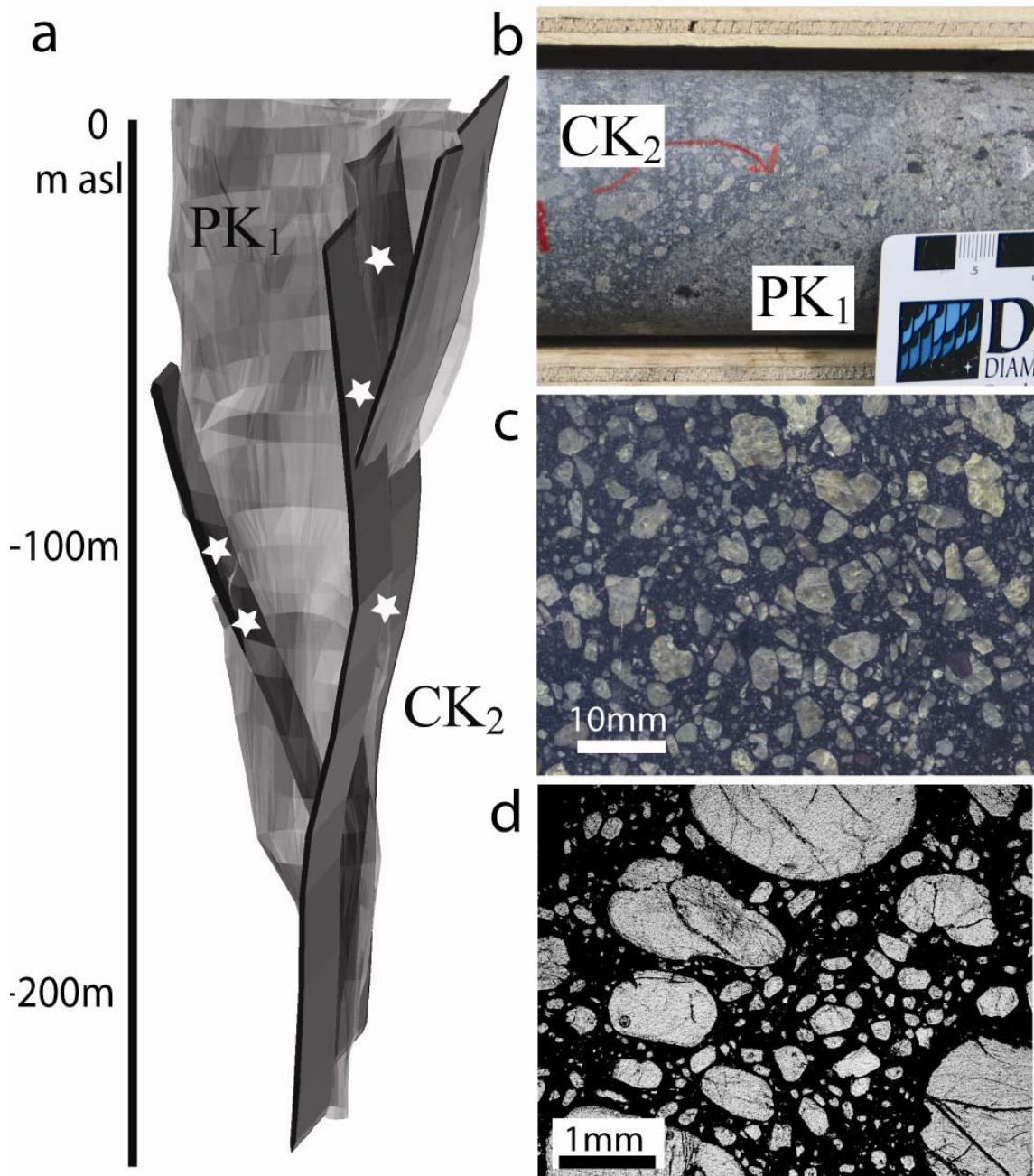


**Figure 4.4:** Distribution and properties of CK<sub>2</sub> within lower section (0 to -200 m asl) of A154N: (a) 3-D model of CK<sub>2</sub> of A154N (stars indicate sample locations); (b) drillcore showing sharp contact between CK<sub>2</sub> and PK<sub>1</sub>; (c) polished sample of crystal-rich CK<sub>2</sub>; (d) polished thin-section of CK<sub>2</sub> showing round to euhedral olivine crystals set in a fine-grained groundmass.

investigation of the temporal evolution of the physical characteristics of magma(s) responsible for different facies within the same volcanic succession. Although the relative timing between events is well-constrained, the absolute time elapsed between events is unknown. Previous Rb-Sr (phlogopite) dating of PK<sub>1</sub> and PK<sub>2</sub> in A154N yielded dates of 56.0 +/- 0.7 Ma (Amelin, 1996; Moser and Amelin, 1996). Rb-Sr dating of both pyroclastic and coherent rocks from adjacent economic pipes at Diavik (A154S, A21, A418) show age ranges from 55.7 +/- 2.1 Ma to 54.8 +/- 0.3 Ma (Barton, 1996; Heaman et al., 2004). The level of precision in these dates precludes speculation on the time intervals between events (e.g. PK<sub>1</sub> vs. PK<sub>2</sub>) or the order in which each pipe (Fig. 4.1) was emplaced. Moreover, further age dating is not undertaken in this study. However, based on the inclusion of lithified PK<sub>1</sub> within CK<sub>2</sub>, we infer that the emplacement of CK<sub>1</sub> and PK<sub>1</sub> was followed by at least a short hiatus before the emplacement of CK<sub>2</sub>.

### 4.3 Componentry

Our characterization of kimberlite samples uses image analysis techniques developed in Chapter 3 (Appendix 7.2) to quantify abundances and size variations of olivine, vesicles, amygdales, miarolitic cavities, and primary and secondary carbonate phases within the groundmass. We use these attributes to uniquely characterize the individual samples of coherent (CK<sub>1</sub> and CK<sub>2</sub>) and fragmental kimberlite (PK<sub>1</sub>). Outlines of olivine crystals in coherent rocks and juvenile pyroclasts in pyroclastic rocks are manually traced at two scales (polished slabs, 3000 - 10,000 mm<sup>2</sup>; polished thin sections, 27 x 46 mm) using a digitizing pad and Adobe Illustrator<sup>TM</sup> and analyzed using ImageJ<sup>TM</sup> to calculate particle areas. These data sets are then normalized to the largest scale of observation. For the pyroclastic deposit (PK<sub>1</sub>) we also use image analysis techniques to characterize the individual juvenile kimberlite pyroclasts. Thus, we are able to determine estimates of the size and enclosed modal olivine content of pyroclasts. We also have recorded textural relationships between olivine, vesicles, carbonate phenocrysts, and groundmass.

#### 4.3.1 Olivine crystal abundances

Olivine crystal contents for CK<sub>1</sub> and CK<sub>2</sub> were estimated for samples collected from three levels in the open pit (315, 275, and 230 m asl), and from drill-core intercepts of two separate dykes, respectively. Modal abundance of olivine crystals increases towards the centre of CK<sub>1</sub>, and crystals are rare to absent at the margins; the margins are volumetrically dominated by carbonate amygdales and miarolitic cavities (Fig. 4.2d). Conversely, olivine crystals are evenly-distributed in CK<sub>2</sub> dykes except at the immediate (< 1 cm wide) margins of the dyke where modal olivine content decreases to < 25% and crystal sizes are generally < 3 mm. Therefore, for comparison, samples were collected from the relatively crystal-rich interior portions (> 5 cm from the dyke margins) of both CK<sub>1</sub> and CK<sub>2</sub>, respectively.

Results from image analysis of slabs and thin sections from two representative samples of CK<sub>1</sub> and five from CK<sub>2</sub> are expressed as modal area % olivine vs. size (mm<sup>2</sup>), and shown in Figure 4.5. Samples of CK<sub>1</sub> contain a truncated size range of olivine crystals (0.2-100 mm<sup>2</sup>) relative to CK<sub>2</sub> (0.03-100 mm<sup>2</sup>), and have lower overall modal abundances of olivine (~5-15% vs. 40-58%) (Fig. 4.5). The difference in olivine crystal size ranges for CK<sub>1</sub> and CK<sub>2</sub> may be due to alteration; smaller-sized olivine crystals (0.03 – 0.2 mm) in CK<sub>1</sub> are ubiquitous, but are commonly pseudomorphed by serpentine. As a result, the boundaries between pseudomorphs and groundmass are difficult to distinguish, and preclude these grains from accurate measurement using image analysis. Lower overall abundances in CK<sub>1</sub> relative to CK<sub>2</sub>, however, cannot be due alteration alone; coarser olivine sizes (> 0.2 mm) in CK<sub>1</sub> are generally fresh, and smaller-sized olivine comprises a relatively small fraction of the total abundance (Fig. 4.5) of olivine in fresh CK<sub>2</sub>. Therefore, this discrepancy is interpreted to result from intrinsic differences in the amount of olivine in CK<sub>1</sub> vs. CK<sub>2</sub>.

#### 4.3.2 Juvenile pyroclasts from PK<sub>1</sub>

To assess the crystal content of the magma parental to PK<sub>1</sub>, we have examined the population of juvenile pyroclasts comprising crystalline kimberlite +/- olivine crystals

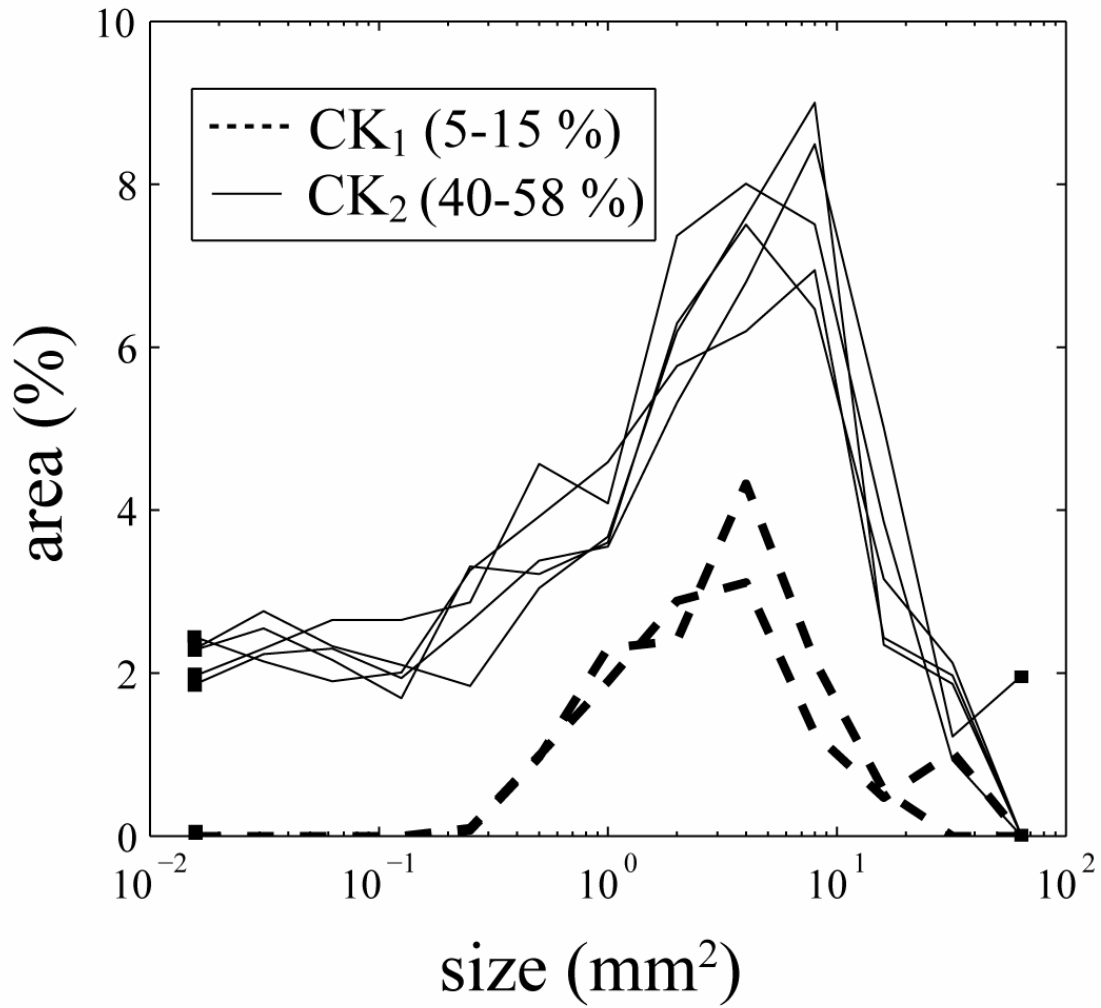


**Figure 4.5:** Olivine size distributions: (a) modal area % olivine vs. olivine size (as mm<sup>2</sup>) for early dyke (grey lines; CK<sub>1</sub>) and late dykes of coherent kimberlite (black lines; CK<sub>2</sub>). Range of total area % for CK<sub>1</sub> and CK<sub>2</sub> samples in parentheses.

(JPs). Twenty samples were collected at ~10 m intervals throughout a 200 m vertical section of the PK<sub>1</sub> (Fig. 4.3a); ten or more JPs were chosen from each thin section for analysis based on observable groundmass mineralogy and lack of alteration. The size (e.g. area) of individual pyroclasts and their olivine crystal contents (area %) were calculated by analyzing for total pyroclast area (mm<sup>2</sup>) and the area occupied by olivine in each clast; the difference is the area of crystallized kimberlite melt. Pyroclast size vs. olivine crystal contents (modal %) are shown in Figures 4.6a and b, in which pyroclasts are subdivided into groups based on observations of texture and mineralogy. In Figure 4.6a, JPs are sub-divided into vesiculated (v), non-vesiculated (non-v), carbonate microphenocryst-bearing (i.e. calcite or dolomite; carb), and vesiculated and carbonate microphenocryst-bearing (v + carb). In Figure 4.6b, JPs are sub-divided according to textural relationships between olivine crystals and surrounding crystallized kimberlite melt: (1) pyroclasts containing ‘multiple’ olivine crystals (M-type) in a groundmass of crystallized kimberlite magma; (2) single olivine crystals with selvages of crystallized kimberlite (S-type); (3) single olivine crystals with partial selvages of crystallized kimberlite (PS-type); and (4) pyroclasts cored by a single olivine crystal (< 70% of total juvenile pyroclast area) surrounded by other, smaller olivines and crystallized kimberlite magma (C-type). Juvenile pyroclasts range in size from 0.03 to 20 mm<sup>2</sup> and have olivine contents of 0 – 90% and minimum sizes of 0.03 mm<sup>2</sup>. Neither small JPs with high crystal:melt ratios, nor large JPs with low crystal : melt ratios are observed (shaded regions; Fig. 4.6a). The combined modal % olivine crystals in JPs is 43.7%.

#### 4.3.3 Textural evidence of volatile content

In this section, we describe and quantify textures indicating the presence of an exsolved fluid phase; their abundance is used as a proxy for the relative fluid content of the magma at the time of eruption. Vesicles indicative of the presence of an exsolved fluid phase are found in all deposits; they are differentiated by the amount of infill, and include: ‘vesicles’ denoting spherical to sub-spherical gas cavities; ‘miarolitic cavities’ denoting gas cavities partially lined by late-stage minerals (e.g. carbonate) in intrusions; ‘amygdales’ denoting gas cavities that are essentially filled by late-stage minerals (e.g.

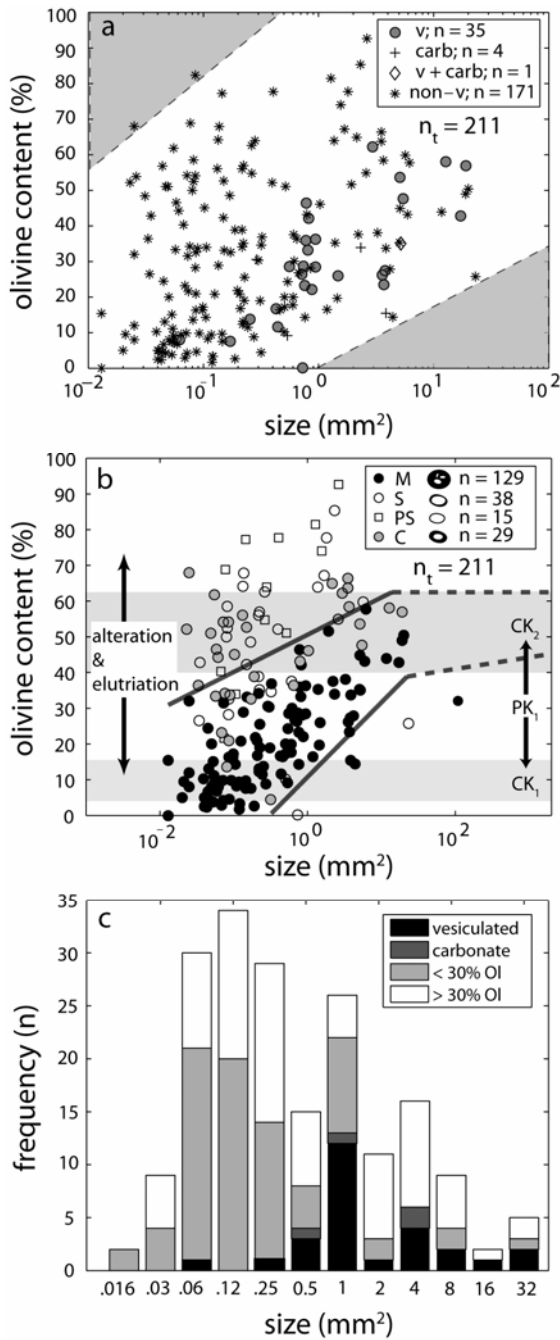


**Figure 4.6:** Parametric analysis of juvenile pyroclasts from PK<sub>1</sub> of A154N: (a) olivine content (area %) within juvenile pyroclast vs. size (mm<sup>2</sup>) of juvenile pyroclasts containing: vesicles (v), groundmass carbonate (carb), both (v + carb), or that are vesicle-free (non-v). Shaded regions denote olivine : melt relationships that are not observed; (b) olivine content (%) vs. size (mm<sup>2</sup>) for textural subgroups of juvenile pyroclasts, including: pyroclasts with multiple olivine crystals (M), selvages of melt on olivine crystals (S), olivine grains with partial selvage (PS), and cored (C) pyroclasts. Shaded bands indicate measured modal olivine (%) for CK<sub>2</sub> and CK<sub>1</sub>; solid lines indicate observational limits of olivine content vs. size for M; dashed lines indicate projected limits. Note the similarity of observed sizes of juvenile pyroclasts and olivine crystal populations (Fig. 5). Absence of smallest juvenile pyroclast sizes attributed to alteration and elutriation processes (double-arrow); (c) histograms of components within textural subgroups of juvenile pyroclasts (vesiculated, carbonate-bearing, >30% olivine, <30% olivine).

carbonate, serpentine). At the slab and thin section scale, CK<sub>1</sub> contains miarolitic cavities, abundant lath-shaped groundmass carbonate, as well as spherical to sub-spherical patches of serpentine + carbonate within the groundmass. These domains are distinguishable from serpentinized olivine grains by remnants of fresh olivine within serpentinized grains and by the orientation of serpentine fibers perpendicular to the outer edge of the domains. It also features extensive post-emplacment carbonate alteration of olivine and groundmass phases (e.g., Fig. 4.2d). Many miarolitic cavities within CK<sub>1</sub> are lined or partially filled with carbonate crystals (i.e. calcite, dolomite).

Juvenile pyroclasts from PK<sub>1</sub> range in size from 0.06 mm<sup>2</sup> to 32 mm<sup>2</sup>, and ~14% of pyroclasts contain vesicles or amygdales filled with carbonate and/or serpentine (Fig. 4.6c). Vesicle contents range from 0 – 20% by area (i.e. 0 - 40% of non-olivine groundmass or crystallized melt). Textural sub-types of JPs show restricted size ranges for vesiculated (0.25 – 32 mm<sup>2</sup>) and carbonate-bearing JPs (0.5 – 4 mm<sup>2</sup>) (Fig. 4.6c). Vesicles occur as both void spaces and as amygdales, infilled with carbonate and serpentine (Fig. 4.7a). The infills are mineralogically and texturally diverse, occurring as: granular carbonate, serpentine, euhedral carbonate-linings with serpentine infills, or fibrous or botryoidal serpentine linings with carbonate crystals in their interiors. The majority of vesiculated juvenile pyroclasts do not contain groundmass or phenocrystic carbonate, while the majority of groundmass carbonate-bearing juvenile pyroclasts do not contain vesicles (Fig. 4.7a). In contrast to CK<sub>1</sub> and PK<sub>1</sub>, late CK<sub>2</sub> magmas contain minimal groundmass carbonate, minimal patches of serpentine and/or carbonate (Fig. 4.4c,d) in the groundmass, and rare miarolitic cavities.

#### **4.4 Discussion and Interpretation:**

This investigation reveals important variations in mineralogy, texture and componentry between CK<sub>1</sub>, PK<sub>1</sub> and CK<sub>2</sub>. In this section, I discuss the origins of variations in olivine crystal size, olivine crystal abundance, and the inferred proportions of gas and/or fluid. These observations are then combined with inferred physical properties of kimberlite magma to estimate possible mass fluxes involved in each

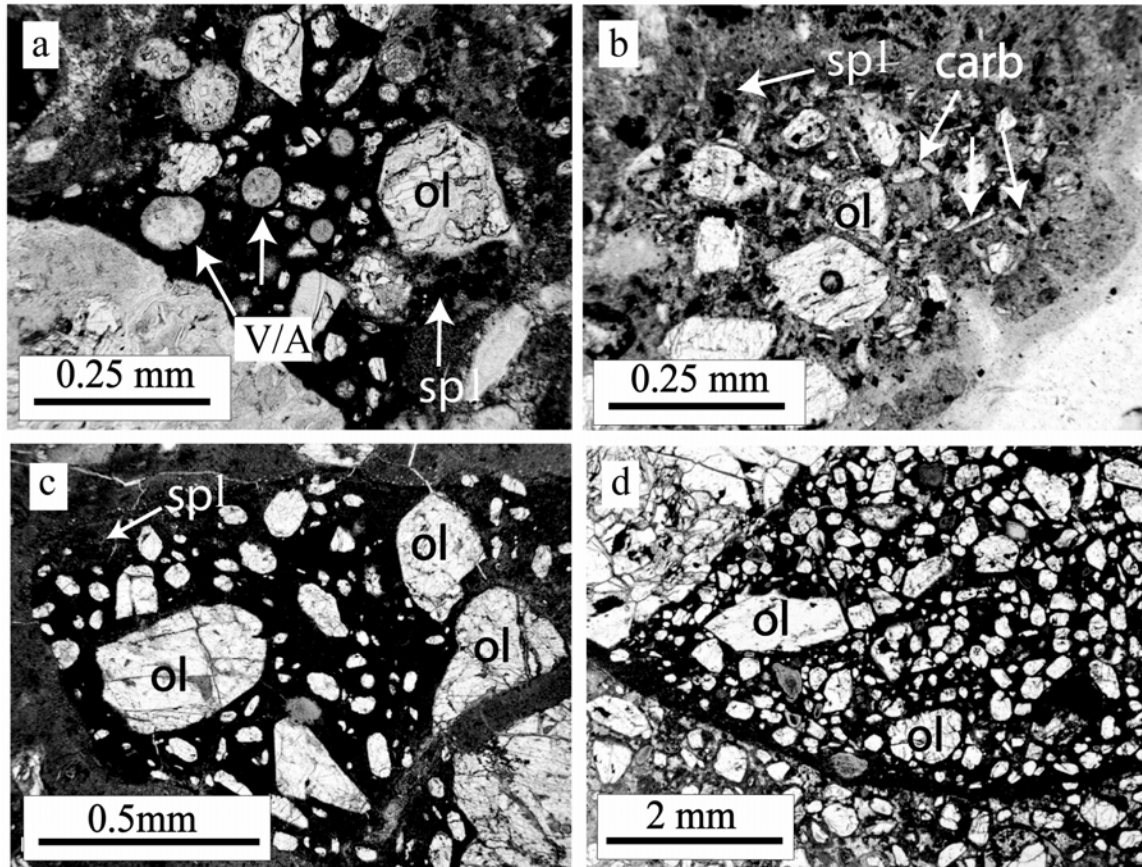


**Figure 4.7:** Photomicrographs of selected juvenile pyroclasts (Jp) from PK<sub>1</sub>: (a) JP containing olivine (ol), spinel (spl), serpentine +/- carbonate filled amygdules (V/A) in serpentine groundmass; (b) JP with carbonate laths (carb), olivine (ol) and spinel (spl) in serpentine and carbonate groundmass; (c) JP with < 30 area % olivine content (ol) in spinel (spl) and serpentine groundmass; (d) JP with > 50 area % olivine content (ol), and thin, olivine-free quenched-melt rim and serpentine and carbonate groundmass.

emplacement event and attempt to constrain the dynamics of kimberlite emplacement in the A154N pipe.

#### 4.4.1 Variations in olivine content with time

Variations in the olivine crystal contents (area %) of the CK<sub>1</sub> and CK<sub>2</sub> magmas are substantial (Table 4.1). These variations are interpreted as first-order differences between early (CK<sub>1</sub>) and late (CK<sub>2</sub>) emplaced magmas. Modal estimates (area %) of olivine contents also vary widely (0 – 90%) for all sizes of JPs in PK<sub>1</sub>. Despite this variability, there is no detectable sorting of JPs by size or type within PK<sub>1</sub>. Moreover, JPs from the same thin section and possessing similar groundmass mineralogy (e.g. spinel, serpentine, perovskite) and grain size can have highly variable olivine contents. Possible explanations for the variation in olivine content within JPs are discussed below and include: (1) PK<sub>1</sub> hosts JPs derived from multiple eruptions; (2) single batches of magma can have intrinsically heterogeneous olivine contents (i.e. total modal %); or (3) single batches of magma having a constant olivine content (i.e. vol. %) can have variable olivine size distributions (0.01 – 100mm<sup>2</sup>).

The PK<sub>1</sub> is a massive deposit and the lack of any apparent cross-cutting, pyroclastic kimberlite deposits suggests that it results from a single eruption. To determine if the variations in the olivine contents of JPs are a function of the modal % or the crystal size distribution of the olivine in the original magma, the JPs are sub-divided into four textural classes (Fig. 4.6b): pyroclasts with multiple olivine crystals (M), selvages of melt on olivine crystals (S), olivine grains with partial selvage (PS), and cored (C) pyroclasts comprising an olivine crystal core and < 30% enclosing groundmass. These subdivisions (M; S; PS; C) allow us to filter out the influence of single crystals (i.e. crystal size) in measurements of JPs which show high crystal : melt ratios; i.e. if an individual crystal is dominantly responsible for the observed olivine content (e.g. S, PS, or C).

Each sub-type has an olivine content expected of the textural relationship between olivine and surrounding crystallized melt (e.g. S > 50% olivine). The presumed low viscosity of kimberlite melt (cf. Sparks, 2006), likely influences its interaction with

Table 4.1

Summary of component properties in coherent kimberlite and juvenile pyroclasts of units in A154N

unit	CK <sub>1</sub>	PK <sub>1</sub>	CK <sub>2</sub>
number of samples	4	211*	5
sample size (mm <sup>2</sup> )	5200 - 12,000 <sup>†</sup>	0.02 - 100 <sup>‡</sup>	3619
% olivine crystals	5 - 15	5 - 44	40 - 58
% vesicles	0 - 60	0 - 40	0 - 2
olivine sizes (mm)	0.2 - 10	0.03 - 6	0.03 - 10
vesicle sizes (mm)	0.2 - 5	0.1 - 1	-

\* number of juvenile pyroclasts of crystalline kimberlite

<sup>†</sup> sizes of polished slabs

<sup>‡</sup> sizes of juvenile pyroclasts

crystals during fragmentation, and may determine the selvage thickness (i.e. S) and wetting angles between crystals and melt (i.e. PS) observed in JPs. Observations of the M sub-type, therefore, likely represent the closest approximation of the crystal : melt ratios present in the pre-eruptive magma responsible for PK<sub>1</sub>. However, multiple olivine (M) pyroclasts of all sizes (0.1 – 80 mm<sup>2</sup>) still show large ranges in olivine crystal content (i.e. % low – % high for a given size = 30-50%).

Primary elutriation of fines during eruption and deposition and secondary alteration can also have an effect on pyroclast diversity. Smaller pyroclasts are less likely to be preserved; higher surface area to volume ratios of smaller pyroclasts encourage size reduction or even complete destruction due to alteration, and the finer pyroclasts are also more susceptible to elutriation and loss during eruption (Fig. 4.6b). Moreover, thin selvages of crystallized kimberlite magma around large olivine crystals are also susceptible to corrosion and possible eradication due to alteration. Preserved JPs, therefore, likely represent a sample bias towards crystal-rich magmas and may over-estimate the olivine content.

Larger pyroclasts (> 100 mm<sup>2</sup>) and cognate lithic fragments of coherent kimberlite are rarely observed, but the few that are found have high olivine crystal content similar to that seen in CK<sub>2</sub>. The lack of large, crystal-free juvenile pyroclasts could imply that either the magma was entirely crystal-rich or that the inferred low viscosity and high gas contents of erupting kimberlite magma leads to efficient disaggregation of larger clots of kimberlite magma when abundant crystal surfaces are not available to provide surface tension. However, the presence of smaller JPs having low olivine contents (Fig. 4.6b), combined with an inferred loss of fine ash-sized JPs of quenched kimberlite melt provides some evidence for fragmentation of a crystal-poor magma. Therefore, if the observed JPs are representative of the starting eruptive magma, then the combined modal % of olivine in JPs (43.7%) likely represents a maximum in olivine content.

Our reconstruction of olivine contents for these three kimberlite deposits constrains the olivine contents of the corresponding magmas. These data suggest that the erupting magmas increased in olivine content with time: CK<sub>1</sub> (modal % ol) < PK<sub>1</sub> (modal % ol) < CK<sub>2</sub> (modal % ol) (Table 4.1). I suggest that the textural and mineralogical

diversity of pyroclast types within a single pyroclastic deposit (i.e. PK<sub>1</sub>) is a result of heterogeneous olivine distributions and crystal:melt ratios within the erupting magma, rather than representing products of different magma batches. Furthermore, these results suggest that the variable olivine content relative to the melt fraction inferred for PK<sub>1</sub> (5 - 44%), may be more representative of explosively erupted kimberlite magma than that observed in CK<sub>2</sub> (40-58%).

#### 4.4.2 CO<sub>2</sub> and H<sub>2</sub>O variation with time

The sequence of kimberlite deposits exposed at A154N document substantial variations in the proportions of volatiles (i.e. exsolved and dissolved) during emplacement or eruption. For example, the earliest phase of eruption represented by the CK<sub>1</sub> dyke contains groundmass carbonate, abundant carbonate-serpentine (i.e. CO<sub>2</sub> and H<sub>2</sub>O) domains or pools, and abundant miarolitic cavities. These features imply the following for CK<sub>1</sub>: (1) the presence of an exsolved CO<sub>2</sub>-H<sub>2</sub>O fluid phase physically coupled to the melt (e.g. miarolitic cavities) at the time of eruption; and (2) the presence of dissolved CO<sub>2</sub> within the melt which allowed for crystallization of groundmass carbonate.

Juvenile pyroclasts from PK<sub>1</sub> record variable amounts of volatiles. Juvenile pyroclasts can contain 0 – 20% vesicles, however, vesicles are present in only 14% of the measured JPs within a limited size range (0.5 – 20 mm<sup>2</sup>). The small proportion of vesiculated JPs may be the result of elutriation of low-density particles during eruption and emplacement, or gas-escape from small JPs with high melt temperatures and low melt viscosities (Cas et al., 2008). Moreover, the small size of kimberlite pyroclasts (all < 5 cm) enables an efficient release of gas during fragmentation in the erupting system. However, single sizes of JPs contain both vesiculated and non-vesiculated textures. Some JPs also contain both lath-shaped carbonate laths and carbonate-serpentine domains (Fig. 4.7). The diversity in vesicle content found within JPs of PK<sub>1</sub> of all sizes implies that a single magma experienced variable degrees of exsolution prior to disruption into discrete fragments. The occurrence of groundmass carbonate, carbonate laths and carbonate-lined or filled vesicles in the same JP is rare (1 sample); the presence or

absence of groundmass carbonate and carbonate laths may be due to a heterogeneity in CO<sub>2</sub> solubility reflective of subtle compositional differences within the ascending magma (Brooker et al., 2001).

Late dykes (CK<sub>2</sub>) contain only rare carbonate-serpentine domains, minor miarolitic cavities and never contain microphenocrysts of carbonate minerals. The lack of textural evidence for an exsolved fluid phase could imply either efficient post-emplacement de-gassing of the dyke, or exsolution and escape of gases during its ascent. However, the crystal-rich nature and presumed rapid-cooling time for thin (< 1 m thick) dykes would severely inhibit the vertical movement and/or removal of exsolved gases from a static dyke. Therefore, I suggest CK<sub>2</sub> had minimal exsolved fluid when it was emplaced; the implication is that the majority of fluid exsolution occurred during transport.

Taken together, these variations in the mineralogical and textural expression of CO<sub>2</sub> and H<sub>2</sub>O in deposits having an established sequence of emplacement tell us about the relative proportion of both exsolved and dissolved fluid phases present in erupting kimberlite magmas:  $CK_1 X_{CO_2+H_2O} > PK_1 X_{CO_2+H_2O} > CK_2 X_{CO_2+H_2O}$ .

#### 4.4.3 Fluid phase separation in kimberlite

These observations lead to several possible hypotheses regarding emplacement of kimberlite magmas (CK<sub>1</sub>, PK<sub>1</sub>, and CK<sub>2</sub>) at A154N through time: (1) as three magma pulses distinct in space and time origins related only by the path they take to the near-surface; (2) as distinct magma pulses originating from the same location in the mantle at different times; or (3) as a single, separated three-phase flow originating at the same time from the same location.

I submit that different physical attributes (% solids, gases, etc.) coupled with clear differences in emplacement style (fissure dykes, explosive eruption, passive intrusion), and known relative timing suggest CK<sub>1</sub>, PK<sub>1</sub>, and CK<sub>2</sub> are genetically-related in space, time, and composition.

The presumed low viscosity and high volatile contents (Price et al., 2000) in kimberlite melts implies that buoyant and coalescing gas bubbles may be able to ascend

at different velocities than kimberlite melt (e.g. Vergnolle and Jaupart, 1990). In this case, gas-streaming may develop, and the ascending magmas can be described as an “open-system” (sensu Cashman and Mangan, 1994). During open-system degassing, gas bubbles can migrate from deeper to shallower parts of a body of magma (Gonnermann and Manga, 2007; Namiki and Manga, 2008).

If CK<sub>1</sub>, PK<sub>1</sub> and CK<sub>2</sub> are derivatives of a single magma pulse, clear differences in exsolved gas proportions in the magma suggest gas was efficiently moving through the kimberlite melt in open-system behavior. However, phase separation was not efficient enough to suppress explosive eruption; high amounts of exsolved gas and a breach of the present-day surface suggest CK<sub>1</sub> was likely explosive, followed by the clearly explosive PK<sub>1</sub> event. This implies that exsolving gas was still coupled to the melt (e.g. Parfitt et al., 1995). This could result from fast ascent rates which would reduce the differences in rise velocity between bubbles and the kimberlite melt (Gonnermann and Manga, 2007). Alternatively, high volatile contents could support continuous production of a fluid phase during ascent to the point of eruption, whether or not the fluid phase had begun separating earlier during transport. Furthermore, fresh, unaltered rocks and juvenile pyroclasts from each unit (CK<sub>1</sub>, PK<sub>1</sub>, CK<sub>2</sub>), contain minerals that may reflect the primary volatile content of the magma at the time of emplacement (e.g. H<sub>2</sub>O in serpentine, CO<sub>2</sub> in calcite), and suggests incomplete exsolution of the volatiles. The increasingly higher crystal content with time (CK<sub>1</sub> to PK<sub>1</sub> to CK<sub>2</sub>) could also act to inhibit efficient out-gassing of exsolved phases (Klug and Cashman, 1996).

The apparent variations in fluid contents at the time of emplacement and eruption are interpreted to reflect the efficiency of fluid exsolution and fluid separation within a single magma pulse during transport from mantle to surface. In addition, observed variations in olivine crystal content are interpreted to reflect decoupling of the ‘crystal cargo’ (Davidson et al., 2004) from its host melt. The decoupling of fluid and solids from the melt is facilitated by the long ascent path (> 200 km) and the high volatile content and low viscosity (0-100 Pa s) of the kimberlite magma. Moreover, the settling velocities of particles (i.e. olivine crystals) in turbulent flows can be higher than those in still fluids (Wang and Maxey, 1993; Yang and Shy, 2005). Combined, these processes resulted in an ascending magma column that was strongly stratified. The ascending

column of magma would feature a gas-rich, relatively crystal-poor top or front followed by relatively fluid-depleted magma that increased in olivine content with depth. The eruption of the stratified column of ascending magma would tap sequentially a gas-dominated magma, a less gas-rich magma showing a range of olivine contents, and lastly a crystal rich, largely degassed magma. This evolution in magma composition (e.g. proportions of gas:melt:solid) would greatly modulate the style (i.e. effusion vs. explosive) of emplacement.

#### 4.4.4 Vent geometry and mass flux ( $M_f$ )

One advantage offered to volcanologists by mining of kimberlite is direct observation of the shape and size of the volcanic conduit. The combination of drill-core intercepts, downhole geophysical measurements, and open-pit surveys at A154N provides a robust 3-D model geometry for the volcanic conduit (Figs. 4.1, 4.8a and b). From this model it is possible to deduce the shape of the vent/conduit system for each phase of the eruption, and use these geometries to constrain associated mass flux rates.

Here, model cross-sectional areas taken at 615 m below present-day surface (-200 m asl) are used for CK<sub>1</sub>, PK<sub>1</sub> and CK<sub>2</sub> to constrain our eruption model of the A154N kimberlite: CK<sub>1</sub> = 500 m<sup>2</sup>; PK<sub>1</sub> = 253 m<sup>2</sup>; CK<sub>2</sub> = 143 m<sup>2</sup>. These intersections are used because they represent the minimum cross-sectional areas that all kimberlite magma (extrusive and intrusive) must have passed through. These conduit geometries are combined with measured (e.g. olivine content) and inferred magma properties (e.g.  $\rho_{\text{melt}}$ ,  $X_{\text{CO}_2+\text{H}_2\text{O}}$ ) to provide first-order estimates on mass fluxes for the different phases of the eruption.

The mass flux ( $M_f$ : kg s<sup>-1</sup>) of kimberlite magma through a dyke and supporting the eruption of CK<sub>1</sub> is computed from:

$$M_f = h \cdot l \cdot \rho_B \mu \quad (4.1)$$

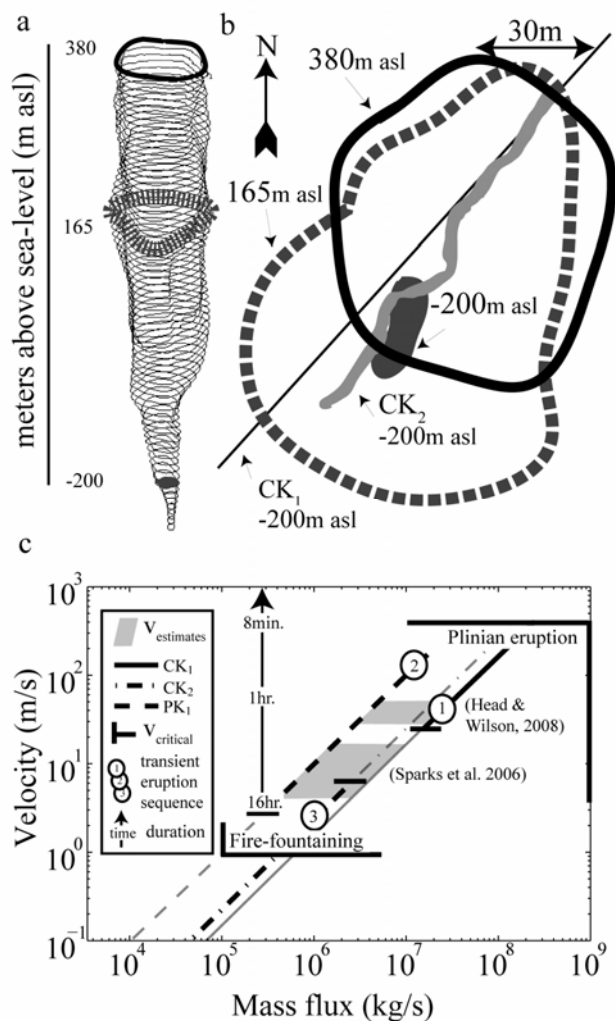


**Figure 4.8:** Vent geometries for A154N and calculated mass fluxes: (a) Inclined profile view of A154N delineated by 5m horizontal slices showing smooth, irregular vent margins and geometries near surface (black; 35m depth), at the widest intersection (grey dashed; 255 m), and narrowest intersection (grey shaded; 615m); (b) outlines of cross-sectional areas of PK<sub>1</sub> are shown at surface (35 m below surface), at maximum cross-sectional area (255 m), and minimum cross-sectional area (615 m). Outlines of vent geometry also for CK<sub>1</sub> and CK<sub>2</sub> at 615m below present-day surface; (c) calculated relationship between velocity vs. mass flux for CK<sub>1</sub> (solid line) and PK<sub>1</sub> (dashed line) eruptions, and intrusion of CK<sub>2</sub> (dash-dot) based on estimated magma properties. Brackets indicate observational limits for least explosive (fire-fountaining) and most-explosive eruption (Plinian) styles. Bars indicate critical velocities necessary for turbulence in dykes given conduit geometry and estimated viscosity. A likely progression based on the nature of emplacement (fissure dyke, pipe-excavation, passive intrusion) is indicated by numbers (1,2,3). Expected eruption durations for constant mass flux in PK<sub>1</sub> are indicated for a range of velocities (arrow).

where  $h$  is the dyke thickness,  $l$  the dyke length,  $\rho_B$  the bulk density of the erupting mixture of gas, crystals and melt, and  $\mu$  the velocity of the mixture (Wilson and Parfitt 2007). Bulk density of the magma is estimated from:

$$\rho_B = (1 - n_f - n_x) \cdot \rho_m + (n_f \cdot \rho_f) + (n_x \cdot \rho_x) \quad (4.2)$$

where  $\rho_m$  is the density of the melt,  $\rho_f$  and  $\rho_x$  are the densities of the exsolved fluid phase and the solids, respectively, and  $n_f$  and  $n_x$  are the corresponding volume fractions.

For these estimates, a ratio of H<sub>2</sub>O:CO<sub>2</sub> of 1 is assumed, and  $n_f$  of 60%, 90% and 5% for CK<sub>1</sub>, PK<sub>1</sub> and CK<sub>2</sub>, respectively. Assumptions of volumetric gas fractions are based on: i) estimates of maximum gas fractions for inflated but non-disrupted (i.e. coherent; e.g. CK<sub>1</sub>) magmas (< 65%; e.g. Melnik et al., 2005); ii) conditions for magma fragmentation (70-99%; e.g. Melnik et al., 2005; Sparks and Wilson, 1982) capable of producing pyroclastic deposits (e.g. PK<sub>1</sub>); and iii) textural observations (Section 3.3) on intrusive rocks (e.g. CK<sub>2</sub>). Measured modal olivine abundance (Sections 3.1, 3.2) is used for  $n_x$ . The model calculated densities include: 117 kg m<sup>-3</sup> for the fluid phase (500 bars at 1200°C), 2900kg m<sup>-3</sup> for the melt and 3300kg m<sup>-3</sup> for olivine crystals (cf. Russell et al., 2006). Calculated  $\rho_B$  of solid, fluid and melt mixtures are 1238kg m<sup>-3</sup>, 405kg m<sup>-3</sup>, and 2951kg m<sup>-3</sup> for CK<sub>1</sub>, PK<sub>1</sub>, and CK<sub>2</sub>, respectively.

Model values of mass flux are computed from the observed conduit cross-sectional areas and an assumed range of possible eruption velocities (Fig. 4.8c). Our discussion uses mass eruption fluxes and eruption velocities estimated for two end-member styles of explosive eruption: Hawaiian (fire-fountaining) and Plinian (arrow brackets; Fig. 4.8c). Minimum estimates of mass fluxes and eruption velocities for low-intensity Hawaiian-style eruptions are 10<sup>4</sup> kg s<sup>-1</sup> and 1 m s<sup>-1</sup> (Parfitt et al., 1995), respectively; Plinian style eruptions have maximum mass fluxes of 10<sup>9</sup> kg s<sup>-1</sup> and eruption velocities of 400 m s<sup>-1</sup> (Schmincke, 2004). An additional constraint is provided by assuming that transport of gas-rich kimberlite magmas is likely to be turbulent (Head and Wilson, 2008; Sparks et al., 2006). In order to sustain turbulent flow in an ascending and erupting kimberlite magma, a critical Reynolds' number ( $Re_c \sim 1 - 4 \times 10^3$ ; variable

with flow geometry) must be maintained (Rott, 1990) requiring a minimum, critical velocity ( $v_c$ ):

$$v_c = \frac{(\text{Re}_c) \cdot \eta}{d_c \cdot \rho_B} \quad (4.3)$$

where  $\text{Re}_c$  is the Reynolds number threshold for turbulent behaviour in dykes,  $\eta$  is magma viscosity,  $d_c$  is characteristic dyke width or pipe diameter, and  $\rho_B$  is the bulk density.

Assuming a  $\text{Re}_c$  of 2000 (e.g. Campbell, 1985), the critical velocity is calculated for turbulent ascent of a melt with a  $\eta$  of 10 Pa s and characteristic conduit widths of 0.5, 15 and 1 m for CK<sub>1</sub>, PK<sub>1</sub>, and CK<sub>2</sub>, respectively. Given the  $\rho_B$  calculated above, the corresponding critical velocities for sustained turbulent flow are 32.3, 3.3, and 6.8 m s<sup>-1</sup>. These calculated velocities, therefore, provide an independent constraint on the minimum eruption velocities at A154N (Fig. 4.8c). These values are in accord with those estimated by Sparks et al. (2006) (4-16 m s<sup>-1</sup>) based on turbulent flow, buoyancy-driven crack-propagation, xenolith transport, and minimum velocities required to avoid freezing. Head and Wilson (2008) suggest large average pressure gradients (60 kPa m<sup>-1</sup>) between the source and surface presumed for ascending kimberlite magmas can lead to even higher minimum velocities (~30-50 m s<sup>-1</sup>). These velocity criteria are shown as shaded parallelograms in Figure 4.8c.

Given these constraints, several observations can be made regarding eruption behavior at A154N. First, the minimum ascent velocities required for turbulent transport of kimberlite magma demand relatively high minimum mass flux rates. For example, if a constant velocity of 10m s<sup>-1</sup> is assumed, as estimated for kimberlite magma moving through dykes (Sparks et al., 2006), minimum mass fluxes would still range between 10<sup>6</sup>-10<sup>6.5</sup> kg s<sup>-1</sup> (Fig. 4.8c), several orders of magnitude higher than a low-intensity basaltic fire-fountaining event (e.g. Houghton and Gonnermann, 2008; Parfitt et al., 1995). Second, changing vent geometries require either transient eruption velocities or transient mass fluxes. If mass flux is constant for the three events (CK<sub>1</sub>, PK<sub>1</sub>, CK<sub>2</sub>), velocity must increase at least one order of magnitude in time from CK<sub>1</sub> to PK<sub>1</sub> (Fig. 4.8c) followed by

a subsequent decrease in the transition from PK<sub>1</sub> to CK<sub>2</sub>, due to changes in bulk density and conduit geometry. If the three emplacement events at A154N are part of a single eruption cycle, this implies a highly transient eruption style. The eruption of the A154N kimberlite would have featured both waxing (CK<sub>1</sub> to PK<sub>1</sub>) and waning (PK<sub>1</sub> to CK<sub>2</sub>) stages in terms of velocity and or mass flux. It is noted, however, that neither velocity nor mass flux are likely to be steady-state parameters in kimberlite eruptions. In addition, conduit geometry likely changes during eruption, and may increase in cross sectional area and deepen as the eruption continues. The implication is that the observed conduit diameters are absolute maxima.

A more-likely, hypothetical velocity-flux path reflecting transient activity in the emplacement at A154N is shown with numbers (1,2,3) in Figure 4.8c. Initial eruption from a fissure dyke would likely begin with a high eruption velocity and high mass flux ( $M_f$ ) but, as the vent enlarged with time, velocity would decay. However, given that the equivalent-area circular radii of vents at A154N are relatively small (< 60 m), it is likely that the eruptions (CK<sub>1</sub>, PK<sub>1</sub>) remained in a highly-pressurized, “choked flow” state at 615 m below surface for the duration of the eruption, until very low magma supply rates were reached. In this state, gases leaving the vent would expand violently upward and sideways, as the pressure of the mixture adjusts to atmospheric pressure, maintaining high eruption velocities.

#### 4.4.5 Eruption duration calculations

Given the mean density and volume of erupting kimberlite involved in the emplacement events, it is possible to determine the minimum eruption times for emplacement using:

$$t = \frac{V_k}{M_f \cdot \frac{1}{\rho_B}} \quad (4.4)$$

where  $t$  is time (in seconds),  $V_k$  is minimum volume of erupting kimberlite (e.g. solid + melt + fluid),  $M_f$  is mass flux, and  $\rho_B$  is the bulk density.

The fully erupted volume through conduit CK<sub>1</sub> is unknown, and therefore eruption durations for this stage of emplacement at A154N cannot be easily estimated. However, given properties of CK<sub>1</sub> ( $M_f = 10^7 \text{ kg s}^{-1}$ ;  $v = 33 \text{ m s}^{-1}$ ;  $\rho_B = 1238 \text{ kg m}^{-3}$ ) eruption of a similar volume found in PK<sub>1</sub> ( $V_{PK1} = 5.0 \times 10^6 \text{ m}^3$ ) through the CK<sub>1</sub> conduit would take  $\sim 12 \frac{1}{2}$  minutes. Given properties of the pipe-forming eruption of A154N ( $\rho_B = 405.7 \text{ kg m}^{-3}$ ;  $V_{PK1} + V_{gas} = 5.0 \times 10^7 \text{ m}^3$ ), the portion of the eruption responsible for the PK<sub>1</sub> deposit would have lasted at least  $16 \frac{1}{2}$  hours if the style were Hawaiian ( $M_f \sim 10^{5.2} \text{ kg s}^{-1}$  and  $v \sim 3.3 \text{ m s}^{-1}$ ). If, however, upon leaving the geometric constraints of the conduit at A154N, the erupting mixture (i.e. mass flux) could become fully inflated and match Plinian-style intensities ( $v \sim 400 \text{ m s}^{-1}$ ), the PK<sub>1</sub> deposits could be produced in a minimum of  $\sim 8$  minutes (Fig. 4.8c). Given the mean density and an assumed minimum volume of kimberlite in CK<sub>2</sub> above 615m depth ( $\rho_B = 2951 \text{ kg m}^{-3}$ ;  $V_{CK2} = 1.1 \times 10^5 \text{ m}^3$ ) the emplacement of the late dykes would take place in at least  $\sim 14$  minutes (at  $10^{6.5} \text{ kg s}^{-1}$  and  $1 \text{ m s}^{-1}$ ).

Calculated emplacement times of minutes to hours are much shorter in duration than those hypothesized by Sparks et al. (2006) (hours to days) based on magma supply rate limitations and inferred properties of kimberlite magmas. However, kimberlite eruptions likely eject more kimberlite than is preserved intra-vent (e.g. Porritt et al., 2008; Sparks et al., 2006); thus, the emplacement times for PK<sub>1</sub> are likely a small fraction of the true, total eruptive times for the entire A154N system, and may be up to an order of magnitude longer. For example, if an extra-crater edifice formed from the eruption of PK<sub>1</sub> was 80m tall and extended to a radius of 0.5 km away from the vent ( $V_{PK1total} \sim 3.0 \times 10^7 \text{ m}^3$ ) emplacement of PK<sub>1</sub> would take place in at least 1 hour if Plinian in intensity, and at least 100 hours if the style were Hawaiian.

If extreme ascent velocities (e.g.,  $50 \text{ m s}^{-1}$  vs.  $1 \text{ m s}^{-1}$ ) are assumed for end-member portions of a single magma pulse (gas-rich vs. gas-depleted) interpreted to result from phase separation, a maximum total time interval between CK<sub>1</sub>, PK<sub>1</sub>, and CK<sub>2</sub> can also be calculated. Gas-rich ( $\sim 50 \text{ m s}^{-1}$ ) and gas-depleted ( $\sim 1 \text{ m s}^{-1}$ ) portions of a single magma would ascend 200 km in approximately  $\sim 1$  hrs and  $\sim 55$  hrs, respectively, leading to – at most – a time interval of  $\sim 2$  days for the emplacement of CK<sub>1</sub>, PK<sub>1</sub>, and CK<sub>2</sub>.

#### 4.5 Emplacement model for the A154N kimberlite

The three events at A154N (CK<sub>1</sub>, PK<sub>1</sub>, CK<sub>2</sub>) are interpreted to record emplacement of a separated three-phase flow involving kimberlite melt, crystals and a proportion of exsolved CO<sub>2</sub>-H<sub>2</sub>O fluid (Fig. 4.9). The timing and nature of the emplacement style (fissure dyke, pipe excavation, intrusive dykes) is suggested to be a direct result of varying physical properties (crystal, melt and gas content) of the magmas supplied to the A154N context. First, a transient, low-volume, gas-charged (i.e. CO<sub>2</sub>, H<sub>2</sub>O) fissure eruption of olivine-poor kimberlite magma emplaced CK<sub>1</sub>. Breach of the surface would immediately lower the pressure in the ascending magma, triggering rapid downward movement of a de-pressurization wavefront, allowing for exsolution of volatile phases (e.g. CO<sub>2</sub> and H<sub>2</sub>O), wall rock erosion and therefore a change in the vent geometry.

Second, a sustained (i.e. high flux, long duration) eruption of variable gas and olivine content excavated the A154N pipe and deposited the PK<sub>1</sub>. De-pressurization of the magma erupting through the fissure dyke would initially accelerate the eruption velocity, lower the bulk density, and enhance magma fragmentation. Late-exsolving gases within magma whose crystal content was increasing with time remain coupled to the melt, and rapidly expand as the magma approaches the surface, eventually over-pressurizing the system, thus leading to explosive excavation of surrounding country rock. The degree of overpressure in the magma prior to eruption directly determines the initial vent diameter and geometry (Fig. 4.9). Wall rock erosion would initiate at zones of structural weakness or lithology contrasts within the country rock, explosively widening the fissure dyke where these weaknesses intersect. This explosive vent-widening focuses the erupting mixture of gas, solids and liquid from the fissure dyke into a circular vent, which becomes the path of least frictional resistance. The sustained eruption proceeds to “drill” down into the country rock, efficiently excavating down to >750m below surface.

Third, non-eruptive, olivine-rich and gas-poor coherent kimberlite (CK<sub>2</sub>) was passively emplaced into the interior of PK<sub>1</sub> and along the contacts between PK<sub>1</sub> and adjacent country rock. The terminus of the intrusions within PK<sub>1</sub> represent levels of

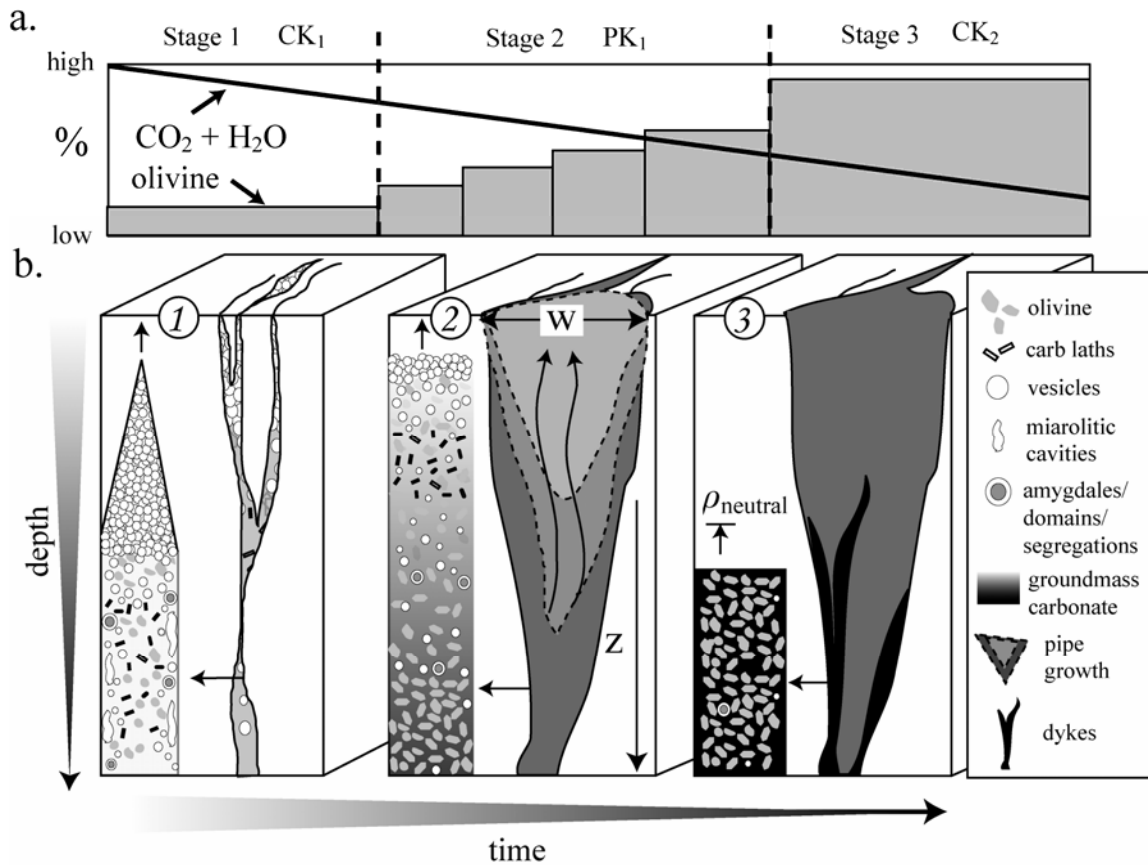


**Figure 4.9:** Progressive model for emplacement and eruption of A154N. Upper panel (a) shows the expected evolution (relative time) in olivine and volatile (CO<sub>2</sub>+H<sub>2</sub>O) contents throughout the eruption cycle. The lower panel (b) denotes the major changes in the nature (melt:solid:fluid ratios) of the erupting magma, and the size and shape of the conduit/feeder system. Panels schematically portray presence and proportions of fluid, olivine and carbonate content for CK<sub>1</sub>, PK<sub>1</sub>, and CK<sub>2</sub>. Stages include: (1) pre-cursor dyke and fracture system (CK<sub>1</sub>) is irregular in orientation, and contains intermittent intervals of coherent kimberlite of variable thickness and country-rock content; (2) PK<sub>1</sub> emplacement initially excavates a crater with width (w), and systematically excavates deeper (z) into the country-rock with time; (3) late, crystal-rich CK<sub>2</sub> only ascends to 0 m asl (i.e., to within 415 m below the surface).

neutral buoyancy for the coherent kimberlite magmas: the mixture of liquid, crystals and gas was not buoyant enough to rise to the surface ( $\rho_{\text{magma}} > \rho_{\text{country rocks}}$ ), despite the relatively low density and semi-permeable texture of the fragmental kimberlite it was ascending through. This event may have significantly post-dated the eruption which formed the A154N pipe, but the time gap between events cannot be further constrained.

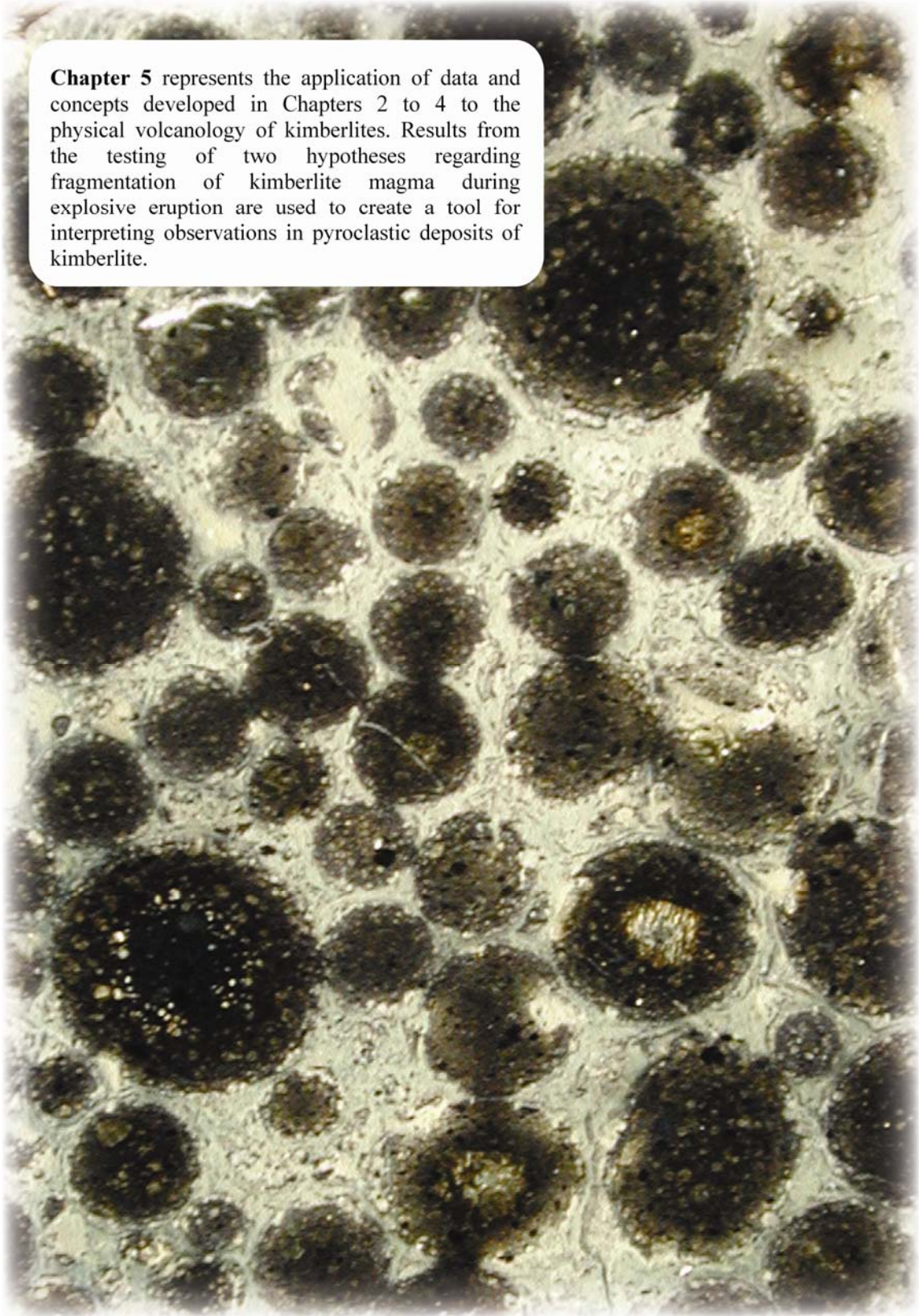
## 4.6 References

- Amelin, Y. (1996) Report on Rb-Sr and U-Pb study of kimberlite samples VR44444A through VR44465A. Confidential Report for Kennecott, Canada Inc., p. 7.
- Barton, E.S. (1996) Rb-Sr Mica age results from the Diavik kimberlite field. Confidential Report for Kennecott Canada, Inc., 5.
- Bower, S.M., and Woods, A.W. (1998) On the influence of magma chambers in controlling the evolution of explosive volcanic eruptions. *Journal of Volcanology and Geothermal Research*, 86(1-4), 67-78.
- Brooker, R.A., Kohn, S.C., Holloway, J.R., and McMillan, P.F. (2001) Structural controls on the solubility of CO<sub>2</sub> in silicate melts: Part II: IR characteristics of carbonate groups in silicate glasses. *Chemical Geology*, 174(1-3), 241-254.
- Campbell, I.H. (1985) The difference between oceanic and continental tholeiites: a fluid dynamic explanation. *Contributions to Mineralogy and Petrology*, 91, 37-45.
- Cas, R.A.F., Porrit, L., Hayman, P., and Pittari, A. (2008) Pyroclast formation processes during explosive kimberlite eruptions. 9th International Kimberlite Conference, extended abstract no. 9IKC-A-00030.
- Cashman, K.V., and Mangan, M.T. (1994) Physical aspects of magma degassing II, Constraints on vesiculation processes from textural studies of eruptive products In M.R. Carroll, and J.R. Holloway, Eds. *Reviews in Mineralogy. Volatiles in Magmas*, 30, p. 446-478. Mineralogical Society of America, Washington D.C.
- Davidson, J.P., Hora, J.M., Garrison, J.M., and Dungan, M.A. (2004) Crustal forensics in arc magmas. *Journal of Volcanology and Geothermal Research*, 140(1-3), 157-170.
- Eggler, D.H. (1978) The stability of dolomite in a hydrous mantle, with implications for the mantle solidus. *Geology*, 6, 397-400.
- Gonnermann, H.M., and Manga, M. (2007) The Fluid Mechanics Inside a Volcano. *Annual Review of Fluid Mechanics*, 39(1), 321-356.
- Graham, I., Burgess, J.L., Bryan, D., Ravenscroft, P.J., Thomas, E., Doyle, B.J., Hopkins, R., and Armstrong, K.A. (1999) Exploration History and Geology of the Diavik Kimberlites, Lac de Gras, Northwest Territories, Canada. In J.J. Gurney, J.L. Gurney, M.D. Pascoe, and S.H. Richardson, Eds. *Proceedings of the VIIth International Kimberlite Conference*, 1, p. 262-279. Red Roof Design, Cape Town, South Africa.
- Head, J.W., and Wilson, L. (2008) Integrated model for kimberlite ascent and eruption. 9th International Kimberlite Conference Extended Abstracts, 1-3.
- Heaman, L.M., Kjarsgaard, B.A., and Creaser, R.A. (2004) The temporal evolution of North American kimberlites. *Lithos*, 76(1-4), 377-397.
- Houghton, B.F., and Gonnermann, H.M. (2008) Basaltic explosive volcanism: Constraints from deposits and models. *Chemie der Erde - Geochemistry*, 68(2), 117-140.
- Klug, C., and Cashman, K.V. (1996) Permeability development in vesiculating magmas: implications for fragmentation. *Bulletin of Volcanology*, 58, 87-100.
- Melnik, O., Barmin, A.A., and Sparks, R.S.J. (2005) Dynamics of magma flow inside volcanic conduits with bubble overpressure buildup and gas loss through

- permeable magma. *Journal of Volcanology and Geothermal Research*, 143(1-3), 53-68.
- Moser, D.E., and Amelin, Y.V. (1996) Report on Rb-Sr geochronology of kimberlite samples BDK, and 9501 through 9504. . Confidential report for Kennecott Canada Inc., p. 3.
- Namiki, A., and Manga, M. (2008) Transition between fragmentation and permeable outgassing of low viscosity magmas. *Journal of Volcanology and Geothermal Research*, 169(1-2), 48-60.
- Parfitt, E.A., Wilson, L., and Neal, C.A. (1995) Factors influencing the height of Hawaiian lava fountains: implications for the use of fountain height as an indicator of gas content. *Bulletin of Volcanology*, 57, 440-450.
- Porritt, L.A., Cas, R.A.F., and Crawford, B.B. (2008) In-vent column collapse as an alternative model for massive volcanoclastic kimberlite emplacement: An example from the Fox kimberlite, Ekati Diamond Mine, NWT, Canada. *Journal of Volcanology and Geothermal Research*, 174(1-3), 90-102.
- Price, S., Russell, J.K., and Kopylova, M. (2000) Primitive magma from the Jericho pipe, N.W.T., Canada: Constraints on primary melt chemistry. *Journal of Petrology*, 41, 789-808.
- Rott, N. (1990) Note on the history of the Reynolds number. *Annual Review of Fluid Mechanics*, 22, 1-11.
- Russell, J.K., Giordano, D., Kopylova, M., and Moss, S. (2006) Transport properties of kimberlite melt. Long Abstract, Kimberlite Emplacement Workshop, <http://www.venuewest.com/8IKC/9ikc.htm>, Saskatoon, Canada.
- Scandone, R. (1996) Factors controlling the temporal evolution of explosive eruptions. *Journal of Volcanology and Geothermal Research*, 72(1-2), 71-83.
- Scandone, R., and Malone, S.D. (1985) Magma supply, magma discharge and readjustment of the feeding system of mount St. Helens during 1980. *Journal of Volcanology and Geothermal Research*, 23(3-4), 239-262.
- Schmincke, H.U. (2004) *Volcanism*. 324 p. Springer, Berlin.
- Sparks, R.S.J., Baker, L., Brown, R.J., Field, M., Schumacher, J., Stripp, G., and Walters, A. (2006) Dynamical constraints on kimberlite volcanism. *Journal of Volcanology and Geothermal Research*, 155(1-2), 18-48.
- Sparks, R.S.J., and Wilson, L. (1982) Explosive volcanic eruptions - V. Observations of plume dynamics during the 1979 Soufriere Hills eruption, St Vincent. *Geophysical Journal of the Royal Astronomical Society*, 69, 551-570.
- Stasiuk, M., Barclay, J., Carroll, M.R., Jaupart, C., Ratte, J., Sparks, R.S.J., and Tait, S. (1996) Degassing during magma ascent in the Mule Creek vent (USA). *Bulletin of Volcanology*, 58, 117-130.
- Vergnolle, S., and Jaupart, C. (1990) Dynamics of degassing at Kilauea Volcano, Hawaii. *Journal of Geophysical Research*, 95, 2793-2809.
- Wang, L.P., and Maxey, M.R. (1993) Settling velocity and concentration distribution of heavy particles in homogeneous isotropic turbulence. *Journal of fluid mechanics*, 256, 27-68.
- Wilson, L., Sparks, R.S.J., and Walker, G.P.L. (1980) Explosive volcanic eruptions: IV. The control of magma properties and conduit geometry on eruption column behavior. *Geophysical Journal Royal Astronomical Society*, 63, 117-148.

Yang, T.S., and Shy, S.S. (2005) Two-way interaction between solid particles and homogeneous air turbulence: particle settling rate and turbulence modification measurements. *Journal of fluid mechanics*, 526, 171-216.

**Chapter 5** represents the application of data and concepts developed in Chapters 2 to 4 to the physical volcanology of kimberlites. Results from the testing of two hypotheses regarding fragmentation of kimberlite magma during explosive eruption are used to create a tool for interpreting observations in pyroclastic deposits of kimberlite.



## 5 Fragmentation in kimberlite: products and intensity of explosive eruption<sup>6</sup>

### 5.1 Introduction

Eruptions of kimberlite volcanoes are a poorly-understood phenomena (c.f. Chapter 1). There have been no historical eruptions of kimberlite, and kimberlite volcanoes are rarely preserved. As a consequence, the styles of explosive eruption of kimberlite magma are undocumented. In particular, the mechanisms of fragmentation have not been established for explosive eruption of kimberlite. However, mining of kimberlite pipes for diamonds has allowed for detailed petrographic and mineralogic observation of rock textures and pyroclastic products produced by kimberlite eruptions. Here, fragmentation processes in explosive kimberlite eruptions are explored by making observations on pyroclastic kimberlite. Pyroclastic products derived from kimberlite eruptions at Diavik, NWT, Canada and from around the world (Table 5.1) show the following traits:

- A limited size range of pyroclasts relative to eruption of other magma types (Fig. 5.1, Plate I: a,b);
- the presence of fine ash, as a poorly-preserved component of deposits (Plate I: a);
- pyroclast morphologies are dominantly spherical to sub-spherical, and can show curvilinear amoeboid morphologies (Fig. 5.1 Plate II: a,b,c,d);
- crystal:melt ratios are variable within juvenile pyroclasts of crystallized or quenched kimberlite magma (Fig. 5.1, Plate I: g,h);
- pyroclasts show variable amounts of internal vesiculation (Fig. 5.1, Plate I: e,f);
- ‘free’ olivine crystals are the dominant pyroclast type (Fig., 5.1, Plate II: g,h);
- accretionary lapilli (Fig. 5.1, Plate I: c,d) comprising small, angular olivines and fine ash-sized particles are present in many but not all deposits.
- olivine crystals may be partially to fully-coated by jackets of crystallized kimberlite melt (Plate II: e,f).

---

<sup>6</sup> A version of this chapter will be submitted for publication. Moss, S., Russell, J.K. Fragmentation in kimberlite: products and intensity of explosive eruption.

**Table 5.1: Summary of key observations on the nature of kimberlite pyroclasts in deposits described in literature that constrain the nature of eruptions**

Attribute	Where observed/described	Notes	Reference
1) deposits contain fine ash-size particles	Diavik, NWT, Canada	rounded	Moss, 2008; Chapter 5
	Ekati, NWT, Canada	in accretionary lapilli	Porrit et al., 2008
	Star, SK, Canada	fine ash-sized olivine	Harvey et al., 2008; Zonneveld et al., 2004
	Aries, WA, Australia	inferred ash	Downes et al., 2006
	Tokapal, India	serpentinized ash	Mainkar et al., 2004
2) deposits lack large (> 50mm) pyroclasts	Diavik, NWT, Canada	up to 50mm	Moss et al., 2008; Chapter 5
	Venetia, South Africa	lithics < 20cm; olivine < 4mm	Walters et al., 2006
	Star/Orion, SK, Canada	used to recognize individual eruptions	Kjarsgaard, 2008
	Mwadui, Tanzania	up to 18mm	Stiefenhofer and Farrow, 2004
3) deposits contain abundant 'free' or liberated olivine crystals	Diavik, NWT, Canada	dominant	Moss et al., 2008, 2009; Chapters 4,5
	Ekati, NWT, Canada	dominant	Porrit et al., 2008; Nowicki et al., 2004
	Orapa, Botswana	dominant	Brown et al., 2008
	Star, SK, Canada	in sedimentary rocks	Zonneveld et al., 2004
4) olivine crystal shapes range from rounded to angular	Victor, ONT, Canada	broken crystals in apparent coherent rocks	VanStraaten et al., 2008
	Diavik, NWT, Canada	minor crystal shape modification	Moss et al., 2008; Chapter 5
	Ekati, NWT, Canada	mostly angular in VK rocks	Nowicki et al., 2008
	Venetia, South Africa	rounded or highly fractured	Walters et al., 2008
	Orapa, Botswana	rounded to broken	Brown et al., 2008
	Udachnaya, Russia	broken crystals	Kamenetsky, 2008
5) deposits contain variable ratios of 'free' olivine crystals to clots of crystallized kimberlite melt	Diavik, NWT, Canada	measured	Moss et al., 2009; Chapter 4
	Victor, ONT, Canada	measured	Webb et al., 2004; VanStraaten et al., 2008
	Kimberley, South Africa	described	Clement, 1982
	Buffalo Head Hills, AB, Canada	described	Boyer et al., 2003
	Orion, SK, Canada	described	Pittari et al., 2008
	Ekati, NWT, Canada	described	Nowicki et al., 2008
	Mwadui, Tanzania	described	Stiefenhofer and Farrow, 2004
	Star, SK, Canada	variable between volcanoclastic deposits	Zonneveld et al., 2004
6) juvenile pyroclasts contain variable amounts of vesicles	Diavik, NWT, Canada	variably vesicular	Moss et al., 2008, 2009; Chapters 4,5
	Attawapiskat, ONT, Canada	present	Lefebvre et al., 2008
	Victor, ONT, Canada	minor	VanStraaten et al., 2008; Webb et al., 2004
	Aries, WA, Australia	present	Downes et al., 2006
	FALC, SK, Canada	abundant	Leckie et al., 1997; Scott-Smith, 2008;
	Buffalo Head Hills, AB, Canada	present	Boyer et al., 2004; Field&Scott-Smith, 1999
	Sturgeon Lake, SK, Canada	present	Scott-Smith, 1995
	Tokapal, India	present	Mainkar et al., 2004
7) juvenile pyroclasts have spherical external morphologies	Victor, ONT, Canada	photographs	Webb, 2006;
	Diavik, NWT, Canada	dominant	Moss et al., 2008; Chapter 5
	Ekati, NWT, Canada	generally rounded but also elongate	Nowicki et al., 2004
	Mountain Lake, AB, Canada	typically cored by single olivine crystal	Wood et al., 1998
8) juvenile pyroclasts have "amoeboid" or irregular-shaped external morphologies	FALC, SK, Canada	abundant	Field and Scott-Smith, 1999
	Candle Lake, SK, Canada	present	Field and Scott-Smith, 1999; Mitchell, 1997
	Sturgeon Lake, SK, Canada	present, curvilinear to amoeboid	Field and Scott-Smith, 1999
	Buffalo Head Hills, AB, Canada	present	Boyer et al., 2004; Field&Scott-Smith, 1999
	Ekati, NWT, Canada	maybe due to alteration	Porrit et al., 2008
9) olivine crystals have complete or partial selvages of melt	Gahcho Kue, NWT, Canada	abundant in "TK"	Hetman et al., 2003
	Diavik, NWT, Canada	ubiquitous	Moss et al., 2009; Chapter 4
	Ekati, NWT, Canada	ubiquitous, "cored" juvenile clasts	Crawford et al., 2008
	Pimenta Bueno, Brazil	abundant in "TK"	Masun et al., 2008
	Koffiefontein, South Africa	"pelletal" lapilli with very thin rims	Naidoo et al., 2004
	Lethakane, South Africa	"pelletal" lapilli	Trickett et al., 2006
	Yakutia, Russia	in crystal-supported rocks; photographs	Kurszlaukis et al., 2008
10) deposits contain accretionary lapilli	Diavik, NWT, Canada	present	Moss et al., 2008; Chapter 5
	Ekati, NWT, Canada	present	Porrit, 2008; Mustafa et al., 2003
	Jwaneng, Botswana	rare	Webb et al., 2004
	Attawapiskat, ONT, Canada	present	Lefebvre et al., 2008
	Venetia, South Africa	abundant	Tait et al., 2004; Kurszlaukis&Barnett, 2003
	DO-27, NWT, Canada	rare	Harder et al, 2008
	Archangelsk, Russia	rare	Mahotkin et al., 2003
	Buffalo Head Hills, AB, Canada	present	Boyer et al., 2004

**Figure 5.1:** Photographic plates (Plate I, II) showing types and shapes of juvenile pyroclasts derived from explosive eruption of kimberlite magma in A154N, Diavik, NWT:

**Plate I:** Types of pyroclasts: (a) very fine ash-sized (<0.1 mm in diameter), round juvenile pyroclasts of kimberlite cored by olivine crystals; (b) large juvenile pyroclast (>3.5 cm in diameter); (c) large, concentrically-zoned, rim-type accretionary lapillus (sensu Shumacher and Schmincke, 1991) comprising a core of very fine-grained ash, a central band of olivine crystal fragments, and outer rims of successively finer-grained ash particles; (d) multiple rim-type accretionary lapilli (AL) comprising olivine crystal fragments, fine ash-sized juvenile pyroclasts of crystalline kimberlite (JP), and very fine-grained ash; (e) vesiculated juvenile pyroclast (v) with serpentinized olivine crystals and groundmass spinel crystals; (f) dense, non-vesiculated and olivine crystal-rich juvenile pyroclast with a serpentinized outer edge; (g) crystal-poor juvenile pyroclast of crystalline kimberlite with groundmass spinel crystals; (h) crystal-rich juvenile pyroclast of crystalline kimberlite cored by kelyphitized garnet.

**Plate II:** Morphologies of pyroclasts (a) round juvenile pyroclasts of crystalline kimberlite cored by olivine crystals; (b) round, fine ash-sized juvenile pyroclast of crystalline kimberlite enclosing multiple small (<0.125 mm in diameter) olivine crystals, in a matrix of serpentine; (c) curvilinear outside margin of juvenile pyroclast; (d) ash-sized, “amoeboid”-shaped juvenile pyroclast of crystalline kimberlite with vesicles, olivine crystals, and groundmass spinel; (e) partial and complete selvages of crystalline kimberlite around fresh olivine crystals in crystal and clast-supported fabric; (f) fine ash-sized juvenile pyroclast with complete, thin (<0.125 mm) selvaige of crystalline kimberlite around a single olivine crystal; (g) round, serpentinized olivine crystals in a crystal and clast-supported matrix; (h) sub-round to angular, fresh olivine crystals and ash-sized juvenile pyroclasts of crystallized kimberlite in a fine-grained matrix.

Plate I:

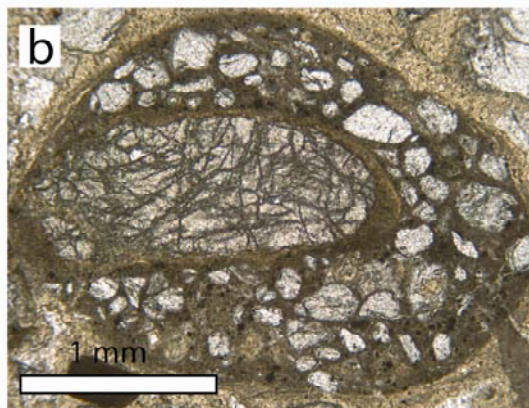
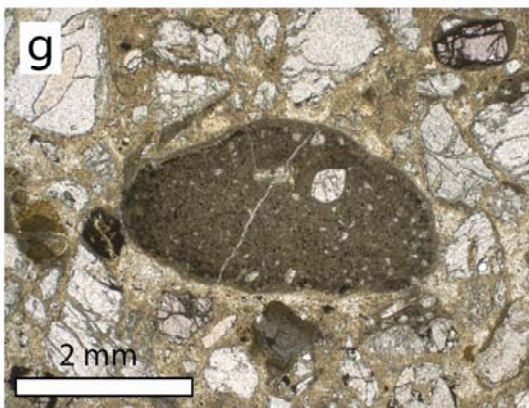
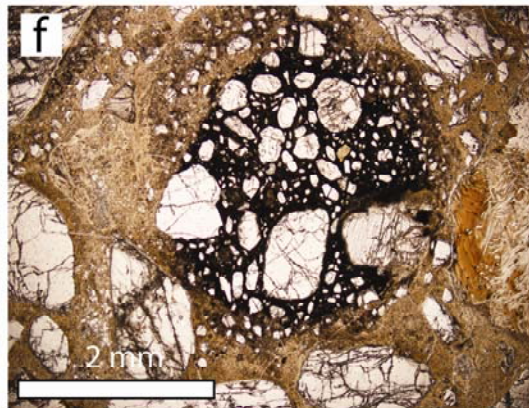
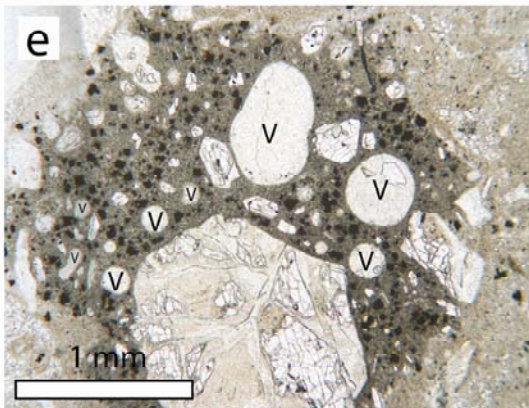
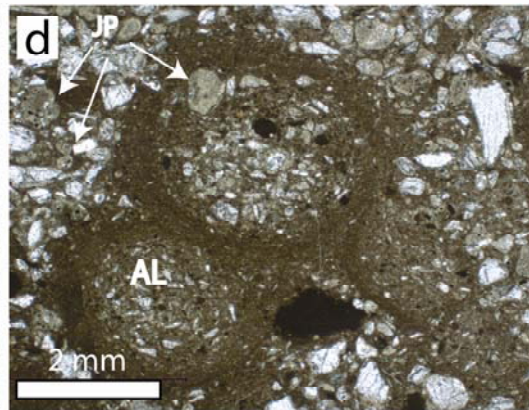
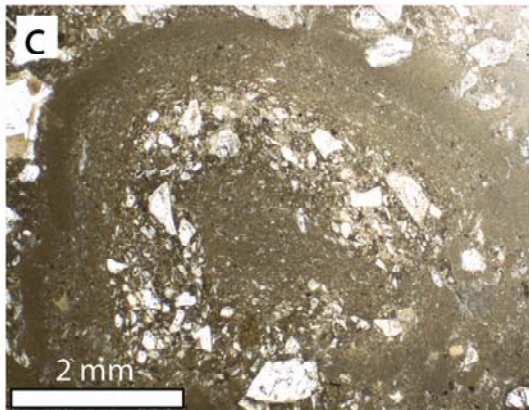
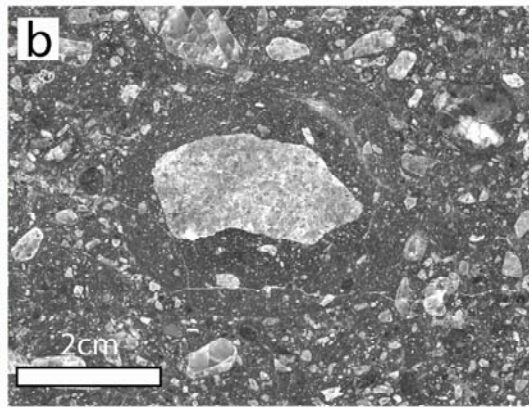
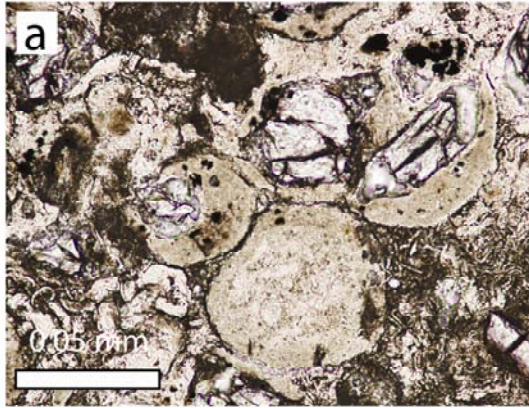
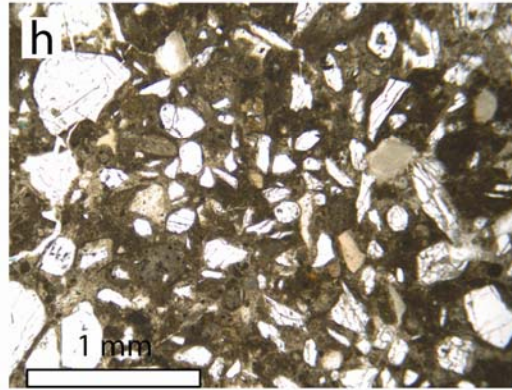
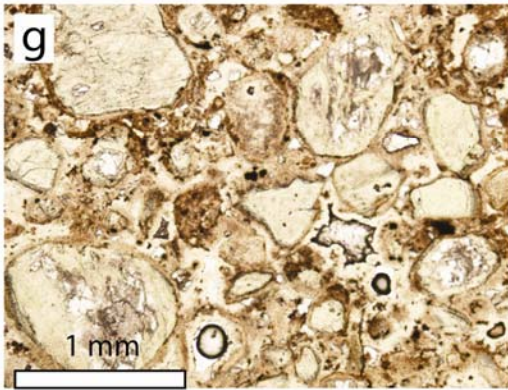
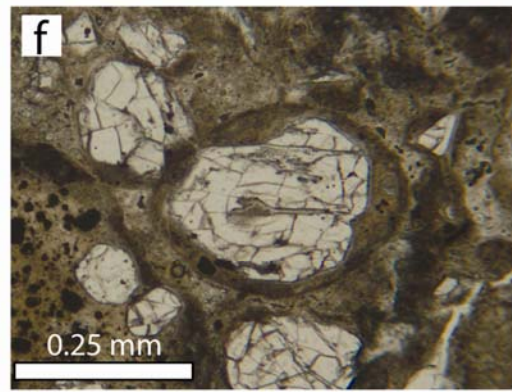
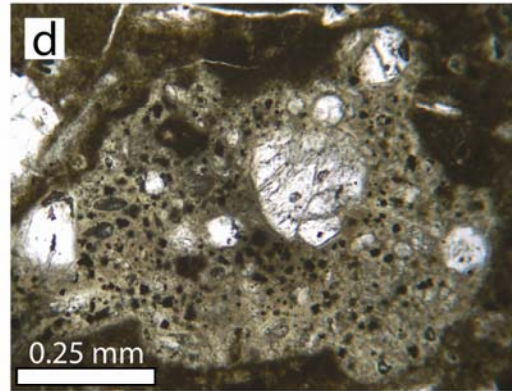
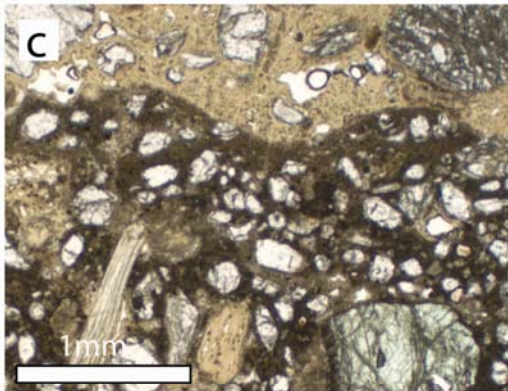
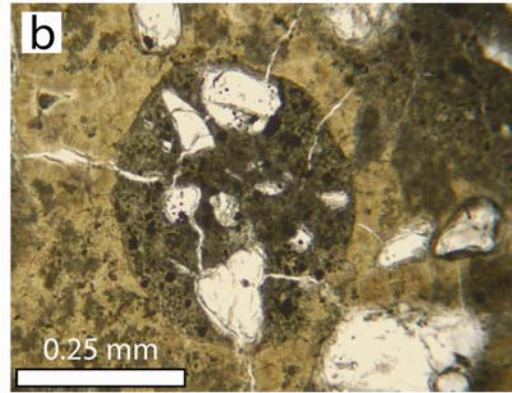
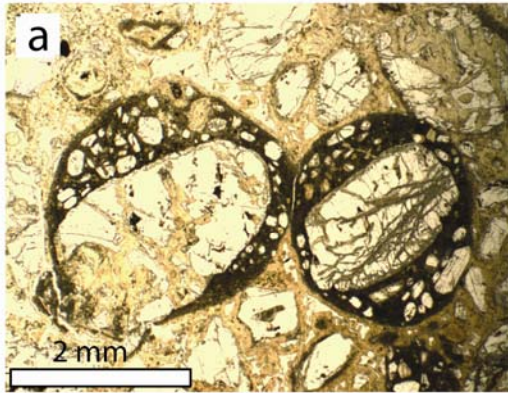


Plate II:



From such observations, it is clear that kimberlite eruption styles are capable of producing a variety of pyroclast types. Any hypothesis regarding the manner(s) in which kimberlite magma disrupts must address this textural diversity. However, all deposits of pyroclastic kimberlite are dominated by free olivine crystals and juvenile pyroclasts of crystallized kimberlite magma. Thus, discussions of kimberlite eruption styles must consider properties of these two pyroclast types.

Here, two hypotheses are proposed for how kimberlite magmas are modified due to explosive eruption: (1) olivine crystals break during kimberlite eruption, and (2) kimberlite melt can efficiently separate from crystals during eruption. These ideas are tested against data collected from field study and image analysis of coherent kimberlite (CK<sub>2</sub>; Chapter 2) and pyroclastic kimberlite (PK<sub>2</sub>) within a kimberlite pipe at Diavik, NWT. Based on these data, possible controls on the formation and modification of pyroclasts during eruption are discussed. Olivines are expected to break because of rapid pressure changes during the explosive eruption and from particle-to-particle collisions.

Disruption of kimberlite magma into pyroclasts is driven by ductile deformation processes, rather than by brittle fragmentation. The extent to which melt separates from olivine crystals is a consequence of the relative proportions of gas, melt and crystals. Finally, properties and proportions of juvenile pyroclasts in deposits of pyroclastic kimberlite are used to index the relative intensity of kimberlite eruptions. Specifically, a fragmentation index is proposed for kimberlite eruption based on: a) olivine crystal populations, and b) ratios of 'free' olivine crystals to juvenile pyroclasts of crystalline kimberlite enclosing olivine crystals.

## **5.2 Hypothesis 1: olivine fragmentation during explosive eruption**

Angular crystals are common components in pyroclastic deposits resulting from explosive volcanic eruptions (Cas and Wright, 1987; Best and Christiansen, 1997; Schmincke, 2004). The angular shape of crystals as a consequence of volcanic eruption has been attributed to crystal-to-crystal interactions in volcanic vents, plumes and flows, and the failure of melt and mineral inclusions due to rapid pressure changes (Best and Christiansen, 1997; Bindeman, 2005). Angular, fractured olivine crystals are common in

kimberlite deposits (Webb et al., 2004; Nowicki et al., 2008), and have been interpreted to result from explosive magmatic eruption (e.g., Pittari et al., 2008), phreato-magmatic explosions (e.g., van Straaten et al., 2008), decompression associated with intrusive emplacement (e.g., Basson and Viola, 2004), and secondary reworking of primary deposits (e.g., Boyer et al., 2004).

Preliminary observations of pyroclastic rocks in the A154N kimberlite volcano at Diavik, NWT suggest olivine crystal shapes and sizes in coherent rocks are different than those observed in some pyroclastic rocks (Fig. 5.2). For example, olivine crystals in CK<sub>2</sub> are ellipsoidal in shape, vary from round to sub-round, cover a large size range, and have a characteristic CSD slope (Chapter 3). In contrast, olivine crystals from PK<sub>2</sub> in A154N range from sub-round to angular, may comprise smaller sizes, and are, internally, highly cracked or fractured (Chapter 2). The PK<sub>2</sub> and CK<sub>2</sub> reside in the same volcano, and are approximately the same age (Chapter 2; Graham et al., 1999). Assuming that the olivine crystal contents in the magmas that produced the pyroclastic rocks are the same as those forming dykes within A154N, then the crystal populations from PK<sub>2</sub> and CK<sub>2</sub> can be used to evaluate the effects of volcanic eruption on olivine crystal shapes, sizes, and overall population properties.

### 5.2.1 Methods

The working hypothesis is that olivine crystals break during eruption. To test this hypothesis, field study and image analysis are used to characterize olivine crystal populations in coherent (CK<sub>2</sub>) and pyroclastic rocks (PK<sub>2</sub>) from the A154N kimberlite at Diavik (Fig. 5.3). For olivine in coherent rocks, data collected in Chapter 3 is used. Data on olivine in pyroclastic rocks derives from Chapter 2. Using image analysis techniques described in Chapter 3, the olivines are tested for modal area percent (%), size (area), perimeter (length), total size distributions (frequency, area), and crystal shape (circularity).

Comparing the CK<sub>2</sub> and PK<sub>2</sub> data sets is done by comparison of crystal size distribution plots, descriptive numerical parameters, and statistical descriptors of shape.

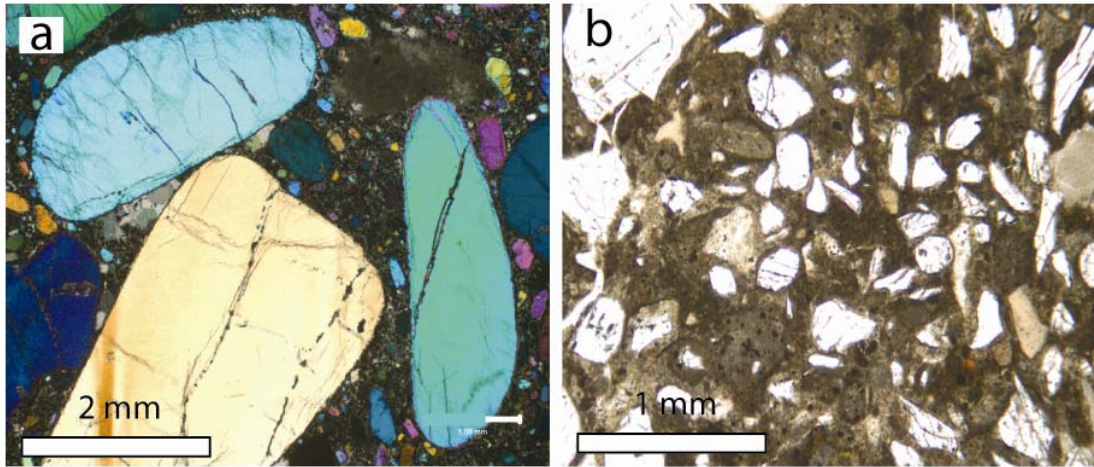


**Figure 5.2:** Olivine crystal shapes: (a) in coherent kimberlite; and (b) pyroclastic kimberlite.

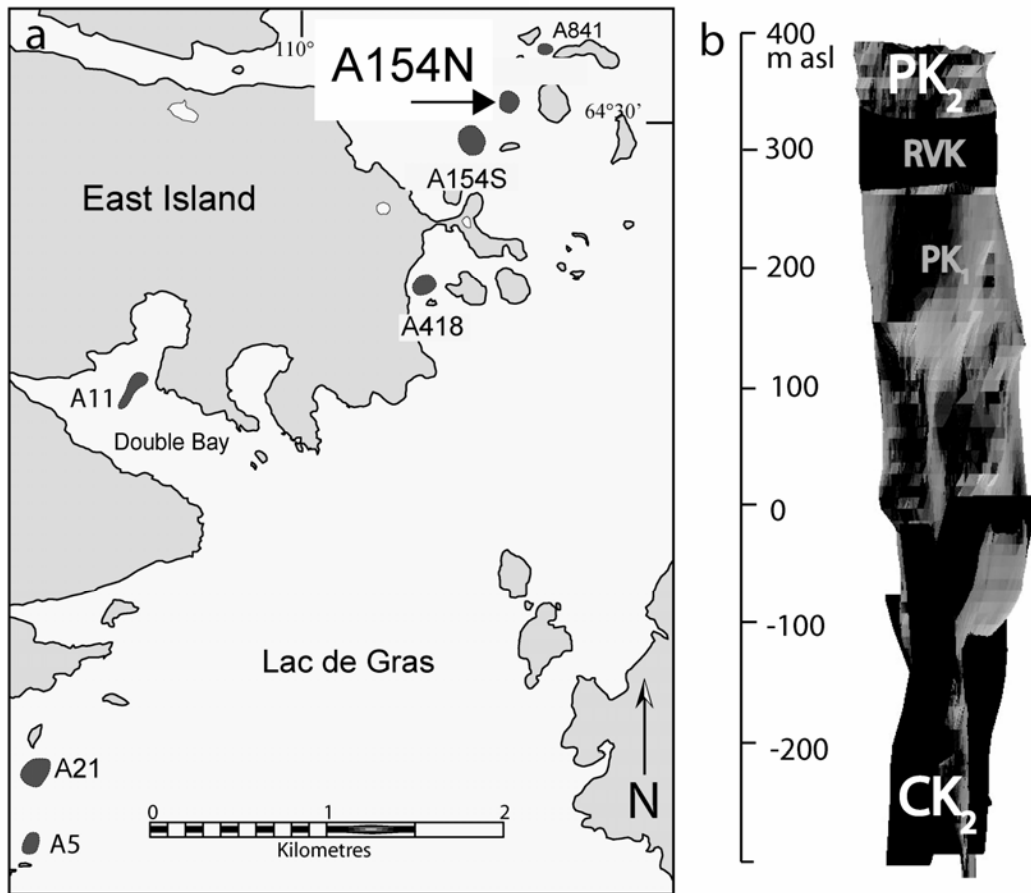


**Figure 5.3:** Location of the Diavik kimberlite field and internal units of A154N: (a) Kimberlite pipes at Diavik, East Island of Lac de Gras, NWT, Canada; (b) Inclined 3-D model of A154N looking E, showing four separate units of kimberlite, including: pyroclastic kimberlite (PK<sub>1</sub>); coherent kimberlite dykes (CK); re-sedimented volcanoclastic kimberlite (RVK); upper pyroclastic kimberlite (PK<sub>2</sub>).

This allows us to test if eruption changes the sizes, shapes, and overall population characteristics of olivine crystal size distributions (CSDs).

## 5.2.2 Results

The comparative properties of the olivine populations are shown in Figure 5.4, and summarized in Table 5.2. A plot of cumulative frequency vs. size shows a larger size range in olivine crystals from PK<sub>2</sub> than those in CK<sub>2</sub>, but less coarse olivines (Fig. 5.4). To characterize overall differences in the two populations, conventional grain size parameters are used in sedimentology and volcanology (Table 5.1): median size ( $Md\phi$ ), sorting efficiency ( $\sigma$ ), and skewness ( $\alpha$ ) (Inman, 1952; Cas and Wright, 1987), where:

$$Md\phi = median(-\log_2(d)) \quad (5.1)$$

$$\sigma = \frac{\phi_{84} - \phi_{16}}{2} \quad (5.2)$$

$$\alpha = \frac{\phi_{84} + \phi_{16} - Md\phi}{\sigma} \quad (5.3)$$

PK<sub>2</sub> olivine crystals have a smaller median size ( $\phi = 4.0$  vs. 3.8), are more poorly sorted ( $\sigma = 3.6$  vs. 3.5), and more skewed in distribution (0.8 vs. 0.5) than olivine crystals from CK<sub>2</sub> (Fig. 5.4). Log-log plots of cumulative frequency vs. size show olivine in coherent kimberlite to approximate power-law distributions<sup>7</sup>, with a characteristic slope ( $D$ ) and zero intercept ( $\lambda$ ) relationship (Chapter 3). Power-law equations are fitted to olivine crystals in PK<sub>2</sub>, and the values of slope ( $D$ ) and intercepts ( $\lambda$ ) are shown in Figure 5.4 and Table 5.2. Comparison of power-law slopes ( $D$ ) and intercepts ( $\lambda$ ) show an increase in

---

<sup>7</sup> There are many two-parameter model equations which appear similar over small ranges of observation (e.g., gamma, power, log-normal) (Bonnet et al., 2002; Clauset et al., 2007). Here, power-law equations of the form  $N_v(X \geq x) = \lambda x^{-D}$  are used to approximate, rather than describe, olivine crystal populations after Chapter 2.

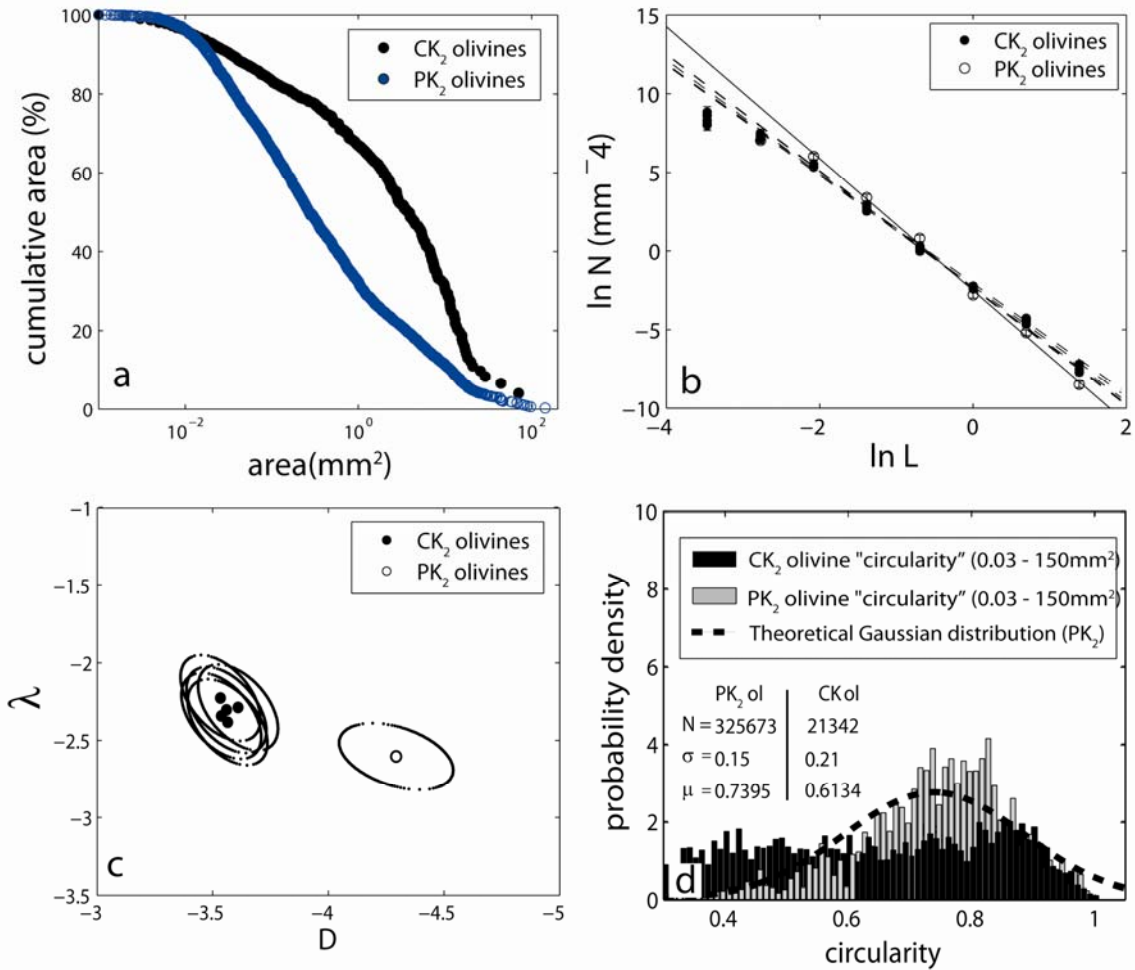


**Figure 5.4:** Tests for olivine crystal modification due to explosive eruption of kimberlite magma for olivine crystals in coherent kimberlite (CK<sub>2</sub>) and pyroclastic kimberlite (PK<sub>2</sub>): (a) cumulative area % vs. area (mm<sup>2</sup>); (b) ln N (mm<sup>-4</sup>) vs. ln L with best-fit power-law approximations over 6 logarithmic bin sizes (dashed lines = CK<sub>2</sub>; solid line = PK<sub>2</sub>). Analytical error bars are smaller than the symbols; (c) power-law parameters ( $\lambda$ , or zero-intercept for ln N; D, or slope) from best-fit lines in (b), with calculated covariance envelopes (after Chapter 3) for olivine crystals in CK<sub>2</sub> and PK<sub>2</sub>; (d) inter-leaved probability plots of circularity values for truncated size distributions (0.03 – 150mm<sup>2</sup>) of olivine crystals in CK<sub>2</sub> (black) and PK<sub>2</sub> (grey), where circularity =  $(4\pi * A) / P^2$ . Theoretical Gaussian distributions are shown for the PK<sub>2</sub> dataset (dashed line). Inset table shows the frequency of crystals (N), standard deviation ( $\sigma$ ), and mean shape value ( $\mu$ ) for olivine crystals in PK<sub>2</sub> and CK<sub>2</sub>, respectively.

**Table 5.2** Properties of olivine within coherent (CK) and pyroclastic (PK<sub>2</sub>) kimberlite

property	CK	PK <sub>2</sub>
Area (%)	46.7 - 51.2	39.4
size range (mm)	0.03 - 12.4	0.025 - 15.16
ol(n) : OL(n)	72 : 1 to 138 : 1	248 : 1
MdΦ <sup>†</sup>	3.3 - 3.8	4.0
σ <sup>‡</sup>	2.9 - 3.5	3.6
α <sup>§</sup>	0.3 - 0.5	0.8
D <sup>  </sup>	3.53 - 3.61	4.29
λ <sup>#</sup>	2.22 - 2.38	2.60
RMSE <sup>**</sup>	0.16 - 0.31	0.28
3D shape (R <sup>2</sup> )	1 : 1 : 1 (~0.8)	1 : 1 : 1 (0.83)

Note: 3D aspect ratios and correlation coefficients obtained using CSDSlice (Jerram and Morgan, 2006)

\* ol = olivine < 1 mm; OL = olivine ≥ 1 mm

† MdΦ = Median phi size (-log<sub>2</sub>(d))

‡ σ = sorting efficiency =  $\frac{(\phi_{84}) - (\phi_{16})}{2}$

§ α = skewness =  $\frac{(\phi_{84}) + (\phi_{16}) - Md\phi}{\sigma}$

|| D = slope of best-fit power-law

# λ = intercept of best-fit power-law

\*\* Root mean standard error

slope (3.61 to 4.29) and a decrease in the intercept (-2.38 to -2.60) for olivine crystals from CK<sub>2</sub> to PK<sub>2</sub> (Table 5.2).

Crystal shapes for olivine from CK<sub>2</sub> and PK<sub>2</sub> are compared in Figure 5.4d and Table 5.2. PK<sub>2</sub> olivine circularity ranges from 0.25 to 0.99, with a  $\mu$  of 0.73, and possess a normal, Gaussian distribution of crystal ‘circularities’. CK<sub>2</sub> olivines show circularity ranges from 0.2 to 0.99, with a geometric mean value ( $\mu$ ) of 0.61, and do not adhere well to a normal, Gaussian distribution. A simple comparison of the standard deviation of data about the mean circularity suggests that the two populations are distinct. Comparison of 3D axial ratios for the two olivine populations is accomplished using CSDSlice™ (Morgan and Jerram, 2006). In the CSDSlice™ database, a minimum of 10,000 slices are taken through poly-disperse (*sensu* Higgins, 2000), randomly-oriented model populations created from over 700 crystal shapes; these data are compiled in a database, and used to identify the 3D axial ratio which best represents 2D olivine crystal intersection data from CK<sub>2</sub> and PK<sub>2</sub> (see Appendix 8.2). CSDSlice™ shows 2D intersection data from CK<sub>2</sub> olivines to be best-approximated by a 1:1:1 ratio, which is statistically indistinguishable from PK<sub>2</sub> olivines (1:1:1; Table 5.2).

### **5.3 Hypothesis 2: melt is stripped from olivine by eruption processes**

A large proportion of the juvenile pyroclasts found in deposits of kimberlite occur as single, ‘free’ crystals of olivine. Here, I use ‘free’ crystals to denote crystals that were formed in a magma but are liberated or separated from this magma because of eruption, and are common in many highly energetic volcanic eruptions (Cas and Wright, 1987). However, the free crystal pyroclasts found in kimberlite are somewhat unique relative to free crystals of plagioclase, quartz and hornblende found in most andesite and dacite systems (e.g., Fisher, 1963; Heiken, 1972; Blake et al., 1992; Hammer et al., 2004; Dunbar et al., 2008; Michol et al., 2008) because: (a) they feature little to no coating or jacket of glass or crystallized melt, and (b) if a crystalline jacket is present, it is round to curvilinear in external morphology, and commonly vesicle-free.

In addition to free crystals, other juvenile pyroclasts derived from kimberlite eruptions show a variety of textural relationships between olivine crystals and quenched

or crystallized kimberlite melt (Fig. 5.1). For example, olivine crystals can form the cores of juvenile pyroclasts of crystallized kimberlite, or can be partially or completely enclosed by a thin jacket or coating of crystallized kimberlite (Chapter 2; Webb, 2006). Olivine-free juvenile pyroclasts of crystallized kimberlite are rare, and typically ash or fine-ash in size (Chapter 4). Round or spherical juvenile pyroclasts comprising any combination of crystalline kimberlite and attached or enclosed olivine crystals have been called ‘pelletal ash/lapilli/bombs’ (sensu Cas et al., 2008b) and ‘magmaclasts’ (sensu Field and Scott Smith, 1999). However, to simplify the array of crystal and melt textures observed in kimberlite deposits (i.e., pseudo or real; uncored or cored; pelletal, blocky, or convoluted; ash or lapilli; Cas et al., 2008), I will hereafter refer to pyroclasts comprising olivine crystals with any attached, crystalline or quenched kimberlite with the umbrella term “juvenile pyroclasts”, or JP. Though ‘free’ olivine crystals are technically also juvenile pyroclasts, I will hereafter refer to them as free olivines, or FO.

The sizes, abundances, and morphologies of JPs can vary significantly, even within a single pyroclastic deposit sourced from one eruption (Chapter 2; Mitchell, 2009; Porritt and Cas, 2009). Moreover, the amount of FO relative to ash and lapilli-sized JPs can also vary from deposit to deposit (Webb et al., 2004; Scott Smith, 2008b). In some cases, deposits may comprise almost exclusively FO, while other deposits comprise abundant JPs (e.g., Fig. 5.5). The occurrence of FO and JP together in virtually all pyroclastic deposits of kimberlite (e.g., Table 5.1), however, suggest olivine crystals are liberated from melt during all kimberlite eruptions. Based on these global observations, it is hypothesized that melt is separated from olivine crystals during explosive kimberlite eruption.

### 5.3.1 Methods

To test this hypothesis, data collected from a primary pyroclastic deposit (PK<sub>2</sub>) from the A154N kimberlite pipe (c.f., Chapter 2) is compared with olivine abundance data from coherent kimberlite (CK<sub>2</sub>). The PK<sub>2</sub> data includes modal abundances of FO and JPs, and the data is collated to investigate the ratio of FO to JPs within the entire PK<sub>2</sub> deposit (Table 5.3). A further test is required to determine the ratio of total olivine

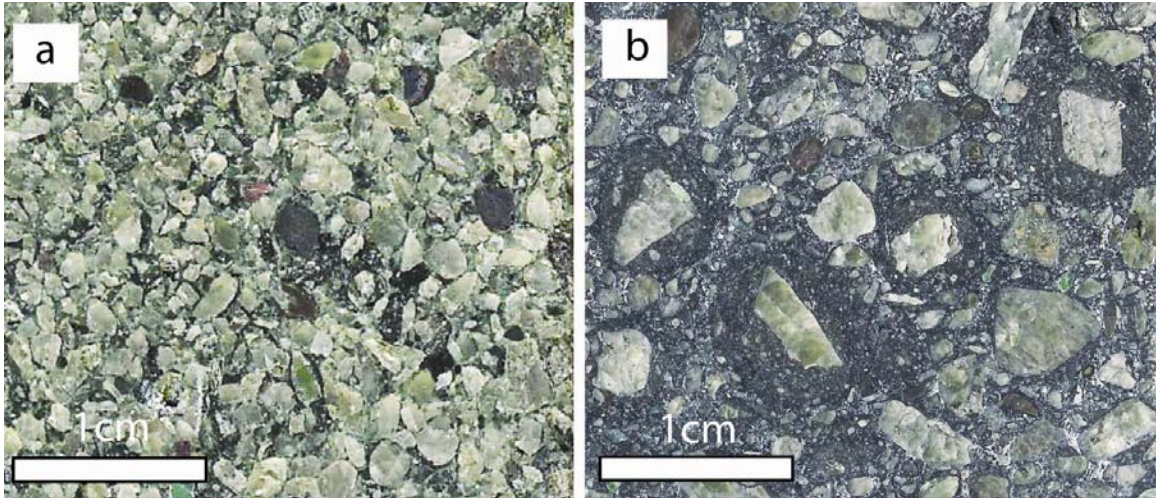


**Figure 5.5:** Variable crystal – melt relationships in pyroclastic kimberlite deposits: (a) abundant ‘free’ olivine crystals in a poorly-sorted, crystal-supported matrix within a deposit of pyroclastic kimberlite at Diavik, NWT; (b) abundant juvenile pyroclasts of crystalline kimberlite with olivine crystal cores in a poorly-sorted, crystal and clast-supported matrix within a deposit of pyroclastic kimberlite at Diavik, NWT.

crystals (FO + olivine inside JPs) to crystalline kimberlite still attached to crystals within JPs (Table 5.3). To evaluate this total ratio, I use image analysis methods from Chapter 4 on over 200 juvenile pyroclasts of crystalline kimberlite magma from 10 different thin sections sampled at 5m vertical intervals throughout the PK<sub>2</sub> to determine the size and modal abundance (area %), and calculate total surface areas (SA<sub>ol</sub>) of the olivine content *within* each juvenile pyroclast. If it can be assumed the juvenile pyroclasts observed in this study of thin sections are representative of the rest of the PK<sub>2</sub>, this allows us to determine a value for total crystallized kimberlite attached to olivine that is preserved in the deposit. The measurement of modal % and SA<sub>ol</sub> within each juvenile pyroclast also allows for evaluation of whether olivine abundance influences the ability of melt to separate from crystals. These data are then compared with olivine to groundmass ratios in CK<sub>2</sub> to establish how much melt was separated from the olivine crystals during the eruption which produced PK<sub>2</sub>.

### 5.3.2 Results

Results are shown in Table 5.3. FO content in the PK<sub>2</sub> ranged from ~25% to 60%. JPs comprise from ~1 to 20% of the deposit. The remaining volume in PK<sub>2</sub> comprises mantle xenoliths (eclogites, peridotites, dunites), and xenocrysts (e.g., garnet, clinopyroxene), country rock fragments (e.g., black mudstone, granite, biotite schist), unconsolidated mud fragments, and matrix (e.g., serpentine, carbonate). Ratios of FO to JPs in PK<sub>2</sub> range from ~2:1 to > 40:1. Combining all samples in PK<sub>2</sub> shows an FO:JP ratio of 6.7.

Plots of the size of juvenile pyroclast relative to its enclosed olivine crystal content for PK<sub>2</sub> of A154N are shown in Figure 5.6; results from PK<sub>1</sub> (Chapter 4) are shown for comparison. These data show juvenile pyroclasts range in size from 0.03 to 30 mm<sup>2</sup>, have olivine contents of 0 – 90% and minimum sizes of 0.03 mm<sup>2</sup>, similar to observations of a different pyroclastic body in A154N from Chapter 4. Overall, there is no correlation between size and enclosed olivine content; pyroclasts can have any size to olivine content relationship, except for some extreme ratios. For example, there are no small juvenile pyroclasts with high olivine to groundmass ratios, or

**Table 5.3:** Representative olivine content\* in: coherent kimberlite (CK), pyroclastic kimberlite (PK<sub>2</sub>) and juvenile pyroclasts (JP) of crystallized kimberlite

sample	Area %			Area %		
	ol	gm	ol : gm	'free' ol	jp	ol : jp
CK01 <sup>†</sup>	50.0	43.7	1.1			
CK02 <sup>†</sup>	48.2	44.1	1.1			
CK03 <sup>†</sup>	48.1	40.3	1.2			
CK04	46.7	42.4	1.1			
CK05	51.2	38.8	1.3			
CK_AVG	48.9	41.9	1.2			
PK_330 <sup>‡</sup>				26.9	3.9	6.9
PK_340 <sup>‡</sup>				53.2	2.3	22.9
PK_350 <sup>‡</sup>				56.9	1.3	43.8
PK_360 <sup>‡</sup>				26.1	5.1	5.1
PK_370 <sup>‡</sup>				32.9	5.2	6.3
PK_380 <sup>‡</sup>				35.2	18.2	1.9
PK_TOT <sup>§</sup>				35.8	5.4	<b>6.7</b>
JP_TOT <sup>  </sup>	66.3	33.7	2.0			
PKJP_TOT <sup>¥</sup>	39.4	1.8	22.4			

\* olivine content measured as area % from slab and t.s.

† Replicate samples from a single dyke; gm = groundmass

‡ Representative sample horizons within 50m-thick PK<sub>2</sub>

§ Linear combination of 10 samples at 5m intervals in PK<sub>2</sub>

|| Linear combination of olivine in juvenile pyroclasts (jp) from PK<sub>2</sub>

¥ Combined modal % of olivine in PK and resident jp in PK<sub>2</sub>

large juvenile pyroclasts with low olivine to groundmass ratios (shaded region, Fig. 5.6a). The combined modal percentage of olivine crystals in juvenile pyroclasts is 66.3%, yielding a 2:1 ratio of olivine crystals to groundmass in juvenile pyroclasts (Table 5.3). If it can be assumed the ratio of olivine content (%) to crystalline kimberlite measured within the juvenile pyroclasts in this study are representative and can be applied to all juvenile pyroclasts from PK<sub>2</sub>, the total (FO + olivine inside JPs) olivine to crystalline kimberlite ratio for PK<sub>2</sub> is > 22:1. In contrast, ratios of olivine crystals to crystallized kimberlite groundmass in coherent kimberlite (CK<sub>2</sub>) show ~1:1 relationships. If olivine to groundmass ratios in magma which erupted to produce PK<sub>2</sub> were similar to the ratios measured in CK<sub>2</sub> rocks (Table 5.3), these data suggest up to 94 % of the melt fraction may have been separated from olivine crystals during eruption.

## 5.4 Discussion

In this section, I discuss implications of the observations described above. First, factors which may encourage breaking of olivine crystals are discussed. Secondly, ideas are developed to show how the properties of kimberlite magma during eruption can explain the observed shapes, sizes, textures, and abundances of juvenile kimberlite pyroclasts.

### 5.4.1 Olivine crystal breaking

Olivine crystals measured in pyroclastic kimberlite rocks show clear differences from those measured in intrusive coherent kimberlite. Shape indices, sedimentological population parameters, and crystal size distribution model equations all indicate a fundamental difference in the olivine crystal populations from CK and PK<sub>2</sub>. The simplest explanation is that eruption of kimberlite magmas modifies the shapes, sizes, and overall population characteristics of olivine crystals. Here, I discuss the properties of olivine crystals in kimberlite magma and the environmental influences which can cause crystals to break. Then, I discuss potential controlling factors responsible for differences in the populations of olivine crystals observed in pyroclastic deposits.

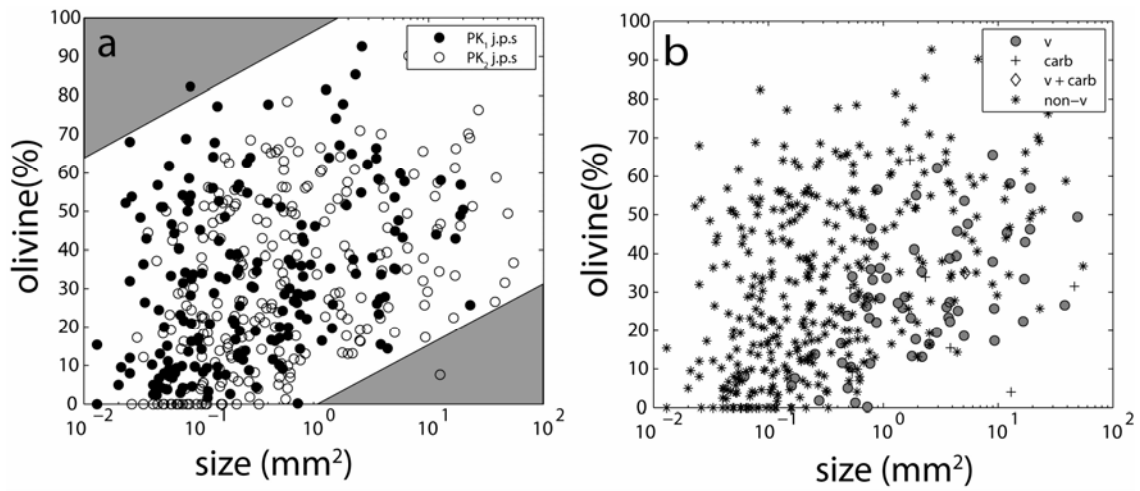


**Figure 5.6:** Parametric analysis of juvenile pyroclasts (JPs) from PK<sub>1</sub> and PK<sub>2</sub> of A154N: (a) olivine (%) vs. size (mm<sup>2</sup>) for PK<sub>1</sub> (after Chapter 4), and PK<sub>2</sub> of A154N. Shaded regions indicate a lack of observations; (b) olivine content (%) vs. size (mm<sup>2</sup>) of juvenile pyroclasts in PK<sub>1</sub> and PK<sub>2</sub> containing: vesicles (v), groundmass carbonate (carb), both (v + carb), or that are vesicle-free (non-v).

### Properties of olivine crystals in kimberlite magma

Olivine crystals in kimberlite have several physical attributes which lend themselves to shape and size modification during explosive eruption. First, the majority of olivine crystals in kimberlite magma are likely xenocrystic in origin (Arndt et al., 2006; Kamenetsky et al., 2007a; Brett et al., 2009), derived from depths as great as 200km below surface. As such, many crystals store stresses imposed by mantle processes as evidenced by undulose extinction, or appear to have accommodated stress by cracking or fracturing, though incompletely (Fig. 5.7a,b). Detailed petrography of olivine crystals in coherent and fragmental rocks at Diavik have indicated evidence of crack-healing and crack-sealing within olivine crystals (Brett et al., 2009). Second, olivine crystals in kimberlite magma also contain abundant mineral and melt inclusions (Fig. 5.7c). Together, these physical characteristics act as points, lines and planes of intrinsic weakness within individual olivine crystals (e.g., Fig. 5.7d).

### Environmental factors within magma

There are also environmental factors within ascending and erupting kimberlite magma which may enhance the breaking of olivine crystals. First, pressure changes associated with rapid ascent through the mantle and subsequent eruption can cause solid-state expansion of olivine crystals, volatilization of gas from fluid or melt inclusions (Bindeman, 2005), and re-cracking of pre-conditioned zones of weakness, leading to failure of olivine crystals. Secondly, turbulent ascent conditions are required by the presumed viscosities, conduit geometries and source locations of kimberlite magmas (Sparks et al., 2006; Head and Wilson, 2008). Turbulent behaviour in solid, liquid and gas mixtures lead to higher numbers of particle to particle interactions (Kruis and Kusters, 1997), particularly with respect to larger crystals and in systems with high density contrasts between solid particles and their host fluids (Zhou et al., 2001); such interactions create high-energy impacts between crystals that can exceed the tensile strength of olivine.

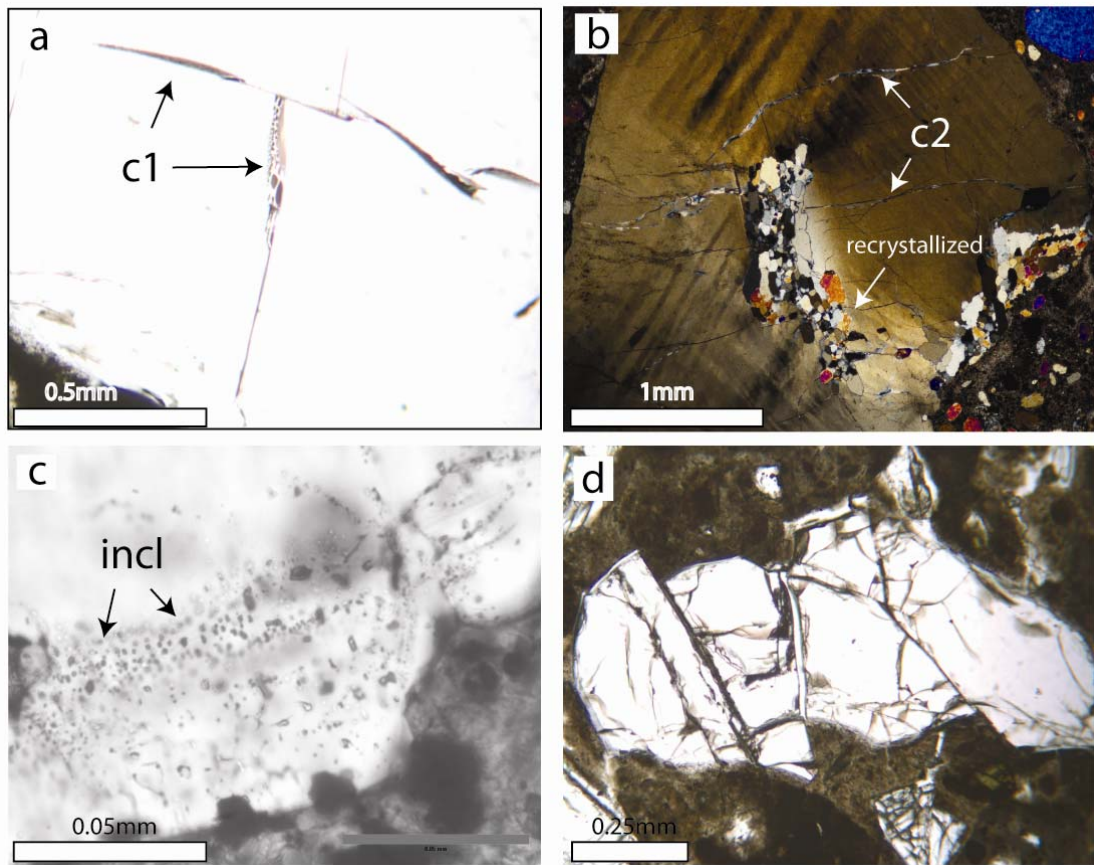


**Figure 5.7:** Properties of olivine crystals contributing to crystal breaking during eruption: (a) partially-healed (c1) cracks within an olivine crystal in CK which terminate before the edge of the crystal; (b) cross-polarized photomicrograph of large, strained (undulose extinction) olivine macrocryst within CK containing cracks filled with carbonate (c2) and internal zones of recrystallized olivine (recrystallized); (c) melt and mineral inclusions (incl) in an olivine overgrowth; (d) angular, fractured olivine within PK<sub>2</sub> of A154N.

### Reasons for differences in olivine crystal properties

Experiments have shown the slopes of particle size distributions in log-log plots (i.e., D-values) to positively-correlate with the magnitude of pressure drop attending fragmentation (Kueppers et al., 2006), the amount of particle-to-particle comminution (Kueppers et al., 2006), and the number of fragmentation generations (Kaminski and Jaupart, 1998). Models calculating new CSDs by fragmentation of existing olivine crystal population also suggest a positive increase in the CSD slope due to fragmentation (Chapter 3).

Differences in olivine properties (e.g., D-values, Inman parameters, crystal shapes) among pyroclastic deposits may result from differences in: (a) the amount of strain, cracks and inclusions in the pre-eruptive crystals; (b) the pre-eruptive olivine crystal size distributions; (c) magnitude of pressure drop during emplacement, or (d) the number of particle-to-particle collisions during eruption. However, the intrinsic properties described for olivine (strain, cracks, inclusions) are repeatedly observed in coherent kimberlite (Kamenetsky et al., 2007a; Brett et al., 2009). Moreover, global olivine crystal size distributions in coherent kimberlite are believed to be relatively consistent (Scott Smith, 2008c). Thus, the most likely cause for significant differences in olivine crystal size distributions and shapes in pyroclastic deposits are relative differences in pressure changes and the number of particle-to-particle collisions during emplacement.

#### 5.4.2 Melt separation during eruption

The physical properties of kimberlite magma govern the nature and time scales of magma transport as well as the style of volcanic eruption. Kimberlite is presumed to be a low-viscosity, volatile-rich melt (Price et al., 2000; Sparks et al., 2006). Kimberlite magmas can also comprise up to ~51% olivine crystals (Chapter 3). Ultimately, kimberlite magmas become three-phase systems during ascent (gas, liquid melt, crystals); the low viscosity, high crystal contents and increasing gas volume fraction can lead to full decoupling of the gas phase from the melt (Chapter 4). The relative ratios of phases

may be responsible for the degree to which melt can separate from olivine crystals, and, thus, most crystal/melt textures observed in pyroclasts derived from kimberlite eruption.

Below, aspects of each phase (melt, gas, crystals) are discussed which influence primary pyroclast formation and the degree to which melt separates, or ‘strips’ from crystals, including: (1) the impact of melt viscosity; (2) mechanisms by which gas content could facilitate melt disruption and separation from olivine crystals; and (3) the role of crystal content (i.e., olivine) in determining the size, shape and crystal-melt ratios of juvenile pyroclasts.

### Viscosity and pyroclast formation

The low viscosity and high volatile contents of kimberlite melts have important consequences for the formation of pyroclasts. Computed viscosities for estimates of kimberlite melt composition show little decrease in glass transition temperature [ $T_g$  (K)] with increasing  $H_2O$  contents (Russell et al., 2006). This reflects the fragile nature of these melts and contrasts with the behaviour of basaltic melts where  $\sim 2$  Wt. %  $H_2O$  causes a  $200^\circ C$  depression of  $T_g$  (Russell et al., 2006). Normally the depression of  $T_g$  with increased  $H_2O$  content provides a simple vehicle for rapid quenching and production of glass during an eruption. Ascent and eruption causes volatile loss and a concomitant increase in  $T_g$  to the point that  $T_g$  rises to meet magma temperature. At this point melt is quenched to glass: kimberlite melts do not show the same depression in  $T_g$  and, thus, lack this means of aiding glass formation. In addition, the  $\Delta T$  between  $T_{magma}$  and  $T_g$  is higher than in many other magmas (Russell et al., 2006). As a consequence, kimberlite melts can remain molten and fluid longer after disruption or fragmentation than most silicate melts. For this reason, crystal/melt relationships and external morphologies (i.e., spherical geometry, contact angle between melt and crystal) of juvenile pyroclasts are most likely determined by viscous properties such as the surface energy between liquid melt and gas ( $\gamma_{m-g}$ ), and the interfacial energy between liquid melt and crystals ( $\gamma_{m-x}$ ), rather than brittle failure.

### Gas content and melt disruption

Gas content can encourage separation of kimberlite melt from olivine crystals and disruption of kimberlite melt in several ways (Fig. 5.8). First, nucleation of exsolving gas bubbles is energetically easiest on solids (Blander and Katz, 1975). Kimberlite contains abundant xenocrysts of olivine (e.g., Brett et al., 2009) as crystal cargo, and therefore any exsolved gas will preferentially nucleate on these crystals. Rapid exsolution of gases may cause coalescence of adjacent bubbles on a crystal surface; as gas expands and coalesces, it may overcome the interfacial tension between melt and crystal and begin to wet the crystal, thereby displacing the melt (Fig. 5.8b).

Second, high gas fractions within a low-viscosity melt has been shown to lead to out-gassing through permeability networks, or ‘gas-streaming’ through a body of magma (Herd and Pinkerton, 1997; Parfitt, 2004; Gonnermann and Manga, 2007). Two kinds of fluid mechanical instabilities are created at the interface between a streaming gas and liquid: (1) Kelvin-Helmholtz (K-H) instabilities<sup>8</sup>, which create waveforms at the interface, and (2) Rayleigh-Taylor (R-T) instabilities<sup>9</sup> which disrupt liquid from wave-crests formed by the K-H instability by rolling-over the crest of the wave-forms in a fashion similar to white-caps on a lake (Villiermaux, 1998; Villiermaux, 2007). Gas streaming can disrupt the kimberlite melt by creating such instabilities along the melt/gas interface due to velocity contrasts between less-dense gas and surrounding kimberlite melt (Fig. 5.8b,c).

Third, high volatile content, rapid ascent of magma, and narrow conduit geometry could lead to very high exit velocities for the gas phase in erupting kimberlite magma (Chapter 4; Sparks et al., 2006; Head and Wilson, 2008). The high density of the pyroclasts involved in a kimberlite eruption (Chapter 2; Cas et al., 2008a; Gernon et al., 2008b) would reduce the exit velocity of particulate matter being ejected from a vent. The collective behaviors of gas, melt and solid particles in a vent undergoing a flux

---

<sup>8</sup> Kelvin-Helmholtz shear instabilities forms asymmetric waves at the boundary between gas and liquid of wavelength;  $\lambda = \delta \sqrt{\rho / \rho_g}$ , where  $\lambda$  is wavelength,  $\delta$  is the boundary layer thickness,  $\rho$  is the density of the liquid, and  $\rho_g$  is gas density.

<sup>9</sup> Rayleigh-Taylor instabilities form as a transverse destabilization of existing waveforms, due to accelerations imposed on the liquid-gas interface by the passage of primary undulations. Such transverse waveforms have a wavelength:  $\lambda_{\perp} / \delta \cong 3We_{\delta}^{-1/3} (\rho / \rho_g)^{1/3}$ , with  $We_{\delta} = \rho_g (\Delta v)^2 \delta / \gamma$ , where  $\Delta v$  is the relative gas velocity.

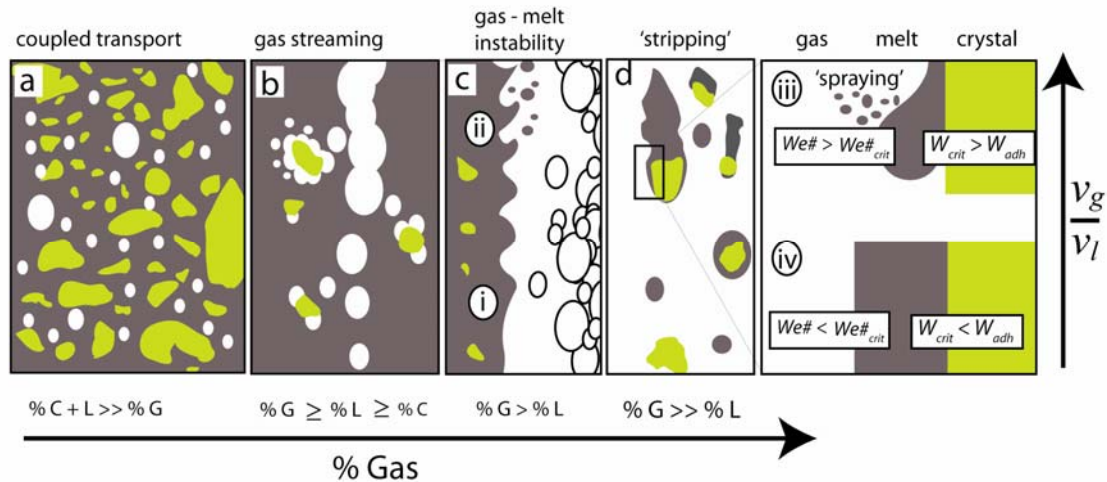


**Figure 5.8:** Relative volume fractions vs. velocity ratios ( $v_g / v_l$ ) of gas, liquid (i.e., melt) and crystals, and consequences for disruption of kimberlite magma: (a) relatively high crystal + melt content (as volume %) leads to coupled transport of crystals, melt and exsolved gases; (b) nucleation of gas bubbles on crystal cargo leads to first separation of crystals from melt. Relatively low crystal content leads to gases streaming through low viscosity kimberlite melt; (c) velocity contrasts between melt and gas create two kinds of fluid mechanical instabilities at interface: i) Kelvin-Helmholtz<sup>2</sup>, and ii) Rayleigh-Taylor<sup>3</sup> (see text); (d) 'stripping' of melt from olivine crystals by fluxing gases. Enlarged box shows gas-liquid-crystal interfaces and critical relationships for Weber numbers ( $We\#$ ,  $We_{crit}\#$ , eq. 5.4), work of dispersion, and work of adhesion ( $W_{crit}$ ,  $W_{adh}$ ; eqs. 5.5, 5.6) required for 'stripping' of melt from crystals (iii) and spherical restoration of melt around olivine crystals due to surface tension (iv).

of melt+solids+gas would yield a substantial but highly variable velocity contrast between phases. In fluid mechanics, such velocity differentials are a key influence in conversion of bulk liquid into a spray or mist (i.e. collection of drops), known as ‘atomization’ (Villermaux, 2007). Atomization is triggered when the relative magnitude between inertial (i.e., stagnation pressure) and curvature (i.e., capillary restoring pressure) forces for droplets of liquid in a gas suspension exceeds a critical value. This critical ratio can be expressed as a dimensionless critical Weber number ( $We_c$ ):

$$We_c = (\rho_g (\Delta v)^2 (d_0)) / \gamma \quad (5.4)$$

where  $p_g$  is gas density,  $\Delta v$  is the velocity differential between liquid and gas,  $d_0$  is the initial liquid droplet diameter, and  $\gamma$  is surface tension. One indication of high velocity contrasts ( $\Delta v$ ) are the size distribution of the droplets created by atomization, as the size of droplets sprayed off from a liquid surface decreases with the velocity contrast (Faeth et al., 1995; Wu and Faeth, 1995), and scales as a function of energy input (Hinze, 1959). If velocity contrasts are great enough between large clots, blebs or droplets of kimberlite melt and ambient gas, the pieces of magma could efficiently disaggregate into much smaller droplets (figs. 5.6, 5.8d). It is well established that the exit velocity of an erupting gas-pyroclast mixture is sensitive to the gas content of the magma, with larger gas contents leading to higher exit velocities (Head and Wilson, 2008). As the terminal settling velocity of melt globules and crystals are relatively constant, higher exit velocities imply greater velocity contrasts between gas and entrained particles.

#### *Olivine crystal content and melt separation*

The olivine crystal content in kimberlite magma may also influence the disruption of kimberlite magma. For example, interfacial energies which cause kimberlite melt to wet the outer surfaces of olivine crystals in kimberlite magma may inhibit separation of melt from itself or from crystals. The total surface area of a population of particles is a function of the abundance and size distribution of the particles. Thus, the abundance (i.e., modal %) and size distribution of olivine content

within an erupting kimberlite magma may ultimately control the crystal to melt ratios within juvenile pyroclasts, as well as the sizes of juvenile pyroclast produced.

To assess the influence of crystal content (i.e., modal %, surface area) on the ability of melt to separate from olivine crystals, I compare a) olivine content (modal %) with sizes of JPs (Section 5.3), and b) estimated surface area of olivine crystals within JPs with estimated volumes of JPs. Olivine content (modal %) is plotted against size for all JPs from Figure 5.6 in Figure 5.9a, and are sub-divided according to textural relationships between olivine crystals and attached or enclosing crystalline kimberlite groundmass, as in Chapter 4. These data indicate a general increase in olivine content with size for JPs with multiple olivine crystals (M; dashed lines; Fig. 5.9a), similar to observations in Chapter 4. The surface areas of equivalent-radii spheres are calculated from the 2D intersections of olivine crystals within JPs and for JP outlines to find the ratio of estimated surface area of olivine within each juvenile pyroclast ( $SA_{ol}$ ) to the estimated volume of groundmass in each juvenile pyroclast ( $V_m$ ) within the PK<sub>2</sub> dataset. The estimated  $SA_{ol} : V_m$  ratio is plotted against the estimated size ( $V_{jp}$ ) of the juvenile pyroclast in Figure 5.9b. The  $SA_{ol}$  increases with the size of JP, but there is an overall decrease in the  $SA_{ol}:V_m$  ratio with an increase in the size of JP. Thus, olivine content (modal %) and surface area ( $SA_{ol}$ ) both show positive correlations with the size of JP. The overall decrease in  $SA_{ol}:V_m$  with increasing size of JP may be due to more boundary-layer effects between neighbouring olivine crystals and the decreasing significance of surface tension with size.

To separate a liquid from a solid surface in a three-phase system of gas, liquid and solid, a dispersive pressure (force/unit length) on the outer surface of a liquid droplet enclosing solids must overcome the work of adhesion ( $W_{adh}$ ) coupling the liquid to the solids (Bangham and Razouk, 1937), defined by the Young – Dupree equation:

$$W_{adh} = \gamma(1 + \cos\theta) \quad (5.5)$$

where  $\gamma$  is the liquid surface tension, and  $\theta$  is the contact angle between solid and liquid (Fig. 5.10a).  $W_{adh}$  is a force per unit length, or equivalently energy per unit area. The

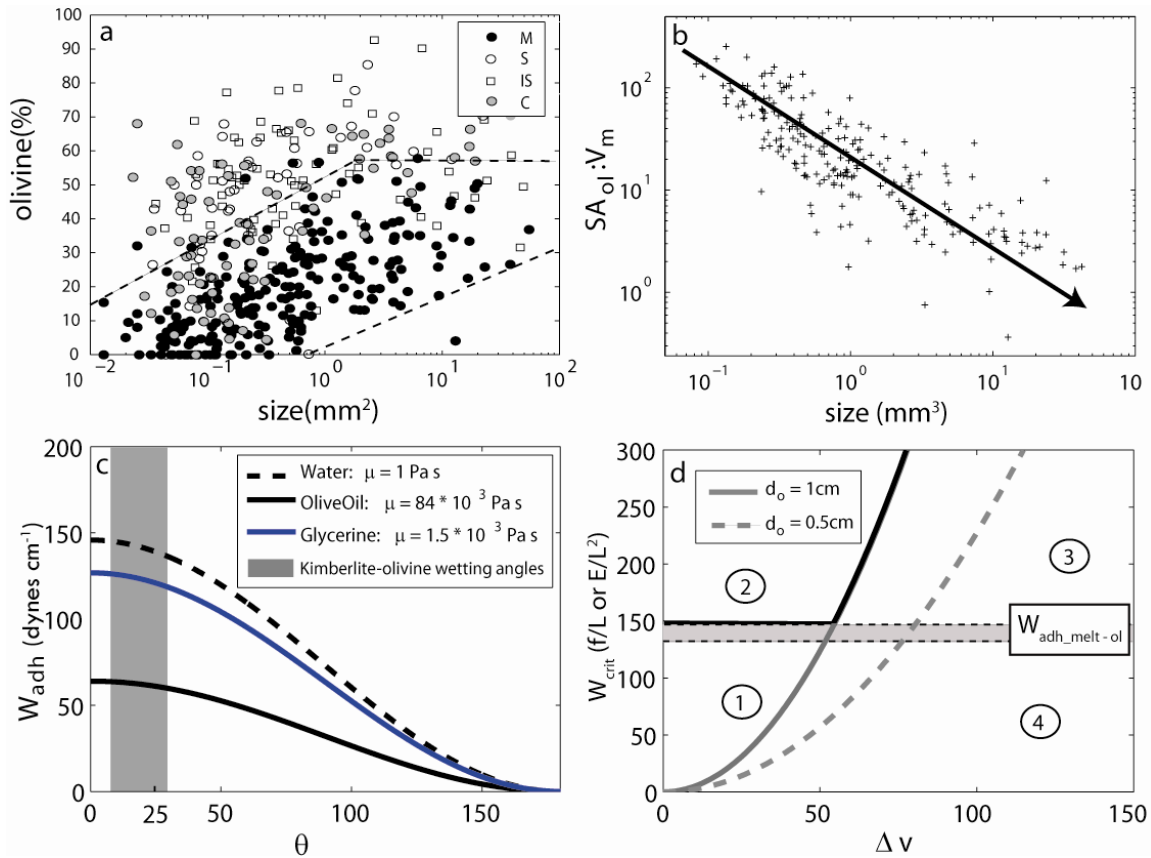


**Figure 5.9:** Fluid mechanics properties relating gas, liquid and solid surfaces: (a) olivine content (%) vs. size (mm<sup>2</sup>) for textural subgroups of juvenile pyroclasts for PK<sub>1</sub> and PK<sub>2</sub>, including: pyroclasts with multiple olivine crystals (M), selvages of melt on olivine crystals (S), olivine grains with partial selvage (IS), and cored pyroclasts (C); (b) estimations of ratio of total surface area of olivines within juvenile pyroclasts (SA<sub>ol</sub>) to volume of groundmass in enclosing juvenile pyroclast (V<sub>m</sub>) vs. size of juvenile pyroclast (mm<sup>3</sup>). Note the decrease in SA<sub>ol</sub> : V<sub>m</sub> ratio with increasing size of juvenile pyroclast (arrow); (c) work of adhesion ( $W_{adh}$ ; eq. 5.1) vs. wetting angle between liquid and a solid surface ( $\theta$ ) for water (dashed line; viscosity ( $\mu$ ) = 1 Pa s), olive oil (solid line;  $\mu$  = 84 · 10<sup>3</sup> Pa s), and glycerine (blue line;  $\mu$  = 1.5 · 10<sup>3</sup> Pa s). Shaded region indicates range of observed contact angles between crystalline kimberlite selvages and olivine crystals on the outer edge of juvenile pyroclasts from PK<sub>2</sub>; (d) “critical” work fields defined by intersection of  $W_{adh}$  (water) with  $W_T - \Delta v$  curve for starting drops 1cm in diameter: (1) no ‘atomization’ or stripping of liquid off of crystals, (2) no ‘atomization’ but liquid is stripped off of crystals, (3) both ‘atomization’ and stripping of liquid off of crystals, (4) ‘atomization’ of liquid but no stripping of liquid off of crystals.

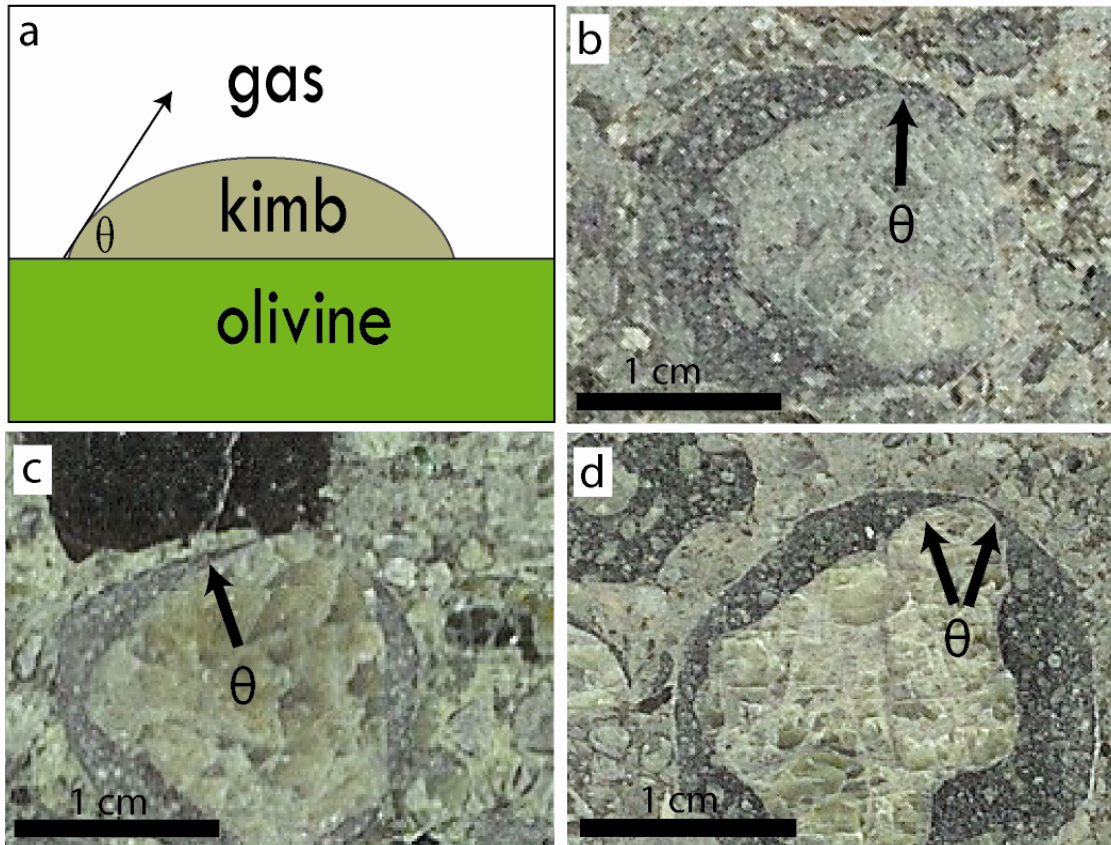


**Figure 5.10:** Wetting angles between olivine crystals and kimberlite melt for pyroclasts in PK<sub>2</sub>: (a) schematic showing the wetting angle ( $\theta$ ) between kimberlite melt (kimb) and crystal (olivine) in a gas medium (gas); (b – d) large (~1 cm) juvenile pyroclasts comprised of a large olivine crystal ‘core’, incompletely coated by crystalline kimberlite. Note low contact angles ( $\theta < 30^\circ$ ) between crystalline kimberlite and olivine crystals.

total energy required to separate liquid from a solid surface would increase proportionally with increasing total surface area (e.g., crystal surfaces).

Thin, complete selvages of kimberlite on olivine crystals ( $\sim 0.1$  mm) and low contact angles (approx.  $10 - 30^\circ$ ) between olivine crystals and partial selvages of kimberlite are observed in many juvenile pyroclasts in PK<sub>2</sub> (Fig. 5.10b-d). Such low contact angles indicate a stronger attraction between the olivine and adjoining melt ( $W_{adh}$ ) than of the liquid to itself (i.e., work of cohesion), allowing the liquid melt spread upon, or ‘wet’, the olivine. The  $W_{adh}$  for liquids of known viscosities which span the best estimates for kimberlite melt (e.g., 1-10 Pa s; Sparks, 2006) is modeled for different contact angles ( $\theta = 0 - 180^\circ$ ) in Figure 5.9b. Observations of contact angles between crystalline kimberlite and olivine crystals on the outside margin of juvenile pyroclasts suggest a likely range for  $W_{adh}$  required to separate liquid melt from olivine crystals (Fig. 5.9b, shaded region;  $\sim 60-140$  dynes  $\text{cm}^{-1}$ ).

Therefore, the sizes, morphologies, and types of pyroclasts produced by an explosive eruption of low viscosity kimberlite magma may be influenced by: a) the ratio of inertial to curvature forces ( $We\#_{crit}$ ), b) the energy of melt adhering to crystals ( $W_{adh}$ ), and c) stagnation pressure ( $\rho_g \cdot (\Delta v)^2 \cdot d_o$ ) of fluxing volcanic gases. By combining equation 5.4 with equation 5.5, the “critical” work ( $W_{crit}$ ) can be found in terms of velocity contrast required to both ‘atomize’ liquid and ‘strip’ crystals of melt (Fig. 5.9b):

$$W_{crit} = \left[ \frac{(1 + \cos \theta) \cdot \rho_g \cdot d_o}{We\#_{crit}} \right] (\Delta v)^2 \quad (5.6)$$

To estimate possible critical work and velocity contrasts required to ‘atomize’ kimberlite melt and ‘strip’ melt from crystal surfaces, I assume the fluid properties (e.g.,  $\mu = 1$  Pa s,  $\gamma = 76.4$  dynes  $\text{cm}^{-1}$ ) of water at room temperature as a reasonable analogue to best-estimates of kimberlite melt: a  $We\#_{crit}$  similar to that required for water to ‘atomize’ ( $\sim 10$ ; Wierzba, 1990),  $d_0$  of  $\sim 1$  cm, and  $\rho_g$  of  $50$   $\text{kg m}^{-3}$ . Given these assumptions, critical relationships between viscosity contrasts and total work dictate four theoretical relationships between kimberlite melt and olivine crystals (Fig. 5.9d): (1) kimberlite melt is neither separated from olivine crystals (i.e.,  $W_{crit} < W_{adh}$ ) nor ‘sprayed’ or ‘atomized’

( $We\# < We\#_{crit}$ ); (2) kimberlite melt is separated from olivine crystals (i.e.,  $W_{crit} > W_{adh}$ ), but is not ‘sprayed’ or ‘atomized’ by the flux of surrounding gas ( $We\# < We\#_{crit}$ ); (3) both melt separation (i.e.,  $W > W_{adh}$ ) and ‘atomization’ ( $We\# > We\#_{crit}$ ); (4) kimberlite melt remains attached to olivine crystals (i.e.,  $W < W_{adh}$ ), but droplets are ‘sprayed’ or ‘atomized’ by the flux of surrounding gas ( $We\# > We\#_{crit}$ ).

## 5.5 Interpretation

In this section, I interpret processes responsible for observations from the two tests in this study. First, olivine crystals are shown to be modified due to explosive eruption. These changes to the sizes and shapes of olivine populations are most likely the result of pressure drops, thermal shocks, and particle-to-particle collisions experienced by the ascending magma, and are easily characterized by looking at D-values. Together, these causes indicate the pressure differential as a likely factor in the extent to which olivine breaks during eruption: rapid pressure changes, thermal shock, and particle-to-particle collisions induced by turbulent behaviour within an ascending and/or erupting kimberlite magma could facilitate break-up or fragmentation of olivine crystals along internal, pre-conditioned areas of weakness. Thus, I suggest D-values of olivine CSDs are modified in proportion to the change in pressure experienced by the magma, and serve as a gauge of the violence of kimberlite eruption.

Second, it has been shown that pyroclastic deposits contain both abundant free olivine and juvenile pyroclasts comprising olivine crystals and attached or enclosing crystalline kimberlite. Gas contents, exit velocities or velocity contrasts in an erupting kimberlite magma can be reflected in pyroclastic products of kimberlite eruptions in two ways: (1) the relative ratios of juvenile pyroclasts of crystalline kimberlite (JPs) to free olivine crystals observed in a deposit (FO), and (2) the size distribution of JPs (i.e., droplets of crystalline kimberlite enclosing olivine) produced during eruption. Therefore, crystal-melt textures in pyroclasts suggesting high velocity contrasts (e.g., ‘stripped’ olivine crystals) imply greater gas content in the erupting kimberlite magma. Moreover, differences in the degree of melt-stripping (i.e., FO:JP ratios) among or within pyroclastic deposits likely reflect differences in gas content in the magma from which the pyroclasts

derive. In addition, the higher olivine content and corresponding surface area observed in larger JPs suggest that primary breakup of kimberlite magma and secondary breakup of existing pyroclasts by melt 'stripping' is attenuated by high olivine contents, and may lead to a bias of pyroclasts with high olivine contents and surface areas preserved in pyroclastic deposits relative to the starting magma. The gas content of erupting kimberlite magma is also known to correlate with eruption column height in other low-viscosity magmas (e.g., Parfitt et al., 1995), suggesting the FO:JP ratio may also be a proxy for the power of the eruption. Thus, I suggest that the volumetric properties of gas, melt, and solids determine how readily melt can separate from crystals in low viscosity kimberlite magma, and these phase proportions can be approximated by the FO:JP ratios in deposits.

## **5.6 New eruption index**

The observation of diverse pyroclast assemblages in pyroclastic deposits worldwide implies that eruption dynamics for kimberlite vary from volcano to volcano (Table 5.1). Conventional metrics of volcanic eruptions include magnitude (erupted mass, in kg), intensity (eruption rate, in kg/s), peak eruption height (km), energy release (thermal + kinetic + seismic, in J), power output (W), and destructive potential (Sigurdsson, 2000). Though efforts have been made to create a single index which can effectively account for these different metrics (e.g., Volcano Explosivity Index, or VEI), such indices are incapable of describing the behaviour of all volcanic eruptions. For example, there is not a simple or consistent relationship between magnitude and intensity for many eruption styles and/or magma types. In addition, eruption duration, deposit volumes, and vent geometries vary independently of either magnitude or intensity.

Many of these parameters are based on the characteristics of the eruption, and some have been developed to correlate the phenomenon with the resulting pyroclastic deposit. For example, Walker (1973) recognized the need to investigate the wealth of global pyroclastic deposits for clues into eruption behaviour for active and ancient systems. Relative comparisons of volcanic energy are made for unobserved eruptions by using the combination of grain size distributions and areal extent of pyroclastic deposits

(Walker, 1973). For example, 'F' values which represent the % of fragments < 1 mm at isopach contour of 0.10 Thickness<sub>max</sub> are used for comparative purposes and to deduce volcanic style and energy from grain-size properties of pyroclastic deposits (Walker, 1973; Cas and Wright, 1987). These parameters were designed to reflect the rate of energy release and the manner in which it is released during volcanic eruption (Walker, 1973).

Kimberlite volcanoes rarely preserve extra-crater deposits that would support this type of analysis. Poor exposure of extra-crater deposits and post-emplacement alteration means it is only possible to constrain minimum estimates of mass involved in eruptions from kimberlite pipes (Porritt et al., 2008). Thus, accurate assessment of magnitude (kg) or intensity (kg/s) for kimberlite eruptions using methods described above are not possible. Furthermore, many volcanoclastic deposits of kimberlite are enriched (> 50%) in crystals (e.g., olivine) and, thus, the energetics behind fragmentation of crystal-rich kimberlite magmas may be considerably different from other magmas. Moreover, the high density of juvenile pyroclasts (Chapter 2; Porritt et al., 2008) combined with relatively high volatile contents presumed for kimberlite eruptions (Sparks et al., 2006) would inherently impact the transport distance and plume stability, thereby complicating the application of a conventional fragmentation and dispersal index.

In addition, no one has ever observed a kimberlite eruption, requiring models or inferences of the peak eruption heights and exit velocities based on physical properties of kimberlite magmas (Russell et al., 2006). As a further complication, kimberlite volcanologists and petrologists continue to debate the depositional styles (e.g., fall, surge, flow, fluidized fountain) responsible for most pyroclastic deposits observed within kimberlite pipes (Walters et al., 2006a; Gernon et al., 2008b; Porritt et al., 2008), precluding use of Walker's D-F index (Walker, 1973) which assumes the examined deposits are the result of pyroclastic airfall. Given these constraints, we must look to either a) conduit and crater geometries of kimberlite pipes and dykes (e.g., Field and Scott Smith, 1999), or b) pyroclastic products derived from kimberlite eruptions and contained within kimberlite pipes and dykes to characterize eruption magnitude, intensity and associated style(s).

Here, I present a new fragmentation index for kimberlite eruptions. The index is a metric for the relative fragmentation intensity attending kimberlite eruptions (Fig. 5.11), and is based on data collected from coherent and pyroclastic rocks, models of dynamical fluid behaviour presented above, and is in the spirit of the original F-D diagram of Walker (1973).

Slopes from power-law approximations of olivine crystal populations (Chapter 3), or “D” values, are used to characterize the extent to which olivine crystals have broken during eruption (‘D’ values; Fig. 5.11). D-values are useful because they are scale-independent (i.e. dimensionless), and require significant changes in the overall properties of olivine crystal populations to change their values (Kaminski and Jaupart, 1998; Walters et al., 2006a). As changes in D-values are shown to positively correlate with the magnitude of pressure changes, the “D” parameter is then analogous to Walker’s “F” (Walker, 1973) as a proxy for increased violence of eruption, and may be highly affected by environmental influences. For example, external groundwater, vent clogging (after Walker, 1973) or overpressures built up by cap-rocks (e.g., Field and Scott Smith, 1999) can lead to more violent explosions, and therefore a higher D-value.

The FO:JP ratio is used to characterize the degree to which melt has separated from crystals during eruption (‘S’ values; Fig. 5.11). This ratio is useful because it is dimensionless and because it does not require a dataset which includes all of the eruptive products of kimberlite eruptions; deposits contained within kimberlite pipes can be examined, and it is not necessary to know the full extent of ash production (crystalline or quenched kimberlite w/o olivine crystals) in order to determine a reasonable estimate FO:JP ratio. Many of the possible causes for separation discussed above depend upon the gas content and velocity. Eruption column height and transport distance are also directly related to gas content, and are a proxy for the ‘power’ of an eruption. The “S” parameter strongly correlates to the power of the gas blast, is the most affected by relative proportions of phases intrinsic in the magma, and thus analogous to Walker’s “D” (Walker, 1973). For example, increasing magma viscosity, exsolved gas content, or the depth at which gas bubbles begin to form can lead to explosions with a higher “S” value.

This index utilizes data collected on olivine crystals and juvenile pyroclasts from the PK<sub>2</sub> and CK<sub>2</sub> from A154N kimberlite volcano (Fig. 5.11). Characterizing kimberlite

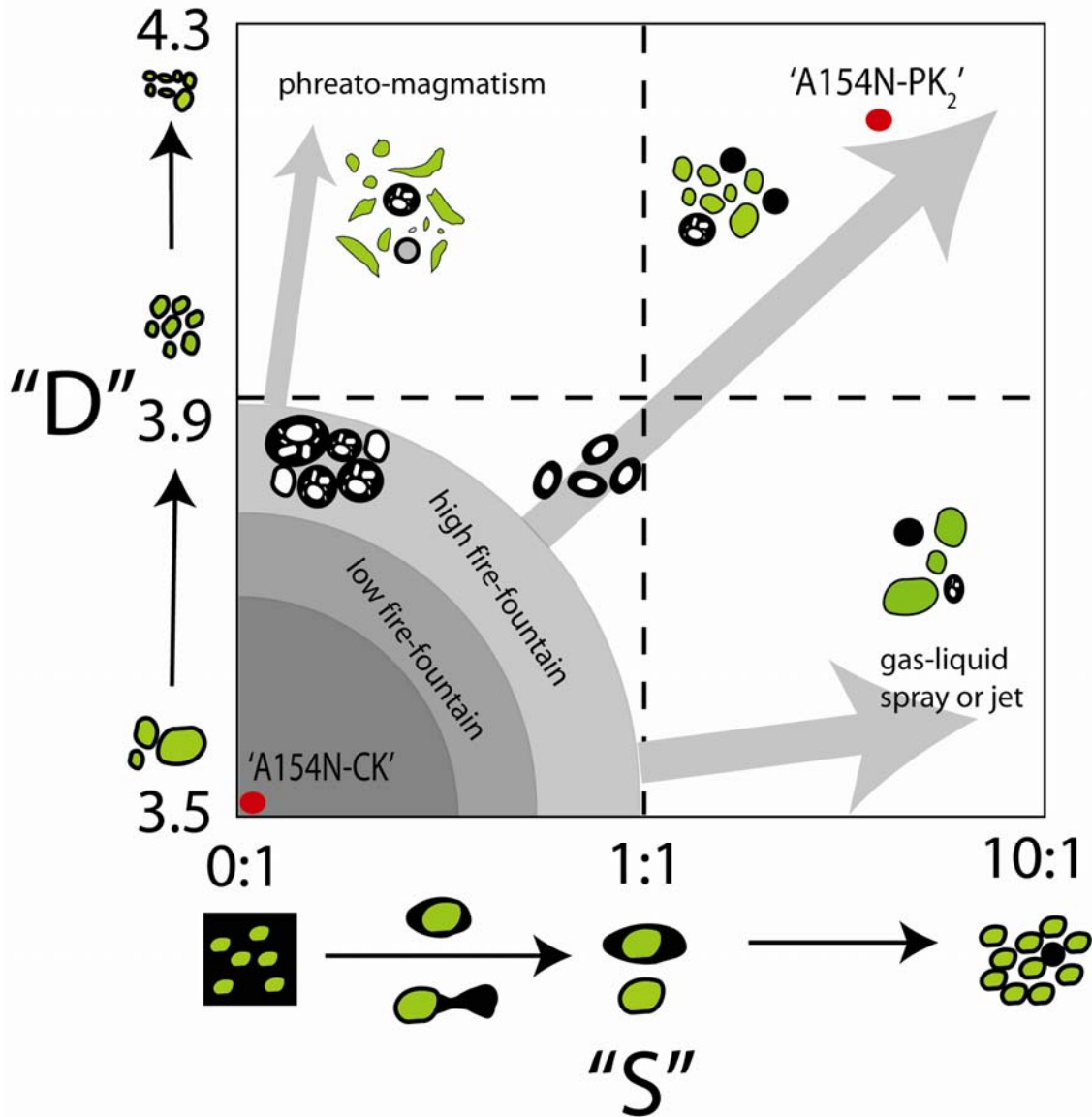


**Figure 5.11:** New fragmentation index for erupting kimberlite magmas based on measurable characteristics of pyroclastic deposits of kimberlite. The vertical axis are olivine crystal size distribution (CSD) slopes, or “D” values. CSD slopes are dimensionless numbers which reflect the pressure differentials for kimberlite magma during an eruption of kimberlite, and are largely controlled by external influences, analogous to Walker’s fragmentation or “F” parameter (Walker, 1973). The horizontal axis are ratios of ‘free’ olivine crystals (FO) to juvenile pyroclasts of crystalline kimberlite enclosing olivine crystals (JP). The separation ratio, “S”, is also a dimensionless number which reflects the intrinsic power of the erupted kimberlite, and is largely controlled by the relative ratios of gas, liquid (i.e., melt) and solids (i.e., crystals, xenoliths). Two kimberlite deposits from the present study of A154N at Diavik are shown as red dots: intrusive coherent kimberlite dykes (A154N-CK) and pyroclastic kimberlite (A154N-PK<sub>2</sub>).

eruptions using this fragmentation index has several applications. First, the index can assist in identifying the volcanic facies (i.e. pyroclastic vs. effusive, welding, etc.) of kimberlite. Secondly, the index may be used to assess the relative intensity (i.e. kg/s, exit velocity and volatile content) of kimberlite eruptions. Thirdly, the index may act as a tool for evaluating potential diamond grade enhancement or diminishment for a pyroclastic deposit of kimberlite.

*Caveat emptor*

An important assumption before using this index is that observed or studied deposits in kimberlite pipes capture or are representative of the entire suite of products from a kimberlite eruption. However, elutriation of ash or fines may lead to a bias in preservation. This could retain higher olivine crystal to preserved crystalline or quenched kimberlite ratios in a deposit than what was actually produced by the eruption. Moreover, alteration of kimberlite ash and the smallest fraction of olivine crystals and crystal fragments in the matrix of pyroclastic rocks may mask its presence in the original deposit, also leading to skewed olivine to preserved crystalline kimberlite ratios in a deposit than what was actually produced by the eruption. However, a key point to remember is that we are only concerned with the degree to which melt has separated from olivine crystals (FO:JP). This is a relative relationship, and can be adequately captured if one is confident they have made representative observations of either all of the olivine crystals or all of the JPs.

## 5.7 References

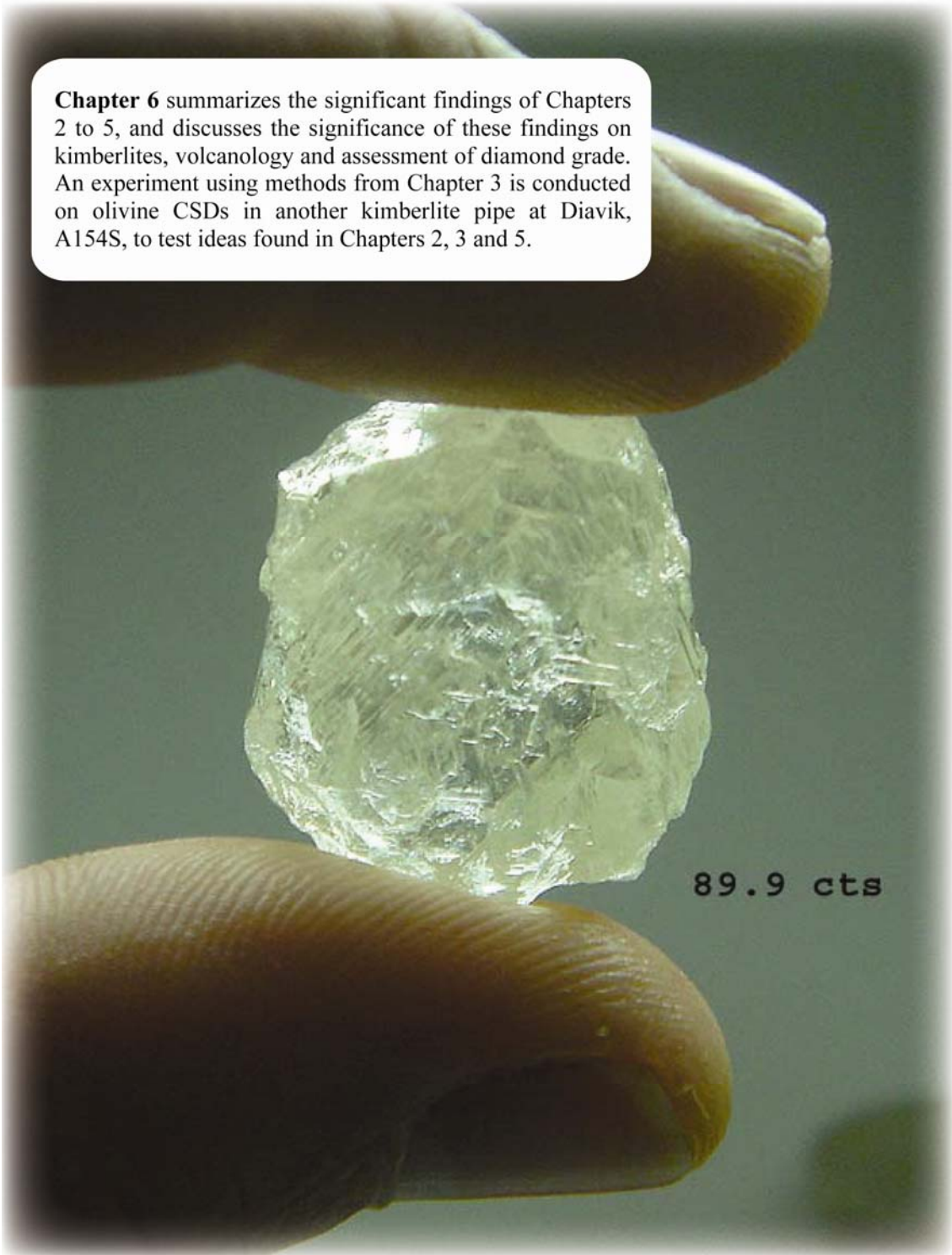
- Arndt, N.T., Boullier, A.M., Clement, J.P., Dubois, M. and Schissel, D., 2006. What olivine, the neglected mineral, tells us about kimberlite petrogenesis. *eEarth* 1, 15-21.
- Bangham, D.H. and Razouk, R.I., 1937. Adsorption and wettability of solid surfaces. *Transactions of the Faraday Society* 33, 1459-1463.
- Basson, I.J. and Viola, G., 2004. Passive kimberlite intrusion into actively dilating dyke-fracture arrays: evidence from fibrous calcite veins and extensional fracture cleavage. *Lithos* 76(1-4), 283-297.
- Best, M.G. and Christiansen, E.H., 1997. Origin of broken phenocrysts in ash-flow tuffs. *Geol Soc Am Bull* 109(1), 63-73.
- Bindeman, I.N., 2005. Fragmentation phenomena in populations of magmatic crystals. *American Mineralogist* 90, 1801-1815.
- Blake, S., Wilson, C.J.N., Smith, I.E.M. and Walker, G.P.L., 1992. Petrology and dynamics of the Waimihia mixed magma eruption, Taupo Volcano, New Zealand. *Journal of the Geological Society* 149(2), 193-207.
- Blander, M. and Katz, J.L., 1975. Bubble nucleation in liquids. *AIChE Journal* 21(5), 833-848.
- Boyer, L., Hood, C.T., McCandless, T.E., Skelton, D. and Tosdal, R.M., 2004. Volcanology of the Buffalo Hills Kimberlites, Alberta, Canada: some preliminary observations. 8th International Kimberlite Conference Long Abstract.
- Brett, R.C., Russell, J.K. and Moss, S., 2009. Origin of olivine in kimberlite: phenocryst or imposter? 9th International Kimberlite Conference Extended Abstract 9IKC-A-00298, 3.
- Cas, R., Porrit, L., Hayman, P. and Pittari, A., 2008. Pyroclast formation processes during explosive kimberlite eruptions. 9th International Kimberlite Conference extended abstract no. 9IKC-A-00030.
- Cas, R.A.F., Porrit, L., Hayman, P. and Pittari, A., 2008. Some major problems with existing models and terminology associated with kimberlite pipes from a volcanological perspective, and some suggestions. *Journal of Volcanology and Geothermal Research* 174(1-3), 209-225.
- Cas, R.A.F. and Wright, J.V., 1987. Volcanic successions, modern and ancient. Chapman & Hall, London, 528 pp.
- Dunbar, N.W., McIntosh, W.C. and Esser, R.P., 2008. Physical setting and tephrochronology of the summit caldera ice record at Mount Moulton, West Antarctica. *Geol Soc Am Bull* 120(7-8), 796-812.
- Faeth, G., Hsiang, L.-P. and Wu, P.-K., 1995. Structure and breakup properties of sprays. *International Journal of Multiphase Flow* 21, 99-127.
- Field, M. and Scott-Smith, B.H., 1999. Contrasting geology and near-surface emplacement of kimberlite pipes in southern Africa and Canada, VIIth International Kimberlite Conference. Red Roof Designs, Cape Town, South Africa, pp. 214-237.
- Fisher, R.V., 1963. Bubble-wall texture and its significance. *Journal of Sedimentary Research* 33, 224-227.

- Gernon, T.M., Gilbertson, M.A., Sparks, R.S.J. and Field, M., 2008. Gas-fluidisation in an experimental tapered bed: Insights into processes in diverging volcanic conduits. *Journal of Volcanology and Geothermal Research* 174(1-3), 49-56.
- Gonnermann, H.M. and Manga, M., 2007. The Fluid Mechanics Inside a Volcano. *Annual Review of Fluid Mechanics* 39(1), 321-356.
- Graham, I., Burgess, J.L., Bryan, D., Ravenscroft, P.J., Thomas, E., Doyle, B.J., Hopkins, R. and Armstrong, K.A., 1999. Exploration History and Geology of the Diavik Kimberlites, Lac de Gras, Northwest Territories, Canada. In: J.J. Gurney, J.L. Gurney, M.D. Pascoe and S.H. Richardson (Editors), *Proceedings of the VIIth International Kimberlite Conference*. Red Roof Design, Cape Town, South Africa, pp. 262-279.
- Hammer, J.E., Coombs, M.L., Shamberger, P.J. and Kimura, J.-I., 2006. Submarine sliver in North Kona: A window into the early magmatic and growth history of Hualalai Volcano, Hawaii. *Journal of Volcanology and Geothermal Research* 151(1-3), 157-188.
- Head, J.W. and Wilson, L., 2008. Integrated model for kimberlite ascent and eruption. 9th International Kimberlite Conference Extended Abstracts, 1-3.
- Heiken, G., 1972. Morphology and Petrography of Volcanic Ashes. *Geological Society of America Bulletin* 83(7), 1961-1988.
- Herd, R.A. and Pinkerton, H., 1997. Bubble coalescence in basaltic lava: Its impact on the evolution of bubble populations. *Journal of Volcanology and Geothermal Research* 75(1-2), 137-157.
- Higgins, M.D., 2000. Measurement of crystal size distributions. *American Mineralogist* 85, 1105–1116.
- Hinze, J.O., 1959. Turbulence, an introduction to its mechanisms and theory. McGraw-Hill, New York.
- Inman, D.L., 1952. Measures for describing the size distribution of sediments. *Journal of Sedimentary Petrology* 22, 125–145.
- Kamenetsky, V.S., Kamenetsky, M.B., Sobolev, A.V., Golovin, A.V., Demouchy, S., Faure, K., Sharygin, V.V. and Kuzmin, D., 2007. Olivine in the Udachnaya-East Kimberlite (Yakutia, Russia): Types, Compositions and Origins. *Journal of Petrology* 00, 1-17.
- Kaminski, E. and Jaupart, C., 1998. The size distribution of pyroclasts and the fragmentation sequence in explosive volcanic eruptions. *Journal of Geophysical Research* 103, 29759–29779.
- Kruis, F.E. and Kusters, K.A., 1997. The collision rate of particles in turbulent flow. *Chemical Engineering Communications* 158(1), 201 - 230.
- Kueppers, U., Perugini, D. and Dingwell, D.B., 2006. "Explosive energy" during volcanic eruptions from fractal analysis of pyroclasts. *Earth and Planetary Science Letters* 248(3-4), 800-807.
- Michol, K.A., Russell, J.K. and Andrews, G.D.M., 2008. Welded block and ash flow deposits from Mount Meager, British Columbia, Canada. *Journal of Volcanology and Geothermal Research* 169(3-4), 121-144.
- Mitchell, R.H., 2009. Mineralogy of juvenile lapilli in Fort a la Corne pyroclastic kimberlites, 2009 Joint Assembly AGU-GAC. American Geophysical Union (AGU), Toronto, ON.

- Morgan, D.J. and Jerram, D.A., 2006. On estimating crystal shape for crystal size distribution analysis. *Journal of Volcanology and Geothermal Research* 154(1-2), 1-7.
- Nowicki, T., Porritt, L., Crawford, B. and Kjarsgaard, B., 2008. Geochemical trends in kimberlites of the Ekati property, Northwest Territories, Canada: Insights on volcanic and resedimentation processes. *Journal of Volcanology and Geothermal Research* 174(1-3), 117-127.
- Parfitt, E.A., 2004. A discussion of the mechanisms of explosive basaltic eruptions. *Journal of Volcanology and Geothermal Research* 134(1-2), 77-107.
- Parfitt, E.A., Wilson, L. and Neal, C.A., 1995. Factors influencing the height of Hawaiian lava fountains: implications for the use of fountain height as an indicator of gas content. *Bulletin of Volcanology* 57, 440-450.
- Pittari, A., Cas, R.A.F., Lefebvre, N., Robey, J., Kurszlaukis, S. and Webb, K., 2008. Eruption processes and facies architecture of the Orion Central kimberlite volcanic complex, Fort à la Corne, Saskatchewan; kimberlite mass flow deposits in a sedimentary basin. *Journal of Volcanology and Geothermal Research* 174(1-3), 152-170.
- Porritt, L.A. and Cas, R.A.F., 2009. Reconstruction of a kimberlite eruption, using an integrated volcanological, geochemical and numerical approach: A case study of the Fox Kimberlite, NWT, Canada. *Journal of Volcanology and Geothermal Research* 179(3-4), 241-264.
- Porritt, L.A., Cas, R.A.F. and Crawford, B.B., 2008. In-vent column collapse as an alternative model for massive volcanoclastic kimberlite emplacement: An example from the Fox kimberlite, Ekati Diamond Mine, NWT, Canada. *Journal of Volcanology and Geothermal Research* 174(1-3), 90-102.
- Price, S., Russell, J.K. and Kopylova, M., 2000. Primitive magma from the Jericho pipe, N.W.T., Canada: Constraints on primary melt chemistry. *Journal of Petrology* 41(6), 789-808.
- Russell, J.K., Giordano, D., Kopylova, M. and Moss, S., 2006. Transport properties of kimberlite melt, Long Abstract, Kimberlite Emplacement Workshop, Saskatoon, Canada.
- Scott Smith, B.H., 2008. The Fort a la Corne Kimberlites, Saskatchewan, Canada: Geology, Emplacement and Economics. *Journal Geological Society of India* 71, 11-55.
- Scott Smith, B.H., 2008. Introduction to kimberlites. Short Course Notes: Kimberlites - Geological Principles Relevant to Evaluation, Resource Classification and Mining, Mineral Exploration Roundup 08, Vancouver, pp. 21.
- Sigurdsson, H. (Editor), 2000. *Encyclopedia of Volcanoes*. Academic Press, San Diego, 1417 pp.
- Sparks, R.S.J., Baker, L., Brown, R.J., Field, M., Schumacher, J., Stripp, G. and Walters, A., 2006. Dynamical constraints on kimberlite volcanism. *Journal of Volcanology and Geothermal Research* 155(1-2), 18-48.
- van Straaten, B.I., Kopylova, M.G., Russell, J.K., Webb, K.J. and Scott Smith, B.H., 2008. Discrimination of diamond resource and non-resource domains in the Victor North pyroclastic kimberlite, Canada. *Journal of Volcanology and Geothermal Research* 174(1-3), 128-138.

- Villermaux, E., 1998. On the role of viscosity in shear instabilities. *Physical Fluids* 10, 368-373.
- Villermaux, E., 2007. Fragmentation. *Annual Review of Fluid Mechanics* 39, 419-446.
- Walker, G.P.L., 1973. Explosive volcanic eruptions--A new classification scheme. *Geol Rudsch* 62, 431-446.
- Walters, Phillips, J.C., Brown, R.J., Field, M., Gernon, T., Stripp, G. and Sparks, R.S.J., 2006. The role of fluidisation in the formation of volcanoclastic kimberlite: Grain size observations and experimental investigation. *Journal of Volcanology and Geothermal Research* 155(1-2), 119-137.
- Webb, K.J., 2006. Juvenile clasts in kimberlites: Standardizing comprehensive description towards unravelling emplacement models, Kimberlite Emplacement Workshop, Saskatoon, Saskatchewan.
- Webb, K.J., Scott Smith, B.H., Paul, J.L. and Hetman, C.M., 2004. Geology of the Victor Kimberlite, Attawapiskat, Northern Ontario, Canada: cross-cutting and nested craters. *Lithos* 76(1-4), 29-50.
- Wierzba, A., 1990. Deformation and breakup of liquid drops in a gas stream at nearly critical Weber numbers. *Experiments in Fluids* 9(1), 59-64.
- Wu, P.K. and Faeth, G.M., 1995. Onset and end of drop formation along the surface of turbulent liquid jets in still gases. *Physics of Fluids* 7(11), 2915-2917.
- Zhou, Y., Wexler, A.S. and Wang, L.P., 2001. Modelling turbulent collision of bidisperse inertial particles. *Journal of fluid mechanics* 433, 73-104.

**Chapter 6** summarizes the significant findings of Chapters 2 to 5, and discusses the significance of these findings on kimberlites, volcanology and assessment of diamond grade. An experiment using methods from Chapter 3 is conducted on olivine CSDs in another kimberlite pipe at Diavik, A154S, to test ideas found in Chapters 2, 3 and 5.



89.9 cts

## **6 The volcanology of A154N: implications for kimberlites and diamonds**

The investigation of the A154N kimberlite pipe at Diavik has resulted in descriptive data for a variety of kimberlite deposits. These data are intended to contribute to the following areas in kimberlite volcanology:

- metrics to characterize the volcanic style and intensity of kimberlites;
- the physical properties of kimberlite magma
- quantification of pyroclastic deposits.

The descriptive data from this thesis has led to interpretations of volcanic processes at A154N, and resulted in several contributions to our knowledge of the physical volcanology and emplacement of kimberlite volcanoes. Here, I summarize the most important data results from Chapters 2-4, and review the interpreted emplacement model of A154N. I then highlight the most significant implications of the data and emplacement model for kimberlite volcanology and diamond grade evaluation within kimberlite deposits. The chapter concludes with a breviary of areas for future study.

### **6.1 Summary of descriptive data on A154N from chapters 2 – 4**

**Chapter 2:** Contact relationships between PK<sub>1</sub>, RVK, and PK<sub>2</sub> in A154N also indicate a logical sequence of emplacement: PK<sub>1</sub> followed by RVK, followed by PK<sub>2</sub>. The PK<sub>1</sub> deposit fills approximately 80% of A154N (~5.0 x 10<sup>6</sup> m<sup>3</sup>; Table 6.2). Facies analysis of PK<sub>1</sub> (i.e., MVK<sub>1</sub> and MVK<sub>2</sub>; Ch. 4) indicates a progressive vertical change from massive, poorly sorted, shale-poor volcanoclastic deposits to crudely sorted, finer-sized, and shale-rich deposits. Facies analysis of the RVK (i.e., SVK; Ch.4) deposits indicate a gradual change from coarse, massive to poorly-bedded volcanoclastic kimberlite, to smaller volume, finer, mantle-depleted, shale-enriched, well-bedded deposits. Granulometry data show a progressive vertical change in the relative abundance and types of components within the PK<sub>2</sub> unit. Olivine crystals show incremental changes in median size, and sorting efficiency from the bottom to the top of

PK<sub>2</sub> (Fig. 5.8; Table 6.1). Analysis of the cumulative population of components in PK<sub>2</sub> show an approximately log-normal distribution of pyroclasts (Fig. 5.8), and can be described by a power-law equation with a slope (D-value) of 3.3 (Fig. 5.9b; Table 6.1). The Inman parameters of the entire PK<sub>2</sub> deposit are consistent with > 96% of those observed in pyroclastic flow deposits (Fig. 5.9a; Table 6.1). Pyroclasts in PK<sub>2</sub> include spherical, fine-ash sized pyroclasts, juvenile pyroclasts with relatively few vesicles (generally < 10%), and are restricted in maximum size (< 5cm) relative to those produced by eruption of other magma types.

**Chapter 3:** Quantitative characterization of olivine crystal size distributions (CSD) using 2D image analysis techniques (Chapter 3) yields characteristic properties for olivine in intrusive coherent kimberlite at A154N (CK<sub>2</sub>), including: modal abundance (44 – 51 %), size range (0.03 – 10 mm diameter), shapes (equant, ellipsoidal, 1:1:1 axial ratios), sorting efficiency ( $\sigma = 2.9 - 3.5$ ), skewness ( $\alpha = 0.3 - 0.5$ ) and D-values (i.e., power-law slopes;  $\sim 3.55$ ) (Table 6.1). Characterizing olivine crystal populations can be accomplished by either manual (Chapter 3) or automatic (Appendix 7.3.2) methods. While there are advantages and disadvantages to both methods, the automatic method carries a distinct advantage in successfully reproducing the quality of data obtained using the manual method in a fraction of the time.

**Chapter 4:** Contacts between the CK<sub>1</sub>, PK<sub>1</sub> and CK<sub>2</sub> deposits at A154N indicate a logical sequence of emplacement: CK<sub>1</sub>, followed by PK<sub>1</sub>, followed by CK<sub>2</sub>. The modal abundance of olivine in CK<sub>1</sub>, CK<sub>2</sub>, and juvenile pyroclasts deriving from the eruption of PK<sub>1</sub> are shown to be variable (Table 6.1). Sub-types of juvenile pyroclasts are observed within PK<sub>1</sub> (Table 6.1). Textural evidence of exsolved fluid within CK<sub>1</sub>, CK<sub>2</sub>, and the juvenile pyroclasts of PK<sub>1</sub> are also variable (Table 6.1). The minimum geometries of CK<sub>1</sub>, PK<sub>1</sub>, and CK<sub>2</sub> are found in 3D-models, and used to estimate mass flux and eruption durations at A154N (Table 6.2). Estimates of mass flux rates are  $10^6 - 10^{6.5} \text{ kg s}^{-1}$ , orders of magnitude larger than low-intensity fire-fountain eruptions of basalt (Table 6.2). The minimum duration of the eruption which formed the A154N pipe and deposited PK<sub>1</sub> is constrained by conduit geometry, and estimates range from a minimum of  $\sim 8$  minutes to more than 16 hours (Table 6.2).

**Table 6.1:** Summary of component properties in CK<sub>1</sub>, PK<sub>1</sub>, CK<sub>2</sub>, and PK<sub>2</sub> in A154N

A154N deposit	CK <sub>1</sub>	CK <sub>2</sub>	PK <sub>1</sub>	PK <sub>2</sub>
samples studied	4	5	>50	>50
sample sizes (mm <sup>2</sup> )	~5200 - 12,000	3619	~4000 - 10,000	~4000 - 15,000
<b>Key component properties (Ch. 2,6)</b>				
ol : crystalline groundmass (gm)	0.05 - 0.15	1	(-)	~22
% free olivine (FO)	(-)	(-)	(-)	35.8
% juvenile pyroclasts (JP)	(-)	(-)	(-)	5.4
FO : JP	(-)	(-)	(-)	6.7
σ <sup>‡</sup> range (whole deposit)	(-)	(-)	(-)	0.82 - 3 (2.6)
D <sup>  </sup> -- all clasts	(-)	(-)	(-)	3.3
<b>Olivine properties (Ch. 2,4,6)</b>				
modal (%)	5.2 - 15.1	46.7 - 51.2	(-)	39.4
sizes (diameters, in mm)	0.27 - 9.7	0.03 - 12.4	(-)	0.025 - 15.16
ol(n):OL(n)*	0.18 - 0.26	72 - 138	(-)	248
OL(%) : ol(%)	16.7 - 19.1	1.6 - 2.0	(-)	0.41
MdΦ <sup>†</sup>	-0.42 to -0.49	3.3 - 3.8	(-)	4
σ <sup>‡</sup>	0.67 - 0.68	2.9 - 3.5	(-)	3.6
α <sup>§</sup>	-6.8 to -6.9	0.3 - 0.5	(-)	0.8
D <sup>  </sup>	-	3.53 - 3.61	(-)	4.29
λ <sup>#</sup>	-	2.22 - 2.38	(-)	2.6
mean crystal 'circularity'*** (stdev.)	0.74 (0.11)	0.61 (0.21)	(-)	0.74 (0.15)
3D shape (R <sup>2</sup> )	1 : 1 : 1 (~0.73)	1 : 1 : 1 (~0.8)	(-)	1 : 1 : 1 (~0.83)
<b>Volatile properties (Ch. 4,6)</b>				
% vesicles	0 - 60	0 - 2	0 - 40 <sup>††</sup>	0 - 10 <sup>††</sup>
vesicle sizes (mm)	0.2 - 5	0.2 - 1	0.1 - 1 <sup>††</sup>	0.1 - 1 <sup>††</sup>
<b>Pyroclast properties (Ch. 4,5,6)</b>				
types <sup>§§</sup>	(-)	(-)	FA/FO/M/PS/C S/C/V/Carb/AL	FA/FO/M/PS/CS /C/V/Carb/AL
JPs studied (# of samples)	(-)	(-)	211 (20)	248 (10)
size range (diameter in mm)	(-)	(-)	0.03 - 4	0.03 - 3.5
total ol : gm in JPs	(-)	(-)	~2 to 1	~1 to 1
% ol in JPs	(-)	(-)	0 - 90	0 - 90
% ol in JPs w/ mult. Olivine	(-)	(-)	0 - 44	0 - 56
% JP w/ vesicles	(-)	(-)	16.6	14.7
% JP w/ carbonate	(-)	(-)	1.9	1.5
% JP w/ multiple olivine	(-)	(-)	58.8	49
% JP w/ complete selvage	(-)	(-)	19.4	17.8
% JP w/ partial selvage	(-)	(-)	7.1	24.7
% JP w/ olivine core	(-)	(-)	14.7	8.5

Note1: 3D shapes (aspect ratios) and correlation coefficients obtained using CSDSlice (Jerram and Morgan, 2006)

Note2: For more information on methods of measurement, refer to Methods sections of Ch.2,4,5, and 6. Details of methods included in Appendices

(-) indicates property was not measured

|| D = slope of best-fit power-law

\* ol = olivine < 1 mm; OL = olivine ≥ 1 mm

# λ = intercept of best-fit power-law

† MdΦ = Median phi size (-log<sub>2</sub>(d))

\*\* circularity = (4\*Area\*pi)/(Perimeter)<sup>2</sup>

‡ σ = sorting efficiency =  $\frac{(\phi_{84}) - (\phi_{16})}{2}$

§ α = skewness =  $\frac{(\phi_{84}) + (\phi_{16}) - Md\phi}{\sigma}$

§§ types are: fine-ash (FA); free olivine (FO); multiple olivine (M); partial selvage (PS); complete selvage (CS); cored (c); vesiculated (V); carbonate-bearing (Carb); accretionary lapilli (AL)

†† measured within juvenile pyroclasts

**Table 6.2:** Summary of deposit attributes and eruption estimates for CK<sub>1</sub>, PK<sub>1</sub>, CK<sub>2</sub>, and PK<sub>2</sub> in A154N

A154N deposit	CK <sub>1</sub>	CK <sub>2</sub>	PK <sub>1</sub>	PK <sub>2</sub>
<b>Deposit attributes (Ch. 2, 4, 5)</b>				
volume (m <sup>3</sup> )*	~3.2 x 10 <sup>5</sup>	~1.1 x 10 <sup>5</sup>	~5.0 x 10 <sup>6</sup>	~0.55 x 10 <sup>6</sup>
min. cross-sectional area (m <sup>3</sup> )*	500	143	253	(-)
descriptive rock type	coherent	coherent	fragmental	fragmental
interpreted rock type	coherent kimberlite	coherent / hypabyssal kimberlite	pyroclastic kimberlite	pyroclastic kimberlite
alteration	serp., carb.	fresh	serp., carb.	fresh
interpreted emplacement order	1st	3rd or 4th	2nd	3rd or 4th
<b>Eruption estimates (Ch. 4)</b>				
mass flux rate (kg s <sup>-1</sup> )	10 <sup>7.1</sup> - 10 <sup>8</sup>	10 <sup>5.5</sup> - 10 <sup>6.1</sup>	10 <sup>5.3</sup> - 10 <sup>7.1</sup>	(-)
eruption duration (minutes)	(-)	> 14	8 to > 960	(-)
interpreted deposit style	fissure eruption	passive intrusion	column collapse and fluidization	pyroclastic density current deposited in crater lake

Note: Mass flux rate and eruption duration estimates are based on inferred and measured properties of kimberlite magma. For more information on these properties, see Chapter 4

(-) indicates property was not possible to estimate

\* as modelled in Vulcan<sup>TM</sup> mining software

**Chapter 5:** Pyroclastic deposits of kimberlite at Diavik show a variety of textural, mineralogical, and morphological types of juvenile pyroclasts (Fig. 6.1). Pyroclasts from the PK<sub>2</sub> deposit in A154N are studied to characterize differences in olivine componentry from pyroclastic deposits with those in crystallized kimberlite magma (e.g., CK<sub>2</sub>, Chapter 3). Olivine crystals in the PK<sub>2</sub> deposit of A154N have different size, shape and distribution properties than olivine crystals in CK<sub>2</sub> (Table 6.1). The PK<sub>2</sub> deposit comprises abundant ‘free’ olivine crystals (FO) and juvenile pyroclasts of crystalline kimberlite (JP), with a modal (area%) FO : JP ratio of 6.7 to 1. Juvenile pyroclasts (JP) within PK<sub>2</sub> are shown to contain ~65% modal abundance of olivine (Table 6.1). Combining the FO : JP ratio with the modal abundance of olivine within JPs show a modal (area%) olivine to crystalline kimberlite melt ratio of 22 : 1. Olivine content within multiple-olivine juvenile pyroclasts (M; Chapters 4, 6) shows a positive correlation with the size of the pyroclast. The total surface area of olivine crystals within individual juvenile pyroclasts (SA<sub>T</sub>; Chapter 5) also shows a positive correlation with the size of the pyroclast. However, the ratio of surface area to volume of crystalline groundmass shows a negative correlation with the size of the pyroclast.

## 6.2 Emplacement summary for A154N

The deposits within the A154N kimberlite pipe ( $\sim 6.1 \times 10^6 \text{ m}^3$ ) are interpreted to be the result of five emplacement events (CK<sub>1</sub>, PK<sub>1</sub>, RVK, PK<sub>2</sub>, CK<sub>2</sub>).

- First, a transient, low-volume, gas-charged (i.e. CO<sub>2</sub>, H<sub>2</sub>O) fissure eruption of olivine-poor kimberlite magma emplaced CK<sub>1</sub>.
- Second, a sustained (i.e. high flux, long duration) eruption of variable gas and olivine content excavated the A154N pipe. The sustained eruption proceeded to “drill” down into the country rock, efficiently excavating down to >750 m below surface. Infilling of A154N immediately ensued, filling ~80% ( $5.0 \times 10^6 \text{ m}^3$ ) of the present-day pipe volume with PK<sub>1</sub>. During the waning stages of eruption, depositional style progressed from en-masse, vertical collapse of the eruption

column as a conduit filling density current to fall-out and crude sorting of the finer size fractions suspended in the upper portion of the column (MVK<sub>2</sub>; Chapter 2). The eruption that excavated the A154N pipe and deposited PK<sub>1</sub> likely lasted from minutes to hours (Chapter 4), and left a large crater >200 m deep (Chapter 2).

- Third, during the waning stages of eruption, or immediately post-eruption, coarse, loose volcanic debris began to re-deposit into the open crater from all sides (RVK). Groundwater ultimately fills the crater with water at the same time that denudation of the crater walls and sedimentation into the conduit are taking place. Hot aqueous fluids serpentinize the interior of the volcanic pile and basal RVK deposits (Chapter 2). Systematically smaller-volume, finer, mantle-depleted, and shale-enriched kimberlite continues to deposit into a deepening crater lake (RVK, Chapter 2).
- Fourth, a pyroclastic density current sourced from one of the many adjacent pipes in the Diavik area inundated the A154N pipe (PK<sub>2</sub>; Chapter 2). Facies analysis of the PK<sub>2</sub> deposit suggest a pyroclastic origin and hydraulic sorting during *en-masse* deposition of pyroclastic kimberlite into a deep water column.
- Finally, non-eruptive olivine-rich and gas-poor coherent kimberlite dykes (CK<sub>2</sub>) were passively emplaced into the interior of PK<sub>1</sub> and along the contacts between PK<sub>1</sub> and adjacent country rocks. This event may have pre-dated the emplacement of PK<sub>2</sub> or significantly post-dated the eruption that formed the A154N pipe, but the time gap between events cannot be further constrained.

### **6.3 Implications of this work for kimberlite volcanology**

The descriptive data and interpretation of emplacement events at A154N have the following implications for kimberlite volcanology:

- a. *Quantification of characteristic properties of olivine crystals in intrusive coherent kimberlite.* Olivine crystals are the dominant component in intrusive coherent kimberlite rocks, and may have characteristic properties, including modal %, size range, shape

variability, and population parameters. These characteristic properties can serve as a baseline in understanding kimberlite eruption style and fragmentation, and in accurately describing and interpreting deposits of pyroclastic kimberlite.

b. *Documentation of component variations in kimberlite magmas in time and space.*

Kimberlite magmas are proposed to phase separate during ascent, yielding different phase proportions (crystals : melt : gas) within and/or between emplacement events (Chapter 4) that can determine:

- i. the emplacement style of kimberlite volcanoes (e.g., passive intrusive vs. explosive eruption)
- ii. degree of melt separation from olivine crystals during eruption
- iii. and therefore the amount of primary, preserved crystallized kimberlite melt around olivine crystals in deposits.

c. *Kimberlite pipes can contain deposits from multiple eruptions from spatially-separate sources.* Coalescing or cross-cutting kimberlite pipes and nested craters are well-documented at other kimberlite bodies (e.g., Field et al., 1997; Webb et al., 2004). Individual kimberlite pipes are also shown to contain deposits deriving from multiple eruption events sourced from the same kimberlite pipe. However, study of the graded pyroclastic kimberlite (PK<sub>2</sub>) from A154N shows that kimberlite volcanoes can also act as receptacles for primary volcanic products from the eruptions of nearby, but spatially-separate kimberlite pipes (Chapter 2).

d. *Durations of explosive kimberlite eruption are constrained by conduit geometry:*

Measured and estimated physical properties of kimberlite magmas may be combined with 3-D models for the geometry of the conduit at the time of eruption to constrain the mass flux and minimum duration of eruption events at A154N (Chapter 4). Steady-state assumptions for velocity and magma flux yield minimum total eruption durations of minutes to hours. The mass flux rates estimated for the A154N kimberlite pipe based on minimum ascent velocities are orders of magnitude higher than a low-intensity, fire-fountain eruption of basalt. These estimates can be improved with better constraints on

the physical properties of kimberlite magma, and provide a baseline for comparison with other kimberlite volcanoes with well-constrained conduit geometries.

*e. Pyroclast properties are tools for estimating eruption style:* Observations of primary pyroclastic products in kimberlite deposits can serve to approximate eruption style. Eruptions can act to both modify the sizes, shapes and distributions of olivine crystals and separate melt from olivine. The degree to which olivine breaks reflects the pressure differential experienced by magma during eruption, and is a proxy for the explosivity or violence. The efficiency of melt separation reflects the gas content and velocity, and is a proxy for the power of the eruption. Relative changes in the proportion of these two parameters may serve as a proxy for the overall intensity of eruption kimberlite (Chapter 5).

#### **6.4 Diamond distributions in volcanic kimberlite deposits**

Several factors control the diamond potential and diamond population of a given kimberlite body. Firstly, kimberlite magma must pass through the diamond stability field in the mantle and that portion of the mantle must be diamondiferous. Second, the host magma is caustic to the diamonds (e.g., oxidizing). Processes before, during and after emplacement can also directly affect the size and distribution of diamonds in kimberlite bodies. For example, magmatic processes such as magmatic differentiation or gas phase separation can separate components and/or phases of different size, density, buoyancy, or viscosity in time and space, possibly leading to grade zonation (Field et al., 2008). Volcanic processes can affect the distribution of the components in kimberlite volcanoes (including diamond; Chapman and Boxer, 2004; Porritt, 2008). These processes include sub-aerial and/or sub-aqueous sorting, en-masse gravitational collapse of a pyroclastic column, mass wasting of a crater edifice into a volcanic vent, and down-slope grain flows of kimberlite components into a crater off the slope of the volcanic pile (Scott Smith, 2009b). Physical volcanic processes can also impact diamond sizes. Fragmentation intensity and style during eruption, gravitational fall, and grain freedom during transport are likely to control the amount of diamond breakage during kimberlite emplacement.

The impacts of magmatic and volcanic processes described in Chapters 2 - 5 on diamond distributions are evaluated below.

#### 6.4.1 Olivine and diamond in intrusive coherent kimberlite

Diamond is subject to the same physical and chemical processes as those impacting olivine crystals, highlighted in Chapter 3. Thus, the behavior and crystal size distribution of dominant phases such as olivine has been hinted to be an important proxy for diamond sizes (Field et al., 2008; Scott Smith, 2009b). A relationship between the CSDs of olivine and diamond has not been established. However, there are several factors that likely prevent direct comparison of olivine CSDs with diamond in coherent kimberlite.

First, diamonds generally derive from eclogitic and peridotitic sources (Meyer and Boyd, 1972; Sobolev et al., 1976; Creighton et al., 2007). As a result, not all diamonds in kimberlite will have grown in equilibrium with peridotitic olivine. Furthermore, the relative proportion of these two mantle rock types within individual kimberlite bodies is usually poorly known (Creighton et al., 2007).

Second, transport processes modify both olivine and diamond populations. Olivine crystals commonly show evidence of milling and/or resorption, and/or evidence of late crystallization on older xenocrysts (Kamenetsky et al., 2007a; Brett et al., 2009) and locally as new phenocrysts or groundmass crystals (Woolley et al., 1996; Fedortchouk and Canil, 2004). In addition, it has been shown that diamonds are resorbed in both reducing and oxidizing conditions and high temperatures in kimberlite melts (Fedortchouk et al., 2005); the longer 'free' diamonds reside as liberated or partially exposed crystals in the melt, the smaller they become. If such resorption is considered alongside the crystallization of fresh olivine around xenocryst crystal margins and/or as newly nucleated crystals, the slopes of CSDs for diamond and olivine could be moving in opposite directions (steeper vs. shallower; +/- in D-values, Fig. 6.1) with added time in the hot kimberlite magma. Thick olivine overgrowth rims or the presence of large,

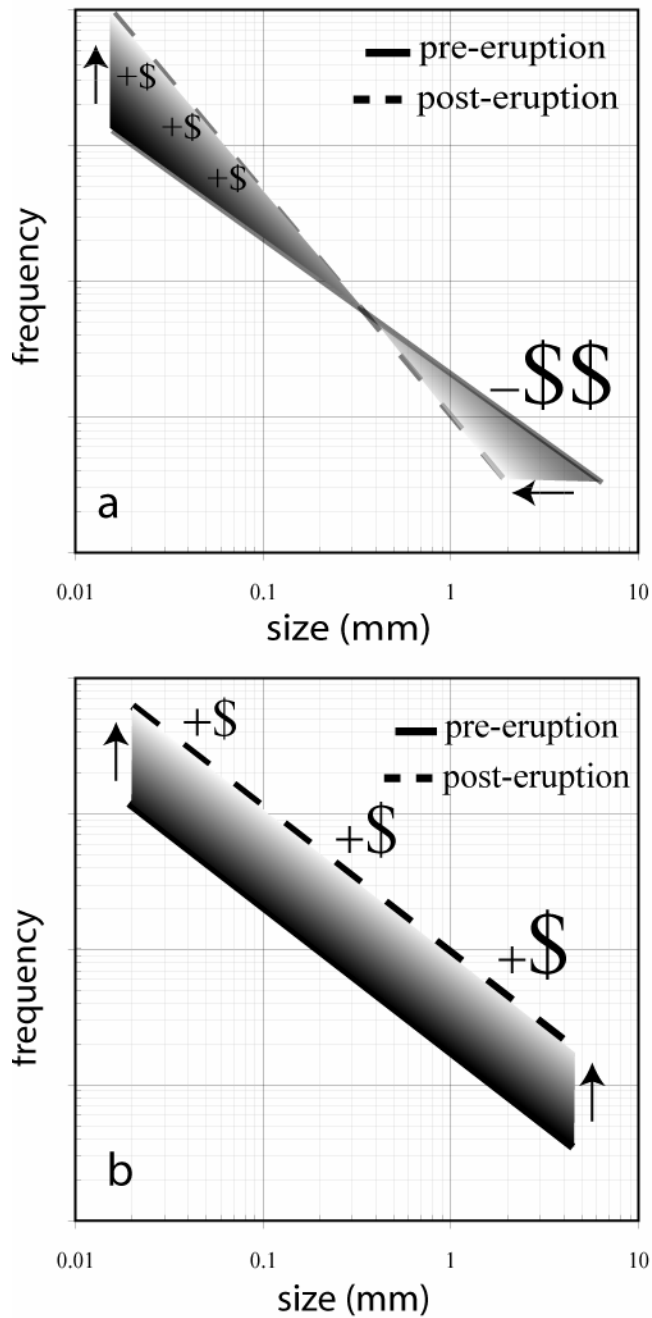


**Figure 6.1:** Hypothetical effects of volcanic processes on diamond size distributions: (a) crystal fragmentation; (b) crystal concentration. Solid lines indicate hypothetical starting, pre-eruption diamond population; dashed lines indicate post-eruption result of population modification due to (a) and (b).

ehedral crystals, therefore, may imply a relatively lower diamond grade. As olivine and diamond have different hardness and therefore fragmentation tendencies, it is also unlikely that diamond and olivine would break in the same fashion during transport through the crust in the kimberlite magma.

Thus, diamond and olivine CSDs in intrusive coherent rocks are unlikely to imitate each other in size ranges, shapes, or frequency distribution. However, if diamonds are free crystals in an emplaced kimberlite melt, diamond CSDs will show similar *shifts* in response to volcanic processes (i.e., hydraulic sorting) highlighted for olivine CSDs in Chapter 3 (Fig. 3.10), and postulated by Field (2008) and Scott Smith (2009b). Hypothetical shifts in CSDs for diamond are shown in Figure 6.1; concomitant changes in values are indicated with dollar signs (\$).

#### 6.4.2 Distinguishing magma ‘pulses’ or ‘batches’ using juvenile pyroclasts

Olivine contents within juvenile pyroclasts have been used to distinguish between deposits with distinct diamond grades (Webb et al., 2004). Moreover, mineralogical and textural diversity in juvenile pyroclasts is believed by some authors to be diagnostic of multiple eruption phases (Webb, 2006; van Straaten et al., 2008). In some cases, these observations can be supported by diamond size distributions and mineral chemistry (Webb et al., 2004; pers. comm., Scott Smith, 2009a). However, the observations of textural diversity in juvenile pyroclasts within a single pyroclastic deposit (fig. 4.6; fig. 6.6) suggests that mineralogically or texturally heterogeneous pyroclasts need not derive from distinct magma batches or eruptions separated by time. An implication of these observations is that using ‘type’ pyroclasts as a discriminator of distinct magma ‘batches’ is not a line of evidence that can stand alone; mineral chemistry, diamond size distributions, and other textural and mineralogical information must also correlate with any potential distinctions before any reasonable interpretations can be made.

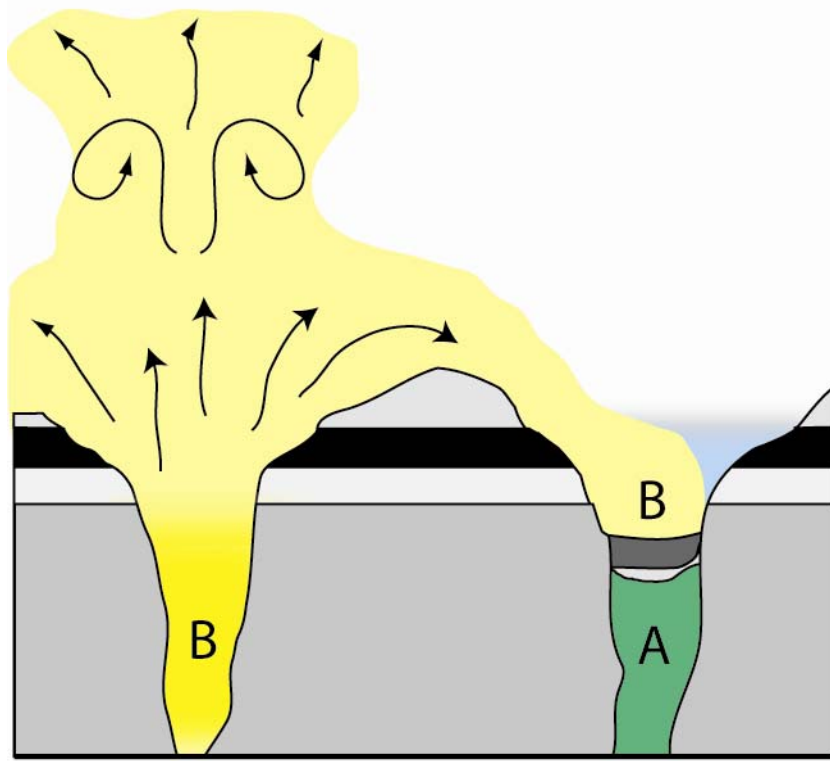
### 6.4.3 Single pipes can contain deposits sourced from multiple pipes

The deposits in A154N suggest that infill of kimberlite pipes can be the result of multiple eruptions sourced from different kimberlite volcanoes (Chapter 2). Efforts to identify volcanic sources of economic grade for a given pipe must take the possibility of ‘cross-fertilization’ into account. Cross-fertilization of kimberlite deposits in a single kimberlite pipe has the following implications on grade evaluation:

a) *“Global” grade evaluation of a kimberlite pipe.* Recognition of cross-fertilization from multiple eruptions can aid in the identification of deposits resulting from the eruption of discrete ‘phases’ of kimberlite magma (sensu Scott Smith, 2009) with potentially different diamond populations. The failure to distinguish deposits deriving from separate phases of kimberlite may lead to a statistical oversimplification of the diamond distribution for the entire pipe, and, thus, significant misrepresentations of a diamond population.

b) *Exploration and pipe evaluation.* Most initial exploration drilling concentrates cost expenditures and drillhole density in near-surface environments (<300 m below surface). However, cross-fertilized kimberlite deposits may lead to a stratigraphic succession of kimberlite deposits with variable diamond grades (Deposit A<sub>SS</sub> > Deposit B<sub>SS</sub>; Deposit B<sub>SS</sub> > Deposit A<sub>SS</sub>; Fig. 6.2). Shallow-level microdiamond or bulk sampling within such stratigraphy could lead to any of the following scenarios: a) overestimation of diamond potential, b) underestimation of diamond potential, or c) a fortuitous accurate representation of diamond populations (Fig. 6.3). Furthermore, identification of a ‘rootless’, high-grade deposit filling the top of a kimberlite pipe suggests the presence of an (possibly) un-identified, high-grade source in close proximity.

c) *Kimberlite indicator mineral dispersion.* The presence and distribution of kimberlite indicator minerals (KIM) around kimberlite pipes is widely used as an initial vectoring tool for identifying kimberlite pipes (McClenaghan and Kjarsgaard, 2001; e.g., Masun et al., 2004). Moreover, the mineral chemistry of KIM is readily used to identify the diamond potential of their source kimberlite bodies (e.g., Grütter et al., 2004). In highly-eroded cratonic terranes, the most recent erosion of kimberlite pipes removes and



volcano B

volcano A

**Figure 6.2:** Schematic illustration of two cross-fertilizing volcanic eruptions. Eruption of Volcano A is followed by eruption of Volcano B, creating a stratigraphy of deposits (B above A) in Volcano A.

True Value Scenarios	B: fertile	B: barren
A: fertile	fortuitous suggests presence of high-grade B 	misleading "shows" uneconomic when profitable 
A: barren	misleading "shows" profitable pipe when uneconomic 	fortuitous top indicates true low-grade nature of pipe 

**Figure 6.3:** Scenarios of true value for fertile (diamond-bearing), and barren (diamond-absent) deposits of kimberlite.

distributes mostly intra-pipe deposits. This would distribute the contents previously within the pipe to the immediate surroundings via a variety of transport means (fluvial, Aeolian, glacial, etc.). If a kimberlite pipe whose primary pipe-forming eruption was a diamond-bearing, high-grade deposit, has been cross-fertilized by a late, low-grade or diamond-less deposit of kimberlite, kimberlite indicator mineral trains adjacent to the pipe would show an unfavorable diamond-carrying capacity (i.e., low-grade). Moreover, deep craters formed by eruption could also fill with deposits of foreign kimberlite detritus or non-kimberlite country rock and sediment over time. In either case, the abundances, distribution and/or chemistry of KIM could misrepresent the true diamond potential of the kimberlite pipe (e.g., Graham et al., 1999).

d) *Kimberlite clusters and cross-fertilization.* Kimberlite pipes are known to occur in clusters, close in space and time (e.g., Kurszlaukis and Barnett, 2003; Nowicki et al., 2004). Moreover, many kimberlite eruptions have been shown to leave deep craters, which fill with sedimentary deposits from the collapsing tephra rim, as well as exotic sediments, and can form long-standing crater lakes (e.g., Edwards and Howkins, 1966). An implication of these observations is that there may be many kimberlite pipes that are subject to cross-fertilization. For example, if a minimum tephra blanket of ~1 km is superimposed on each known kimberlite in the Diavik kimberlite cluster, virtually every kimberlite pipe could have been “cross-fertilized” by a neighbouring pipe (Fig. 6.4).

#### 6.4.4 Eruption style, intensity and diamond grade

Analysis in the present study suggests that olivine crystals break during kimberlite eruptions (Chapter 5). As discussed above, CSDs of olivine crystals in intrusive, coherent kimberlite are unlikely to imitate the CSDs of diamonds in the same rocks. However, olivine and diamond have very similar physical properties. For example, olivine crystals and diamond possess similar size ranges (~0.02 – 20 mm) and densities ( $\rho_{ol} = 3.30 \text{ g cm}^{-3}$ ;  $\rho_d = 3.45 \text{ g cm}^{-3}$ ). If diamonds crystals are ‘free’ or ‘liberated’ from their xenolith hosts in kimberlite magmas that undergo explosive volcanic eruption, the settling velocities and energy of particle to particle collisions of diamond and olivine should be similar. Thus, both components may act the same during explosive volcanic

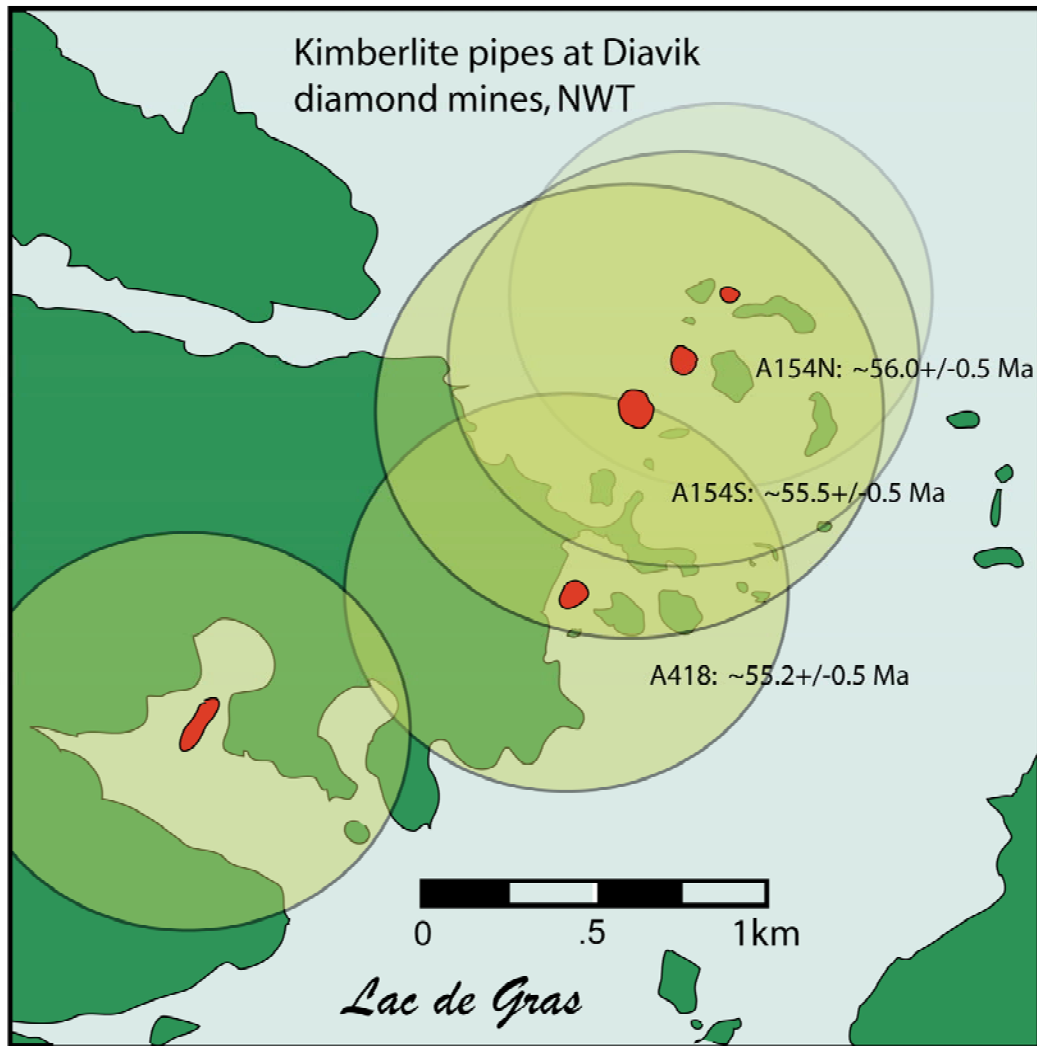


**Figure 6.4:** Schematic map showing economic implications of coeval, closely-spaced kimberlite pipes (red). Hypothetical tephra blankets are represented by yellow circles of  $\sim 750$ m in d. Note the overlapping dispersal blankets, and importantly the potential for ‘cross-fertilization’ from one eruption into an open-crater of an adjacent kimberlite for 4 of 5 kimberlite pipes shown.

eruption and contribute to primary pyroclastic deposits in the same manner. For example, the breaking of diamond crystals would profoundly impact the overall diamond size distribution (Fig. 6.1), and, therefore, the net value of the deposit.

In addition, kimberlite melt can be separated from olivine crystals and efficiently removed during kimberlite eruptions. The degree to which melt separates from crystals during eruption can have a profound effect on concentrating diamond grade. For example, if we assume no loss of the solid fraction from eruption to deposit, separating and elutriating all the melt fraction from olivine crystals during eruption can effectively double the solid contents (i.e., diamond grade) in a pyroclastic rock relative to the original magma.

These processes, crystal fragmentation and melt separation, are implied to be the result of the explosivity and power of the eruption, respectively, and may be approximately represented by the parameters “D”, and “S” (Chapter 5). Hypothetical relative-value relationships between crystal population parameters (i.e., D), the percentage of melt that separates and elutriates (volume subtracting) (i.e., S), and the percentage of country-rock contamination (volume adding) in deposits of pyroclastic kimberlite (“C”), are shown in Figure 6.5, with concomitant relative changes in deposit value indicated by colour shading. Details of methods used to create value functions for each deposit parameter are included in Appendix 8.7. Linear combinations of each parameter in Figure 6.5 suggest that the relative contribution to value change by the maximum amount of fragmentation of diamonds due to eruption from measured populations (diamond CSD slopes, fig. 6.5) is less significant (2 contours lines) than elutriation and contamination.

### **6.5 A comparison of olivine and diamond: olivine CSDs in A154S**

To test the hypothesis that olivine crystals and diamonds exhibit similar behavior in kimberlite eruptions, crystal size distributions from both olivine and diamond in pyroclastic kimberlite must be collected and compared. However, direct comparison of the distribution of olivine and diamond crystals in pyroclastic rocks is inherently problematic: the volume of rock required to collect statistically significant numbers of

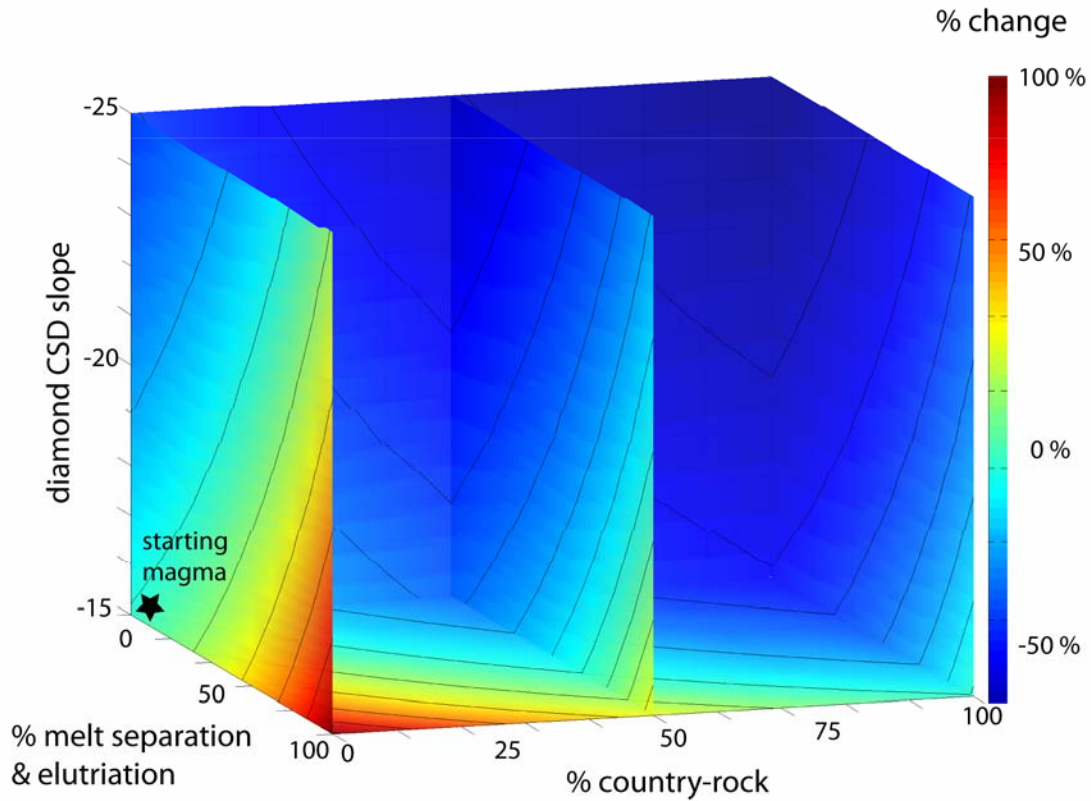


**Figure 6.5:** Deposit characteristics and relative value scale. Value functions for measurable properties from pyroclastic deposits of kimberlite are linearly combined to create relative value scale: log-linear diamond CSD slopes, percentage (%) of separation and elutriation of melt from crystals, and percentage (%) of country-rock contamination are shown. Relative changes in deposit values on a \$ / unit volume basis are indicated by colour shading (i.e., dark red = 100% increase, dark blue = 50% decrease).

crystals (e.g., 600) for each component is drastically different ( $V_d = 3,000 - 6,000\text{kg}$ ;  $V_{ol} = 0.5\text{kg}$ ). For example, in pyroclastic kimberlite at Diavik, for each diamond crystal there are approximately  $1 \times 10^6$  olivine crystals (Moss, 2009). This means that a characteristic CSD for diamond cannot be defined for scales of observation smaller than several tonnes (i.e., 2-4 m<sup>2</sup>), while a representative CSD for olivine can be defined within a thin section. Thus, because olivine is easier to statistically quantify at smaller scales of observation, it is better suited than diamond CSD data to describe component distributions within kimberlite pipes. Information learned about component distributions through olivine CSDs may then be re-applied to estimations of diamond distributions throughout a deposit of pyroclastic kimberlite.

For example, mean stone sizes (MSS) of a population of diamonds from best-fit model equations are typically used to describe diamond CSDs for specific deposits of kimberlite (Chapman and Boxer, 2004). Calculation of a MSS can be accomplished for global (throughout the entire pipe) or local scales. The degree to which a mean stone size is consistent throughout the deposit is reflective of the homogeneity in particle distributions. We can use olivine CSDs collected from multiple scales of observation to test the hypothesis that a single central value (i.e., median or mean crystal size) can accurately describe component distributions within volcanoclastic kimberlite at deposit-scale.

To test this concept, a pilot study assessing the olivine CSDs from one bench level within the A154S kimberlite pipe at Diavik (see Figs. 1.9, 1.11) was completed in 2008. The A154S kimberlite pipe was chosen as the location of the study because of potential implications of the study on mining practices at Diavik. The dominant infill of the A154S kimberlite pipe mainly comprises chaotic, bedded to massive volcanoclastic kimberlite, with minor variations in componentry and bedding (Graham et al., 1999). Samples for this study were collected from multiple locations throughout a single bench horizon (175 m asl; 240 m below present-day surface) of the A154S kimberlite pipe (Fig. 6.6). In addition, 5 replicate hand samples were collected within a single sample location, and 10 sample surfaces were cut from a single, large hand sample. This sampling methodology allows us to test whether a single set of population parameters (e.g., central value, spread/dispersion of data, symmetry of data) can accurately describe

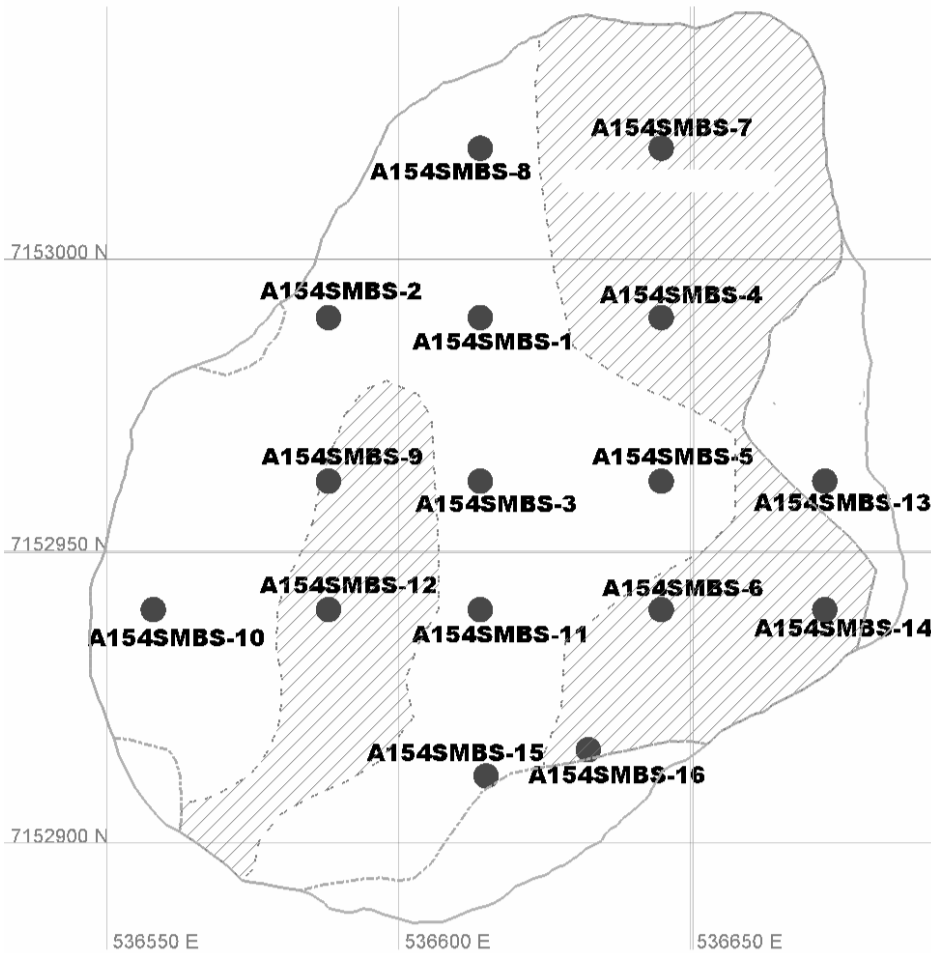


**Figure 6.6:** Plan view map (175 m asl) showing sample locations for A154S olivine CSD pilot study. Samples were collected from 15 locations around the pit. Replicate hand samples ( $n = 5$ ) were collected from within a single, 1 x 1m sample locale (e.g., A154SMBS\_15). Multiple surfaces were cut from a single hand sample (i.e., serial sectioning,  $n = 10$ ).

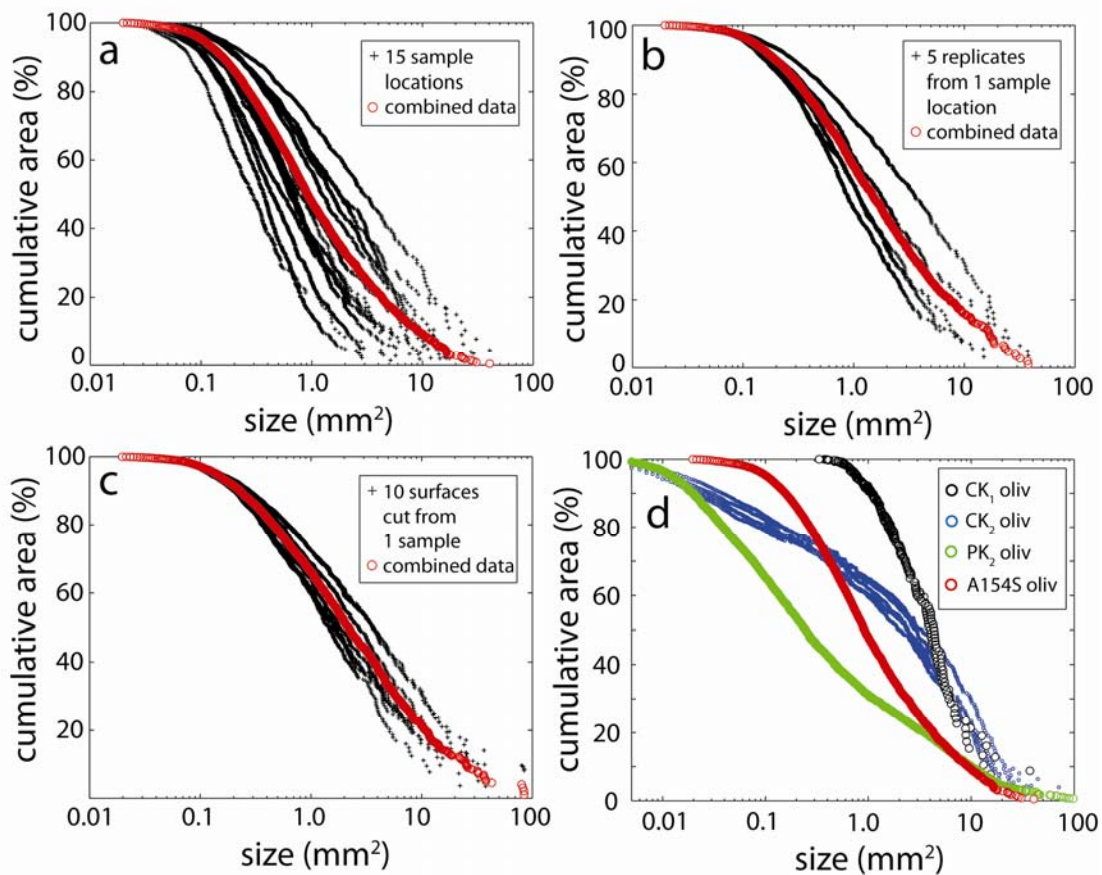


**Figure 6.7:** Olivine crystal size distributions (CSDs) from volcaniclastic kimberlite at 175 m asl bench of A154S as cumulative area % vs. size for olivine crystals measured from: (a) deposit-scale (15 samples; 100 x 100m area); (b) replicate samples from 1 pit sample location (1 x 1m area); (c) multiple sample surfaces from a single hand sample (20 x 20cm); and (d) olivine CSDs from CK<sub>1</sub> (black), CK<sub>2</sub> (blue), PK<sub>2</sub> (green) and A154S (red; all samples from 175 m asl). Red squares for A154S indicate combined CSD for all samples from each scale of observation, respectively. Slopes of cumulative area % vs. size plots indicate spread of data about a central value.

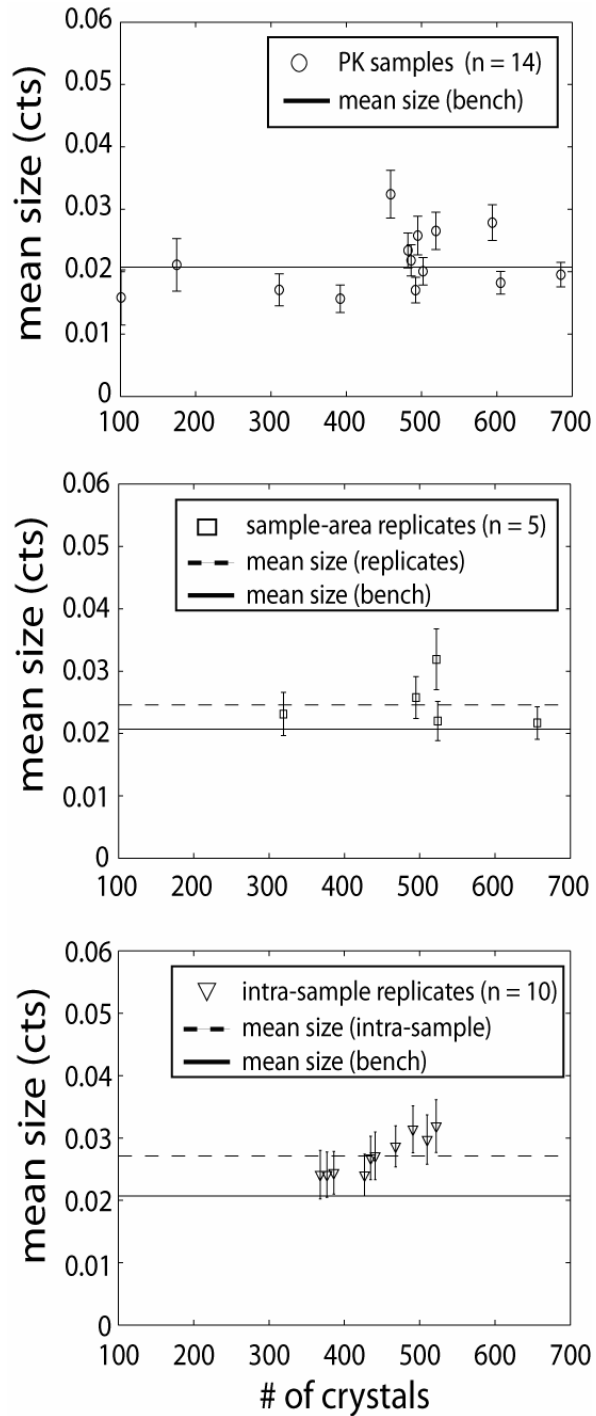


**Figure 6.8:** Mean crystal size (carats; 1 ct = 200 mg) of olivine vs. number of olivine crystals measured from: (a) deposit-scale (15 samples; 100 x 100m area); (b) replicate samples from 1 pit sample location (1 x 1m area); (c) multiple sample surfaces from a single hand sample (20 x 20cm);. Uncertainties reflect the total expected standard deviation due to sample size and experimental error. The geometric mean central value for all samples is shown as a solid line; geometric mean central values for replicates and multiple sample surfaces are shown with dashed lines.

the components of a deposit of volcanoclastic kimberlite at any scale (e.g., 100 x 100 m, 1 x 1 m, or 20 x 20 cm scale). Samples were slabbed and polished, and image analysis was conducted to obtain olivine crystal size distributions using methods described in Chapter 3. In addition, this test further evaluates ideas on the modification of olivine crystals due to explosive eruption developed in Chapter 5.

Results from the pilot study are shown in Figure 6.7 and Figure 6.8. Data collected from each scale of observation are shown for comparison (Fig. 6.7a,b,c). In Figure 6.7, olivine CSD's are shown as cumulative area % vs. size plots. On cumulative area % vs. size plots, data distributions with relatively steep slopes indicate a tight spread of data around a central value [i.e., sorting efficiency ( $\sigma$ ); Chapter 2]. Olivine CSD data collected at the slab scale (~50 x 70 mm) from CK<sub>2</sub> (blue line; Chapter 3), and PK<sub>2</sub> (green line; Chapter 2) are shown for comparison. In Figure 6.8, the mean stone size expressed as carats (cts; 1ct = 200mg) of olivine crystals are shown with uncertainties from 3 different scales of observation (e.g., 100 x 100m, 1 x 1m, 20 x 20cm). Uncertainties reflect the total expected standard deviation due to sample size and experimental error (Fig. 6.8).

Several observations can be made from the results of this study. First, there is a clear difference in mean size and sorting efficiency of the olivine CSDs in the volcanoclastic deposits of A154S and the those of CK<sub>2</sub> and PK<sub>2</sub> of A154N (Fig. 6.7d). Second, the size distribution of olivines collected at the largest scale of observation (i.e., 100 x 100m) in the volcanoclastic rocks of A154S exhibit a greater spread of data relative to the smallest scale of observation (i.e., 20 x 20cm; Fig. 6.7a,c). Third, it is apparent that samples from 15 locations around A154S have statistically different central values (i.e., geometric means; Fig. 6.8a).

From these observations, it is clear that at the deposit scale (100 x 100m), the olivine crystal populations within the volcanoclastic deposits of A154S cannot be defined by a single mean central value. Only olivine crystal data collected from multiple surfaces cut from the same hand sample from can be statistically described by a mean of central values (dashed lines; Fig. 6.8c).

The data in Figure 6.7d represent olivine crystal populations from a diverse suite of kimberlite bodies. These bodies have been shown to have distinct olivine crystal

populations (Chapters 4,5; Table 6.1), and are interpreted to result from distinct emplacement histories. The olivine CSDs in the volcanoclastic rocks at A154S also show differences in properties (i.e., median size, sorting efficiency, size range) relative to the olivine CSDs in CK<sub>1</sub>, CK<sub>2</sub> and PK<sub>2</sub> (Fig. 6.7d).

The differences among olivine CSDs may be the result of a number of factors. First, the data derive from two different methods: the manual method was used for CK<sub>1</sub>, CK<sub>2</sub> and PK<sub>2</sub> (Chapters 2,3,4), and the automatic method for A154S. Each method has limitations (e.g., lower size limit of automatic method, Appendix 7.3.2), and could lead to a bias in observations. Second, alteration of small olivine crystals is documented in CK<sub>1</sub>, and may also impact the olivine population in A154S. Third, the variation may be true geological variation resulting from different emplacement histories. The paragenesis of the volcanoclastic rocks in A154S has not been interpreted. However, the differences in the coarse fraction of the A154S olivines relative to CK<sub>1</sub> and CK<sub>2</sub> may suggest the crystal population has been modified by geological process. This observation is consistent with models for fragmentation of a starting population of olivine crystals shown in Chapter 3, and interpretations of olivine crystal modification due to explosive eruption discussed in Chapter 5.

## **6.6 Limitations of the methods, results and implications within thesis**

The significant findings of this thesis have begun to address gaps in our understanding of volcanic processes in kimberlite volcanoes. However, there are some limitations to applying the facies analysis approach, methods, and data of this thesis in future studies.

First, the facies analysis methods and data types presented in this thesis were the result of a unique opportunity to map and work at an active diamond mine. Data collection from bench faces in the open pit of a mine was severely limited by the mining schedule and by the short exposure times of bench faces (e.g., minutes to hours), and presents a challenge for producing high-quality maps. Moreover, kimberlite is typically a pervasively altered rock, and the majority of particles are < 5 cm in diameter, preventing accurate analysis of componentry in deposits using conventional volcanological methods

at large scales. Thus, componentry analysis of this thesis was typically limited in scale (e.g., thin section or polished slab). As a result, datasets are precise, but do not cover a large enough scale to make statistically backed assertions regarding component distributions at a deposit-scale.

Second, the image analysis techniques presented in Chapter 2 have some intrinsic limitations. To successfully integrate scales of observations using these methods, rocks textures must be massive (e.g., Chapter 2,3); heterogeneous rock fabrics may lead to high normalization errors ( $\sigma^2_N$ ; Chapter 3). Heterogeneous rock fabrics are a common occurrence in many kimberlite deposits, thus precluding this methodology. The automatic method shown in Chapter 3 was successfully developed for fresh samples of coherent kimberlite, but most kimberlites are pervasively altered, making crystal and clast boundaries indistinguishable from the background matrix or groundmass. For both the manual and automatic methods, the smallest particles in kimberlite rocks are commonly the most difficult to accurately represent (e.g., shape, number), but make up an important part of particle size distributions. Moreover, the automatic method is thus far only applicable to polished slabs, and must be adjusted in order to analyze scanned images of polished thin sections.

Third, the applicability of interpretations of coherent and pyroclastic deposits of kimberlite at A154N to other kimberlite deposits is limited by the scope of data collected. For example, the ‘type’ properties identified for olivine in coherent kimberlite were based on two dykes from a single kimberlite pipe. Such limited sampling is unlikely to characterize the olivine crystal properties of all kimberlite magmas. More accurate determination of the characteristic properties of olivine crystals in coherent kimberlite rocks is necessary before olivine crystals can be relied upon as a metric for gauging kimberlite eruptions. Moreover, the Fragmentation Index presented in Chapter 5 is based on two deposits of kimberlite from within a single kimberlite pipe. By comparison, the fragmentation index of Walker (1973) was based on deposits produced by many magma types, from many localities around the world. Thus, the ‘type’ properties of olivine crystals in kimberlite and the Fragmentation Index presented in this thesis may need to be substantiated or refined by further studies.

## 6.7 Areas for future study

### 6.7.1 Olivine CSDs

Olivine crystals are clearly an important component in kimberlite rocks. This thesis has shown that olivine crystals possess ‘type’ properties within dykes of coherent kimberlite at a single kimberlite volcano. Further studies in olivine CSDs may serve as a vehicle to test hypotheses on the similarity of intrusive coherent kimberlite rocks within a cluster of kimberlites, in a kimberlite field, or around the world. Olivine CSDs in coherent kimberlite may also assist in testing hypotheses on the nature of the mantle, and possibly the relationship between diamond and olivine in kimberlite deposits. Measurement of olivine CSDs in pyroclastic deposits with juvenile components different than those described for A154N may also be used to further test ideas on olivine crystal breaking due to explosive eruption (Chapter 5).

### 6.7.2 Image analysis and components in kimberlite rocks

This thesis demonstrated the use of image analysis to generate component data for kimberlite rocks. However, the high degree of alteration, variable colour, and friability of many kimberlite rocks makes it difficult identifying discrete particles and components. There is a clear need for the development of a software tool that can rapidly identify discrete components in *all* textural varieties of kimberlite rocks (e.g., Appendix 7.3.2). Such work would further animate studies in kimberlite petrology and volcanology, and likely be of great interest to kimberlite mine geologists.

### 6.7.3 Analogue experiments to determine magma properties

In Chapter 4, conduit geometries were combined with inferred properties of kimberlite magmas to constrain eruption dynamics at the A154N kimberlite pipe. In Chapter 5, observations of kimberlite pyroclasts together with fluid dynamics concepts were used to develop ideas for the impact of volumetric properties of gas, liquids and

solids on kimberlite fragmentation. Concepts developed in dimensionless terms (e.g.,  $We\#$ , Chapter 6;  $Re\#$ , Chapter 4) in fluid dynamics are transferable to kimberlite systems. However, such dimensionless relationships are only helpful if the assumptions regarding analogue fluid properties ( $\eta$ ,  $\gamma$ ; Chapter 5) are correct.

Kimberlite magmas are presumed to have a low viscosity, contain abundant volatile phases (up to 30%), and can host up to 60% solids content (Price et al., 2000; Russell et al., 2006; Sparks et al., 2006). This is a combination of physical properties that is unique with respect to other magma types. As such, kimberlite magmas may exhibit profoundly different rheological behaviour (e.g., glass transition, coupling and/or phase separation, viscosity models, shear-thinning behavior, etc.) during ascent and eruption than other, better-understood magma types. However, few experiments in rheology have been conducted with kimberlite magmas, largely due to the difficulty of high temperature experiments involving melts with abundant fluid phases (Blank, 1994; Brooker et al., 2001b). This indicates the need for creative experimentation to determine the viscosity of kimberlite melts and better constraints on the gas properties of kimberlite magmas. In addition, analogue experimentation using low viscosity liquids, gases, and solids could offer insights on the transport and eruption behaviour of a 3-phase system such as kimberlite, and further test the ideas presented in Chapters 4 and 5.

#### 6.7.4 Phreatomagmatic eruptions and deposits

Lorenz and co-workers (Lorenz, 1998; Zimanowski, 1998; Kurszlaukis and Barnett, 2003; Lorenz, 2003) have suggested that the best analogue for kimberlite volcanoes is contemporary phreatomagmatic<sup>10</sup> and/or monogenetic volcanism (maars, scoria cones, fire-fountaining). However, it remains unproven to what extent--if any--hydrovolcanic processes are involved in kimberlite eruptions. The relatively narrow confines of a pipe provide thermo-mechanical limitations on what processes can take place. Eruptive and gravitational movements within a pipe will be dominantly vertical

---

<sup>10</sup> Phreatomagmatic fragmentation: Where the interaction between external water and magma produces explosive eruption of magmatic ejecta driven by both external and magmatic volatiles. Such eruptions are thought to occur where the water:magma mass ratios are equal to or slightly greater than 0.3, and are caused by major increases in the degree of superheating and energy transfer (Cas & Wright, 1987).

and thermally constrained, while extra-crater volcanic processes can involve lateral and tractional movements, deposition, and bedding formation (Koyaguchi and Woods, 1996). The availability of groundwater was likely in nearly all kimberlite emplacements, yet few kimberlite pipes contain textural features suggesting water – magma interaction was a dominant mechanism for magma fragmentation.

The A418 kimberlite pipe at Diavik is texturally dominated by fine bedding and accretionary lapilli, which contrasts greatly with the features observed in A154N. The A418 pipe displays what Volker Lorenz (personal commentary) believes to be the greatest abundance of accretionary lapilli he has ever seen in kimberlite. Field study of the A418 pipe could shed insight into what (if any) analogies can be drawn between deposits resulting from phreatomagmatic eruptions (e.g., maars) and kimberlites. Moreover, the apparent difference in pyroclastic products between A154N and A418 make the deposits in A418 an ideal candidate to further test the Fragmentation Index proposed in Chapter 5.

## 6.8 References

- Blank, J.G., Brooker, R.A., 1994. Experimental studies of carbon dioxide in silicate melts: solubility, speciation and stable isotope behaviour. In: M.R. Carroll, Holloway, J. (Eds.) (Editor), *Volatiles in Magmas. Reviews of Mineralogy*, pp. 157–186.
- Brett, R.C., Russell, J.K. and Moss, S., 2009. Origin of olivine in kimberlite: phenocryst or imposter? 9th International Kimberlite Conference Extended Abstract 9IKC-A-00298, 3.
- Brooker, R.A., Kohn, S.C., Holloway, J.R. and McMillan, P.F., 2001. Structural controls on the solubility of CO<sub>2</sub> in silicate melts: Part II: IR characteristics of carbonate groups in silicate glasses. *Chemical Geology* 174(1-3), 241-254.
- Chapman, J.G. and Boxer, G.L., 2004. Size distribution analyses for estimating diamond grade and value. *Lithos* 76(1-4), 369-375.
- Creighton, S., Stachel, T., McLean, H., Muehlenbachs, K., Simonetti, A., Eichenberg, D. and Luth, R.W., 2007. Diamondiferous peridotitic microxenoliths from the Diavik Diamond Mine, NT. *Contributions to Mineralogy and Petrology* 10, 1-14.
- Edwards, C.B. and Howkins, J.B., 1966. Kimberlites in Tanganyika with special reference to the Mwadui occurrence. *Economic Geology* 61, 537-554.
- Fedortchouk, Y. and Canil, D., 2004. Intensive variables in kimberlite magmas, Lac de Gras, Canada and Implications for Diamond Survival. *Journal of Petrology* 45(9), 1725-1745.
- Fedortchouk, Y., Canil, D. and Carlson, J., 2005. Dissolution forms in Lac de Gras diamonds and their relationship to the temperature and redox state of kimberlite magma. *Contributions to Mineralogy and Petrology* 150, 54-69.
- Field, M., 2008. Variations of olivine abundance and grain size in the Snap Lake kimberlite intrusion, Northwest Territories, Canada: A possible proxy for diamonds. 9th International Kimberlite Conference Extended Abstract No. 9IKC-A-00287, 3.
- Field, M., Gibson, J.G., Wilkes, T.A., Gababotse, J. and Khutjwe, P., 1997. The Geology of the Orapa A/K1 Kimberlite Botswana: Further insights into the emplacement of kimberlite pipes. *Russian Geology and Geophysics* 38(1), 24-39.
- Graham, I., Burgess, J.L., Bryan, D., Ravenscroft, P.J., Thomas, E., Doyle, B.J., Hopkins, R. and Armstrong, K.A., 1999. Exploration History and Geology of the Diavik Kimberlites, Lac de Gras, Northwest Territories, Canada. In: J.J. Gurney, J.L. Gurney, M.D. Pascoe and S.H. Richardson (Editors), *Proceedings of the VIIth International Kimberlite Conference. Red Roof Design, Cape Town, South Africa*, pp. 262-279.
- Grütter, H.S., Gurney, J.J., Menzies, A.H. and Winter, F., 2004. An updated classification scheme for mantle-derived garnet, for use by diamond explorers. *Lithos* 77(1-4), 841-857.
- Kamenetsky, V.S., Kamenetsky, M.B., Sobolev, A.V., Golovin, A.V., Demouchy, S., Faure, K., Sharygin, V.V. and Kuzmin, D., 2007. Olivine in the Udachnaya-East Kimberlite (Yakutia, Russia): Types, Compositions and Origins. *Journal of Petrology* 00, 1-17.

- Koyaguchi, T. and Woods, A.W., 1996. On the formation of eruption columns following explosive mixing of magma and surface-water. *J. Geophys. Res* 101((B3)), 5561–5574.
- Kurszlaukis, S. and Barnett, W.P., 2003. Volcanological and structural aspects of the Venetia kimberlite cluster — a case study of South African kimberlite maar-diatreme volcanoes. *South African Journal of Geology* 106, 165–192.
- Lorenz, V., Kurszlaukis, S., 2003. Kimberlite Pipes: Growth models and resulting implications for diamond exploration, Program Abstracts, VIIIth International Kimberlite Conference, pp. 4.
- Lorenz, V., Zimanowski, B., Buttner, R., Kurszlaukis, S., 1998. Formation of kimberlite diatremes by explosive interaction of kimberlite magma with groundwater: field and experimental aspects. In: J.J. Gurney, ed. (Editor), *Proceedings of the VIIth International Kimberlite Conference*, pp. 522-528.
- Masun, K.M., Doyle, B.J., Ball, S. and Walker, S., 2004. The geology and mineralogy of the Anuri kimberlite, Nunavut, Canada. *Lithos* 76(1-4), 75-97.
- McClenaghan, M.B. and Kjarsgaard, B.A., 2001. Indicator mineral and geochemical methods for diamond exploration in glaciated terrain in Canada. In: M.B. McClenaghan, P.T. Bobrowsky, G.E.M. Hall and S.J. Cook (Editors), *Drift Exploration in Glaciated Terrain*. Geological Society, London, Special Publications, London, pp. 83-123.
- Meyer, H.O.A. and Boyd, F.R., 1972. Compositions and origin of crystalline inclusions in diamonds. *Geochimica et Cosmochimica Acta* 36, 1255-1273.
- Moss, S., 2009. Olivine and diamond crystal size distributions at A154s. Confidential internal report prepared for Diavik Diamond Mine Incorporated (DDMI) Internal report prepared for Diavik Diamond Mine Incorporated (DDMI), 25.
- Nowicki, T., Crawford, B., Dyck, D., Carlson, J., McElroy, R., Oshust, P. and Helmstaedt, H., 2004. The geology of kimberlite pipes of the Ekati property, Northwest Territories, Canada. *Lithos* 76(1-4), 1-27.
- Porritt, L., 2008. The volcanology and sedimentology of the Ekati kimberlites, NWT, Canada, with consideration of the implications for diamond grade, Monash University, Melbourne, 333 pp.
- Price, S., Russell, J.K. and Kopylova, M., 2000. Primitive magma from the Jericho pipe, N.W.T., Canada: Constraints on primary melt chemistry. *Journal of Petrology* 41(6), 789-808.
- Russell, J.K., Giordano, D., Kopylova, M. and Moss, S., 2006. Transport properties of kimberlite melt, Long Abstract, Kimberlite Emplacement Workshop, Saskatoon, Canada.
- Scott Smith, B.H., 2009a. consultant, Scott Smith Petrology Incorporated (SSCI), personal communication. In: S. Moss (Editor).
- Scott Smith, B.H., 2009b. The Economic Implications of kimberlite emplacement. 9th International Kimberlite Conference extended abstracts 9IKC-A-00335, 3.
- Sobolev, N.V., Efimova, E.S., Koptil, V.I., Lavrentiev, I.G. and Sobolev, V., 1976. Inclusions of coesite, garnet, and omphacite in Yakutian diamonds - 1st finding of coesite paragenesis. *Doklady Akademii Nauk SSSR* 230, 1442-1444.

- Sparks, R.S.J., Baker, L., Brown, R.J., Field, M., Schumacher, J., Stripp, G. and Walters, A., 2006. Dynamical constraints on kimberlite volcanism. *Journal of Volcanology and Geothermal Research* 155(1-2), 18-48.
- van Straaten, B.I., Kopylova, M.G., Russell, J.K., Webb, K.J. and Scott Smith, B.H., 2008. Discrimination of diamond resource and non-resource domains in the Victor North pyroclastic kimberlite, Canada. *Journal of Volcanology and Geothermal Research* 174(1-3), 128-138.
- Webb, K.J., 2006. Juvenile clasts in kimberlites: Standardizing comprehensive description towards unravelling emplacement models, Kimberlite Emplacement Workshop, Saskatoon, Saskatchewan.
- Webb, K.J., Scott Smith, B.H., Paul, J.L. and Hetman, C.M., 2004. Geology of the Victor Kimberlite, Attawapiskat, Northern Ontario, Canada: cross-cutting and nested craters. *Lithos* 76(1-4), 29-50.
- Woolley, A.R., Bergman, S.C., Edgar, A.D., Le Bas, M.J., Mitchell, R.H., Rock, N.M.S. and Scott Smith, B.H., 1996. Classification of lamprophyres, lamproites, kimberlites and the kalsilitic, melilitic, and leucitic rocks. *Journal of the Mineralogical Association of Canada* 34, 175-186.
- Zimanowski, B., 1998. Phreatomagmatic explosions. In: A. Freundt, Rosi, M. (Editor), *Developments in Volcanology 4: From Magmas to Tephra, modelling physical processes of explosive volcanic eruptions*. Elsevier, pp. 25-54.

## **7 Appendices**

### **7.1 Organization of appendices**

Details of methods and data discussed in each chapter are part of an adjoining digital appendix found at the back of the thesis, and can be navigated using a directory therein. The Appendix for each chapter is organized into five categories:

- 1) General notes, unused datasets, and software macros
- 2) Digital images
- 3) Matlab script for figures and numerical modeling
- 4) Methods
- 5) Output Data.

In most chapters, general notes, datasets and software macros are included which were either directly or indirectly used in the chapter. General data include graphic logs, rock and petrographic descriptions, notes and maps from the open pit, and notes from interactions with mine geologists at Diavik. Though most data sets which were not directly of use for the writing of the thesis are generally not included in the Appendix, there are some supplementary data in some chapters. However, whole rock geochemistry, electron microprobe, density and magnetic susceptibility data collected during this thesis are not included. Drillhole logs completed using Diavik Diamond Mine Inc. (DDMI) logging template software are not included for proprietary reasons. Photographic logs of drillholes in A154N were made available for use during this study, but are not included in the digital appendix for proprietary reasons. Data collected in the study of three other kimberlite pipes (A154S, A418, A21) at the Diavik property are not included in the thesis appendix. Software macros used in the software programs contributing to this thesis are included when appropriate, to facilitate reproduction of these datasets in further research. Not every chapter contains data in each subfolder in the digital appendix. This is because the data presented in each chapter did not always involve or generate the same kind of output.

Digital images in the Appendix comprise a combination of photographs from the open pit at the Diavik mine site, image captures of 3D models developed in Vulcan™ and GoCad™ mining software packages, digital scans of polished slabs and thin sections, photomicrographs of thin section textures, and manual and computer-generated particle outlines and tracings. Most images in the digital appendix are not directly used in the thesis.

Matlab scripts for both figures and numerical modeling are included as .m files, and can be successfully opened, run and manipulated in MATLAB™ computing software. To facilitate use, all functions (e.g., .m), sub-functions, raw data files (e.g., .xls, .dat) and matlab arrays (e.g., .mat) necessary for running a given .m file are found within the same file folders. Matlab script for Chapter 3 is not included in the Appendix for proprietary reasons.

Details and descriptions of methodologies used for image analysis, geostatistical analysis, field mapping, and sampling are recorded in the methods section. In many cases, the details of methodologies involve the use of computing functions well described in MATLAB, and the reader is directed to subfolder within each chapter containing Matlab scripts or to MATLAB and Simulink™ software utility to find them.

Output data files are mostly .xls files, and most contain particle data (olivine crystals, etc.) obtained using image analysis methods. Headings are labeled for each data column. Other output files include manual and computer-traced images.

The following software packages were used in this thesis, and are fully licensed with either University of British Columbia or Diavik Diamond Mines Inc. (DDMI), and in accord with copyright protection:

- \* MSWord, MExcel
- \* Adobe Illustrator™
- \* CSDCorrections™; CSDSlice™
- \* Adobe Photoshop™
- \* MATLAB and Simulink™
- \* ImageJ™; ScionImage™
- \* Vulcan™; GoCad™

## 7.2 Appendix – Chapter 2

(digital)

## 7.3 Appendix – Chapter 3

### 7.3.1 Appendix – Chapter 3: Manual image analysis

#### *Digital image creation and analysis*

Our study analyses five oriented samples of kimberlite. To capture the full range of size distributions for all the olivine crystals in kimberlite, two scales of observation were necessary. We used scanned images of slabs (~47x77 mm) and thin sections (12.5x28 mm). Slab images were scanned at 600dpi with a desktop scanner, while thin sections were scanned using a thin section scanner at 4000dpi. Olivine crystals and other components (e.g., garnet, granite) in the scanned images were traced manually in Adobe Illustrator™ using a digital tracing pad. Each component type was assigned a unique grayscale value (0-255) which could be distinctly recognized by an image analysis program (Fig. 3.2). These grayscaled images were then analyzed using ImageJ™ for crystal area, maximum axis length of enclosing ellipsoid, minimum axis length of enclosing ellipsoid, and perimeter length (Fig. 3.2). All raw data from the two scales of observation are included in Appendix 7.3.3 (digital). Resolution for object identification in ImageJ™ was 11.93 pixels/mm. Pencil tool preferences in Adobe Illustrator™ were set to maximize the pixelation along the trace allowing for accurate digital portrayal of the manual trace.

#### *Scale integration*

The two different scales of observation were integrated into a single dataset by normalizing on the basis of area data from the smaller scale of observation into the area of the larger scale (Fig. 3.3). For example, crystal-size data (area, number) generated for thin sections is truncated by removing the coarsest fraction (> 1mm), and then normalized to the area in the polished slab not occupied by crystals measured at the slab scale (crystals 1.0-15 mm), using the following normalization factor:

$$A_i^N = \frac{(A_{TSOL < 1mm})}{(A_{TS} - A_{TSOL < 1mm})} \times (A_{SL} - A_{CR} - A_{MX} - A_{SOL \geq 1mm}) \quad (A7.3.1)$$

where  $A_i^N$  is the area of the slab occupied by olivine crystals within the  $i$ th size interval (e.g.,  $0.5 < x < 1$  mm),  $A_{TSOL < 1 mm}$  is the total area of olivine crystals whose diameter is  $< 1$  mm observed at thin section scale,  $A_{TS}$  is the area of the thin section,  $A_{TSOL \geq 1 mm}$  is the total area of olivine crystals whose diameter  $\geq 1$  mm observed at thin section,  $A_{SL}$  is the total area of the slab,  $A_{CR}$  is the area occupied by country rock xenoliths and xenocrysts,  $A_{MX}$  is the area occupied by mantle xenoliths or xenocrysts (non-olivine), and  $A_{SOL \geq 1 mm}$  is the total area in the slab scale occupied by olivine crystals whose diameter is  $\geq 1$  mm. The normalized values can then be used to describe crystal abundances as area % and as frequency ( $n_A$ ). Such normalization is only applicable in massive rock fabrics; normalization of different scales of observation in rocks with organized or heterogeneous fabric or texture may lead to large uncertainties in crystal populations.

#### *Error calculation*

In order to estimate the analytical uncertainty associated with manual tracing of crystals and subsequent image processing, we performed several experiments. Firstly, duplicate tracings by different observers were analyzed using the same images (slab + thin section) from 1 sample to generate raw grain size data (Tables 3.1, 3.2). Second, multiple acquisitions of data (5x) from the same tracing of a sample were conducted in ImageJ™ to estimate the error caused by changing the threshold parameter of the analyzed image (Tables 3.1, 3.2). Thresholding is the means by which the image analysis program separates or segments particles from the background. Individual pixels in a grayscale image are marked as “object” pixels if their value is greater than some threshold value (provided an object is brighter than the background) and as “background” pixels otherwise. By incrementally changing the threshold value by steps of 5 up to +/- 10 around a default value in ImageJ™ (210 on a 0 to 255 scale), the olivine crystal pixilation could be slightly enhanced or dilated, thereby changing the size and/or number of olivine crystals measured by ImageJ™. Thirdly, normalization factors (eq. A7.3.1) were varied ( $A_i^N$ ) to assess variance due to necessity of rounding this value to the closest integer.

Total analytical error in particle areas and frequencies are the summation of uncertainties due to tracing, thresholding, and normalization ( $\sigma_a^2 = \sigma_{th}^2 + \sigma_{tr}^2 + \sigma_N^2$ ), and is found to be less than the variance due to sampling, such that  $\sigma_a^2 < \sigma_s^2$  (e.g., Fig. 3.5a; 3.5b).

### *Stereological corrections*

Data generated from a two dimensional surface do not necessarily reflect the true sizes of the crystals in three dimensions. They can underestimate crystal size because a surface that randomly cuts spherical or equant particles is more likely to intersect a section that does not include the true (e.g., maximum) diameter. This is termed the ‘intersection-probability effect’. In addition, random planes cut through rocks with similarly-shaped, but differently-sized populations of crystals are more likely to intersect larger crystals, therefore creating a bias in crystal size distributions towards coarser crystals, known as the ‘cut-section effect’. Furthermore, the surfaces of olivine crystals and other clasts are rarely perfectly smooth which complicates the task of objectively measuring the maximum diameters of each clast. To account for these complications, we use a three-step data organization and correction process involving: a) defining characteristic shapes from raw 2D intersection data, using CSDSlice<sup>TM</sup> to obtain best-approximations of 3D ellipse axial ratios; b) organizing crystals in bins (e.g.,  $\log_{0.5}$ ,  $\log_2$ ) by area and number, and; c) inserting binned data into CSDCorrections<sup>TM</sup> 1.3 to mitigate the cut-section and intersection-probability effect and then calculate 3D olivine crystal populations by applying correction factors for known properties (i.e. crystal shape, modal %, rock fabric,). The result is a dataset that comprises scale-normalized, scale-truncated, binned, and stereologically-corrected olivine crystal populations.

**Shape assessment.** To accurately convert data from 2D intersections into 3D volumetric estimates, it is necessary to assume something about the nature of crystal shapes. To determine the best shape approximation, we described data from slabs and thin sections using common shape parameters: edge ‘roughness’ ( $P/A$ ), circularity ( $4\pi \cdot \text{area}/(P^2)$ ), angularity ( $P/(P \text{ of equivalent area circle})$ ), and oblateness ( $1 - \text{major axis} / \text{minor axis}$ ) (Fig. 3.7). The smallest size fraction from each scale of observation are not included in this analysis, due to the effect of pixilation on these shape parameters: for thin

sections,  $ol > 0.04$  mm; for slabs,  $ol > 0.1$  mm. These truncated datasets indicate that the vast majority of olivine crystals are circular to prolate ellipsoidal in shape, do not have irregular or concave edges, and have aspect ratios between 1.5:1 and 1:1 (Fig. 3.7). Olivine crystals show variability in circularity with respect to size: olivine crystal data collected at the thin section scale (0.01 – 10 mm in diameter) show distinctly more crystals with angular and less circular geometries than crystal data collected at the slab scale (0.8– 10 mm) (Fig. 3.7b). Image processing resolution (11.93 pixels/mm) may have a pronounced effect on circularity values, captured in part by the ‘clustering’ of circularity vs. size data for the smallest olivine crystals (Fig. 3.7b). However, 2D intersections may not give an accurate representation of the true crystal aspect ratios (3D); better approximations can be obtained using the CSDSlice<sup>TM</sup> database developed by Morgan and Jerram (2006). In Morgan and Jerram’s database, a minimum of 10,000 slices are taken through poly-disperse, randomly-oriented model populations created from over 700 crystal shapes; these data are compiled in a database for comparison with 2D intersection data obtained in real rocks. This comparison showed the best-fit, 3D, long : int : short aspect ratios to be ~1.5:1:1 for data collected at the thin section scale, and 1:1:1 for random samples of 4000 crystals from normalized and truncated olivine crystal populations (Tables 3.1, 3.2, 3.3). We further test the raw data for the effect of crystal size on the best-estimate for true crystal aspect ratio (Fig. 3.7d): though slightly variable, best-approximations of true 3D aspect ratios for all size bins do not exceed 1.5:1:1. Correlation coefficients ( $R^2$ ) of best-fit approximations for 3D aspect ratios are very low ( $<0.8$ ), and thus these 3D aspect ratios are not considered representative (Tables 3.1, 3.2; 3.3; Fig. 3.6d). However, combined with observations of olivine crystal morphologies, these results suggest that, although no single shape is representative of olivine crystal morphologies, smaller olivines are less circular and can have more irregular external morphologies, and most olivine crystals have an equant geometry. For our stereological conversions, therefore, we elect to use the best-approximation long : int : short ratio of 1:1:1.

Applications of spherical conversion coefficients to non-spherical particles always results in over-estimation of the number of ‘small’ particles and under-estimation of ‘large’ particles. However, using spherical geometry assumptions instead of assuming

various object shapes with unequal axes lengths also restricts possible errors of estimating 3D populations from 2D surfaces.

**Binning.** Olivine crystal size data are sorted into two bin types by diameter:  $\log_2$  (corresponding to integer  $\phi$  values), and  $\log_{0.5}$  (corresponding to typical diamond sieve sizes), each capturing the entire observed population of olivine crystals (0.03 – 12 mm or  $-3$  to  $+5\phi$ ). This allows us to examine normalized, truncated olivine crystal size data in a classic histogram format (Figs. 3.7a,b), to perform stereological conversions of 2D (area) data to 3D (volume) (e.g., Table 3.2), and to subsequently examine the effect of bin size on representations of olivine crystal size data (Fig. 3.8a).

**Section-effect corrections.** To account for the intersection-probability and cut-section effects, we stereologically convert binned, 2D crystal data (maximum diameter of enclosing ellipse) into 3D using a shape assumption in CSDCorrections<sup>TM</sup>. We assume all olivine crystals are equant and approximately spherical in three dimensions with 3D aspect ratios of 1:1:1, and apply the following correction to the logarithmically-binned major axes of olivine crystals:

$$n_V(L_{X-Y}) = \frac{n_A(l_{X-Y})}{D} \quad (\text{A7.3.2})$$

where  $n_V(L_{X-Y})$  is the number of crystals per unit volume for a given length scale,  $n_A(l_{X-Y})$  is the number of crystals per unit area for a given length scale, and  $D$  is the minimum diameter of the spheres in a given size interval. This correction is only applied to bins with diameter  $> 0.03$  mm; for the few crystals smaller than this size, observed crystal outlines are likely projections of the whole crystal outline, as these diameters are thinner than a typical thin-section. Using the number densities of crystals per unit volume obtained by stereological correction above [ $n_V(L_{X-Y})$ ], we find the population density by use of the following equation:

$$N(L_{X-Y}) = \frac{n_V(L_{X-Y})}{W_{X-Y}} \quad (\text{A7.3.3})$$

where the population density  $N(L_{X-Y})$  is the number density of crystals per unit volume

in the size interval,  $n_V(L_{X-Y})$ , divided by the width of the size bin,  $W_{X-Y}$ . To take into account the cut-section effect, we use the variation of the Saltikov method in CSDCorrections<sup>TM</sup> 1.3 for unfolding a population of intersection lengths into their true lengths by using a function of the intersection lengths. Further corrections involving volumetric phase abundance (based on modal area %), crystal roundness, and measurement style (major enclosing ellipse) are employed in CSDCorrections<sup>TM</sup> 1.3 to generate cumulative crystal size distributions. The resulting logarithmically-binned and stereologically-corrected data described above are used to construct several types of CSD's of olivine in coherent kimberlite. The majority of CSD's published in petrology literature use 'classic' semi-logarithmic 'CSD diagrams', in which population density is defined by size intervals. We plot the CSDs from the five samples of coherent kimberlite in a semi-logarithmic classic CSD to allow for comparison with other crystal populations from igneous rocks (Fig. 3.8a), and bi-logarithmic  $\ln N$  vs.  $\ln$  size (Fig. 3.8b) to assess an appropriate model distribution.

#### *Population verification*

To verify our calculation of the 3-D CSD from 2-D data, we use two independent measures of the modal abundance (as %) of olivine crystals: (1) point-counting in thin sections and (2) integration of the crystal volumes resulting from our CSD calculations. By comparing these two data types with the initial measured area of crystals (e.g., Table 3.1), we can verify if the scale integration and CSD corrections applied to our initial data set are in compliance with the measurements initially made by the image analysis program (i.e., area %). Point-counting is based on the understanding that the fraction of random or equally spaced points that lie on a phase,  $P_p$  is also equal to the volumetric fraction of the phase,  $V_V$ , and thus represents a stereologically exact 'global parameter'. One thousand evenly-spaced points on two thin sections were point-counted, and the resulting data are shown in Table A7.1. The volumetric proportion of olivine,  $V_V$ , is calculated by integration of the volume of all the crystals in all bin sizes of our olivine CSD using the following:

$$V_V = \sigma \int_0^{\infty} n_V(L) L^3 dL \quad (\text{A7.3.4})$$

where  $\sigma$  is the ratio of the crystal volume (assumed spheres) to that of a cube of side  $L$ . Higher order moments need to use shape factors ( $\sigma$ ) to account for departures of the crystal shapes from a cube. As our data are modeled as spheres with diameters equivalent to the area measured, we use  $\pi/6$  for  $\sigma$ . The relative volumetric proportions of olivine ( $V_{x-y}$ ) of different size bins are similar to the relative area % obtained by normalizing initial observations made in thin sections and slabs to the slab scale (Table A3.1). These results are also similar to the data obtained by point-counting from a thin section taken from the same slab (Table A3.1), suggesting that observations of modal abundance made at the thin section scale approximate larger scales of observation.

*Goodness-of-fit tests:*

To evaluate the hypothesis that each CSD fits a power-law distribution model, we first identify the best-fit power law equation and subsequently evaluate how well binned data from each sample population correspond to the model equations. This evaluation is accomplished by calculating a weighted least-squares fit to the sample data and root mean standard error (RMSE) for best-fit lines to the data.

Data are first plotted as  $\log N$  vs.  $\log L$ , where  $N_i$  is the population density in the  $i$ th bin size, and  $L$  is the diameter (mm) of the maximum axis. These linear trends are fitted using a weighted, linear least squares fit on data with the following modification of equation (1) to find the slope ( $D$ ) and intercept ( $\lambda$ ) of a straight line:

$$\log N_V = -D \log x + \log \lambda \quad (\text{A7.3.5})$$

**Table A7.2.1:** Comparison of modal abundance (%) of olivine obtained from different scales of observation and by different methods

sample	Image analysis <sup>*</sup>	Image analysis <sup>†</sup>	Image analysis <sup>‡</sup>	Point-counting <sup>§</sup>		Volume estimation <sup>  </sup>
	(t.s.) (%)	(slab) (%)	(t.s. + slab) (%)	A <sub>1</sub> (%)	A <sub>2</sub> (%)	(%)
CK04	41.8	33.8	46.7	49.6	47.3	46.0
CK05	44.3	36.8	51.2	52.8	58.4	50.4

Note: All image analysis modal areas determined by image analysis methods in present study

\* Total areas of all olivine crystals in 12.5mm x 28mm area in thin section

† Total areas of visible olivine crystals in 47mm x 77mm area in slab

‡ Total areas of scale-integrated olivine crystal populations in 47 x 77mm area

§ Est. total areas based on counts of 1000 evenly-spaced points in thin sections, at different orientations (A<sub>1</sub>, A<sub>2</sub>)

|| Denotes third-order moment calculation (eq.A4) of modal volume % (VV) from stereologically-corrected image analysis data (\*) of particle number and size

Errors on each log x, log y data point range from 0.17 to 0.29. We compute slopes ( $D$ ) +/-10, and intercepts ( $\lambda$ ) +/-10, and plot the covariance ellipse at the 95% confidence level (Figure 3.8c). This shows the range of model slopes and intercepts ( $D, \lambda$ ) that are fully consistent (at 95% confidence) with the data and their uncertainty. The variance on the model parameters for samples within a single dyke (e.g.,  $\sigma_{CK4,5p}^2$ ) are smaller than variance between dykes ( $\sigma_{pCK1,2,3; pCK4,5}^2$ ). The variance in parameters for all samples ( $\sigma_{sp}^2$ ) is greater than the variance attributed to analytical methods ( $\sigma_{ap}^2$ ), such that  $\sigma_{ap}^2 < \sigma_{sp}^2$  (e.g., Table 3.3).

We have also computed the root mean standard error (RMSE) as a measure of the differences (i.e. residuals) between values expected by the best-fit power-law models and values observed from the olivine crystal populations. The RMSE is a good measure of accuracy, as it measures the variability expected in the means of samples by repeated random collection from the same population:

$$RMSE = \sqrt{\sum_{i=1}^n \left( \frac{(O_{\lambda} - (M_D \times O_D) - M_{\lambda})^2}{n} \right)} \quad (A7.3.6)$$

where  $n$  is the number of bins,  $M_D$  and  $M_{\lambda}$  the expected model parameter values, and  $O_{\lambda}$  and  $O_D$  the observed parameter values from the iterations. RMSE error estimates for power-law fits to the CSDs are shown in Table 3.5. An RMSE close to zero means the model is a good predictor of the observed data; RMSE for all 5 samples in this study range from 0.16 to 0.31, which accords well with the estimated average uncertainties ( $\sigma_{tr} + \sigma_{thn}$ ) on each data point (0.17-0.29).

### 7.3.2 Appendix – Chapter 3: Automatic image analysis methods for crystal size distributions of olivine in kimberlite<sup>11</sup>

#### *Introduction*

Crystal size distributions (CSDs) are a standard means of describing populations of crystals within magmatic rocks (Cashman and Marsh, 1988; Higgins, 2000). These datasets provide a statistical approximation of the occurrence frequencies of specific sizes of individual grains of the target mineral, and are commonly used for describing or fingerprinting magmatic rocks. In addition, CSDs are useful for diverse petrogenetic applications, including assessing nucleation and growth rates of crystals (Cashman and Marsh, 1988; Cashman, 1990; Peterson, 1990), estimating residence times in magma chambers (Mangan, 1990; Armienti et al., 1994), identifying the effects of crystal-settling (Bindeman, 2003), or quantifying pyroclastic fragmentation intensity (Allen and McPhie, 2003; Bindeman, 2005).

Olivine is an essential mineral of crystallized kimberlite magma and usually comprises up to 50% of the rock (Clement, 1982). Olivine crystals consist of two types: larger ( $\geq 1.0$  mm), round to sub-round olivine macrocrysts that are xenocrysts of disaggregated mantle peridotites (Clement, 1982; Mitchell, 1986; Mitchell, 1995); and smaller ( $< 0.5$  mm), sub-hedral to euhedral crystals that are understood to be cognate phenocrysts resulting from crystallization of kimberlite magma (Clement, 1982; Mitchell, 1986; Mitchell, 1995). Given its modal abundance, we suggest that olivine CSDs should find use as a means of characterising kimberlite, for distinguishing or correlating between kimberlite bodies, or for linking size distributions of olivine to processes related to ascent, emplacement and eruption.

Conventional estimations of olivine modal abundances in kimberlite (area %) typically derive from point counting of rocks and thin sections. An alternative method involves manual tracing of olivine crystals and subsequent image analysis of the traced images. These techniques yield reproducible results and have been used effectively for

---

<sup>11</sup> A version of this chapter has been accepted for publication. Holden, E.J., Moss, S., Russell, J.K., Dentith, M.C., 2008. Image Analysis Methods for Crystal Size Distributions of Olivine in Kimberlite. Computational Geosciences.

coherent (e.g. Clement, 1982) and volcanoclastic kimberlite (Chapter 4; Walters et al., 2006a) but they are time consuming and can be operator dependent.

Automatic detection of olivine CSDs from kimberlite is not a trivial task. Kimberlite is highly susceptible to alteration with the result that olivine is commonly replaced by secondary minerals that are also common to the groundmass (e.g., serpentine or carbonate). A consequence of this style of replacement is that the original edges of individual olivine crystals become less distinct and difficult to identify. Moreover, rims of small olivine crystals often poikilolitically enclose spinel and perovskite crystals, creating complex grain boundaries which are difficult to identify against the groundmass. Another issue, that transcends the effects of alteration, is that the abundance of olivine in these rocks guarantees that many grains of olivine are in physical contact. These factors combine to make it difficult to accurately identify the edges of individual olivine grains to examine their size and shape distributions.

We developed an automated image analysis technique that is capable of identifying individual crystal grains of olivine within digital images of kimberlite. This technique identifies crystal grains by using multiple image cues such as colour, texture and brightness, combined with a segmentation technique to separate the joined grains to detect olivine CSD. Then experiments were conducted to demonstrate the utility of the proposed automated image analysis methods by collecting the requisite data for determining CSDs for olivine in scanned images of polished kimberlite slab samples (Figure 2.1a), and comparing these to a parallel set of olivine CSDs for the same samples using manual tracing of olivine grains (Figure 2.1b).

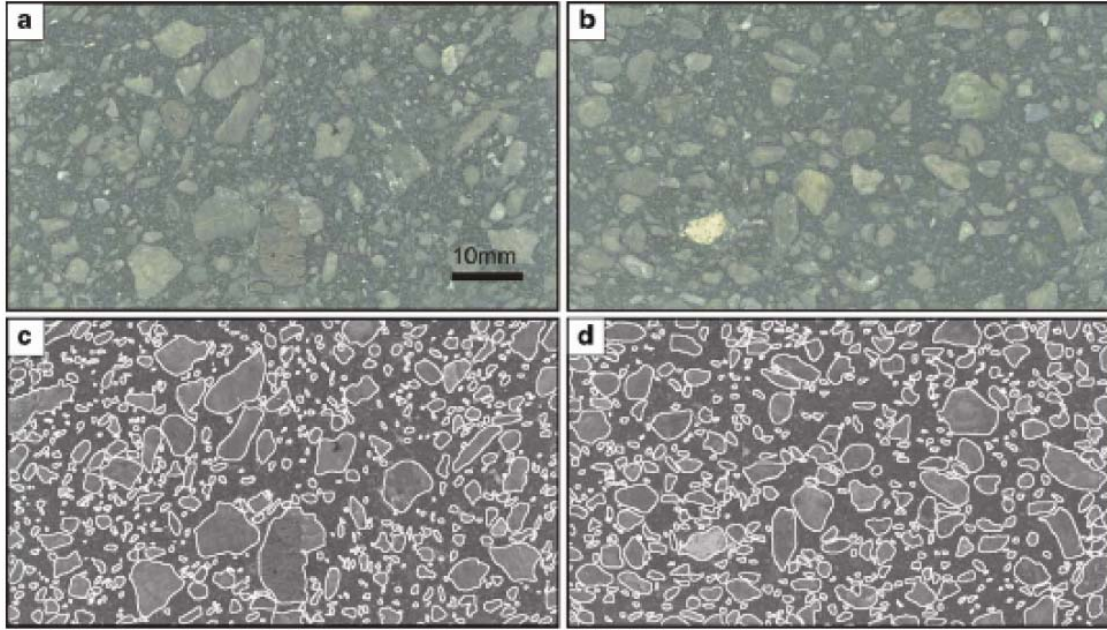


**Figure A3.1:** Images of Sample\_1 and Sample\_2 of kimberlite from Diavik kimberlite field: (a,b) Scanned images of polished rock slab (FOV =  $41 \times 75$  mm) represented by  $627 \times 1,134$  pixels; (c,d) Outputs of manually traced crystal edges from the sample images shown in a and b, respectively.

The following sections provide: (i) a literature reviews of image analysis methods used for detection of mineral grains; (ii) an overview of our automatic image analysis system; (iii) description of the methods we used for producing olivine CSD; (iv) experimental results from samples analysed using the manual and automatic methods; and (v) a comparative analysis of the two sets of results. We conclude with a discussion of possible future developments.

#### *Previous image analysis methods for mineral grain detection*

Numerous mineral grain detection methods based on image analysis have been previously reported. Some of the proposed methods process thin section images from optical polarising microscopy to identify various mineral grains. Zhou et al. (2004) use a set of sequential birefringence colour intensity images from various angular rotations of the polariser in order to identify mineral grains. From the sequential images, they generate two synthetic images using the maximum intensity of the birefringence colour and the corresponding rotation angle. The Canny edge detection technique is applied to both of these synthetic images and these results are combined and processed with a region growing algorithm and to generate grain boundaries. Some mineralogical systems are complicated by the effects of twinning within minerals which commonly causes incorrect segmentation of a mineral grain (Obara et al., 2007; Smith & Beermann, 2007). For example, Obara et al (2007) were able to more accurately segment individual calcite grains within optical polarising microscopy images of marble by decreasing the influence of twinning within mineral grains. They then applied the watershed algorithm to define the individual grains. While the above example focussed on the detection of grain boundaries, Ross et al. (1999) developed a system that can identify grain specimen based on a pattern recognition method called the genetic algorithm. Given microscopic images from a rotating polariser, they extract colour and texture information using image analysis techniques, which are then used to learn the mineral grain patterns for the genetic algorithm. Colour information consists of hue and saturation values as well as the value that represents the pleochroism using the difference between the maximum and minimum intensities of the plane light images. Texture information is represented by

standard properties of local co-occurrence matrix, such as contrast, entropy, energy and homogeneity.

Automatic detection of mineral grains within images captured from plane or cross polarised light in microscopy is a difficult task (Ross et al. 1999). For the plane polarisation, mineral grains appear as colourless, which make it difficult to segment the boundaries when two grains are adjoined. For cross polarisation, a mineral grain may appear in the images with varying colour intensities depending on the mineral type and crystal lattice orientation. Thus some researchers use scanned images of polished rock samples to identify mineral grains using reflected light rather than transmitted light, to classify mineral grains. Marschallinger (1997) use scanned images of polished rock samples including granite, quartz-syenite and metagabbro to identify minerals using red green and blue visual colour range responses. Various supervised and unsupervised learning algorithms were tested, and they showed that the supervised maximum likelihood method performed superior than the others. Launeau et al. (1994) used multi-spectral image classification technique by using RGB colours captured from scanners and CCD cameras as well as multi-element X-maps captured from electron microprobe. Principle Component Analysis (PCA) was used to de-correlate the spectral images and classification was performed using a minimum distance to the mean classification method based on a careful selection of training data.

### *System overview*

The proposed system uses scanned images of rock samples and focuses on utilising multiple image cues to identify olivine crystals, differing from most systems mentioned in Section A3.2. Our olivine CSD detection technique identifies the regions within the image that have olivine characteristics as defined by colour, local texture and brightness. These regions will be referred as olivine Regions Of Interest (ROI). These regions are then examined to identify and separate joined crystal grains to build CSDs. The method consists of 3 separate tasks as illustrated in Figure A3.2, including: (i) olivine ROI detection; (ii) segmentation; and (iii) CSD determination. Note that while our method is used explicitly for building olivine CSD within kimberlite, the capacity to

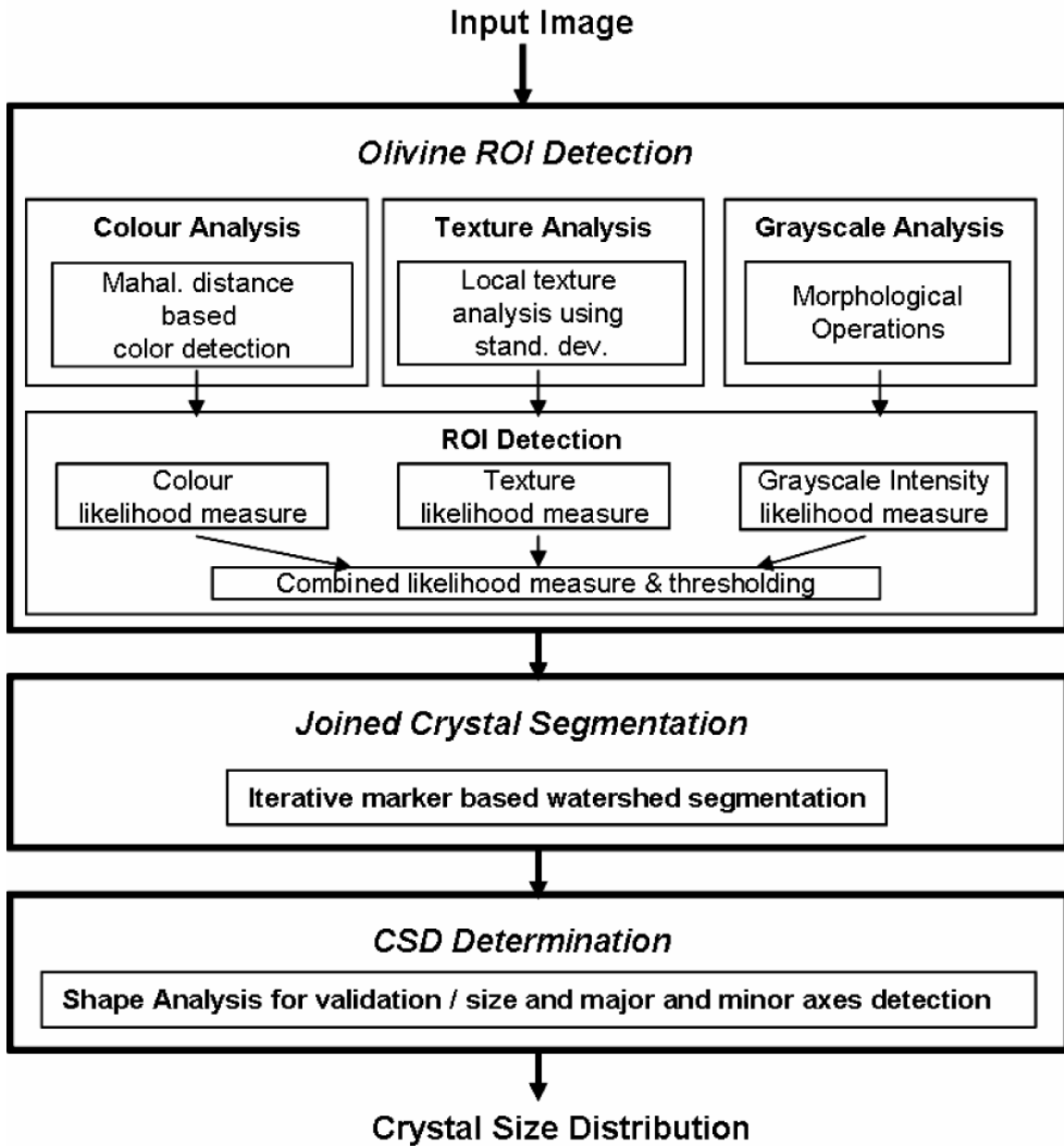


**Figure A3.2:** Summary of olivine detection system showing the three steps of analysis, including ROI detection, segmentation of adjoined crystals and data extraction for CSD determination.

handle these texturally diverse and complicated rocks ensures that our methods could easily be applied to other geomaterials.

The ROI detection process combines multiple image cues such as color, texture, and brightness. Specifically, the process comprises model-based color detection based on Mahalanobis distance; texture analysis based on standard deviation of local pixel intensities; and solid foreground object detection based on brightness and shape. These attributes are combined to determine if an image location is an olivine ROI.

Olivine crystals will commonly show slight shifts in body colour reflecting crystal orientation, internal cracks, or varying degrees of alteration. The ROI process is made more flexible in order to deal with such variations by allowing for user specified colour models. For example, a colour model can be generated by using colour regions selected from a single kimberlite sample featuring a unique style of alteration or could be selected from a range of different kimberlite samples. In addition, brightness and texture models can also be modified to deal with the variations amongst the samples being studied.

In many instances the ROI process is sufficient to identify the individual grains of olivine. However, the detected ROIs will actually comprise regions where multiple crystals are in physical contact. At this point the segmentation process is used to separate adjacent crystals that have been combined into a single ROI into individual particles. Adjoined shapes that require segmentation are identified by shape analysis. Our segmentation process is based on a well-known marker-based watershed segmentation algorithm (Meyer & Beucher, 1990), but is extended to recursively search for crystals of varying sizes while assuming the existence of edges between the crystals for segmentation. For each domain of the segmented individual crystals, shape analysis is applied for validation and identification of shape characteristics such as size, major and minor axes of the crystals.

CSDs are generated by examining characteristic properties of olivine crystals (e.g. frequency, area, perimeter). Below we discuss in detail the critical steps involved in our computer-assisted image analysis of olivine in kimberlite.

### *Olivine ROI detection*

Olivine crystals are generally brighter than the background and show a different range of colours than the matrix of the rock. Olivine grains also have a smooth texture relative to the matrix; this translates to less variations in local pixel intensity than observed in the background. The olivine ROI detection technique accommodates all of these characteristics and combines them to recognize each olivine ROI. This process comprises; colour analysis, texture analysis, grey-scale intensity analysis and then ROI detection based on the results of the first 3 steps:

#### Colour analysis

The colour analysis process uses a model-based technique based on Mahalanobis distance (Manly, 1986). A normalised RGB colour space is used to reduce the effects of brightness in the RGB colour space. That is:

$$(r, g, b) \rightarrow (a, b, c),$$

where:

$$a = \frac{r}{r+g+b}, b = \frac{g}{r+g+b}, \text{ and } c = \frac{b}{r+g+b}. \quad (\text{A3.1})$$

The olivine colour model is generated from a database of sample olivine crystal images, and is represented by its average colour component,  $m$ , where

$$m = (\bar{a}, \bar{b}, \bar{c}),$$

and a covariance matrix (C),

$$C = \begin{bmatrix} C_{aa} & C_{ab} & C_{ac} \\ C_{ba} & C_{bb} & C_{bc} \\ C_{ca} & C_{cb} & C_{cc} \end{bmatrix} \quad (\text{A3.2})$$

where  $C_{ij} = (1/n) \sum_1^n (i - \bar{i})(j - \bar{j})$ ,  $i, j \in [a, b, c]$ , and  $n$  is the number of the olivine colour samples.

The olivine crystal model forms a cluster of the sample population within the normalised RGB space. Given a colour component,  $k$ , the similarity of the colour to the olivine colour model is measured for each pixel in the image using the Mahalanobis distance (Manly, 1986),  $D$ , using:

$$D = (k - m)C^{-1} (k - m)^T \quad (\text{A3.3})$$

## Texture analysis

Image texture is represented by standard deviation of pixel intensities within the neighbourhood of each pixel, representing the degree of local intensity variations. In our implementation, a neighbourhood size of 3x3 is used to determine local textural characteristics.

## Grayscale intensity analysis

A grayscale image of the polished slab is used to enhance the foreground (or bright) objects. It performs established grayscale morphological operations such as ‘opening-by-reconstruction’ and ‘closing-by-reconstruction’ (Vincent, 1993) to remove noise within foreground object regions while retaining the shape of the objects.

## ROI detection based on colour, texture and grayscale intensity

Olivine ROI is determined by combining texture, colour and gray intensity analysis outputs. This process consists of the following two steps. The first step is to generating likelihood images that represent the confidence level within each analysis output of matching olivine. And the second step is to combine the three likelihood images to identify the olivine ROI.

### Step 1

Given the expected values and their allowed variation of colour, texture and grayscale intensity values of olivine, it finds the likelihood of a pixel matching the expected model. Note that this process is to prepare the outputs from three separate analyses that have different ranges of output values for an effective classification. For example, olivine regions are represented as low values within the texture analysis output, but as high values within the grayscale analysis output.

Therefore, given a set of colour, texture and foreground output values,  $H(i, j) = (C(i, j), T(i, j), F(i, j))$  at an image location  $(i, j)$ , the olivine model,  $M = (m_1, m_2, m_3, \sigma_1, \sigma_2, \sigma_3)$  where the colour model is specified using the mean,  $m_1$ , and the standard deviation,  $\sigma_1$ ; the texture model is specified using the mean  $m_2$  and the

standard deviation,  $\sigma_2$ ; and the brightness model is specified using the mean  $m_3$  and the standard deviation,  $\sigma_3$ , their corresponding likelihood image are as follows:

$$p_1(i, j) = e^{-(c_{i,j}-m_1)^2/(2\sigma_1^2)}, p_2(i, j) = e^{-(t_{i,j}-m_2)^2/(2\sigma_2^2)}, \text{ and } p_3(i, j) = e^{-(f_{i,j}-m_3)^2/(2\sigma_3^2)} \quad (\text{A3.4})$$

The likelihood images,  $p_1, p_2$ , and  $p_3$  consist of pixel values in the range of [0,1] where each value indicates the likelihood of the existence of olivine at that image location. Figure A3.3 shows the texture analysis output and its corresponding likelihood image.

### Step 2

This step combines three likelihood images,  $p_1, p_2$ , and  $p_3$  by averaging with their associated weights. Thus the matching likelihood  $P(H(i, j) = M)$  is calculated using a function which is defined as:

$$P(H(i, j) = M) = \alpha_1 p_1 + \alpha_2 p_2 + \alpha_3 p_3, \quad (\text{A3.5})$$

where  $\alpha_1, \alpha_2$ , and  $\alpha_3$  represent the significance of the corresponding component and

$$\sum_{i=1}^3 \alpha_i = 1.$$

This final matching likelihood image  $P(H(i, j) = M)$  is then thresholded to create a binary output, as shown in Figure A3.4.

### *Segmentation & olivine CSD detection*

#### Segmentation method

The detected olivine ROI comprise, both, individual crystals and crystals that are in physical contact. Some olivine crystals are merely touching point-to-point in 3D, while others share crystal boundaries (e.g. olivine in peridotite xenoliths). An example of adjoined crystals is shown in Figure A3.5 (top row). In order to produce accurate CSDs, it

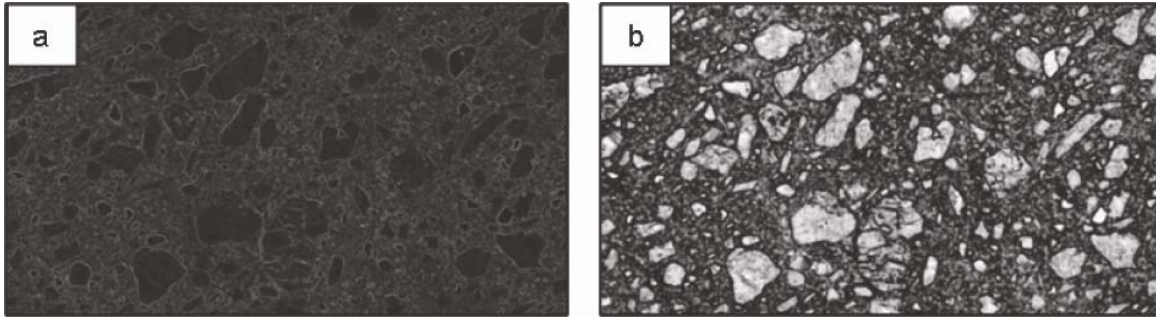


**Figure A3.3:** (a) Texture analysis output of Sample\_1. (b) Texture likelihood image.

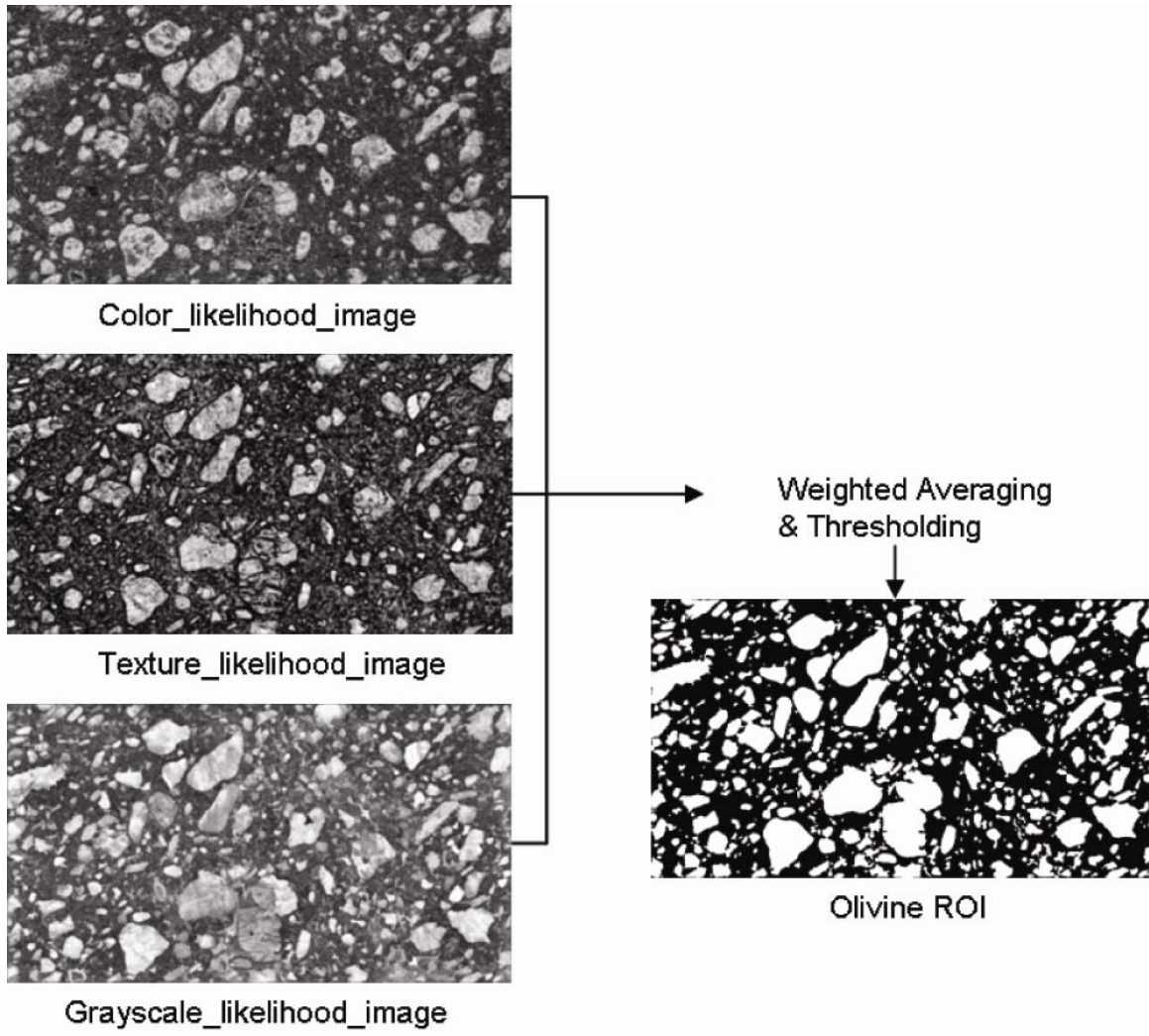


**Figure A3.4:** Combining all of the likelihood images to generate the olivine ROI.

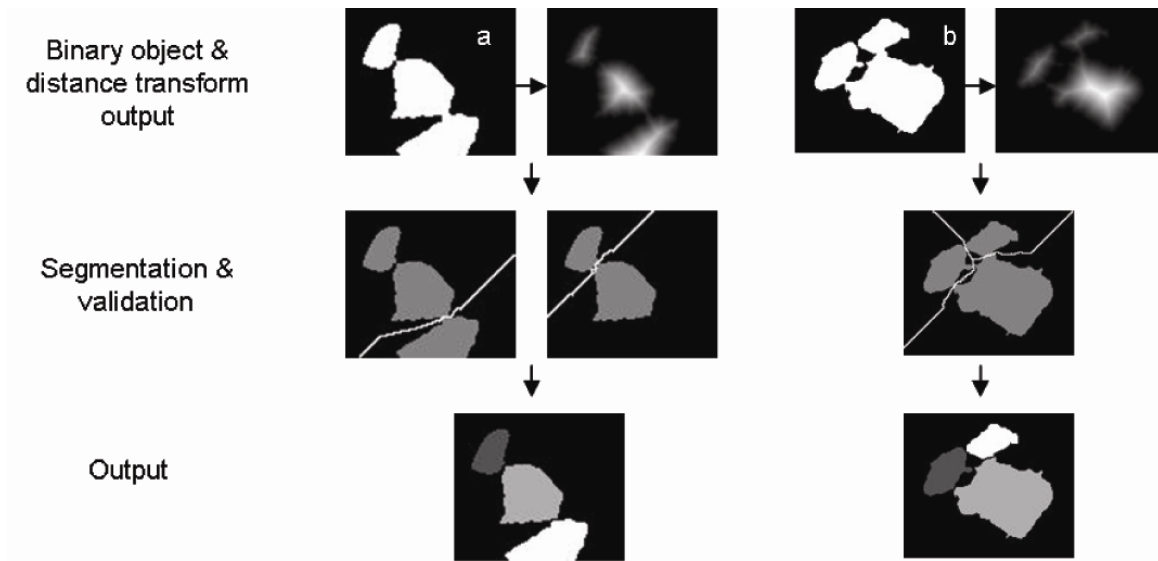


**Figure A3.5:** Two examples of segmentation. For both examples (a) and (b), the *top row* shows images of joined objects and their corresponding distance transform outputs; the *middle row* shows the iterative processes of segmenting the object using our algorithm; the *bottom row* shows the segmentation outputs where multiple objects are separated.

is essential to compensate for this effect by segmenting the crystal clots into the appropriate individual crystals. Our process separates adjoined crystals by adapting and extending the marker-based watershed algorithm. It firstly analyses the shape of each of the isolated regions within the ROI output. An adjoined crystal region is characterised by its significantly large size and a low solidity, where solidity is determined by an existence of significant non-olivine regions within the smallest convex shape that contains the object. This is possible with olivine in particular because of its generally sub-round and convex morphology.

The watershed algorithm (Meyer & Beucher, 1990) considers a grayscale image as a topographic surface where pixel intensities represent heights. Simulating the flooding of this surface, it separates the image into catchment basins and watershed lines or dams that separate water in different basins. This algorithm, however, suffers an over-segmentation problem due to its sensitivity to noise and local irregularities of gradients. A standard extension to deal with this problem is the use of markers as forced minima that are associated with catchment basins. This is called the marker-controlled watershed algorithm where markers are specified either automatically or manually. This algorithm was previously employed in a geoscientific application that segments objects in the photographic images of rocks and stones (Farfan et al. 2007). In Farfan et al's application, markers are chosen by thresholding of grayscale images. Such marker selection is not suitable for our images as a single crystal may have significant variance in pixel intensities within different areas of the crystal, which will cause the detection of multiple markers within the crystal. Our algorithm selects markers using the binary region of adjoined multiple crystals and focuses on recursively segmenting individual crystals of varying sizes using the distance transform and the watershed algorithm. As the binary object is used for the segmentation, the algorithm must verify whether the segmentation is due to adjoining of crystals or due to the shape of an individual crystal. To deal with this, once the watershed segmentation lines are detected, our algorithm validates the segmentation by examining the existence of edge pixels adjacent to the watershed segmentation line, which is the area where multiple crystals are expected to be adjoined. Our segmentation algorithm consists of the following processes:

- Apply the distance transform
- Iteratively threshold the distance transform image to find markers
- Apply marker-controlled watershed algorithm
- Validate all watershed line using the existence of edges

The distance transform operates generally from a binary image, where for each pixel, its distance to the nearest background pixel is represented as the pixel intensity in the transform output. An example of a joined object and its distance transform image are shown in the top of Figure A3.5. In the distance transform image, the pixel intensities at the crystal centres are associated with the size of the crystals. Thus, the next step uses the distance transform output to recursively choose markers to isolate the crystals.

Markers for watershed segmentation are determined by iteratively thresholding the distance transform image using a threshold value that is gradually reduced from large to small within its intensity range. For each iteration, detected markers are enforced as minima and the watershed algorithm finds the segmentation lines as shown in Figure A3.5 (middle row). Note that the example on the left shows markers of different sizes are segmented iteratively, while the example on the right is segmented in one iteration as the sizes of the two adjoining objects are similar. Each segmentation is confirmed by examining their local neighbourhood for the existence of edges. If the ratio of the edge pixels within the neighbourhood is large, the watershed line is validated and used for segmentation of the object.

#### CSD determination

Once the segmentation process completes the identification of individual olivine grains, creation of CSDs allows for shape analysis through validation and identification of their shapes. The object is validated as an olivine crystal if its size is greater than the minimal threshold of 10 pixels and if the object has a solid shape. This solidity is measured by the ratio of the area of the shape and the smallest convex form that contains the shape.

For the validated objects, the shape boundaries are modified to accommodate edge information detected from the grayscale input image. Given a validated binary object, edge pixels within a 6x6 local neighbourhood along the boundary of the object are identified, then the gap between the object boundary and the edge contour is filled using morphological dilation.

Finally, the shape characteristics of the domains, including the areas, major and minor axes lengths and their orientations, are calculated. The area is the number of object pixels, which is then converted into the unit of  $\text{mm}^2$ . The major and minor axis lengths of the bounding ellipse of the object area are calculated using the Eigen method (Horn, 1993), which are then converted into the unit of mm.

### *Experimental results*

In our experiment, the automatic image analysis as described above to collect data on olivine from two samples of kimberlite. The samples are from drill hole intersections of cross-cutting dykes of coherent kimberlite found below the A154N kimberlite pipe at Diavik in northern Canada (Chapter 4; Graham et al., 1998). Representative samples of these dykes were collected on the basis of the freshness of olivine crystals (i.e., unaltered), and the paucity of country rock xenoliths. For each of the samples of kimberlite, digital images of slabs (~45x75 mm) were prepared using a desktop scanner. The scanned digital images were then processed for modal information on olivine using both the traditional manual digitisation method and the automated process described above. In this paper two sample images used in this experiment are referred as Sample\_1, which was shown earlier in Figure A3.1a and Sample\_2 which is shown in Figure A3.6a.

#### Manual digitization method

Despite the difficulty in accurately characterizing crystal outlines, the mind's eye is remarkably adept at using variations in colour, shape, and texture to differentiate between crystals and groundmass. The manual digitization method involves the operator tracing and interpreting boundaries of olivine crystals and other components and

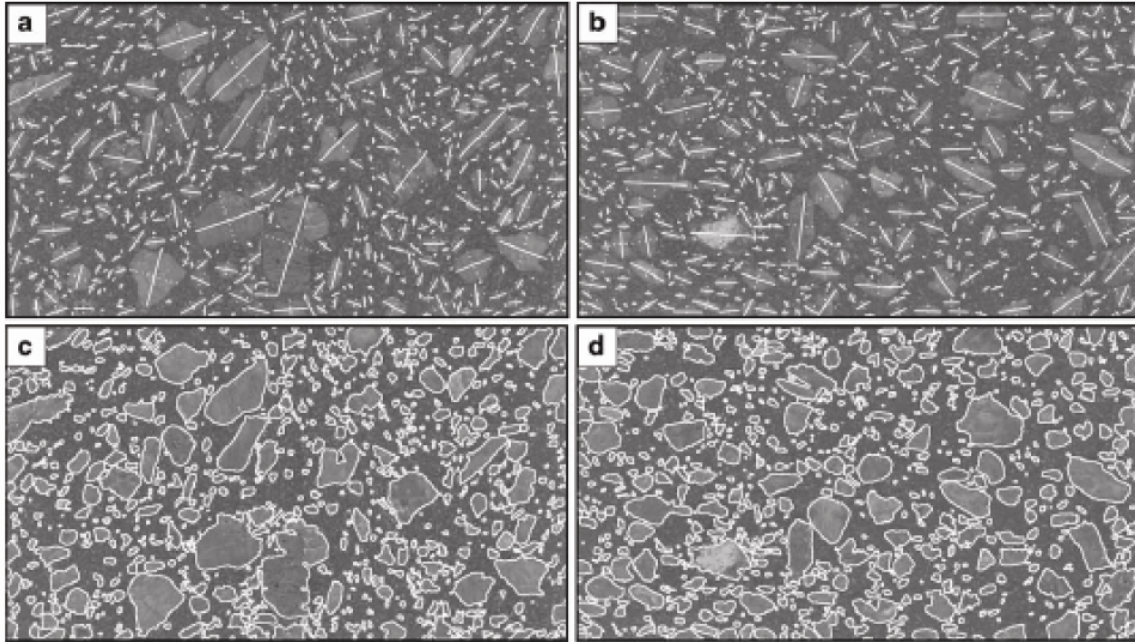


**Figure A3.6:** Results of automatic processing of Sample\_1 and Sample\_2 shown earlier in Fig. 1a and b, respectively: (a, b) Major and minor axes of individual crystals are overlaid on Sample\_1 and Sample\_2, respectively. Major axis is represented by a *solid line* and minor axis is shown as a *dotted line*; (c, d) Object boundaries of individual crystals are shown in *white*, being overlaid on Sample\_1 and Sample\_2, respectively.

therefore relies on this native skill. Examples of manual tracing are shown in Figure A3.1b and A3.6b.

Each olivine crystal outline comprises a single closed boundary. Where two crystals were in contact, each crystal was traced separately. The resulting manually traced images of olivine crystals were then analyzed to determine the number of crystals and the size (area), maximum axis length, minimum axis length, perimeter length, and orientation of each crystal.

#### Automatic crystal detection method

The automatic detection method requires a pre-processing that creates a colour model. Generating a colour model is a simple process where a user is required to select some locations within the input image that has the colour of interest to be searched. Then given a set of parameters required for the olivine ROI, including  $M, \alpha_1, \alpha_2, \alpha_3$  as defined in Section A3.4, the automatic analysis process generates the size and dimensional data for each of the individual grains within the input image.

The sample images used for this experiment contain olivine crystals and garnets, which have two distinct colour ranges. Thus, two colour models are generated and used for the automatic detection, and then these two binary ROI outputs are combined to generate the final ROI image. The colour models are generated solely from Sample\_1 and used for the testing of both Sample\_1 and Sample\_2. The output of the automatic detection for Sample\_2 is shown in Figure A3.7. Note that Sample\_2 contains a few fragments of altered granite and clinopyroxene, which were detected as olivine in this process due to their brightness rather than similarity to the olivine colour.

Example outputs of this crystal shape detection process using Sample\_1 (Figure A3.1a) are shown in Figure A3.8: (a) shows the major and minor axes of the bounding ellipse of crystals, and (b) shows the boundary tracing result.

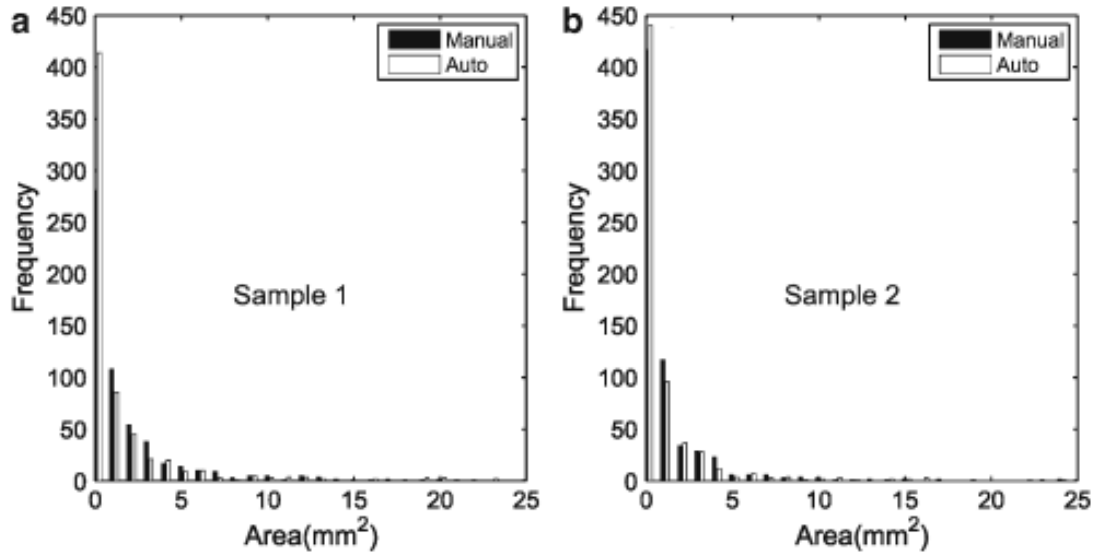


**Figure A3.7:** CSDs from manual and automatic methods applied to olivine particles in the histograms of Sample\_1 and Sample\_2. Crystal sizes are areas in square millimeters.

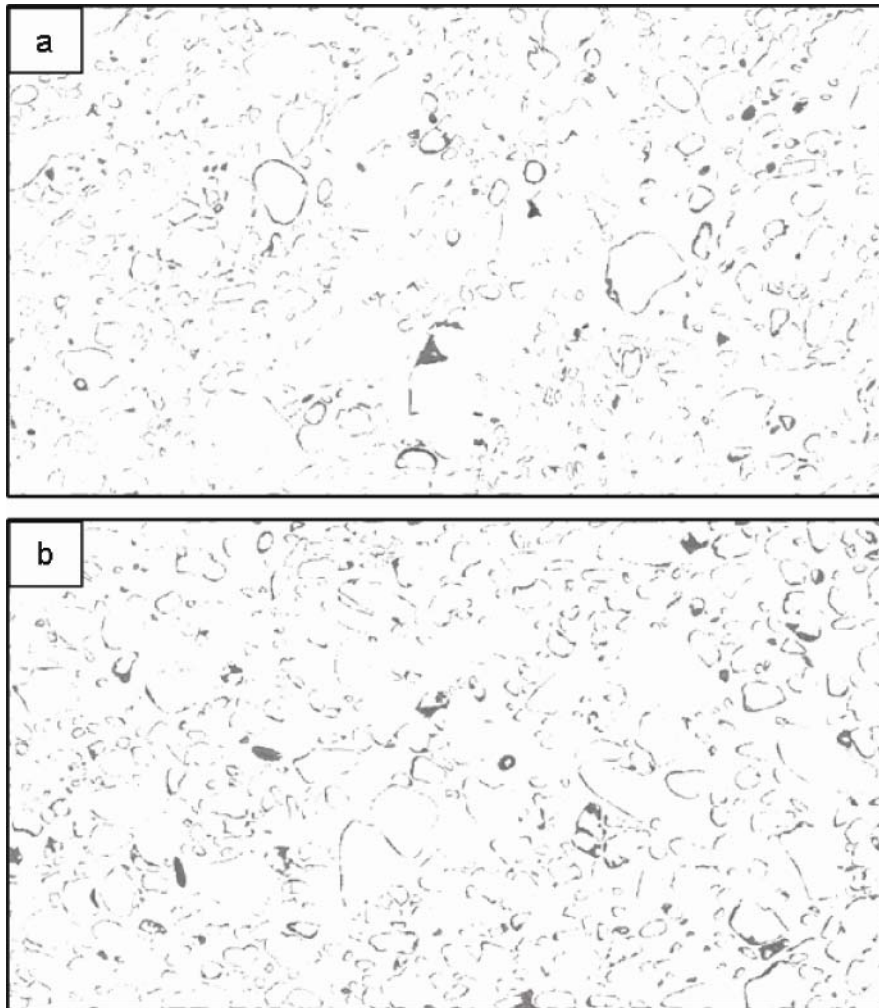


**Figure A3.8:** Regions that are identified by manual methods but not by automatic method (shown as dark regions) for Sample\_1 (a) and Sample\_2 (b).

### *Comparison of manual vs automatic results*

The automatic system was implemented in Matlab and the experiments were conducted in a 2GHz PC. An expert took approximately 6 hours to manually trace the boundaries of olivine crystals. Our automatic system took less than 1 minute for each of the samples. Below, we discuss the results by comparing the metrics (e.g. area, perimeter) produced by the two techniques and assessing the consequences of any differences.

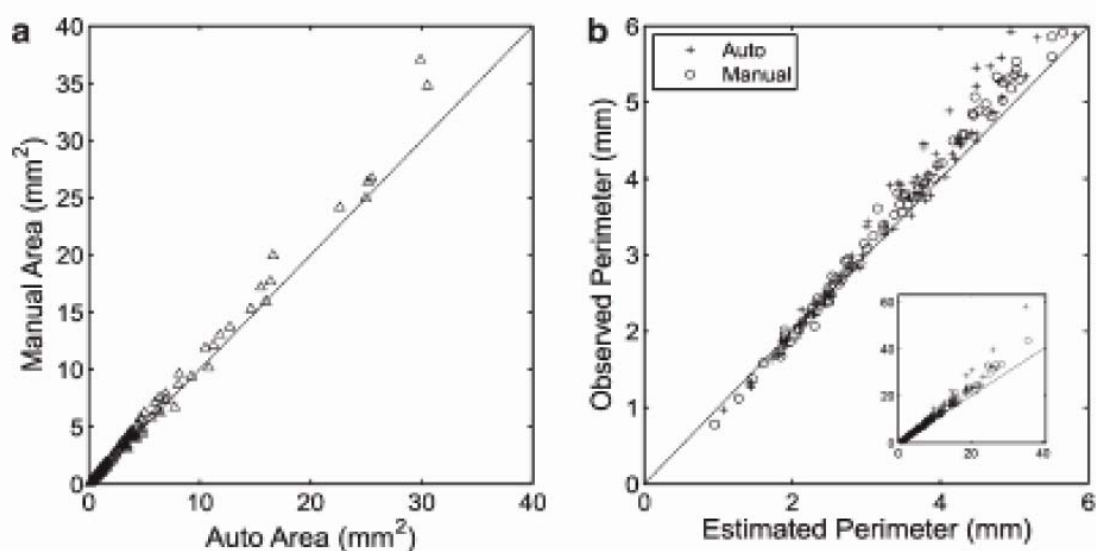
### CSD results

Table A3.2 summarises the comparative analysis results between the manual and automatic processing methods. For each of the samples and processing methods, we calculated the modal proportion (percent) of olivine ROIs over the entire image (Area\_ratio; Table A3.2) and the number of individual crystals (Number\_of\_crystals; Table A3.2). Recognition rates (Recognition\_rate\_A, B; Table A3.2) represent the proportion of the areas within the olivine regions detected from one method that are also recognized by the result from the other method.

In estimating total olivine abundance, the manual method produced an Area\_ratio of ~45%, which is slightly higher than the value (~38%) from the automatic method. These differences are also shown in the recognition rates as they show slight discrepancies between the automatic and manual detection results. The manual method correctly identifies greater than 85% of the olivine areas that were detected by the automatic image analysis. Conversely, the automatic image analysis of slab images finds great than 88% of the olivine areas that were delineated by manual tracing. The two samples however produced similar results in area ratios and recognition rates. As our colour model was generated solely from Sample\_1, the results indicate that a colour model generated from one sample can be effectively applied to process other samples with similar colour characteristics.

**Table 3.2** Recognition results

Sample methods	Sample 1		Sample 2	
	Manual	Automatic	Manual	Automatic
Area ratio (%) (detected_area/total area)	44.9	38.37	46.22	38
Number of crystals	669	655	569	640
Recognition_rate_A (%) (automatic output regions validated by manual output)	89.16		89.68	
Recognition_rate_B (%) (manual output regions validated by automatic output)	88.01		85.24	



**Figure A3.9:** Roughness test using 152 closely matched particles from the outputs of the automatic and manual methods using Sample\_1: (a) Plot of the particle sizes from the automatic method versus the particle sizes from the manual method; (b) Comparison of estimated and observed perimeters of the particles less than 6 mm in perimeter. *Inset plot* shows the distribution for all particles.

Figure A3.9 shows the size distributions detected from two samples. For both samples, size distributions from manual and automatic methods are well matched except for the crystals that are less than  $3 \text{ mm}^2$ . Close examination to the discrepancies in the numbers of small crystals revealed important differences in their capabilities of manual tracings and automatic grain detection. There is a significant difference in the frequency of crystals measured as shown in Table A3.1 (669 vs 655 for sample\_1; and 569 vs 640 for sample\_2 in Table A3.1), the number of small crystals (less than  $3 \text{ mm}^2$ ) showing the most difference (Fig. A3.9). In addition, from Sample\_1, the automatic method detected less small crystals than the manual method whereas from Sample\_2, the automatic method detected more small crystals than the manual method. Close inspection to these results revealed the following three facts. Firstly, the automatic method couldn't detect the crystals of size less than  $0.04 \text{ mm}^2$ . The automatic method applies local neighbourhood analysis for texture and foreground object detection, which reduces the small objects further as boundaries will be smoothed to the background. Further, these small objects may have been removed due when individual grain domain is validated in the CSD determination process, by not satisfying the acceptable size limit ( $< 10$  pixels). This step was necessary to remove noise. Secondly, if a small olivine is just below the actual surface of the slab, humans can see the 'projection' through the thin veil of groundmass which covers it, despite a subdued colour variation from the background which may preclude its recognition by the automatic method. Such objects cannot be detected by the automatic system as the true colour won't appear on the surface. This implies that the automatic method is a more accurate representation of the true 2D intersections of olivine. This was particularly obvious in the manual processing result of Sample\_1, resulting in more small crystals detected than the automatic method. Thirdly, subjectivity or inconsistency of manual tracing have been observed, which resulted in automatic method detecting small crystals more than manual tracing in Sample\_1, but less for Sample\_2. Our observation of the Sample\_2 outputs showed that a human tracer ignored or missed most crystals less than  $1 \text{ mm}^2$ , which were detected in Sample\_1.

## Particle shape analysis

Particle shapes from the automatic and manual methods are compared using their boundary roughness, solidity, and circularity. For this experiment, we selected 152 particles from Sample\_1 that are identified as being closely matched in their locations and sizes within the outputs from the manual and automatic methods.

### Boundary roughness

In the samples, automatic processing detected ~86% of the regions of olivine previously identified by manual tracing. Conversely, the manual tracing technique correctly identified ~89% of the regions that the automatically detection method identified as olivine crystals (Table A3.1). The regions where manual processing detected a crystal that was not identified by automatic processing correspond mostly with crystal edges, as shown in Figure A3.8. Detailed examination of these edges shows that in many cases, the automatic method produces more accurate tracing of irregular olivine crystal boundaries than the manual method. This discrepancy is likely due to default properties (e.g. ‘fidelity’, ‘smoothness’) of the tracing pen in Adobe Illustrator, which can smooth rough traces drawn by the observer. This consistent over-tracing is demonstrated in Figure A3.9a where the sizes of the crystals from the manual method are generally larger than that from the automatic method.

The ‘roughness’ of particle boundaries can be indexed by comparing the ‘observed’ perimeter lengths against the ‘estimated’ perimeter lengths of crystals (Fig. A3.9b). The estimated perimeter length is the perimeter of the bounding ellipse of the crystal that has the perfectly smooth boundary, and is calculated using

$2\pi\sqrt{\frac{(A/2)^2 + (B/2)^2}{2}}$ , where A and B are the observed maximum and minimum axis

lengths, respectively. Crystals from the automatic method have slightly ‘rougher’ or irregular boundaries than those from the manual method represented by larger perimeter lengths (Fig. A3.9b). For perimeters <4 mm, some crystals show estimated perimeters which are slightly shorter than the observed perimeters. This is due to the perimeter

calculation method that is applied to the image pixels within Matlab. Figure A3.10a shows this calculation method using a perfectly circular object that fits into the bounding rectangle of 7 x 7 pixels as an example. Given its radius,  $r$ , of 3.5 pixels, the estimated circle area and perimeter are 39.43 ( $\pi r^2$ ) and 21.99 ( $2\pi r$ ) pixels, while the observed area and perimeters are 37 and 19.31 pixels, respectively.

### Solidity

We use solidity to assess the departure of olivine shapes from convex objects (i.e., circle, ellipse). Solidity is measured by the ratio of the area of the shape (observed area) to the area of the bounding ellipse of the shape (measured area) and is shown in Figure A3.10b. Particles from both methods generally have smaller observed sizes than the estimated sizes with larger crystal sizes showing greater disparities. This means that the particles with larger sizes have more concavity or boundary irregularities. Figure A3.10b confirms this, as similar departures from estimated perimeters are apparent in the observed perimeter, suggesting that either (a) more detail of olivine crystal boundaries is observable in larger crystals or (b) larger crystals have more concavity and shape irregularity than smaller crystals.

### Circularity

To assess the circularity of olivine crystals, we compare size and shape attributes measured in olivine crystals (e.g., area, perimeter, and oblateness) to those of model shapes (circles, 2:1 ellipse, etc.) in Figure A3.11. The two methods show general agreement in olivine circularity over the entire size distribution of olivine (Fig. A3.11a, b). Note that, in Figure A3.11b, oblateness is measured using  $1 - (\text{min. axis length}/\text{max. axis length})$ . In addition, several observations regarding olivine crystals can be made from the data obtained by both methods. Firstly, no olivine particles exceed a 5:1 ratio. Second, the majority of olivine crystals appear to be best approximated by circular to 2:1 elliptical aspect ratios.

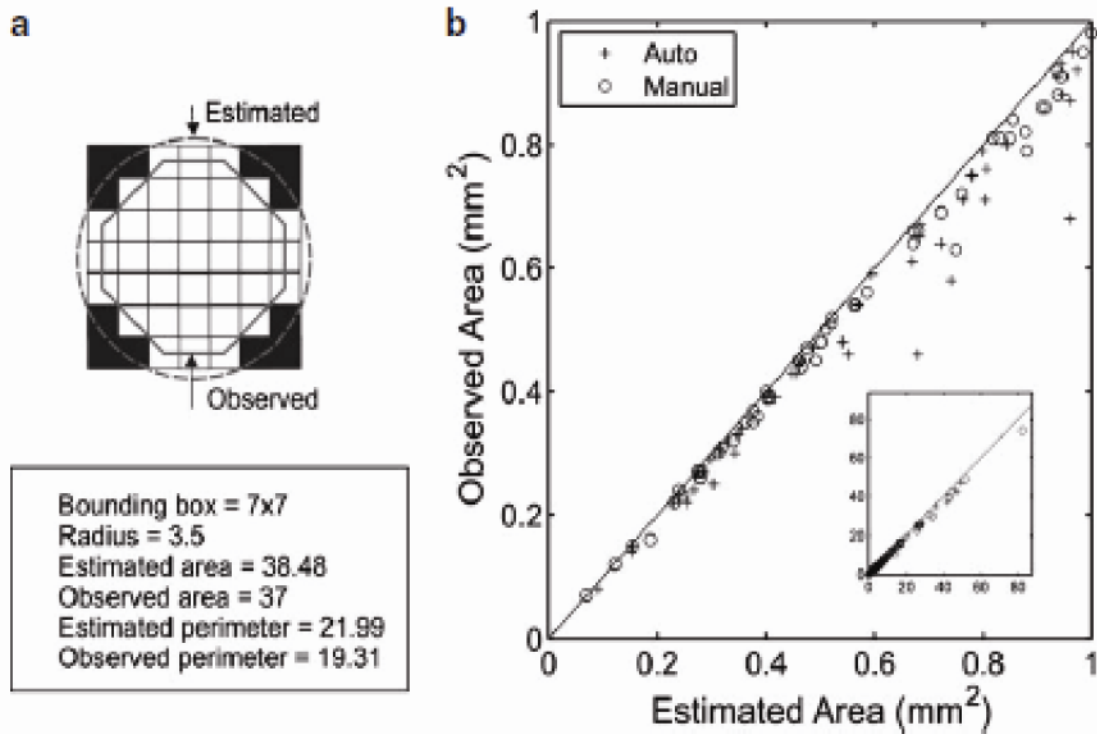


**Figure A3.10:** (a) Discrepancy between the estimated and observed perimeters and areas for an object with a  $7 \times 7$ -pixel bounding box; (b) Solidity test that compares the estimated and observed areas of the particles less than  $1 \text{ mm}^2$ . Given the maximum and minimum axis lengths of a particle,  $A$  and  $B$ , respectively, the estimated area is calculated using  $\pi(A/2)(B/2)$ . Inset plot shows the distribution for all particles.

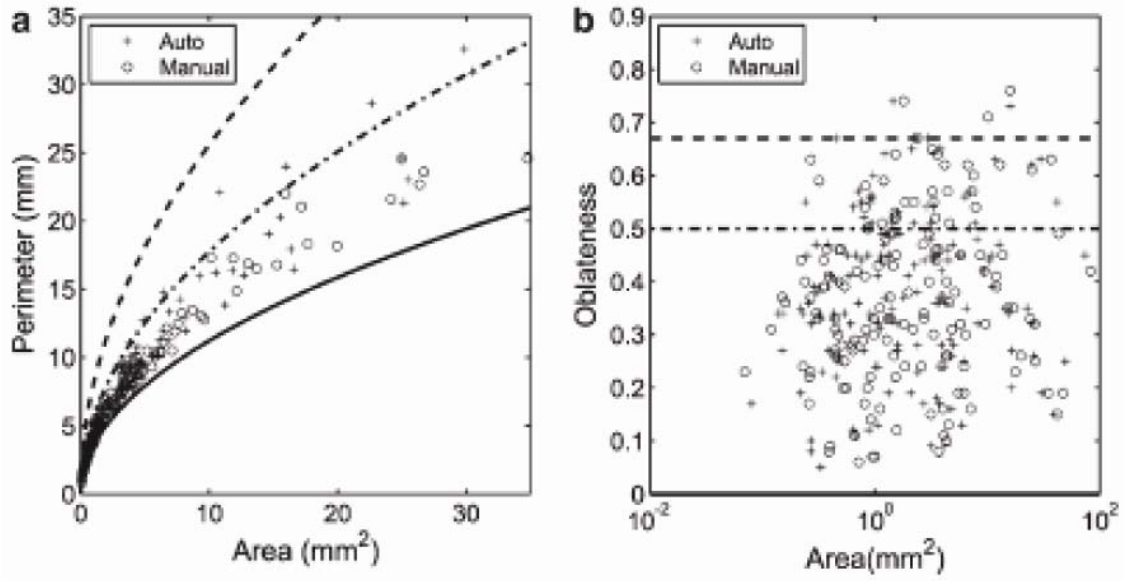


**Figure A3.11:** Circularity test: (a) Plot of area versus perimeter. *Solid line* represents their relationship for perfect circles; *dash-dot line* for the ellipse with the 2:1 axial ratio; *dashed line* for the ellipses with 5:1 axial ratio; (b) Plot of area versus oblateness of the particles. *Solid line* is for perfect circle (i.e. oblateness = 0); *dash-dot line* is for the ellipse with the 2:1 axial ratio (i.e. oblateness = 0.5); *dashed line* is for the ellipse with 3:1 axial ratio (i.e. oblateness = 0.67).

### *Summary & on-going developments*

This paper presented an automatic olivine crystal detection technique to identify individual crystals using: ROI detection based on a combination of colour, brightness and texture; and segmentation using an iterative marker-based watershed algorithm and edge detection. Comparison between the results from manual and automatic methods shows that the automatic method can reproduce similar total modal % of olivine to that obtained with manual tracing. In addition, the automated method yields a more precise perimeter measurement, allowing for a more accurate 2-D shape analysis of olivine crystals. Furthermore, faster output times for the automatic method could allow for processing of large sample sets to generate statistically-significant olivine CSDs for kimberlite bodies. Therefore, the automated method appears to provide a reliable, precise and rapid means of obtaining olivine crystal size distributions from 2-D slabs.

The automatic method, however, requires further developments in the following areas. Firstly, the automatic method can only accurately identify olivine crystals down to a certain size ( $> 0.4 \text{ mm}^2$ ). Accurate analysis of such small crystals requires finer scales of observation such as thin section or backscattered electron images where the results can then be combined to complete a CSD from a slab image. Secondly, the automatic method needs to be tested with 2-D images from a variety of kimberlite occurrences. The deviation of the area ratio between the automatic and manual methods is larger than the geological variance for olivine crystals in coherent kimberlite reported in Chapter 2. Further replicate sampling from a variety of kimberlite dykes would determine true geological variance of olivine in coherent kimberlite, and allow for testing of whether such analytical variance is permissible. Moreover, the successful application of an olivine colour model generated from one sample to another sample from the same locality represents a step towards a more automated system. However, to apply the automatic method with confidence to other kimberlite localities, more colour models for olivines from other occurrences of crystallized coherent kimberlite are necessary. In addition, colour models for olivine from kimberlite rocks with greater component diversity and textural complexity (e.g., pyroclastic kimberlite) must be tested. Lastly, our automatic method needs to be tested with rocks from varying degrees of alteration and to

demonstrate the capability to discriminate olivine crystals (fresh and altered) from other particles (e.g., fresh and altered country rock lithics).

## References

- Allen, S.R. and McPhie, J., 2003. Phenocryst fragments in rhyolitic lavas and lava domes. *Journal of Volcanology and Geothermal Research* 126, 263-283.
- Armienti, P., Pareschi, M.T., Innocenti, F. and Pompilio, M., 1994. Effects of magma storage and ascent on the kinetics of crystal growth. *Contributions to Mineralogy and Petrology* 115, 402-414.
- Bindeman, I.N., 2003. Crystal sizes in evolving silicic magma chambers. *Geology* 31,367-370.
- Bindeman, I.N., 2005. Fragmentation phenomena in populations of magmatic crystals. *American Mineralogist* 90, 1801-1815.
- Cashman, K.V., 1990. Textural constraints on the kinetics of crystallization of igneous rocks. In: P.E. Ribbe (Editor), *Modern methods of igneous petrology* Geological Society of America, Washington D.C., pp. 259-314.
- Cashman, K.V. and Marsh, B.D., 1988. Crystal size distribution (CSD) in rocks and the kinetics and dynamics of crystallization II, Makaopuhi lava lake. *Contributions to Mineralogy and Petrology* 99, 401-405.
- Clement, C.R., 1982. A comparative geological study of some major kimberlite pipes in the Northern Cape and Orange Free State, PhD thesis, University of Cape Town, Cape Town, South Africa.
- Farfan, C., Salinas, R.A., Cifuentes, G., 2007. Estimation of the size distribution of particles moving on a conveyor belt. *Minerals Engineering* 20(1), January, 72-83
- Graham, I., Burgess, J.L., Bryan, D., Ravenscroft, P.J., Thomas, E., Doyle, B.J., Hopkins, R. and Armstrong, K.A., 1998. Exploration History and Geology of the Diavik Kimberlites, Lac de Gras, Northwest Territories, Canada. In: J.J. Gurney, J.L. Gurney, M.D. Pascoe and S.H. Richardson (Editors), *Proceedings of the VIIth International Kimberlite Conference*. Red Roof Design, Cape Town, South Africa, pp. 262-279.
- Higgins, M.D., 2000. Measurement of crystal size distributions. *American Mineralogist* 85, 1105–1116.
- Launeau P., Cruden, A., and Bouchez, J., 1994. Mineral recognition in digital images of rocks: A new approach using multichannel classification, *The Canadian Mineralogist*, 32, 919-933.
- Manly, B. F. J., 1986. *Multivariate Statistical Methods: A Primer*. Chapman and Hall, London
- Mangan, M.T., 1990. Crystal size distribution systematics and the determination of magma storage times: The 1959 eruption of Kilauea volcano, Hawaii. *Journal of Volcanology and Geothermal Research* 44(3-4), 295-302.
- Marschallinger, R., 1997. Automatic mineral classification in the macroscopic scale, *Computers & Geosciences*, 23(1), 119-126.
- Meyer, F., and Beucher, S., 1990. Morphological segmentation, *Journal of Visual Communication and Image Representation*, 1, 21-45.
- Mitchell, R.H., 1986. *Kimberlites: Mineralogy, Geochemistry and Petrology*. Plenum Press, New York, 442 pp.
- Mitchell, R.H., 1995. *Kimberlites, Orangeites and related rocks*. Plenum Press, New York.

- Obara, B., and Kozusnikova, A., 2007. Utilisation of the image analysis method for the detection of the morphological anisotropy of calcite grains in marble, *Computational Geosciences*, 11, 275-281.
- Peterson, T.D., 1990. Petrology and genesis of natrocarbonatite. *Contributions to Mineralogy and Petrology*, 105, 143-155.
- Roerdink, J. B. T. M., and Meijster, A., 2001. The watershed transform: Definitions, algorithms and parallelization Strategies. *Fundamenta Informaticae*, 41, 187-228.
- Ross, B. J., Fueten, F., and Yashkir, D. Y., 2001. Automatic mineral identification using genetic algorithm, *Machine Vision and Applications*, 13(2), 61-69.
- Smith, J. V., and Beermann, E., 2007. Image analysis of plagioclase crystals in rock thin sections using grey level homogeneity recognition of discrete areas, *Computers & Geosciences*, 33, 335-356.
- Vincent, L., 1993, Morphological grayscale reconstruction in image analysis: Applications and efficient algorithms, *IEEE Transactions on Image Processing*, 2(2), April, 176-201.
- Walters, Phillips, J.C., Brown, R.J., Field, M., Gernon, T., Stripp, G. and Sparks, R.S.J., 2006. The role of fluidisation in the formation of volcanoclastic kimberlite: Grain size observations and experimental investigation. *Journal of Volcanology and Geothermal Research* 155(1-2), 119-137.
- Zhou, Y., Starkey, J., and Mansinha, L., 2004. Identification of mineral grains in petrographic thin section using phi- and max-images, *Mathematical Geology*, 36(7), October, 781-801.

7.3.3 Appendix – Chapter 3	(digital)
<b>7.4 Appendix – Chapter 4</b>	(digital)
<b>7.5 Appendix – Chapter 5</b>	(digital)
<b>7.6 Appendix – Chapter 6</b>	(digital)
<b>7.7 Appendix – Chapter 7</b>	(digital)

## **7.8 List of presentations during PhD**

### 7.8.1 Peer-reviewed publications

**Moss, S.**, Russell, J.K., Scott Smith, B.H., Brett, R.C. Olivine crystal size distributions in coherent kimberlite. *American Mineralogist* (submitted April, 2009).

**Moss, S.**, Russell, J.K., Brett, R.C., Andrews, G.D.M., 2009. Spatial and temporal evolution of kimberlite magmas at A154N, Diavik, Northwest Territories, Canada. *LITHOS* (accepted, April, 2009).

Brett, R.C., Russell, J.K., **Moss, S.** Olivine in kimberlite: phenocryst or imposter? *LITHOS* (accepted, April, 2009).

**Moss, S.**, Russell, J.K. and Andrews, G.D.M., 2008. Progressive infilling of a kimberlite pipe at Diavik, Northwest Territories, Canada: Insights from volcanic facies architecture, textures, and granulometry. *Journal of Volcanology and Geothermal Research* 174, 103-116.

Holden, E.J., **Moss, S.**, Russell, J.K., Dentith, M., 2009. An Image Analysis Method to Determine Crystal Size Distributions of Olivine in Kimberlite. *Computational Geosciences* 13, 255-268.

### 7.8.2 Conference abstracts

#### Oral Presentations

**Moss, S.**, Russell, J.K., Brett, R.C., Andrews, G.D.M. Fragmentation of kimberlite: insights into eruption style and energy from Diavik, NWT. 2009 AGU-GAC Joint Assembly in Toronto, Ontario, Canada, May 2009. 15 minutes.

**Moss, S.**, Russell, J.K., McLean, H., Fomradas, G., Eichenberg, D. Spatio-Temporal evolution of kimberlite magmas at Diavik, NWT. 9<sup>th</sup> International Kimberlite Conference (IKC), Frankfurt, Germany, August, 2008. 15 minutes.

**Moss, S.**, Russell, J.K., Brett, R.C., Andrews, G.D.M. Fragmentation of kimberlite: insights into eruption style and energy from Diavik, NWT. International Association of Volcanology and Chemistry of the Earth's Interior (IAVCEI) General Meeting, Reykjavik, Iceland, August, 2008. 15 minutes.

**Moss, S.**, Russell, JK, 2007. Crater infill at Diavik: facies architecture, textures, and implications for volcanic processes. GACMAC Annual Meeting (oral presentation), Yellowknife, NWT, Canada.

**Moss, S.**, Russell, JK, 2006. Kimberlite Garbage Cans? Cross-fertilization in a kimberlite pipe at Diavik. 2006 NWT Geosciences Forum, Yellowknife, NWT, Canada.

**Moss, S.**, 2006. Kimberlite Garbage Cans? Graduate Seminar, University of British Columbia, Vancouver, B.C.

#### Posters

**Moss, S.**, Russell, J.K., Brett, R.C., Andrews, G.D.M., 2008. Fragmentation of kimberlite: insights into eruption style and energy from Diavik, NWT. 9<sup>th</sup> International Kimberlite Conference, Frankfurt, Germany.

**Moss, S.**, Russell, J.K., Brett, C., 2008. Pyroclasts from eruption at Diavik. BC Minerals Roundup, Vancouver, BC.

**Moss, S.**, Russell, J.K., Eichenberg, D., Clarke, G., Young, R., 2007. Crater infill at Diavik: facies architecture, textures, and implications for volcanic processes. IUGG General Meeting, Perugia, Italy.

**Moss, S.**, Russell, J.K., Eichenberg, D., Clarke G., Young, R., 2007. Cross-fertilizing kimberlite eruptions at Diavik: facies architecture, textures, and implications for volcanic processes. BC Minerals Roundup, Vancouver, BC.

**Moss, S.**, Russell, J.K., Eichenberg, D., Clarke, G., Young, R., 2006. Cross-fertilizing pyroclastic kimberlite airfall at Diavik, NWT: textures, granulometry, & implications of subaerial and subaqueous deposits. Kimberlite Emplacement Workshop (poster presentation), Saskatoon, SK.

**Moss, S.**, Russell, J.K., Eichenberg, D., Clarke, G., Young, R., 2006. Pyroclastic origins of mega-graded kimberlite bed at Diavik. GACMAC Annual Meeting (poster presentation), Montreal, QC.

### 7.8.3 Other publications

Harder, M., Pittari, A., **Moss, S.**, and Gernon, T. 2007. Conference News: 2006 Kimberlite Emplacement Workshop. Elements, 3(2), p.127.

**Moss, S.**, Russell, J.K., McLean, H., Fomradas, G., Eichenberg, D., 2008. Spatio-Temporal evolution of kimberlite magmas at Diavik, NWT. 9<sup>th</sup> International Kimberlite Conference Long Abstract, Frankfurt, Germany. 3pgs. 9IKC-A-00302.

Russell, J.K., Gordon, T.M., **Moss, S.**, 2008. Volatiles in kimberlite: Volume Relationships and Implications for Conduit and Eruption Dynamics. 9<sup>th</sup> International Kimberlite Conference Long Abstract, Frankfurt, Germany. 3pgs. 9IKC-A-00299.

Brett, R.C, Russell, J.K., **Moss, S.**, 2008. Origins of olivine in kimberlite: Phenocryst or Imposter? 9<sup>th</sup> International Kimberlite Conference Long Abstract, Frankfurt, Germany. 3pgs. 9IKC-A-00298.

**Moss, S.**, Russell, J.K., Brett, R.C., Andrews, G.D.M., 2008. Fragmentation of kimberlite: insights into eruption style and energy from Diavik, NWT. 9<sup>th</sup> International Kimberlite Conference Long Abstract, Frankfurt, Germany. 3pgs. 9IKC-A-00290.

**Moss, S.**, Russell, J.K., 2006. Pyroclastic origins of the mega-graded bed at Diavik, Kimberlite Emplacement Workshop Long Abstract, 5pgs.

Russell, J.K., **Moss, S.**, 2006. Volatiles and Kimberlite Eruption: Insights from Diavik. Kimberlite Emplacement Workshop Long Abstract volume, 5pgs.

### 7.9 Published papers (as of 06.25.06)

7.9.1 Moss et al., 2008, JVGR (digital)

7.9.2 Moss et al., 2009, LITHOS (digital)

7.9.3 Holden et al., 2008, Computational Geosciences (digital)